Vibration Characteristics of Stepped Thickness Circular Cylindrical Piezoelectric Shells for Ultrasound Amplifications

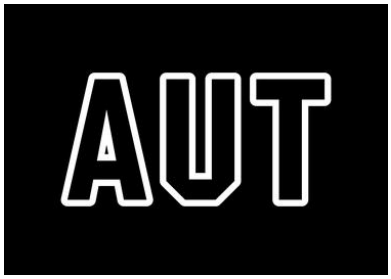

Ata Meshkinzar

A thesis submitted to Auckland University of Technology in fulfilment of the requirements for the degree of Doctor of Philosophy (PhD)

2018

Faculty of Design & Creative Technologies

School of Engineering, Computer & Mathematical Sciences

Institute of Biomedical Technologies (IBTec)

Primary Supervisor: Professor Ahmed Al-Jumaily

Abstract

This research investigates the vibration characteristics of stepped-thickness cylindrical shells with a specific application to ultrasound power amplifications for water particle disintegration. One of the main purposes is to develop an ultrasound transducer with large acoustic power and relatively small power consumption. Stepped-thickness variations are introduced to develop alternative thick-thin regions and then large localized vibration amplitudes within the transducer to maximise the acoustic field for the same driving power input. The curvature of the cylindrical shell combined with piezoelectricity and the localized vibration constructive interferences at the centreline of the transducer work together to enhance the resultant focused acoustic field. This work led to a transducer which generates an acoustic field with approximately double acoustic pressure for the same power supply as compared with a uniform-thickness transducer. Computer simulation as well as experimental investigation are used to optimise the performance of this transducer. The transducer was successfully used to disintegrate water droplets to smaller sizes. It is anticipated that this finding will be implemented to disintegrate particles for various applications including biomedical humidification for lung supportive devices.

Acknowledgements

I would like to express my deepest gratitude to my primary supervisor, Professor Ahmed Al-Jumaily for his input, support and guidance throughout the whole journey. Further, I would like to appreciate my second supervisor, Associate Professor Loulin Huang. Special appreciation for Mr Paul D Harris from Callaghan Innovation, Wellington who helped in manufacturing and machining the material. Mr Brett Holden and Mr Daniel Moore from the Electrical Workshop are also acknowledged for their help and support. I would also like to appreciate my supervisor again for his financial support from IBTec. Ms Jo Stone is also acknowledged for her help and support.

Lastly, I would like to appreciate my parents who have always been by my side emotionally, though far apart physically. Your contribution is extremely acknowledged from the bottom of my heart.

Table of Contents

Attestation of Authorship

I hereby declare that this submission is my own work and that, to the best of my knowledge and belief, it contains no material previously published or written by another person (except where explicitly defined in the acknowledgements), nor material which to a substantial extent has been submitted for the award of any other degree or diploma of a university or other institution of higher learning.

10/10/2018

List of Figures

List of Tables

Chapter 1: Introduction

1.1. Introduction

In this chapter, an introduction and background to our research will be presented. Brief descriptions of the topic, its common applications, pitfalls and shortcomings of the current methods and approaches will be elaborated on. Accordingly, the general framework for our study will be clarified, although the detailed description will be explained in the following chapters after the literature review and discussing the research gaps in the literature.

1.2. Background & Applications

Ultrasonic transducers have been receiving a great deal of attention during the past few decades because of their wide variety of applications as sensors or actuators in flaw detection, thickness gaging, materials research, medical diagnostics and therapy as well as sonar. In many biomedical, pharmaceutical and industrial applications, ultrasonic transducers can be used as atomizers. Humidifiers, micro/nano electronics, nanoparticles synthesis, spray coating, drug delivery, drug preparation for inhalation and others are among the most common applications of atomization for which ultrasonic transducers can play an important role and can be extremely beneficial. Some of these common applications for ultrasonic transducers are illustrated in Figs.1-1 and 1-2 for a humidifier and a spray coating system with nozzle transducer, respectively.

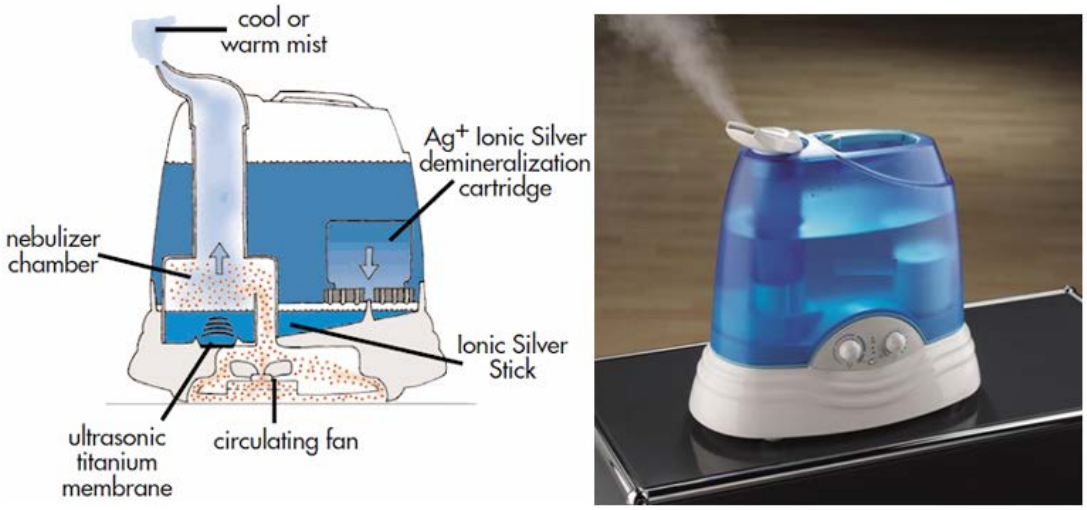

Fig.1-1. A humidifier unit with ultrasound transducer.

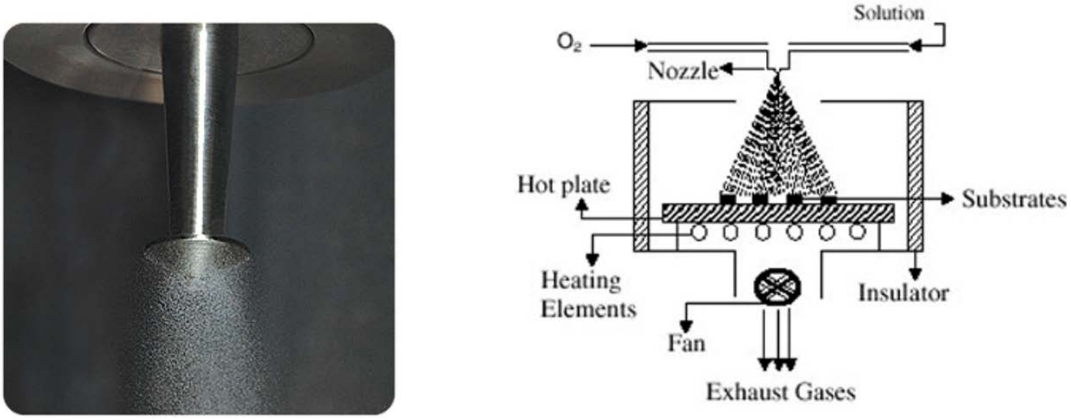

Fig.1-2. Spray coating using ultrasound transducer.

Fig.1-3 shows an ultrasonic transducer for drug delivery purposes. Droplets <10µm in diameter are highly desirable for various medical purposes. For pulmonary microcirculation-related applications, the droplets must be smaller than 7µm in diameter to safely pass through the micro vessels of the lung without causing obstruction [19]. For delivering drugs to the respiratory system, droplets of 3 to 5µm are ideal depending on the disease and its site [20]. For delivery of medications to the alveolar capillary bed, 1–3µm droplets (optimal at 2µm) are ideal [20, 21]. However,

delivery for humidification, such as in lung therapy, requires humidified air where water particles are much smaller than 1 μm. Inhalation is an attractive route for non-invasive delivery of drugs [22-25]. Peptides and proteins easily break down by enzymes in the stomach when taken orally [22, 24]. To tackle this issue, inhalation helps to suitably deliver them to the targeted location without being affected by the stomach enzymes.

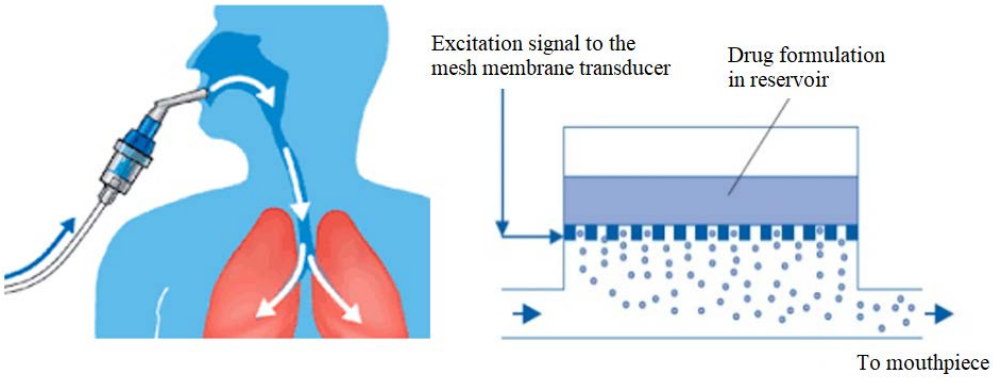

Fig.1-3. Ultrasound transducer for drug delivery.

Current commercial biomedical devices (Misty-Neb, Aero Eclipse, Omron, Pari eFlow, and Philips I-neb) produce droplets or aerosols by compressed air, a vibrating piezoelectric plate together with a metallic mesh or a vibrating mesh. Fig.1-4 clarifies two types of ultrasonic transducers with mesh membranes namely as active and passive nozzles. These common commercial devices suffer from broad droplet size distributions and low throughput, which makes it difficult to deliver sufficient dosages of drugs precisely and rapidly to the targeted sites [26, 27]. Furthermore, the eFlow and I-neb which utilize vibrating mesh technology [28] and are considered the most advanced commercial devices, suffer from clogging of the mesh orifices [29]. Heating can also be used to atomize and produce droplets. However, ultrasonic atomization

provides significant energy and space savings compared to conventional heated humidifiers [30].

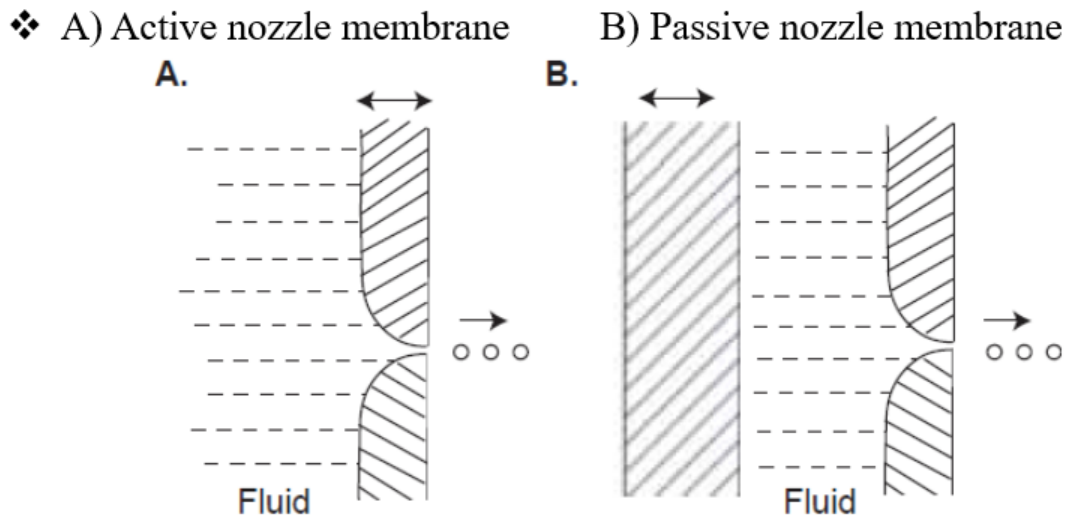

Fig.1-4. Ultrasound transducer with active and passive mesh membranes.

Hence, atomization is an important application of ultrasonic transducers, in particular in biomedical applications. Therefore, some researchers focused on the mechanism of the atomization itself which is definitely of great help and importance to further improve the performance of the transducers. However, most of these studies focus on the performance of such devices for atomization rather than evaporation of the generated droplets. Nonetheless, some investigations were performed on methods to evaporate water droplets. These methods include resonant excitation and disintegration in air, acoustic squeezing and disintegration and finally solid surface excitation [31-37] . The problem is that all these were done on a single large droplet of mm-size diameter not a stream of micro droplets.

To the best of the author's knowledge, the only application of such transducers for evaporation was a cylindrical chamber driven by a piezoelectric transducer which was used for drying foodstuff using the acoustic field generated inside the transducer [15]. Fig.1-5 illustrates the cylindrical chamber (with internal diameter 100 mm, height 310

mm and 10 mm thickness) and the ultrasonic transducer. The same set-up was employed to the aim of evaporating droplets from a first stage atomizer [1]. However, there are issues associated with this. It requires very expensive and bulky electric amplification as in Fig.1-6. The input power is as high as 75W to generate around 155 dB which is required to enhance the evaporation rates. However, it was reported that the generated ultrasound field caused coalescence of droplets forming even larger droplets. Therefore, it is not strong enough to improve droplets size distribution and has an adverse effect on it. Hence, it is unsuitable for biomedical applications such as humidification, drug delivery etc. mainly due to the bulkiness of the drive, high power input, costly equipment and insufficient output sound pressure.

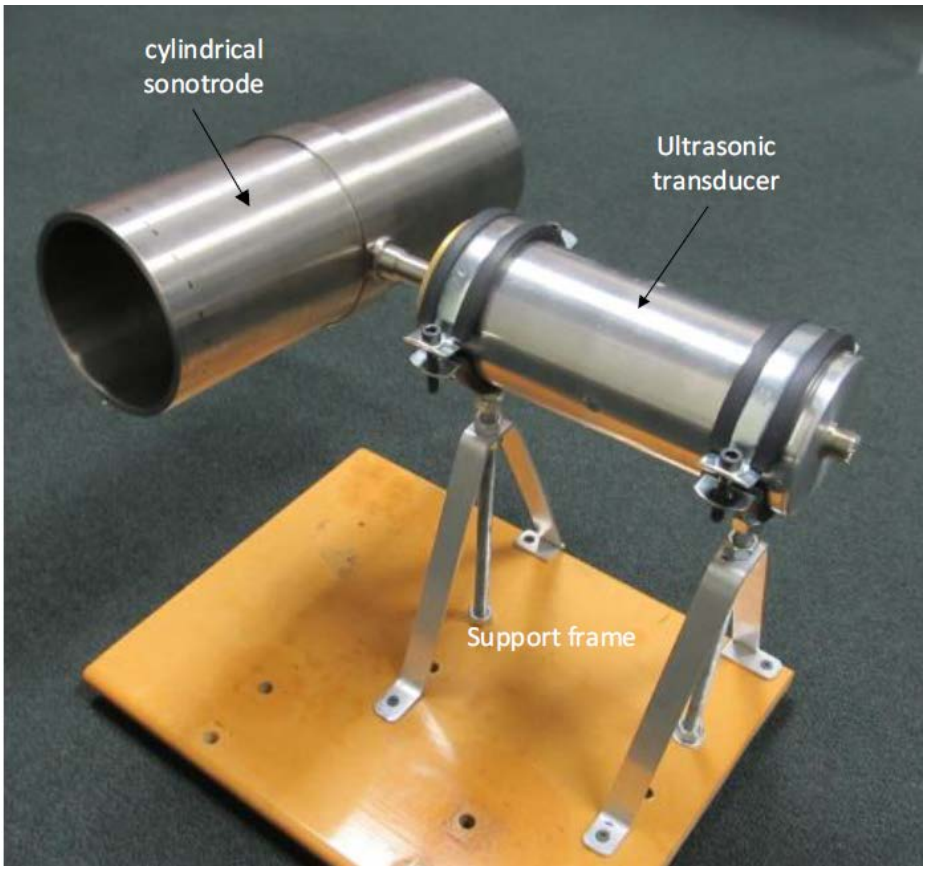

Fig.1-5. Cylindrical shell with Ultrasound transducer [1].

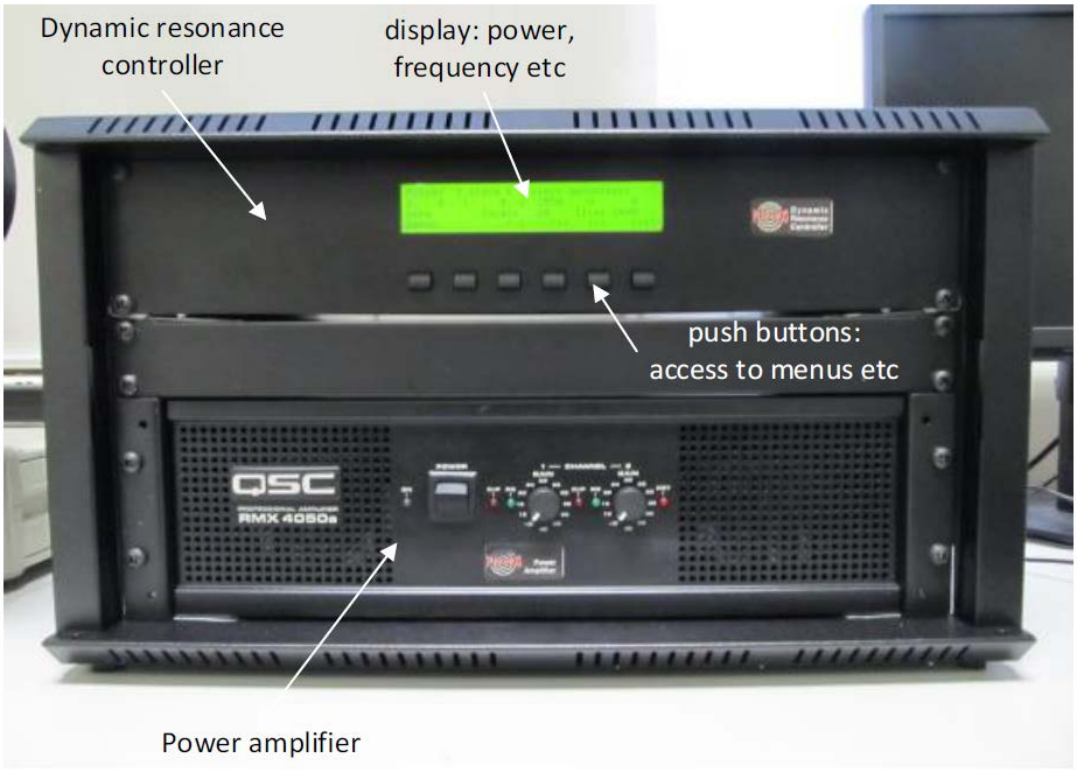

Fig.1-6. Power supply for the ultrasound transducer [1].

1.3. Research Topic

According to the explanations above and deficiencies of the current devices and techniques as mentioned, further improvement of available devices or devising new compact atomizers capable of evaporating water droplets is of practical importance, in particular in medical therapy devices such as those used for lung therapy. Therefore, the optimum goal is to develop a low-cost and low-power ultrasound transducer for liquid particle disintegration and evaporation.

It is worth noting that an inseparable part to further improve existing vaporizing devices and technologies for atomization is to thoroughly investigate and thrive the vibration characteristics of the transducers. Hence, to tackle the issues mentioned in the previous section, it is intended to use a piezoelectric cylindrical shell with a suitable size for the intended application which can be driven by a small and inexpensive PCB.

Further, variations will be introduced in the geometry of the transducer to amplify the acoustic field for the same driving power input as a uniform-thickness transducer. This is anticipated to generate strong enough acoustic fields which are capable of evaporating liquid particles and reducing droplets size distribution. More details and explanations will be given in the following chapters regarding the proposed method and the approach to follow.

Chapter 2: Literature Review

2.1. Introduction

This chapter presents an introduction to the investigations already performed in the literature within the framework of this thesis. Since the literature is so rich and plentiful on the vibration investigations, only the most related topics and researches are included. Vibration, acoustic radiation and amplification of plates, stepped plates, uniform, stepped or variable thickness elastic and piezoelectric shells are presented and elaborated on.

Since it is endeavoured to take into account the required design considerations for one of the applications as a second stage atomization transducer, a brief literature review on the considered application will be presented at the end of this chapter. Accordingly, some researches performed on droplet generation using various piezoelectric transducer configurations will be explained. These will result in clarification of the research gaps which form the framework of this study and will be investigated in this research. The optimum goal of this research is to develop a low-cost and low-power ultrasound transducer for liquid particle disintegration. It is anticipated this goal will lead to liquid particle evaporation and hopefully air humidification for lung supportive devices. Current technologies use bulky evaporative heat transfer to deliver humidified air in lung supportive devices. This research is of the first kind to use ultrasound technology for air humidification. In this work, we are proposing to use piezoelectric cylindrical shells with stepped-thickness variations to generate the proposed low-cost and power transducer. Therefore, this literature survey will focus on the use of stepped-thickness variations for acoustic field amplification in particular using plates and shells.

2.2. Plates

Vibration of plates has been extensively analysed and investigated theoretically and experimentally in the literature. The fundamental equations of classical plate theory are all presented in [38, 39]. Plates of various shapes such as circular, elliptical, rectangular etc. are investigated in each chapter [39]. Anisotropic plates as well as plates of variable thickness have been considered with various types of boundary conditions. This book is a good and comprehensive source for getting familiar with the theory of plates and vibration analysis of various plates. To briefly review, the classical differential equation of motion for the transverse displacement, w, of a plate is given by

$$D\nabla^4 w + \rho \frac{\partial^2 w}{\partial t^2} = 0 \tag{2-1}$$

where D is the flexural rigidity as

$$D = \frac{Eh^3}{12(1-\nu^2)} \tag{2-2}$$

in which E is Young's modulus, h is the plate thickness, ν is Poisson's ratio and ρ is mass density per unit area of the plate. The above equation can be solved for plates of various boundary conditions to give the frequency and mode shapes the results of which can be found in [38, 39] as well as the derivation of the equation of motion and various solution methods.

2.3. Stepped Plates

Vibrating plates can be used as ultrasonic radiators in fluids; however, the directivity of the generated acoustic waves is a matter of great importance. The radiations from different parts of a simple flat plate with constant thickness are in counter-phase

leading to phase cancellation and therefore, poor directivity. On the contrary, if one considers a plate with some steps on the surface raised half a wavelength of the radiated sound, the radiations become in-phase and directivity increases [12]. Several experimental and analytical approaches have been attempted to determine the improvements achieved in delivering stronger ultrasound using various plate geometries and shapes. Circular aluminium plate transducers with steps were designed and their vibration characteristics were investigated experimentally and analytically [2, 12, 40-42]. The structure of the transducer and the radiating plate [2], Fig.2-1, consists of three concentric copper rings with small holes to spray water jets to the nodal circles to cool them. High intensity ultrasound was reported to have been generated in gases with high efficiency and directivity.

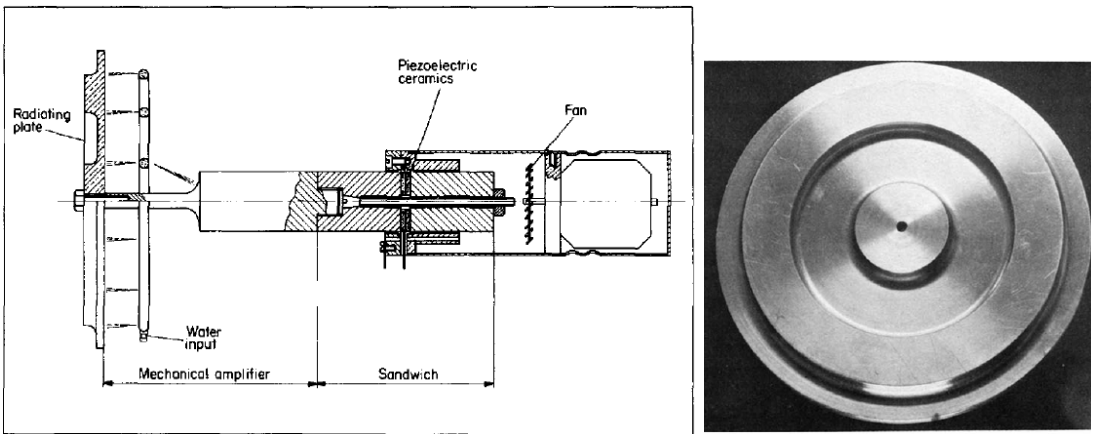

Fig.2-1. Left: The structure of the transducer; Right: The radiating plate [2].

Using uniform plate solution and the energy method, an analytical solution was obtained for the frequency equation by matching boundary conditions at the step interface and free edge condition at the external boundaries [12, 40]. Good agreement was reported between the experimental and the analytical approaches and better directivity was obtained. The following three conditions were considered to be satisfied in their analytical model

1. The radii of the nodal circles must coincide with the radii of the raised areas, b_n. W is the displacement.

$$W(b_1) = W(b_2) = \cdots = W(b_n) = 0 \quad (2\text{-}3)$$

2. The total linear momentum of the plate has to be zero. h is the thickness of the plate which differs in thin regions and raised areas. a is the radius of the plate.

$$\int_0^a hW(r)rdr = 0 \quad (2\text{-}4)$$

3. The maximum kinetic energy T_{max} must be equal to the maximum potential energy V_{max} of the vibrating plate.

$$T_{max} - V_{max} = 0 \quad (2\text{-}5)$$

Analytical vibration analysis of stepped plates without any restriction on the number of steps or on the order of the vibration mode, unlike the earlier works in the literature which were restricted to one step and/or first vibration mode, was conducted by Emeterio et al. [43]. The analytical results agreed well with those of experiments in thick areas of the plate, while discrepancies were observed in thin regions. Therefore, in their analytical model for the deformation function, they proposed a correction factor taking the effect of the base plate and step thicknesses ratio into account and obtained good agreement between their analytical and experimental results. The influence of the Poisson's ratio on the natural frequencies of stepped-thickness circular plate has also been investigated. Al-Jumaily and Jameel determined the natural frequencies of the simply supported and clamped stepped plates using classical plate solutions with exact continuity conditions at the step [44]. They concluded that larger Poisson's ratio indicates stiffer plates and larger natural frequencies. In addition, as the step size increases, the natural frequencies are expected to be larger. They also stated that the Poisson's ratio should not be disregarded in the continuity equation in particular for the fundamental frequency. Gutierrez et al. investigated the vibration of rectangular, circular and polygonal plates having single symmetric step with various

types of elastic restraints [45]. They considered simple polynomial functions for the displacement and Ritz method was employed to get the frequency. Two years later in 1982, Gutierrez and Laura employed the same analytical approach to the same problem but a more general geometrical variation was considered for the steps [46].

2.4. Other Modifications on Plates

To improve directivity for underwater radiation, two design methods were introduced as in Figs. 2-2 and 2-3 [3]. In one method, they implemented helical waveguides and in the other one, a delaying liquid was used with the same acoustic impedance as water but half of the sound velocity as in water. Hence, radiations became in-phase for the regions of the plate which had been previously in counter-phase. Their results showed applicability of their design methods for underwater radiating plates with good directivity.

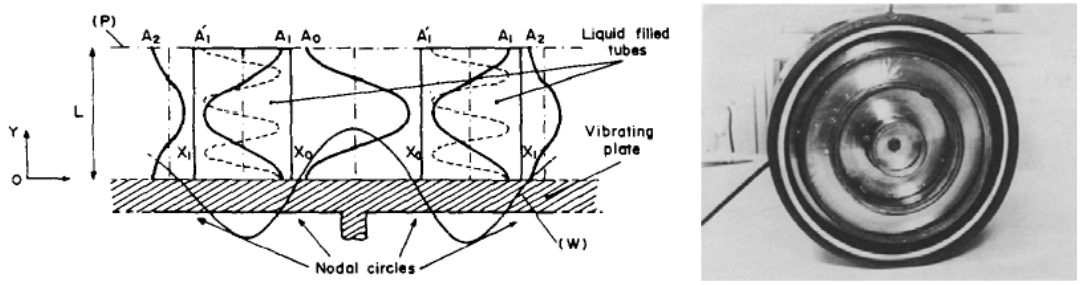

Fig.2-2. Radiating plate with delaying liquid [3].

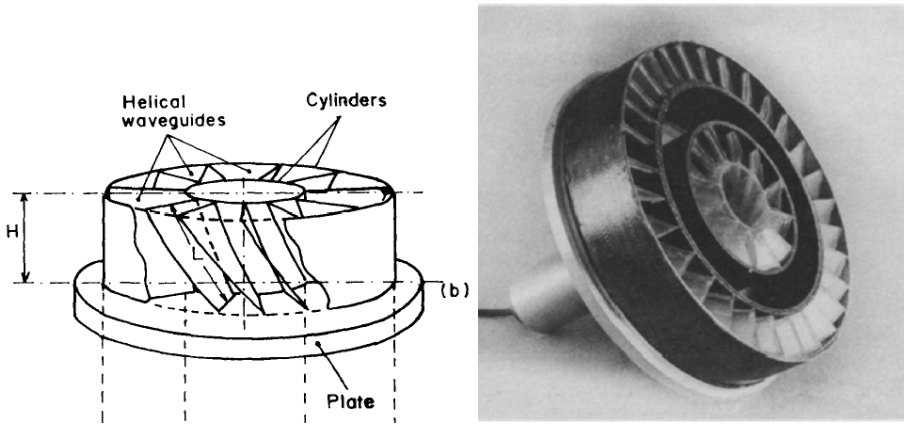

Fig.2-3. Radiating plate with helical waveguides [3].

2.5. Curved & Corrugated

A curved PVDF transducer (poled piezoelectric PVDF film with silver ink electrodes on both sides) was reported to be capable of effectively coupling ultrasound into the air to generate strong sound pressure [14, 47]. Two resonances were observed as length extensional mode and flexural bending mode. Surface vibration profiles of these two modes were measured by a laser vibrometer. Two in-phase displacement peaks were found for the length extensional mode and three out-of-phase peaks for the flexural bending mode. Therefore, the length extensional mode can generate a stronger ultrasound wave than the flexural bending mode. Toda and Tosima investigated a curved, clamped, piezoelectric multilayer film with two types of structure [47]. Type one with two clamps at straight ends and a uniform film curvature, while type two had the same two clamps but a non-uniform curvature where the radii were different for the central region and for side regions. Unlike classical theory, they concluded that the resonance frequency is not necessarily proportional to the inverse of curvature radius. Structure type two with non-uniform curvature generates much higher output pressure than type one (approximately 35 Pa in the best case compared to 15 Pa). Further, resonance was reported to diminish for a certain range of radii, forming a stop band

[4, 47]. Toda and coworkers proposed a new type of corrugated PVDF film air transducer as in Fig.2-4 [4, 48]. Concave and convex curved sections were formed alternately to obtain the corrugated structure. The concave and convex regions vibrate out of phase. When corrugation height is approximately half of the wavelength, these waves add constructively and form a strong acoustic beam. However, since the vibration is distributed over the whole surface from all of the points on the film, the optimum height should be slightly larger than half wavelength. They reported their proposed transducer had a high power output and a sharp beam angle.

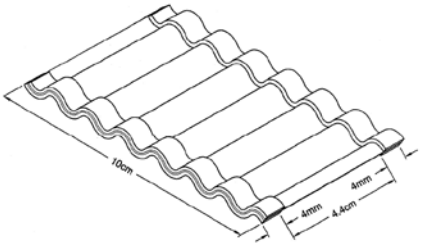

Fig.2-4. PVDF film with corrugation [4].

2.6. Shells

Vibration of shells has been extensively investigated some of which will be briefly summarized and presented here. In an old paper in 1888, Love started with Kirchhoff's first and second theory of plates and continued to theory of shells [49]. Geometrical theory of small deformation and internal strain for an element of the shell were all presented and the equations of motion for the vibration of spherical and cylindrical shells were derived. In 1965, Watkins and Clary experimentally and analytically investigated the vibrational characteristics of thin-walled, circular, cylindrical, and conical frustum shells with free-free and fixed-free boundary conditions [50]. The shells studied included two circular cylinders differing in both length and diameter and a series of four conical frustums differing in cone angle but having a constant ratio of

length to smaller-radius. Good agreement was observed between experimental and theoretical natural frequencies and mode shapes. In 1973, Leissa scrutinized the vibrational characteristics and mechanical properties of shell structures in a book [51]. Fundamental equations of thin shell theory, characteristics of thin circular cylindrical shells, complicating effects such as variable thickness and anisotropy in circular cylindrical shells, noncylindrical shells such as conical, spherical etc. and the solution for three-dimensional equations of motion for cylinders were all addressed. Derivation of various shell theories developed by various researchers was reviewed and the differences were outlined. Soedel proposed a new formula for the natural frequencies of circular cylindrical shells for modes in which transverse deflections dominate [52]. The Donnell-Mushtari-Vlasov equations were used as

$$D\nabla^4 W + \nabla_k{}^2 \Phi - \rho h \ddot{W} = q \tag{2-6}$$

$$Eh\nabla_k{}^2 W - \nabla^4 \Phi = 0 \tag{2-7}$$

where ρ is the mass density, E is Young's modulus, h is shell thickness, W is transverse deflection, D is the bending stiffness as $Eh^3/12(1-\mu^2)$, q is the transverse loading, Φ is the stress function and ∇^4 and $\nabla_k{}^2$ can be defined as below

$$\nabla^4 = \left(\frac{1}{a^4}\right)\partial^4/\partial\theta^4 + \partial^4/\partial x^4 + \left(\frac{2}{a^2}\right)\partial^4/\partial x^2 \partial\theta^2 \tag{2-8}$$

$$\nabla_k{}^2 = \left(\frac{1}{a^2}\right)\partial^2/\partial x^2 \tag{2-9}$$

in which a is the radius of shell and μ is Poisson's ratio. Manipulation of equations (2-6) and (2-7) results in the well-known eighth order equation for the vibration of cylindrical shells as below for $q = 0$,

$$D\nabla^8 W + Eh\nabla_k{}^4 W - \rho h\omega^2 \nabla^4 W = 0 \tag{2-10}$$

where ω is the natural frequency. In order to be able to get a closed form solution for the natural frequency, Soedel employed Yu's approximation [53] neglecting a term and arrived at a fourth order equation instead of the common eight order equation. The deficiency of Yu's approximation is that the equation is not valid when circumferential wavenumber (n)=0 and it improves in accuracy as 'n' increases, but not as axial wave number (m) increases. Soedel also used Galerkin's method instead of Yu's assumption and considered a general beam function satisfying the boundary conditions [53]. It was reported that the method is valid for all boundary conditions for which the roots of the analogous beam problem can be obtained. The good agreement with experimental data for a variety of boundary conditions proved the accuracy of the method.

Wang and Lai implemented Love's equations to analyse the basic vibration behaviour of circular cylindrical shells [54]. They used boundary conditions together with the beam functions to clarify the wavenumbers for predicting natural frequencies of finite length circular cylindrical shells through wave approach, instead of the traditional approach of simplifying Love's equations and solving the simplified equations directly with the boundary conditions at both ends. The results agreed very well with those of FEM (ANSYS) and were reported to be much better than several other methods when compared with experimental data. A similar approach was followed by Zhang et al. who analysed cylindrical shells using Love's theory and wave propagation method [55]. The axial wavenumber was taken to be the same as that of a beam with the same boundary condition and the authors claimed their method as a convenient, effective and accurate method. Li et al. followed the same procedure using wave propagation method to investigate the natural frequencies of thin finite length circular cylindrical shells having various boundary conditions [56]. However, they used Donnell's thin shell theory. They also made some clarifications and explanations on the circumferential mode number 'n' and axial mode number 'm', and also calculated the

natural frequencies numerically and compared them with those of FEM (ANSYS) to confirm the reliability of their model. The effects of some parameters (length-to-radius and radius-to-thickness ratios) on natural frequencies were discussed as well. It was concluded that for long thin shells, the method is more effective. They also concluded the lowest frequency does not occur at the lowest values of 'n', and for different values of 'm', the lowest frequency occurs at different modes. For example, at radius-to-thickness ratios=30 and m=1, the lowest frequency occurs when n=3. In another paper, Xuebin followed the same wave propagation approach but using Flugge's classical thin shell theory [57]. According to the author, the wave propagation method has a high accuracy for longer shells and many researchers have used this method for the analysis of pipeline to predict the frequency.

In 2004, Soedel published a comprehensive book on vibration of shells and plates in which free and forced vibration of shell/nonshell structures with/without the effects of shear deformation and rotary inertia, fluid interactions and thermal effects etc. was presented and considered [58].

In one of the available investigations in the literature, an aluminium cylindrical chamber was driven by a piezoelectric transducer at 21.8 KHz [15]. It was intended to investigate the effect of airflow rate and ultrasonic power on hot-air drying of foodstuff assisted by the proposed ultrasonic system. They reported achieving a high intensity acoustic field inside the tube (154.3 dB of SPL) with 75W applied power.

2.7. Stepped/Variable Thickness Shells

Extensive work has been done on vibration of shells using different methods with various assumptions or considerations, both experimentally and analytically/numerically. Some of these investigations have been briefly summarized

so far in the previous section. In this section, vibration of stepped/variable thickness shells will be presented.

Ganesan and Sivadas studied the free vibration characteristics of circular cylindrical shells with variable thickness along the axial direction (linear symmetric and asymmetric variations in the thickness) [59]. They used Love's first approximation shell theory for the strain terms and employed finite element method to obtain the solution. They investigated clamped-clamped and simply supported-simply supported boundary conditions. For various length/radius ratios and various mode numbers, the effect of thickness distribution on the lowest natural frequency was studied. Increasing the maximum/minimum thickness ratio resulted in different trends for the natural frequency. The simply supported-simply supported boundary condition did not show conspicuous response to thickness distribution. Short shells with clamped-clamped boundaries showed the maximum variation of lowest frequency. In a similar work following the same approach, Sivadas and Ganesan considered linear and quadratic symmetric and asymmetric thickness variations for the same boundary conditions [5]. Fig.2-5 reveals the thickness variations they considered. They concluded that short shells show an increase of the lowest frequency for both boundary conditions as thickness variation increases. Further, quadratic variation of thickness was reported to have a more noticeable effect on the natural frequency compared to linear variation. In another work, they extended their previous works to investigate natural frequencies of cantilever circular cylindrical shells (clamped-free) with linear symmetric and asymmetric thickness variations along the length [60]. For different length to radius ratios and depending on the circumferential mode number, length to radius ratio and thickness ratio, various trends were observed for the natural frequency.

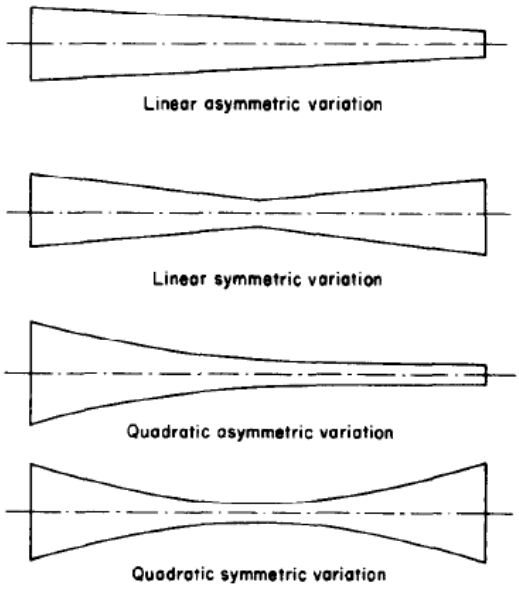

Fig.2-5.Thickness variation profiles [5].

Vibration of circular cylindrical shells with step-wise thickness variations as shown in Fig.2-6 was investigated by [6, 61, 62]. Zhang and Xiang used Flugge thin shell theory together with the state-space technique to derive the homogenous differential equations for a shell segment [6]. Further, to apply equilibrium and compatibility requirements at the interfaces of the shell segments, domain decomposition method was used. Various types of boundary conditions were considered. The fundamental frequency parameters for shells with a larger step thickness ratio h_2/h_1 (thinner part/thicker part ratio as in Fig.2-6) were reported to be always greater than the ones with a smaller step thickness ratio. For the simply supported-simply supported shells, the fundamental frequency parameters increased monotonically as the step thickness ratio h_2/h_1 increased. However, such a conclusion could not be made for the clamped-free shells. Depending on the shell length to radius ratio L/R and the location of the step thickness variation L1/L, an increase of the step thickness ratio h_2/h_1 could result in an increase or a decrease in the fundamental frequency parameters of the shells.

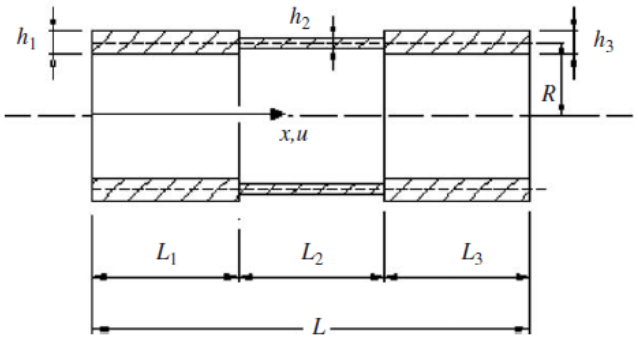

Fig.2-6. Geometry of the stepped thickness cylindrical shell [6].

Vibration of stepped circular cylindrical shells with step-wise thickness variations along the circumference as in Fig.2-7 had not been investigated in the literature before the investigation by [7]. Transfer matrix method was employed based on the Flügge's shell theory. The transfer matrix was derived from the non-linear differential equations system for the cylindrical shell by numerical integration. Vibration frequencies and the corresponding deformations of the symmetrical and anti-symmetrical profiles were obtained. Considerable differences between the modes of uniform and stepped shell for symmetrical and anti-symmetrical modes were observed. For $h_1=h_2$ and $\alpha=2\pi$ (as in Fig.2-7) which is a simple uniform shell, the vibration modes were distributed regularly over the shell surface. However, for $h_1<h_2$ and $\alpha=\pi$, $\pi/2$, the majority of symmetric and anti-symmetric vibration-modes were larger at the thinner region with less stiffness compared to the thicker region with higher stiffness. This implies localization of the vibration modes within the weaker sections of the shell. Decreasing step thickness ratios (increasing the difference between the thicknesses) decreased the vibration frequencies and made mode shapes more pronounced for two and four-stepped shells. They concluded that the geometry of stepped shells reduces the non-dimensional frequency parameter and makes the mode shapes more pronounced [7].

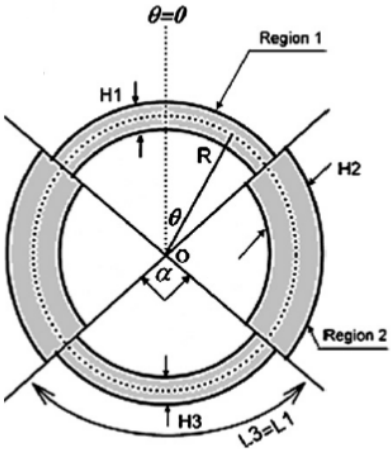

Fig.2-7. Geometry of the circumferentially stepped cylindrical shell with 4 steps [7].

Qu et al. presented a domain decomposition technique for solving vibration problems of uniform and stepped cylindrical shells with arbitrary boundary conditions [61]. Thickness variations were along the length. Both the thickness variations and boundary conditions were reported to significantly affect the transient vibration responses of the stepped cylindrical shells. For free-clamped stepped shells, the step thickness variations were concluded to noticeably affect both the displacement amplitude and oscillation period.

2.8. Piezoelectric Structures

In 1969, Tiersten published a book on the linear theory of piezoelectricity, piezoelectric constitutive equations and the standing wave solutions as well as approximation methods for solving the equations of piezoelectric plate vibrations [63]. In 1975, Adelman et al. investigated the axisymmetric vibrations of radially polarized piezoelectric ceramic long tubes [64]. Inner and outer surfaces had electrodes and were connected to an alternating voltage. PZT-4 transducers were considered under various types of boundary conditions and closed form solutions were obtained using

Bessel and Lommel functions for the radial displacement and electric potential. Accordingly, the characteristic equations for the resonant and anti-resonant frequencies were derived and also electromechanical coupling factors. It was concluded that electromechanical coupling factor was sensitive to the ratio of inner/outer radii and to the type of boundary condition.

In 1993, Tzou published a book in which he dealt with equations of piezoelectric shells vibrations (thin and thick), plates (thin and thick), control, damping and sensing of piezoelectric continua [65].

Lu et al. extended Donnell-Mushtari-Vlasov-type equations of elastic shells to the case for piezoelectric shells [66]. Introduction of generalized bending and membrane stiffness resulted in the unified form Donnell-Mushtari-Vlasov equations for both piezoelectric and elastic shells. Analogous beam functions were used to evaluate the frequencies for the shells with the same type of boundary condition. The obtained results were reported to be exact for the simply supported shell and approximate but with good accuracy for other boundary condition cases.

Ding et al. investigated free vibration analysis of a piezoelectric circular cylindrical panel [67]. Based on the general solution for coupled equations for piezoelectric media and by using the variable separation method, three-dimensional exact solutions were obtained under several boundary conditions. They used combinations of electrical boundary conditions as closed circuit and open circuit on inner and outer surfaces and concluded that the differences among the different types of electric boundary conditions were not noticeable.

Berg et al. investigated vibration of piezoelectric shells polarized in the radial direction [16]. These shells are commonly used as stators in some piezoelectric ultrasonic travelling wave motors. They modified Flugge's equations by replacing the

constitutive relations for elastic shells with those of a linear piezoelectric material. They considered a closed thin electrode on the inner surface and nine evenly divided electrodes on the outer surface. They used Fourier series to solve the equations of motion.

Kim et al. dealt with the radial vibration of piezoelectric cylindrical transducers polarized in the radial direction [68]. They derived the differential equations of piezoelectric radial motion in terms of radial displacement and electric potential and only considered radial variables. To get the characteristic equation of radial vibration, they applied mechanical and electric boundary conditions. It was reported that the fundamental mode has motion without deformation in the thickness direction of a plate with infinite radius of curvature. The piezoelectric natural frequency of the fundamental mode was shown to increase as the radius of curvature decreased, but the frequency of the fundamental mode does not depend significantly on the thickness of the cylinder. It is worth noting that the shells were not thin but rather thick and the lengths were shorter than the outer diameter.

Kim and Lee studied radial vibration of piezoelectric cylindrical transducers [69]. They used similar equations to [64] and then to solve the equations easily, they eliminated a term. They used separation of variable to solve the equations at the next step. Comparison of the results with the experiments showed an approximate error of 10% which was reported to be caused by the elimination of a term during a derivation to obtain solvable equations.

Xu et al. investigated vibration characteristic of a finite-width corrugated shell transducer as in Fig.2-8 [8]. Vibration was in the ultrasonic frequency range and Fourier series method was employed to deal with the boundary conditions on the two ends of the finite width. It was also observed that resonant frequency increases with

decreasing width/length ($\frac{l}{s}$) ratio because of a stronger constraint from the two transverse edges corresponding to a smaller $\frac{l}{s}$ ratio. The constraints on the two sides parallel to the ridges increase both the resonant frequencies of the corrugated shells and the extensional forces in the shell centre for larger width/length ratios.

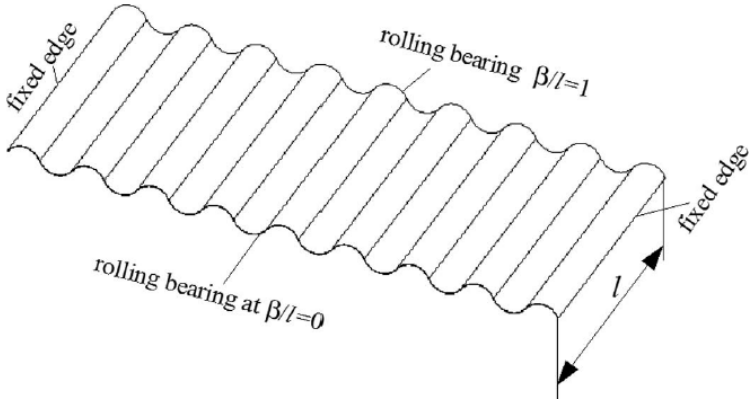

Fig.2-8. A cylindrical shell piezoelectric transducer [8].

2.9. Ultrasound Transducers for Droplet Generation

Ultrasonic transducers have been extensively used for droplet generation and atomization and their application varies from ultrasonic humidification, micro/nano electronics, nanoparticles synthesis, spray coating to drug delivery and drug preparation for inhalation. In this section, their application for atomization purposes is summarized. In the end, a comparison among the available existing methods will be performed in the form of a table to discuss and illustrate the advantages and disadvantages of each method. Al-Jumaily and Meshkinzar presented a paper in which they elaborately explained and compared various configurations for the piezoelectric ultrasound atomizers and their performance [70]. They also proposed guidelines for future studies to modify the piezoelectric transducers to better suit them for potential applications.

Lass et al. presented a paper on the current vibrating membrane nebulizer technology for drug delivery and dealt with current devices in the market which can be of interest [28]. Compressed air, vibrating piezoelectric plates together with a metallic mesh, or a vibrating mesh are common technologies for producing aerosols or droplets in commercial devices (Misty-Neb, AeroEclipse, Omron, Pari eFlow, and Philips I-neb). A disadvantage is their broad droplet size distributions and low throughput making it difficult to deliver sufficient dosages of drugs precisely and rapidly to the targeted sites [26, 27]. In addition, blockage of mesh orifices in the vibrating mesh membrane of eFlow and I-neb which are considered to be the most advanced commercial devices is a pitfall [29]. Recent in vivo studies have indicated that in both adults and children, when inhaling typical aerosols from current commercial devices, the upper airways [71], ventilator, and endotracheal tubes are significant barriers to lung deposition [72]. As a direct result of poly disperse droplet size distributions, drugs are delivered to non-targeted sites, resulting in harmful side effects in the pharynx and losses in the ventilator/endotracheal tubes. Therefore, investigation and development of ultrasonic transducers as atomizers in order to improve their performance is a matter of great importance.

In 1988, Elrod et al. worked on droplet formation using tone bursts of focused acoustic energy [73]. In order to generate a spherically converging acoustic beam, a focusing element (acoustic microscope lens) was used without any nozzle. The liquid surface was adjusted to be at the focal plane, where the beam was concentrated. Droplets of 300 to 5μm were generated within the frequency range of 5 to 300MHz.

2.9.1. Vibrating Plate Atomizers

Vibrating plate transducers are commonly being used for humidifiers and other applications since they possess the best combination of performing specifications compared to other types of devices. In these atomizers, an electrical signal is converted to mechanical oscillation using a piezoelectric material immersed in a reservoir of water. The ultrasonic waves created by the mechanical vibration of the plate are directed towards the water surface creating a mist of water droplets. These atomizers are normally available in a high frequency range of 1.65-3MHz which are capable of producing droplets within the range of 1-5 μm in diameter using 2 up to 30W of power. The flow rate varies within the range of 5-400 ml/h. They are in contact with water and the level of water on top of them affects their performance and should be taken into account for the optimum performance of the device. They are available in various plate dimensions and thicknesses. Examples of such atomizers can be found in references [74-77]. Their flow rate also depends on many external factors such as input power, droplet size, frequency and liquid quality, temperature and level (depth). The good point about them is that they can produce various sizes of droplets and flow rates which makes them suitable for some applications. As already mentioned, flat plates do not produce focused ultrasonic waves. Therefore, curved transducers have been used in some of the aforementioned atomizers providing a little bit of better focus and performance compared to the flat ones as evident in [74-77]. However, depending on the application, a combination of high flow rate, small droplet size and low power demand may be required which has not been achieved yet. Therefore, seeking alternative ways to create more focused ultrasonic waves seems essential and can lead to better performance of the device. Going to higher frequencies to obtain better performance of the device and smaller droplets can lead to overheating and depolarization of the material [78] and also fatigue failure [41]. Therefore, it is a

restricting factor and alternative ways should be sought. One alternative is using stepped-thickness plates. Although, they have been investigated and proven to be useful and practical as discussed in section 2.3, to the author's knowledge they have not been implemented in the current vibrating plate atomizers available in the market.

2.9.2. Surface Acoustic Wave Atomizers

Kurosawa et al. proposed a novel way to produce dry fog using a surface acoustic wave (SAW) transducer of $LiNbO_3$ piezoelectric substrate as in Fig.2-9 [9, 79]. The atomizer consists of a vibrator which has an interdigital aluminium transducer (IDT) consisting of 20 pairs of electrodes supplied with RF (radio frequency) power amplifier at 48MHz frequency. The surface wave called capillary wave generated by the radiation of acoustic wave from the SAW device surface was capable of atomization when the liquid layer on the surface was half a millimetre or less. The atomizing mechanism was reported not to be vapour but spray from crests of the surface wave in a fluid. The mean diameter of the mist was about 5μm. The atomizing rate was 170μl/min at 2.3W input power (36V). Applying 100MHz was reported to be capable of reducing the size of the device to an extent suiting it for medical applications such as spraying a liquid medicine to the diseased target directly with the atomizer on an endoscope.

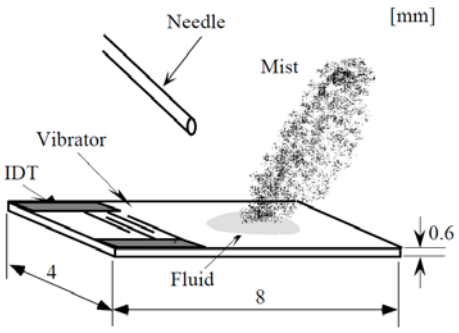

Fig.2-9. Surface acoustic wave atomizer [9].

A low driving power SAW atomizer was developed consisting of a unidirectional interdigital transducer, a horn and a waveguide fabricated on a $LiNbO_3$ substrate to increase the focus [80]. For continuous atomization of water to get droplets of 1.5µm and 40µl/min flow rate, 1 W of driving power was required at a frequency of about 78MHz. Low driving power and small droplets make the atomizer attractive for practical applications in chemistry, biology and medicine.

2.9.3. Ultrasonic Horns

High ultimate particle velocity, low acoustic loss and high thermal conductivity makes silicon ideal for high-amplitude ultrasonic applications superior to titanium alloys [81]. Therefore, high amplitude ultrasound was generated by a micro-machined silicon resonant transducer to atomize liquids. Lead-zirconate-titanate (PZT) plates were used to drive the needle-shaped device which was made by bonding two silicon horns. Water was atomized continuously at a flow rate of 2.4ml/min into a mist with a mean drop size of 25µm at 72 KHz resonance frequency.

Tsai and others investigated, built and tested micro-electro-mechanical system (MEMS)-based miniaturized silicon ultrasonic droplet generators of a new and simple nozzle architecture with multiple Fourier horns in resonance with and without a central channel [10, 26, 27, 82, 83]. A Schematic is depicted in Fig.2-10 [10]. The silicon resonator is made of a multiple-Fourier horn section where each horn is half-wavelength long with a longitudinal (along the y-axis) vibration amplitude magnification of 2. The drive section includes a piezoelectric plate transducer bonded to the rectangular silicon base using silver paste. When PZT transducer plates are excited at the nozzle resonance frequency, a standing acoustic wave is created through the nozzle with maximum longitudinal vibration (displacement) at the nozzle tip. As a

result of the vibration, standing capillary waves are formed on the free surface of the liquid as it issues from the nozzle tip. Atomization occurs by the breakup of these standing capillary waves. It is worth noting that when the ultrasonic drive frequency deviated from the nozzle resonance frequency by more than 1.5 KHz, a large liquid drop with a diameter greater than the tip width was reported to be formed at the nozzle tip without any atomization taking place. Tsai et al. produced monodisperse ethanol droplets of 2.4μm and water droplets of 4.5μm in diameter in ultrasonic atomization using 1.5- and 1.0-MHz MEMS-based silicon nozzles, respectively, each consisting of 3 Fourier horns in resonance (with a central channel). The required electrical drive power was as low as 0.25 W and supply flow rates as high as 350μl/min (21ml/h) [10]. At the resonance frequency, the measured longitudinal vibration amplitude at the nozzle tip increases as the number of Fourier horns (n) increases in good agreement with the theoretical values of 2^n. Using this design allows for very high vibration amplitude gain at the nozzle tip resulting in no reduction in the tip cross-sectional area for contact of liquid to be atomized. This leads to a noticeable reduction in the electric drive power which in turn decreases the possibility of transducer failure during atomization. They also extended their work to externally liquid fed ultrasonic nozzles without a central channel [26]. Droplets with a diameter range 2.2–4.6μm for alcohol (2.9-4.6 for water) were produced at high throughput of 420 μl/min and very low electrical drive power of 80mW. The electrical loss for the lossy PZT transducer was reported to increase with its thickness. Moreover, the nozzles with a central channel require higher drive power for atomization which is due to the fact that they need a pair of PZT transducers. The range of drive power measured was extremely lower than that required in conventional ultrasonic atomization using MHz disk transducers. This was attributable to the new nozzle architecture requiring only a single basic nozzle without a central channel and, thus, a single PZT transducer for activation. The

optimum number of Fourier horns was found to be 3 or 4 with electrical drive power significantly below 0.1 W at throughput of 100µl/min, while the 2-Fourier horn nozzle required a drive power of 0.6 W to initiate atomization. In contrast, no atomization could be initiated with the 1-Fourier horn nozzle even at a drive power as high as 0.8 W. Batch fabrication of nozzles with similar or different design specifications on a common silicon wafer reduces the costs according to the authors. Utilizing the same approach as above, Tsai et al. designed and built a small nozzle requiring low drive power with a pocket-size ultrasonic nebulizer [27]. Various pulmonary drugs were nebulized utilizing the pocket-size unit with different aerosol sizes and output rates. The obtained results demonstrated the capability of the silicon-based MHz MFHUNs (multiple-Fourier horn ultrasonic nozzle) for production of monodisperse droplets of desirable size (2 to 5µm) and moderate output (up to 0.2mL/min) at low electrical drive power (sub Watt). At the typical output rate of 0.15mL/min with 3.5µm-diameter droplets, the required electrical drive power was 0.27 W. It was reported that a higher output rate can be accomplished readily by using an array of identical ultrasonic nozzles. With 2 MHz of frequency, droplets of 3.1µm were produced and the output was 350µL/min.

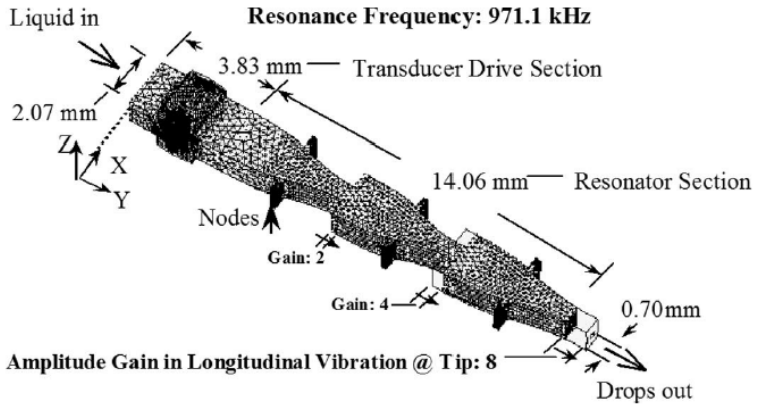

Fig.2 -10. Schematic of a multiple-Fourier horn ultrasonic nozzle [10].

2.9.4. Active and Passive Mesh Membranes

Mesh membranes have also been used for atomization purposes. In some of the cases, the mesh membrane vibrates itself and expels the liquid out of the mesh orifices, whereas in some other cases the liquid is between the mesh membrane and another membrane which is vibrating [28]. The first is called active and the latter is called passive mesh membrane. A new type of piezoelectric array micro-jet was introduced for drug delivery consisting of a fluid chamber, which was formed by a piezoelectric actuator bonded to a silicon chip with nozzles (passive mesh membrane) [84, 85]. Droplets of 5 to 10μm diameter were resulted using piezoelectric transducers operating at around 36KHz to actuate arrays of 5μm diameter micro-machined nozzles. Following the same approach as in Fig.2-11, Meacham focused on a piezoelectrically driven, micro-machined atomizer concept that utilizes fluid cavity resonances in the 0.5–5MHz range combined with acoustic wave focusing for droplet generation or jet ejection [11]. This simple technique capable of producing droplets of sub-5μm diameter (D50 was 4.9μm) had low-temperature and low-power operation. It also had low-cost fabrication with the capacity to scale throughput up or down by using an array. It was reported that when the piezoelectric transducer is driven at the fundamental cavity (fluid reservoir) resonance frequency or any of the higher cavity modes, a standing acoustic wave develops and constructive interference in the pyramidal nozzle focuses the wave so that the peak pressure gradient occurs near the tip of the nozzle. This causes the liquid to be ejected through the nozzles as droplets. The geometry of the chamber can be readily modified to increase or decrease the driving frequency of operation (for example by increasing or decreasing the height of the cavity) according to the desired specifications. Results were presented for various affecting parameters with various orifice diameters at various AC voltages (10, 30, 36V) having different input power. Experiments performed at different resonance

frequencies revealed that the diameter of the ejected droplets decreases with increasing frequency. Doubling the thickness of the piezoelectric transducer reduces the longitudinal resonance of the transducer to half of the original frequency. The power transfer from the piezoelectric transducer to the fluid was more efficient at lower frequencies near the fundamental cavity resonant mode.

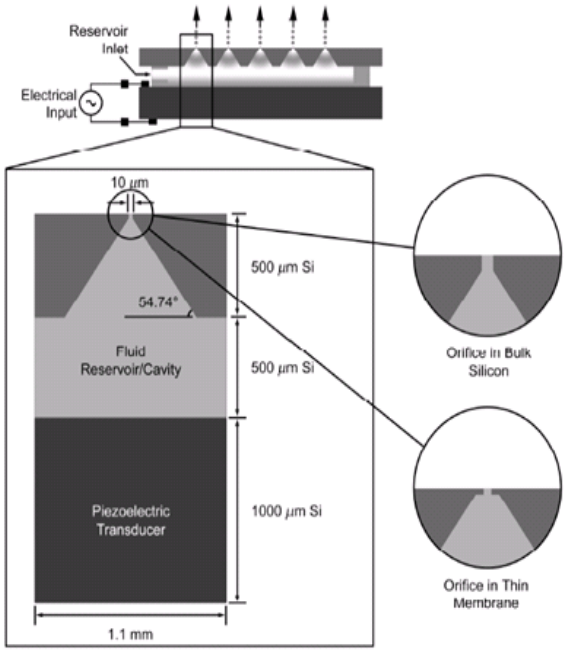

Fig.2-11. Schematic of a piezoelectrically driven, micro-machined atomizer with passive mesh membrane [11].

2.9.5. Remarks

Various methods and piezoelectric transducers used for atomization were presented. The summary can be observed in Table 2-1. As evident, each method has advantages and disadvantages. It can be concluded that despite the fact that some methods have superiority over the others based on specific criteria and performance, none of these methods are perfect and it is required to further improve these methods. On the whole, vibrating plate atomizers possess the best combination of performing specifications,

so that they are very common atomizers. However, it may be still possible to improve the performance of piezoelectric transducers using some of the available approaches and also using the method to be investigated in this study. None of the methods in the table produce complete ultrasound humidification such as that used for lung supportive devices [70]. Biomedical humidification in lung therapies requires complete water vapour in the air rather than water droplets. For this humidification, it is preferable to have an in-line humidifier which can fit in a breathing tube of about 2 cm diameter such as those used in continuous positive airway pressure (CPAP) devices [86]. Therefore, it is strongly required to investigate alternatives and make modifications to the performance of piezoelectric transducers to suit them for each individual application such as biomedical humidification in lung therapies or other applications. This needs further investigation to amplify the acoustic field generated by the piezoelectric transducer. New methods for such amplification and new piezoelectric transducer configurations should be thoroughly investigated to this purpose. Hence, acoustic amplification methods and procedures will be employed in this study to come up with a possible solution.

Table 2-2. Summary of the available methods for atomization.

Method	Properties	Droplet size and Flow rate	Advantages	Disadvantages
SAW [9, 79]	2.3 W; 48MHz, 36 V	5 µm 10.2 ml/h	Small Size & low power	IDT fabrication process & very high frequency & big droplets
SAW driving structure consisting of a unidirectional interdigital transducer, a horn, and a waveguide [80]	1W; 78 MHz	1.5 µm 2.4 ml/h	Small size & Smaller droplets & low power	Very low flow rate & IDT Fabrication & high frequency
Arrays of 5µm diameter micro-machined nozzles [84, 85]	36KHz; 70, 80 V	5-10 µm, According to [28] for typical frequencies of around 100kHz, it is 4 µm	Small Size & low frequency	Fabrication & big droplets
MEM Fourier-horn ultrasonic nozzle with central channel [10]	0.25 W; 971KHz	4.5 µm 21 ml/h	Small size& excellent low power	Fabrication & big droplets & average flow rate
MEM Fourier-horn ultrasonic nozzle without central channel (externally fed) [26]	80mW; 2MHz	2.9-4.6µm 25 ml/h	Small size & Excellent low power	Fabrication & Average droplets & Average flow rate
MEM Fourier-horn ultrasonic nozzle without central channel (externally fed) [27]	0.27W; 2MHz	2-5 µm & Typically=3.5 µm Max 21 ml/h& Typically=9 ml/h	Pocket Size & Battery Operated & Excellent low power	Fabrication & Average droplets & Average or low flow rate
Current Vibrating plate transducers [74-77]	2-30W; 1.65-3MHz	1-5 µm 5-400 ml/h	Various droplet size and flow rate	Low-power devices with small droplets have low flow rate

2.10. Discussion

After going through various geometries and design methods, it can be easily understood that the geometry and the vibration mode play important roles in the ultrasound generation and power demands. Whereas uniform-thickness plates are not capable of producing in-phase and focused waves, the stepped thickness plates proved to be useful [2, 3, 12, 40]. Directivity patterns were compared for uniform and stepped-thickness plates and raising the steps to half a wavelength of the radiated sound in the medium affected the directivity and strength of the ultrasound generation [12]. However, using stepped-thickness plates for low ultrasound frequencies is not practical due to the large height of the steps which in specific applications (i.e. small and thin transducers) may be a restriction [42]. Moreover, for radiation in liquids, the required height for the steps is even more due to higher speed of sound in liquids compared to air [42]. Further, large height of the steps may also affect the frequency and mode shape of vibration and deteriorate the acoustic radiation. Therefore, utilization of stepped-thickness vibrating plates is not feasible and practical in some applications. The operating frequency, size and shape of the structure and the intended application clarify whether the steps are practically possible or not. Further, the acoustic medium is extremely influential to decide on the applicability of introducing steps in the thickness. In order to reduce the required height of the steps, one may consider going to higher frequencies. This may not be possible since higher frequencies have some barriers as overheating and depolarization of the material [78] and also fatigue failure [41]. Therefore, alternatives should be sought to achieve highly directional and focused ultrasonic waves.

One alternative can be implementing curved transducers which have shown to be good at generating strong ultrasound in air [14, 47]. It was observed that curved clamped

film has a uniform vibration mode and flexural modes [47]. These modes couple through boundary conditions of the clamps and resonance diminishes for a certain range of radii forming a stop band. Designing a high quality transducer in the 30-45 KHz range was concluded to be impossible due to the stop band imposed by mode coupling [4, 47]. It was reported that the film radius R in the frequency range below 50 KHz could not control the resonance frequency. Further, slight changes in the film properties (curvature, stiffness, mass of silver ink electrodes) affected these modes resulting in the main resonance being influenced by the flexural modes. It was found that the main mode was close to the stop band and small changes in the film condition varied the acoustic output by a factor of two to three [14, 47]. This stop band and mode coupling is a big barrier for designing such transducers and up/downsizing.

The other alternative to amplify acoustic field and its focus is using corrugated transducers. To this aim, Toda designed and built a large area corrugated transducer (20×20 cm^2) operating at 40 kHz and achieved high power output [4]. However, it was reported that commercially available PZT transducers at 40 kHz have higher acoustic outputs than their proposed transducer with the same area and the same applied voltage. Therefore, although it is an approach to make radiations in-phase and improve directivity, it is not superior to the existing transducers available in the market.

Another option is using an array of transducers [13]. Unfortunately, there are two pitfalls associated with this; slight changes in the spatial position of the transducers has a considerable effect on the signal at the focal line which is a problem for their design and up/downsizing. Further, the highest SPL achieved was 142.70 dB. However, if a different driving amplifier was used to provide a higher input AC voltage, sound pressure levels (SPL) of up to 150 dB could be achieved [13]. This is still insufficient for most potential applications. Moreover, increasing the input voltage

increases the power consumption as well which is not suitable. The effect of voltage increase was investigated and it was concluded that the efficiency decreases as the voltage increases [87]. This was reported to be due to higher losses at higher voltages as well as nonlinear acoustic effects which increase power consumption. Actually, the rate of increase in the input voltage is higher than the increase in the output and consequently, the efficiency decreases.

Another alternative can be using cylindrical shells to increase the directivity and focus of the generated ultrasonic waves. Garcia-Perez et al. employed a shell vibrating at one of its resonance frequencies to produce a high level of focused acoustic intensity in the air inside the tube to dry the fruits [15]. The high level of acoustic intensity achieved in their paper acknowledges the influence of geometry and vibration mode on the ultrasound generation. The same transducer and power drivers were leased to be used for research at AUT, IBTec [1]. There are three issues regarding this type of transducer. One is the extremely expensive power drivers required which cost around $25000. The other problem is that the required power to drive the transducer was 75W which may be suitable for some industrial purposes, while it is unsuitable for biomedical applications. The third problem is related to the sound pressure level of the acoustic field. As part of the research, this transducer was used to investigate the effect of acoustic field on the droplet size and vaporization. In some cases, no improvement and in some cases an adverse effect was observed on droplets size distribution. It was concluded that 155 dB may not be sufficient and a stronger acoustic field may be required to have a positive effect on the size of droplets. Although this may not be a problem for some applications, it is still required to further amplify the acoustic field to have higher SPL. According to the literature and discussions made, it can be concluded that depending on the need and requirements of the application and its

limitations, various approaches are used and there is not a fixed answer for all the problems. Steps, delaying liquid, helical waveguides, reflectors, curved structures, corrugated structures and cylinders can be used to improve directivity, focus, and intensity of the acoustic field. Hence, changes in the geometry of the transducer are of great help and importance. Accordingly, future investigations on such transducers which could have industrial or biomedical applications should be concentrated and targeted on the geometrical manipulation of the transducer to increase the acoustic intensity and its directivity. This may in turn reduce the electrical drives and power requirements as well. The corresponding mode of vibration should also be carefully taken into account since it extensively affects the acoustic radiation. Therefore, extensive investigation on the proper mode of vibration for the considered geometry of the transducer is essential.

2.11. Research Gaps & Our Proposed Approach

As explained above, there is a great need for focused high intensity ultrasound transducers which have a wide variety of industrial and biomedical applications. An example is for atomization which is employed for humidification, drug delivery or even coating. Although some of the available methods have advantages such as low power consumption or small droplet size, nevertheless, they seem not to have priority over existing vibrating plate transducers. Stepped plates have demonstrated better focus and performance compared to flat plates. Also, curved surfaces such as corrugated plates or cylindrical shells have shown to be useful for increasing the focus and intensity of the acoustic field. Therefore, combining curved surfaces with well-designed stepped-thickness variations seems to be an attractive choice for obtaining focused and strong ultrasound wave. To do that, the vibration characteristics of

piezoelectric stepped-thickness shells are required which are not available in the literature except for only a few merely theoretical investigations for stepped elastic shells [6, 61, 62]. Obviously, full understanding of the vibration characteristics of stepped-thickness shells is not clearly explained in the open literature and further investigation is required.

Hence, the vibration characteristics of stepped-thickness piezoelectric cylindrical shells will be investigated in an optimum goal of achieving the strongest ultrasound wave radiation, which can be implemented for the wide span of applications as previously mentioned. More specifically, the required design considerations for the intended application as a second stage atomization transducer are taken into consideration. Accordingly, the following research objectives can be considered.

2.12. Research Objectives

According to the given explanations, the main objectives of the present research can be summarized as below

1. Investigation of the vibration characteristics of uniform-thickness piezoelectric cylindrical shells to identify suitable mode shapes and range of frequencies.
2. Identifying the optimum design for the stepped-thickness piezoelectric cylindrical shells based on the obtained results for the uniform-thickness transducer.
3. Investigation of the vibration characteristics of the identified stepped-thickness piezoelectric cylindrical shell including the operating frequency, vibration mode shape and amplitude corresponding to the strongest acoustic

amplification. The most important objective of this research is to achieve the highest sound pressure level and maximum amplification of the acoustic field using geometrical variations for the same input power.

4. Stress analysis for the designed stepped-thickness piezoelectric shells to assure the reliability and durability of the transducer and avoid transducer failure due to fatigue or crack initiation.
5. Having finalized the design of the suitable stepped-thickness piezoelectric transducer, the next goal is to investigate its performance in preliminary experiments for one of the intended applications as a second stage transducer for atomization.

2.13. Closure

In this chapter**,** extensive literature review was performed on the vibration and acoustic radiation characteristics of various transducers. Application of such transducers for atomization was also reviewed. According to the drawbacks, deficiencies, and available information in the literature, research gaps were identified to be investigated in this study. The approach to be followed in the present work was also outlined and our proposal was presented. Based on the literature, the proposed approach seems promising and therefore, the present research is based on the framework stated to address the issues in an optimum goal of developing a transducer capable of intensifying the acoustic field for the same power input. It is not intended to restrict or in any way limit the scope of this work to details and dimensions considered. Hence, the same approach and concept can be extended to any arbitrary size transducer with any dimensions.

Chapter 3: Theoretical Investigations

3.1. Introduction

As this research investigates the ultrasound generation from stepped-thickness shell with the focus on developing a transducer for liquid particle disintegration, this chapter presents the required theoretical background to proceed with the investigation. It compromises of three sections. First section investigates the vibration characteristics of the stepped-thickness cylindrical shell. Second section is a brief theoretical explanation on how various geometrical modifications amplify the acoustic field and improve directivity of the radiation. This can further clarify the reasons lying behind considering stepped-thickness cylindrical shells for acoustic amplification in this study. In the third section, different background theories on the ultrasound-droplet interaction are presented to investigate how the ultrasound generated by the transducer can affect the droplets.

3.2. Theoretical Formulation

This section includes theoretical formulations for the piezoelectric cylindrical shell either uniform or stepped-thickness and is divided into subsections for each of them.

3.2.1. Piezoelectric Constitutive Equations

At the beginning, constitutive relations for a piezoelectric material is presented. Briefly, these relations can be stated as [63]

$$T = c^E S - eE \tag{3-1}$$

$$D = \varepsilon^S E + eS \tag{3-2}$$

where T is the stress (N/m^2), S is the strain, c^E is the stiffness at constant electric field (N/m^2), e is the piezoelectric stress constant (C/m^2), E is the electric field (V/m), D is

the electric displacement (C/m^2) and $\varepsilon^S$is the permittivity at constant strain (C/V.m). These two equations can be combined and written in the matrix form as below [88]:

$$\begin{bmatrix} \mathrm{T}_1 \\ \mathrm{T}_2 \\ \mathrm{T}_3 \\ \mathrm{T}_4 \\ \mathrm{T}_5 \\ \mathrm{T}_6 \\ \mathrm{D}_1 \\ \mathrm{D}_2 \\ \mathrm{D}_3 \end{bmatrix} = \begin{bmatrix} c_{11}^E & c_{12}^E & c_{13}^E & c_{14}^E & c_{15}^E & c_{16}^E & -e_{11} & -e_{21} & -e_{31} \\ c_{21}^E & c_{22}^E & c_{23}^E & c_{24}^E & c_{25}^E & c_{26}^E & -e_{12} & -e_{22} & -e_{32} \\ c_{31}^E & c_{32}^E & c_{33}^E & c_{34}^E & c_{35}^E & c_{36}^E & -e_{13} & -e_{23} & -e_{33} \\ c_{41}^E & c_{42}^E & c_{43}^E & c_{44}^E & c_{45}^E & c_{46}^E & -e_{14} & -e_{24} & -e_{34} \\ c_{51}^E & c_{52}^E & c_{53}^E & c_{54}^E & c_{55}^E & c_{56}^E & -e_{15} & -e_{25} & -e_{35} \\ c_{61}^E & c_{62}^E & c_{63}^E & c_{64}^E & c_{65}^E & c_{66}^E & -e_{16} & -e_{26} & -e_{36} \\ e_{11} & e_{12} & e_{13} & e_{14} & e_{15} & e_{16} & \varepsilon_{11}^S & \varepsilon_{12}^S & \varepsilon_{13}^S \\ e_{21} & e_{22} & e_{23} & e_{24} & e_{25} & e_{26} & \varepsilon_{21}^S & \varepsilon_{22}^S & \varepsilon_{23}^S \\ e_{31} & e_{32} & e_{33} & e_{34} & e_{35} & e_{36} & \varepsilon_{31}^S & \varepsilon_{32}^S & \varepsilon_{33}^S \end{bmatrix} \begin{bmatrix} \mathrm{S}_1 \\ \mathrm{S}_2 \\ \mathrm{S}_3 \\ \mathrm{S}_4 \\ \mathrm{S}_5 \\ \mathrm{S}_6 \\ \mathrm{E}_1 \\ \mathrm{E}_2 \\ \mathrm{E}_3 \end{bmatrix} \tag{3-3}$$

For the case of PZT materials with hexagonal crystal in class 6mm, this matrix reduces to the following equation. It is worth noting that the polarization axis is in the third direction [63, 88].

$$\begin{bmatrix} \mathrm{T}_1 \\ \mathrm{T}_2 \\ \mathrm{T}_3 \\ \mathrm{T}_4 \\ \mathrm{T}_5 \\ \mathrm{T}_6 \\ \mathrm{D}_1 \\ \mathrm{D}_2 \\ \mathrm{D}_3 \end{bmatrix} = \begin{bmatrix} c_{11}^E & c_{12}^E & c_{13}^E & 0 & 0 & 0 & 0 & 0 & -e_{31} \\ c_{12}^E & c_{11}^E & c_{13}^E & 0 & 0 & 0 & 0 & 0 & -e_{31} \\ c_{13}^E & c_{13}^E & c_{33}^E & 0 & 0 & 0 & 0 & 0 & -e_{33} \\ 0 & 0 & 0 & c_{44}^E & 0 & 0 & 0 & -e_{15} & 0 \\ 0 & 0 & 0 & 0 & c_{44}^E & 0 & -e_{15} & 0 & 0 \\ 0 & 0 & 0 & 0 & 0 & c_{66}^E & 0 & 0 & 0 \\ 0 & 0 & 0 & 0 & e_{15} & 0 & \varepsilon_{11}^S & 0 & 0 \\ 0 & 0 & 0 & e_{15} & 0 & 0 & 0 & \varepsilon_{11}^S & 0 \\ e_{31} & e_{31} & e_{33} & 0 & 0 & 0 & 0 & 0 & \varepsilon_{33}^S \end{bmatrix} \begin{bmatrix} \mathrm{S}_1 \\ \mathrm{S}_2 \\ \mathrm{S}_3 \\ \mathrm{S}_4 \\ \mathrm{S}_5 \\ \mathrm{S}_6 \\ \mathrm{E}_1 \\ \mathrm{E}_2 \\ \mathrm{E}_3 \end{bmatrix} \tag{3-4}$$

where $C_{66}^E = \frac{1}{2}(C_{11}^E - C_{12}^E)$.

3.2.2. Governing Equations for the Piezoelectric Circular Cylindrical Shell

To obtain the governing equations for a stepped piezoelectric shell, the governing equations for a uniform-thickness piezoelectric shell are obtained first. Based on Flugge's shell theory extended for a piezoelectric material, the governing equations for the free vibration can be obtained as below [16]

$$k_{11}u + k_{12}v + k_{13}w = \rho h R\ddot{u} \tag{3-5}$$

$$k_{21}u + k_{22}v + k_{23}w = \rho h R\ddot{v} \tag{3-6}$$

$$k_{31}u + k_{32}v + k_{33}w = \rho h R\ddot{w} \tag{3-7}$$

in which ρ is the density (kg/m^3), h is the tube thickness (m), R is the mean radius (m), (u, v, w) are displacements in axial, circumferential and radial directions, respectively. Double dot denotes second differentiation with respect to time and operator elements k can be defined as below

$$k_{11} = \kappa_1 \frac{h}{2R}\left(-\frac{12R^2+h^2}{12R^2}\frac{\partial^2}{\partial\theta^2} - 2\frac{\partial^2}{\partial x^2}\right) + \kappa_2 \frac{h}{2R}\frac{12R^2+h^2}{12R^2}\frac{\partial^2}{\partial\theta^2} - \kappa_p \frac{h^3}{12R^3+Rh^2}\frac{\partial^2}{\partial x^2} \tag{3-8}$$

$$k_{21} = -\kappa_2 \frac{h}{2R}\frac{\partial^2}{\partial\theta\partial x} - \kappa_1 \frac{h}{2R}\frac{\partial^2}{\partial\theta\partial x}\left(-\frac{12R^2+h^2}{12R^2}\frac{\partial^2}{\partial\theta^2} - 2\frac{\partial^2}{\partial x^2}\right) - \kappa_p \frac{h^3}{12R^3+Rh^2}\frac{\partial^2}{\partial x\partial\theta} \tag{3-9}$$

$$k_{31} = \kappa_1 \frac{h^3}{24R^3}\left(\frac{\partial^3}{\partial\theta^2\partial x} - 2\frac{\partial^3}{\partial x^3}\right) + \kappa_2 \frac{h}{2R}\left(2\frac{\partial}{\partial x} - \frac{h^2}{12R^2}\frac{\partial^3}{\partial x\partial\theta^2}\right) - \kappa_p \frac{h^3}{R}\left(\frac{1}{12R^2+h^2}\frac{\partial^3}{\partial x\partial\theta^2} + \frac{1}{12R^2}\frac{\partial^3}{\partial x^3}\right) \tag{3-10}$$

$$k_{12} = \kappa_1 \frac{h}{2R}\frac{\partial^2}{\partial\theta\partial x} - \kappa_2 \frac{h}{2R}\frac{\partial^2}{\partial\theta\partial x} - \kappa_p \frac{h^3}{12R^3+Rh^2}\frac{\partial^2}{\partial x\partial\theta} \tag{3-11}$$

$$k_{22} = -\kappa_1 \frac{h}{2R}\left(2\frac{\partial^2}{\partial\theta^2} + \frac{4R^2+h^2}{4R^2}\frac{\partial^2}{\partial x^2}\right) + \kappa_2 \frac{h}{2R}\frac{4hR^2+h^2}{8R^3}\frac{\partial^2}{\partial x^2} - \kappa_p \frac{h^3}{12R^3+Rh^2}\frac{\partial^2}{\partial\theta^2} \tag{3-12}$$

$$k_{32} = \kappa_1 \frac{h}{R}\left(-\frac{h^2}{8R^2}\frac{\partial^3}{\partial x^2\partial\theta} + \frac{\partial}{\partial\theta}\right) + \kappa_2 \frac{h^3}{24R^3}\frac{\partial^3}{\partial x^2\partial\theta} - \kappa_p \frac{h^3}{R}\left(\frac{1}{12R^2+h^2}\frac{\partial^3}{\partial\theta^3} + \frac{1}{12R^2}\frac{\partial^3}{\partial x^3}\right) \tag{3-13}$$

$$k_{13} = -\kappa_1 \frac{h^3}{24R^3}\frac{\partial^3}{\partial\theta^2\partial x} + \kappa_2 \frac{h}{R}\left(-\frac{\partial}{\partial x} + \frac{h^2}{24R^2}\frac{\partial^3}{\partial x\partial\theta^2}\right) + \kappa_p \frac{h^3}{R}\left(-\frac{1}{12R^2+h^2}\frac{\partial^3}{\partial x\partial\theta^2} + \frac{1}{12R^2}\frac{\partial^3}{\partial x^3}\right) \tag{3-14}$$

$$k_{23} = \kappa_1 \frac{h}{R}\left(\frac{h^2}{8R^2}\frac{\partial^3}{\partial x^2\partial\theta} - \frac{\partial}{\partial\theta}\right) - \kappa_2 \frac{h^3}{24R^3}\frac{\partial^3}{\partial x^2\partial\theta} + \kappa_p \frac{h^3}{R}\left(-\frac{1}{12R^2+h^2}\frac{\partial^3}{\partial\theta^3} + \frac{1}{12R^2}\frac{\partial^3}{\partial x^2\partial\theta}\right) \tag{3-15}$$

$$k_{33} = \kappa_1 \frac{h^2}{24R^3}\left(4\frac{\partial^2}{\partial\theta^2} + 2\frac{\partial^4}{\partial\theta^4} + 4\frac{\partial^4}{\partial x^2\partial\theta^2} + 2\frac{\partial^4}{\partial x^4} + 2\right) + \kappa_2\frac{h}{R} + \kappa_p\frac{h^3}{R}\left(-\frac{1}{12R^2+h^2}\frac{\partial^4}{\partial\theta^4} + \frac{1}{12R^2}\frac{\partial^4}{\partial x^4}\right) \quad (3\text{-}16)$$

where k_1, k_2, k_p can be defined as [16]

$$k_1 = \frac{c_{13}^2}{c_{33}} - c_{11} \quad (3\text{-}17)$$

$$k_2 = \frac{c_{13}^2}{c_{33}} - c_{12} \quad (3\text{-}18)$$

$$k_d = d_{13}(k_1 + k_2) \quad (3\text{-}19)$$

$$k_p = -\frac{k_d^2}{(2c_{13}d_{13}+c_{33}d_{33})^2+c_{33}\varepsilon_{33}^s} \quad (3\text{-}20)$$

where d is the piezoelectric strain constant (m/V).

In order to get the natural frequencies for the free vibration of the piezoelectric shell, it is required to find a solution for the equations (3-5)-(3-7). Therefore, the displacement fields are considered as

$$u(x,\theta,t) = U(x)\cos n\theta\cos\omega t \quad (3\text{-}21)$$

$$v(x,\theta,t) = V(x)\sin n\theta\cos\omega t \quad (3\text{-}22)$$

$$w(x,\theta,t) = W(x)\cos n\theta\cos\omega t \quad (3\text{-}23)$$

where ω is the natural frequency of the shell and n is the circumferential wave number. Substituting these three equations in the governing equations (3-5)-(3-7) and using the state-space technique [6, 89] together with some mathematical manipulations results in an equation which can be written in the following form

$$\Phi' = H\Phi \quad (3\text{-}24)$$

where

$$\Phi = [U \;\; U' \; V \;\; V' \; W \;\; W' \; W'' \; W''']^T \tag{3-25}$$

Having performed these mathematical simplifications, one can obtain the non-zero arrays of the H matrix as

$$H_{12} = H_{34} = H_{56} = H_{67} = H_{78} = 1 \tag{3-26}$$

$$H_{21} = \frac{\left(12R^2+h^2\right)^2 n^2 (k_1-k_2)}{24R^2(k_p h^2+k_1(12R^2+h^2))} + \frac{R^2\rho\omega^2\left(12R^2+h^2\right)}{(k_p h^2+k_1(12R^2+h^2)} \tag{3-27}$$

$$H_{24} = \frac{\left(12R^2+h^2\right)n(k_1-k_2)}{2(k_p h^2+k_1(12R^2+h^2))} - \frac{k_p h^2 n}{k_p h^2+k_1(12R^2+h^2)} \tag{3-28}$$

$$H_{26} = \frac{\left(12R^2+h^2\right)n^2 h^2 (k_1-k_2)}{24R^2(k_p h^2+k_1(12R^2+h^2))} - \frac{\left(12R^2+h^2\right)k_2+n^2 h^2 k_p}{k_p h^2+k_1(12R^2+h^2)} \tag{3-29}$$

$$H_{28} = \frac{\left(12R^2+h^2\right)h^2 k_p}{12R^2(k_p h^2+k_1(12R^2+h^2))} \tag{3-30}$$

$$H_{42} = \frac{8R^2((k_1+k_2)\frac{n}{2}+\frac{nh^2 k_p}{\left(12R^2+h^2\right)})}{k_1(4R^2+h^2)-k_2(4R^2+h)} \tag{3-31}$$

$$H_{43} = \frac{8R^3(k_1 h\frac{n^2}{R}+\frac{h^3 n^2 k_p}{\left(12R^3+Rh^2\right)}+R\rho h\omega^2)}{k_1 h(4R^2+h^2)-k_2(4hR^2+h^2)} \tag{3-32}$$

$$H_{45} = \frac{8R^2(k_1 n-\frac{n^3 h^2 k_p}{\left(12R^3+h^2\right)})}{k_1(4R^2+h^2)-k_2(4R^2+h)} \tag{3-33}$$

$$H_{47} = \frac{nh^2(k_2-2k_p-3k_1)}{3(k_1(4R^2+h^2)-k_2(4R^2+h))} \tag{3-34}$$

$$H_{81} = \frac{\frac{k_p h^3 H_{21} H_{42}}{12R^3}}{\frac{2h^2(k_p h+k_1)}{24R^3} - H_{28}h^3(\frac{k_1+k_p}{12R^3})} \tag{3-35}$$

$$H_{82} = \frac{\frac{n^2 h^3(k_1-k_2)}{24R^3} - k_2\frac{h}{R} - \frac{k_p n^2 h^3}{(12R^2+h^2)R} + \frac{nh^3 H_{42}(3k_1-k_2)}{24R^3} + (H_{21}+H_{24}H_{42})h^3(\frac{k_1+k_p}{12R^3})}{\frac{2h^2(k_p h+k_1)}{24R^3} - H_{28}h^3(\frac{k_1+k_p}{12R^3})} \tag{3-36}$$

$$H_{83} = \frac{-k_1 h\frac{n}{R} - \frac{k_p n^3 h^3}{(12R^2+h^2)R} + (H_{24}H_{43})h^3\left(\frac{k_1+k_p}{12R^3}\right) + \frac{H_{43}h^3 n}{24R^3}(3k_1-k_2)}{\frac{2h^2(k_p h+k_1)}{24R^3} - H_{28}h^3(\frac{k_1+k_p}{12R^3})} \tag{3-37}$$

$$H_{84} = \frac{\frac{k_p h^3(H_{24}H_{42}+H_{43})}{12R^3}}{\frac{2h^2(k_p h+k_1)}{24R^3} - H_{28}h^3(\frac{k_1+k_p}{12R^3})} \tag{3-38}$$

$$H_{85} = \frac{(H_{24}H_{45})h^3\left(\frac{k_1+k_p}{12R^3}\right) + \frac{nh^3 H_{45}(3k_1-k_2)}{24R^3} - k_2\frac{h}{R} + \frac{k_1 h^2}{12R^3}\left(2n^2-n^4-1\right) - R\rho h\omega^2 + \frac{k_p h^3 n^4}{(12R^2+h^2)R}}{\frac{2h^2(k_p h+k_1)}{24R^3} - H_{28}h^3(\frac{k_1+k_p}{12R^3})} \tag{3-39}$$

$$H_{86} = \frac{\frac{k_p h^3 (H_{26} H_{42} + H_{45})}{12R^3}}{\frac{2h^2(k_p h + k_1)}{24R^3} - H_{28} h^3 (\frac{k_1 + k_p}{12R^3})} \tag{3-40}$$

$$H_{87} = \frac{(H_{26} + H_{24} H_{47}) h^3 \left(\frac{k_1 + k_p}{12R^3}\right) + \frac{k_1 n^2 h^2}{6R^3} + \frac{H_{47} h^3 n}{24R^3}(3k_1 - k_2)}{\frac{2h^2(k_p h + k_1)}{24R^3} - H_{28} h^3 (\frac{k_1 + k_p}{12R^3})} \tag{3-41}$$

$$H_{88} = \frac{\frac{k_p h^3 (H_{28} H_{42} + H_{47})}{12R^3}}{\frac{2h^2(k_p h + k_1)}{24R^3} - H_{28} h^3 (\frac{k_1 + k_p}{12R^3})} \tag{3-42}$$

Solution of Equation (3-24) takes the form

$$\Phi = e^{Hx} B \tag{3-43}$$

in which B is a constant column matrix of 8×1 determined from the boundary conditions. The following common classical boundary conditions can be considered [90]

1. Simply Supported: $v = w = N_x = M_x = 0$
2. Free: $N_{x\theta} = Q_x = N_x = M_x = 0$
3. Clamped: $u = v = w = \frac{\partial w}{\partial x} = 0$

where N_x is the axial force, M_x is the bending moment, Q_x is the lateral shear force and $N_{x\theta}$ is the circumferential shear force [90].

Employing the boundary conditions as above in equation (3-43) results in a homogeneous system of equations of the form

$$KB = 0 \tag{3-44}$$

where K is an 8×8 matrix and B is a constant column matrix. Setting the determinant of K equal to zero, gives the natural frequencies.

Since the solution procedure we employed is different to [16], it is required to check the validity of the method stated above. Hence, the result is obtained for a uniform-

thickness piezoelectric tube with the same material properties and dimensions as in [16]. To do so, the governing equations (3-5)-(3-7) and the solution procedure stated above were followed utilizing the given *H* matrix arrays and the condition for free boundaries. The piezoelectric material is PIC141 the properties of which are taken from [16, 17] as in Table 3-1. The cylindrical shell has length of 10mm, mid-radius of 18mm and thickness of 2mm. Table 3-2 summarizes the obtained result in this study using the present method for the first eigenfrequency of a free-free shell compared to that of experiments and that theoretically obtained by [16]. According to [16], the exact value for the experimentally obtained result was not mentioned; however, they mentioned it was within 4% of the theoretical value and based on a graph they provided in their paper, it was estimated to be approximately 92 KHz. According to the manufacturer of the piezoelectric material, the material constants had an error margin of 5% [16]. Hence, they made no effort to match the theoretical result with that of the experiment by adjusting the material constants. We did not do that adjustment either since the result is within a reasonable range and accuracy.

Table 3-1. Material properties of PIC141 [16, 17].

Material	Density (Kg/m^3)	Elastic stiffness matrix components (Pa)					Relative Permittivity		Stress constant (C/m^2)		
		c_{11}^E	c_{12}^E	c_{13}^E	c_{33}^E	c_{44}^E	$\varepsilon_{11}^S/\varepsilon_0$	$\varepsilon_{33}^S/\varepsilon_0$	e_{31}	e_{33}	e_{15}
PIC141	7800	1.08e11	4.66e10	4.63e10	1.05e11	4.92e10	1500	1300	-2.47	23.9	23.4

Table 3-2. Comparison of the fundamental frequency for a free-free uniform-thickness piezoelectric cylindrical shell.

Frequency (KHz)		
Experimental [16]	Theoretical [16]	Present Study
92	88	99

3.2.3. Governing Equations for the Axially Stepped Piezoelectric Circular Cylindrical Shell

In the previous section, the governing equations for a uniform-thickness piezoelectric shell and the solution procedure were elaborated on and a comparison was made with one available result in the literature. In this section, the approach is extended to axially stepped shells. Fig.3-1 illustrates a shell with 'i' steps. Each segment has its own length and thickness as evident from the figure. Further, a 3D representation of the shell is presented.

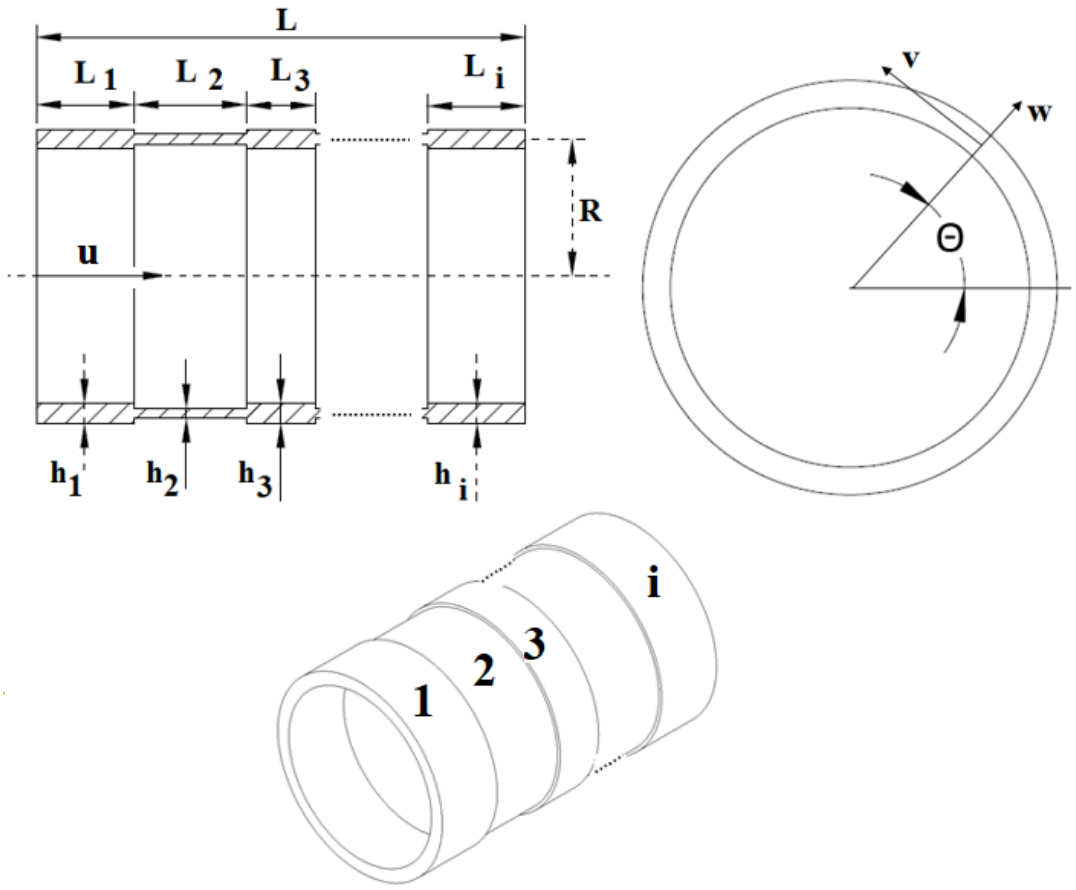

Fig. 3-1. Coordinate system and geometry of a stepped-thickness transducer having 'i' steps with its 3D representation.

In order to present the results for a stepped-thickness piezoelectric cylindrical shell, we utilize the same solution approach and Flugge shell equations as above. Further, it is required to consider matching boundary conditions at the interface between two consecutive sections of the shell with different thicknesses to satisfy the continuity conditions. However, we first need to validate this method for a non-piezoelectric stepped shell. Therefore, we used Flugge shell equations and used state-space technique to proceed with the solution procedure. The Flugge governing equations can be written for each segment of the stepped shell as [51]

$$\frac{\partial^2 u}{\partial x^2}+\frac{(1-\nu)}{2R^2}\frac{\partial^2 u}{\partial \theta^2}+\frac{(1+\nu)}{2R}\frac{\partial^2 v}{\partial x\partial\theta}+\frac{\nu}{R}\frac{\partial w}{\partial x}+\frac{h^2}{12R^2}\left(\frac{(1-\nu)}{2R^2}\frac{\partial^2 u}{\partial\theta^2}-R\frac{\partial^3 w}{\partial x^3}+\frac{(1-\nu)}{2R}\frac{\partial^3 w}{\partial x\partial\theta^2}\right)=$$

$$\rho\frac{(1-\nu^2)}{Y}\frac{\partial^2 u}{\partial t^2} \tag{3-45}$$

$$\frac{(1+\nu)}{2R}\frac{\partial^2 u}{\partial x\partial\theta}+\frac{(1-\nu)}{2}\frac{\partial^2 v}{\partial x^2}+\frac{1}{R^2}\frac{\partial^2 v}{\partial\theta^2}+\frac{1}{R^2}\frac{\partial w}{\partial\theta}+\frac{h^2}{12R^2}\left(\frac{3(1-\nu)}{2}\frac{\partial^2 v}{\partial x^2}-\frac{(3-\nu)}{2}\frac{\partial^3 w}{\partial x^2\partial\theta}\right)=$$

$$\rho\frac{(1-\nu^2)}{Y}\frac{\partial^2 v}{\partial t^2} \tag{3-46}$$

$$\frac{\nu}{R}\frac{\partial u}{\partial x}+\frac{1}{R^2}\frac{\partial v}{\partial\theta}+\frac{1}{R^2}w+\frac{h^2}{12R^2}\left(R^2\frac{\partial^4 w}{\partial x^4}+2\frac{\partial^4 w}{\partial x^2\partial\theta^2}+\frac{1}{R^2}\frac{\partial^4 w}{\partial\theta^4}-R\frac{\partial^3 u}{\partial x^3}+\frac{(1-\nu)}{2R}\frac{\partial^3 u}{\partial x\partial\theta^2}-\right.$$

$$\left.\frac{(3-\nu)}{2}\frac{\partial^3 v}{\partial x^2\partial\theta}+\frac{1}{R^2}w+\frac{2}{R^2}\frac{\partial^2 w}{\partial\theta^2}\right)=\rho\frac{(1-\nu^2)}{Y}\frac{\partial^2 w}{\partial t^2} \tag{3-47}$$

In the above equations, Y is the modulus of elasticity (Young's modulus) and ν is the Poisson's ratio. Similar to the previous section, one can substitute equations (3-21)-(3-23) in the governing equations (3-45)-(3-47) and using the state-space technique as before together with some mathematical manipulations, an equation similar to (3-24) with the same definition as (3-25) can be obtained where the non-zero arrays of the H matrix can be written as

$$H_{12}=H_{34}=H_{56}=H_{67}=H_{78}=1 \tag{3-48}$$

$$H_{21}=\frac{n^2(1-\nu)(1+\frac{h^2}{12R^2})}{2R^2}-\frac{\rho\omega^2(1-\nu^2)}{Y} \tag{3-49}$$

$$H_{24} = -\frac{n(1+\nu)}{2R} \tag{3-50}$$

$$H_{26} = -\frac{\nu}{2} + \frac{n^2h^2(1-\nu)}{24R^3} \tag{3-51}$$

$$H_{28} = \frac{h^2}{12R} \tag{3-52}$$

$$H_{42} = \frac{n(1+\nu)}{R(1-\nu)(1+\frac{h^2}{4R^2})} \tag{3-53}$$

$$H_{43} = \frac{2n^2}{R^2(1-\nu)(1+\frac{h^2}{4R^2})} - \frac{2\rho\omega^2(1-\nu^2)}{Y(1-\nu)(1+\frac{h^2}{4R^2})} \tag{3-54}$$

$$H_{45} = \frac{2n}{R^2(1-\nu)(1+\frac{h^2}{4R^2})} \tag{3-55}$$

$$H_{47} = \frac{-n(3-\nu)\frac{h^2}{12R}}{(1-\nu)(1+\frac{h^2}{4R^2})} \tag{3-56}$$

$$H_{82} = -\frac{\nu}{\frac{h^2}{12}R\left(1-\frac{h^2}{12R^2}\right)} + \frac{n^2(1-\nu)}{R^3\left(1-\frac{h^2}{12R^2}\right)} + \frac{n^2(1-\nu)\frac{h^2}{12R^2}}{2R^3\left(1-\frac{h^2}{12R^2}\right)} - \frac{\rho\omega^2(1-\nu^2)}{YR\left(1-\frac{h^2}{12R^2}\right)} + \frac{n^2(1+\nu)}{R^3(1-\frac{h^2}{12R^2})(1+\frac{h^2}{4R^2})} \tag{3-57}$$

$$H_{83} = -\frac{n}{\frac{h^2}{12}R^2\left(1-\frac{h^2}{12R^2}\right)} + \frac{2n^3}{R^4\left(1-\frac{h^2}{12R^2}\right)(1+\frac{h^2}{4R^2})} - \frac{2n\rho\omega^2(1-\nu^2)}{YR^2\left(1-\frac{h^2}{12R^2}\right)(1+\frac{h^2}{4R^2})} \tag{3-58}$$

$$H_{85} = -\frac{1}{\frac{h^2}{12}R^2\left(1-\frac{h^2}{12R^2}\right)} - \frac{n^4}{R^4\left(1-\frac{h^2}{12R^2}\right)} + \frac{2n^2}{R^4\left(1-\frac{h^2}{12R^2}\right)} - \frac{1}{R^4\left(1-\frac{h^2}{12R^2}\right)} + \frac{\rho\omega^2(1-\nu^2)}{Y\frac{h^2}{12}\left(1-\frac{h^2}{12R^2}\right)} + \frac{2n^2}{R^4\left(1-\frac{h^2}{12R^2}\right)(1+\frac{h^2}{4R^2})} \tag{3-59}$$

$$H_{87} = \frac{2n^2}{R^2\left(1-\frac{h^2}{12R^2}\right)} - \frac{\nu}{R^2\left(1-\frac{h^2}{12R^2}\right)} + \frac{n^2\frac{h^2}{12R^2}(1-\nu)}{2R^2\left(1-\frac{h^2}{12R^2}\right)} - \frac{n^2\frac{h^2}{12R^2}(3-\nu)}{R^2\left(1-\frac{h^2}{12R^2}\right)(1+\frac{h^2}{4R^2})} \tag{3-60}$$

All the above equations are written for one segment of the stepped shell. They can be similarly written for the next segment. However, the following continuity conditions should also be taken into account between each two consecutive segments ‘i’ and ‘i+1’ as shown in Fig.3-2 [6]

$$u_i = u_{i+1};\ v_i = v_{i+1};\ w_i = w_{i+1};\ \frac{\partial w_i}{\partial x} = \frac{\partial w_{i+1}}{\partial x};\ M_{x_i} = M_{x_{i+1}};\ N_{x_i} = N_{x_{i+1}};\ N_{x\theta_i} = N_{x\theta_{i+1}};\ Q_{x_i} = Q_{x_{i+1}} \tag{3-61}$$

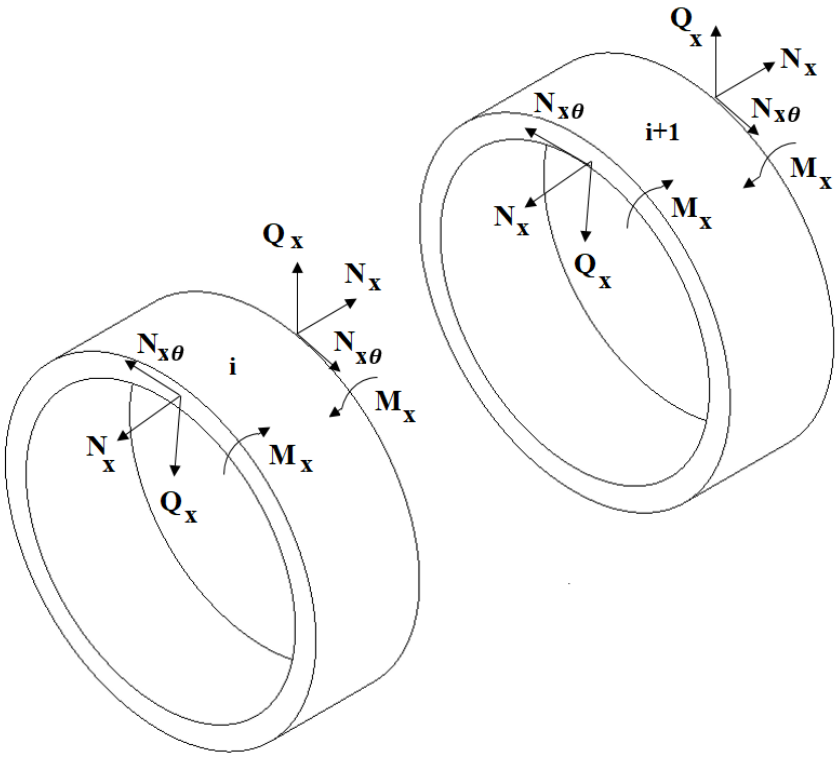

Fig. 3-2. Force and moment components for the stepped transducer segments.

Similar to the previous section, employing the boundary conditions as well as the continuity conditions, equation (3-61), in equation (3-43) with the corresponding *H* matrix, equations (3-48)-(3-60), results in a homogeneous system of equations of the similar form to (3-44).

Setting the determinant of *K* equal to zero, gives the natural frequencies. This has been done for a simply supported axially stepped elastic cylindrical shell with two segments (thicknesses) as in Fig.3-3. Table 3-3 summarizes the obtained results and compares them with those of obtained by Ref. [61]. As evident, there is reasonable agreement between the results obtained here and those by Ref. [61]. The deviation from the results of Ref. [61] is around 7% in the worst case and is less than 5% for most of the cases. This may prove the accuracy of the approach in the present work for the calculation of the frequency for an axially stepped cylindrical shell.

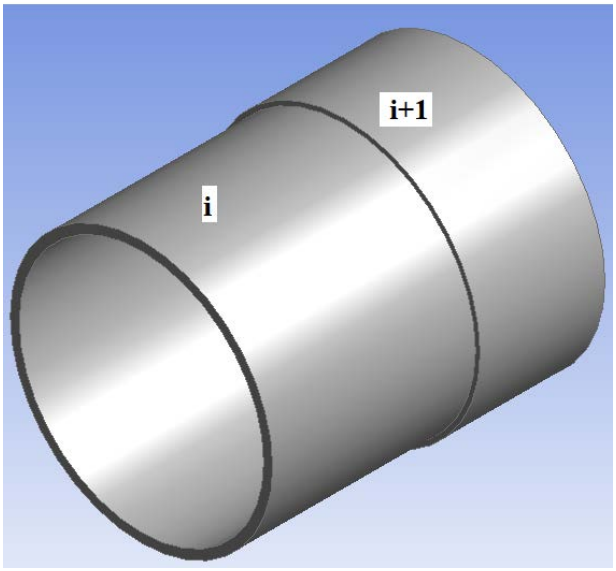

Fig. 3-3. Stepped transducer with two segments.

Table 3-3. Comparison of the first five frequencies for a stepped-thickness shell with two segments ($h_1/R=0.01$; $h_2/h_1=1/2$; $L_2/L=1/2$; ρ =7850 kg/m^3; Y=210GPa; $\nu = 0.3$; Axial wave number (m)=1).

	Non Dimensional Frequency, (Frequency in Hz)			
n	(L/R)=5		(L/R)=10	
	Present	Ref. [61]	Present	Ref. [61]
1	0.18565 (1010.40)	0.176590 (959.73)	0.058963 (320.45)	0.056538 (307.27)
2	0.076018 (413.14)	0.072988 (396.67)	0.021361 (116.09)	0.020750 (112.77)
3	0.041880 (227.61)	0.041159 (223.69)	0.019532 (106.15)	0.020546 (111.66)
4	0.039770 (216.14)	0.041561 (225.88)	0.027313 (148.44)	0.029146 (158.40)
5	0.049835 (270.84)	0.053819 (292.49)	0.037166 (201.99)	0.038195 (207.58)

Now that the approach used in this work has been validated for a uniform-thickness piezoelectric cylindrical shell as well as a stepped-thickness non-piezoelectric one, it can be reliably and readily extended to stepped-thickness piezoelectric shells. The arrays of the *H* matrix are the same as those for a uniform-thickness piezoelectric shell, equations (3-26) to (3-42). Further, continuity conditions, equation (3-61) should also be taken into account similar to that performed for a stepped-thickness non-

piezoelectric shell. This can provide us with the frequencies for the stepped-thickness piezoelectric shell. The material properties of the piezoelectric (PZT-5) shell are given in Table 3-4 and the boundary condition is taken to be simply supported.

Table 3-4. Material properties of PZT-5L [18].

Material	Density (Kg/m^3)	Elastic stiffness matrix components (Pa)					Relative Permittivity		Stress constant (C/m^2)		
		$c_{11}{}^E$	$c_{12}{}^E$	$c_{13}{}^E$	$c_{33}{}^E$	$c_{44}{}^E$	$\varepsilon_{11}{}^s/\varepsilon_0$	$\varepsilon_{33}{}^s/\varepsilon_0$	e_{31}	e_{33}	e_{15}
PZT-5L	7600	1.21e11	7.54e10	7.52e10	1.11e11	2.11e10	916	830	-5.4	15.8	12.3

Table 3-5 summarizes the obtained results. In this table, the obtained results are compared to those obtained for an identical non-PZT cylindrical shell whose modulus of elasticity is defined as the reciprocal of the elastic compliance ($Y = \frac{1}{s_{33}^E}$) of the corresponding PZT material. This can serve as an estimate of the results for the PZT stepped shell. In all cases, the frequencies are within a reasonable range and fairly close. Further, in all the cases, the frequencies for the longer PZT shell are lower than that of the shorter one as expected.

Table 3-5. Comparison of the first five frequencies for a stepped-thickness piezoelectric shell with two segments vs a similar non-PZT shell with $Y = \frac{1}{s_{33}^E} = 53.2GPa$.

n	*($h_1/R=0.01$; $h_2/h_1=1/2$; $L_2/L=1/2$;* $\nu = 0.3$*; m=1)*			
	Frequency in Hz			
	(L/R)=5		(L/R)=10	
	PZT	Non-PZT	PZT	Non-PZT
1	394.31	516.86	143.81	163.92
2	223.99	211.33	93.71	59.38
3	76.29	116.43	8.92	54.30
4	163.83	110.56	37.86	75.93
5	36.60	138.54	31.53	103.32

3.3. Acoustic Amplification

According to the previous chapter and the literature, there are several methods to amplify the acoustic field. Below is a brief theoretical explanation on how these methods affect the acoustic field and its focus and directivity.

3.3.1. Stepped Plate Transducers

One of the common types of ultrasonic transducers used for gas media were aerodynamic ones such as whistles and sirens. A gas jet provided the acoustic energy and despite the fact that they can provide large acoustic power, they have a very low efficiency and cannot reach ultrasonic frequencies, either [2]. Further, electromagnetic, magnetostrictive and piezoelectric ultrasound sources seem incapable of generating high power ultrasound with good efficiency and directivity as they cannot undergo large longitudinal vibration amplitude. The problems lying behind ultrasound generation in gases are attributed to low specific acoustic impedance and high absorption of the medium. Therefore, in order to have an efficient energy transmission, good impedance matching between the transducer and gas medium, large

amplitudes of vibration and highly directional radiation are needed [2]. As mentioned in the previous chapter, for ultrasonic radiation in fluids, vibrating plates can be used. However, the directivity of the generated acoustic waves is very important. As depicted in Fig. 3-4, the radiations from different parts of a uniform-thickness plate are in counter-phase (diagrams A_{2m} and A_{2m+1}). This results in phase cancellation and poor directivity. Nonetheless, introduction of some steps on the surface of the plate which are raised half a wavelength of the radiated sound makes the radiations in-phase and directivity will increase [12]. The results of this modification are shown by the new diagrams A_1', A_3', etc. in Fig. 3-4, that indicate a coherent radiation in the medium.

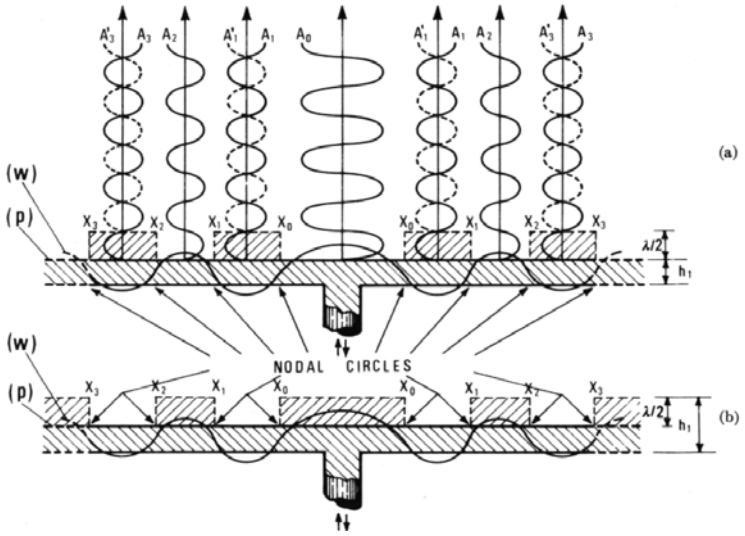

Fig. 3-4. Radiation mechanism and behaviour of the stepped plate. (a) Central region unraised;(b) Central region raised [12].

3.3.2. Curved Configurations

Another approach to increase the efficiency of ultrasound generation in air is implementing several air-coupled ultrasonic transducers into an array to increase signal amplitude as in Fig. 3-5 [13]. This can maximize the signal amplitude at the focal line of the array. However, slight changes in the spatial position of the

transmitting transducers were reported to have a considerable effect on the signal at the focal line. Maximum sound pressure level in air was 142.70 dB SPL, and it might be possible to achieve pressure levels of up to 150 dB SPL. Hence, curved configurations can be an alternative to amplify the generated acoustic field. Further, a single curved transducer can be employed to produce focused radiation. However, mode of vibration plays an important role. As in Figs 3-6 and 3-7, the vibration peaks were in-phase for the length extensional mode and out of phase for the flexural bending mode [14, 47]. Therefore, the length extensional mode can generate a stronger ultrasound wave than the flexural bending mode. The resonance frequencies and vibration amplitudes of the two modes are reported to be dependent on the structure parameters (width, length, thickness and radius of curvature) and the material properties (density, Young's modulus and piezoelectric constants). While designing the transducer, these two resonance frequencies should be separated as far as possible to mitigate bending vibration [14].

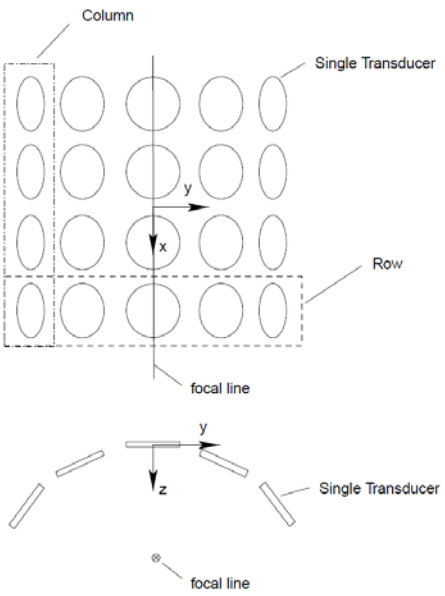

Fig.3-5. Schematic of the array transducer [13].

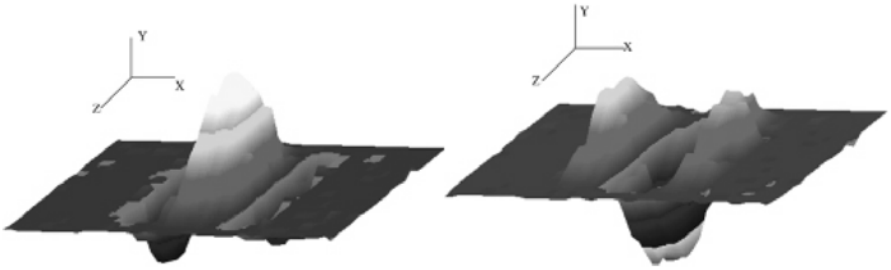

Fig. 3-6. Instantaneous displacement profile for flexural bending mode (f = 31 kHz): Left) phase = 0° and Right) phase = 180° [14].

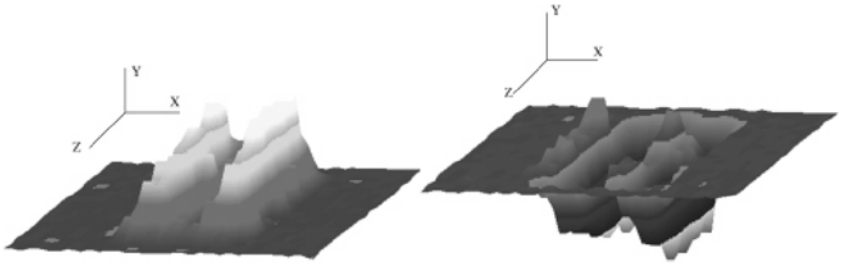

Fig.3-7. Instantaneous displacement profile for length extensional mode (f = 59 kHz): Left) phase = 0° and Right) phase = 180° [14].

3.3.3. Cylindrical Transducers

Another alternative to generate focused amplified acoustic field is a cylindrical shell which resembles a curved one as in the previous section. It focuses the generated waves at the centreline and amplifies the acoustic field. An aluminium cylindrical chamber driven by piezoelectric transducer at 21.8 KHz was successfully employed to achieve high intensity acoustic field inside the tube (154.3 dB of SPL) with 75W applied power [15]. Using a cylindrical shell mitigates the problem associated with the spatial position of the curved array transducers as in 3.3.2. However, suitable mode of vibration for the cylindrical shell should be considered just like curved transducers to effectively focus the generated waves at the centreline and amplify the acoustic field. This can be investigated for each transducer depending on its dimensions and frequency range of operation.

3.3.4. Steps with Curvature

As explained, curved and cylindrical shells can effectively focus the radiated waves toward the centreline as long as a suitable mode shape is considered. Further, steps in plates improve directivity by mitigating phase-cancellation. Hence, a combination of these two was considered as a stepped-thickness cylindrical shell for the present study as elaborately explained in the previous chapter to enhance the focus and directivity. Moreover, steps help localize the vibration within thinner regions at a higher amplitude. Accordingly, it is anticipated to have highly directional and amplified acoustic field inside the transducer for the same input power. This is to be investigated in this study and requires an understanding of the vibration characteristics of the designed stepped-thickness shells to obtain an appropriate mode shape.

3.4. Ultrasound-Droplet Interaction

In this section, the effect of ultrasound on droplets is elaborated on. Since one of the applications of the transducer under study is to implement it as a second stage transducer for atomization of droplets, it is required to briefly present possible scenarios for the interaction effect. This can provide us with the correct insight on what to expect from the proposed transducer while implemented as a second stage transducer and how it works. Below is a summary of various theories to disintegrate water droplets:

- ✓ Resonant excitation and disintegration in air
- ✓ Acoustic squeezing and disintegration
- ✓ Solid surface excitation
- ✓ Enhanced heat and mass transfer

3.4.1. Resonant Excitation and Disintegration in Air

A single droplet of water is acoustically levitated in air and the levitation signal is set in such a way to excite the droplet at one of its resonance frequencies to cause disintegration to smaller droplets [31, 36]. Various studies investigated influential parameters such as oscillation amplitude and asymmetry, aperiodic oscillations, resonance mode coupling, viscosity etc. on the droplet disintegration [91-96]. However, all these studies were limited to single, large droplets in the range of millimetres but not a stream of multi-size droplets within the range of micrometre. One problem associated with resonant excitation for a stream of various size droplets is that each individual droplet has a specific resonance and a broadband transducer is required or a set of transducers each operating at a different frequency. Another issue regarding this technique is that the energy transmission from the transducer to the droplet should be through transducer to air and finally through air to the droplet. Large acoustic mismatch is a big barrier to efficient energy transmission. The reflection coefficient, R_c, for an acoustic wave passing through one medium to another can be defined as:

$$R_c = \left(\frac{Z_2 - Z_1}{Z_2 + Z_1}\right)^2 \tag{3-62}$$

Where Z is the acoustic impedance and the indices refer to the first and second media.

Considering the acoustic impedance values for air and water which are approximately 403 Ray (Pa.s/m) and 1500 MRay, R_c will be around 0.99. This means that less than 0.1% of the energy will be transmitted to the droplet. Hence, this is not a suitable approach.

3.4.2. Acoustic Squeezing and Disintegration

In another but similar approach to the above, a single droplet can be kept floating in an ultrasound field of a levitator and get squeezed acoustically by oscillations until getting flattened and disintegrated [32, 34]. However, a single large droplet of 1mm was investigated and applying this method to a stream of multi-size droplets may not be an easy task.

3.4.3. Solid Surface Excitation

The third technique is solid surface excitation where droplets disintegrate when they are exposed to a surface vibrating at ultrasound range [33, 35, 37]. Various scenarios may occur as the result of droplets coming into contact with a vibrating surface. Droplets may attach to the surface, may spread out on the surface, may break up into smaller ones, may bounce off the surface or a combination of these may occur [35, 37, 97]. Depending on various droplet and surface parameters such as temperature, diameter, viscosity, density, surface tension and roughness, impact velocity and angle, any of these scenarios may occur. Since transmission of energy from air to droplets was cumbersome due to acoustic impedance mismatch, it was proposed to investigate transmission of energy from the transducer directly to the droplet and excite it at its resonance frequency when it touches the transducer surface. This excitation with a suitably large amplitude of vibration can lead to breakup of the droplets as long as all the conditions are satisfied for this mechanism to be dominant. Alternatively, they may break into smaller droplets due to the impact. This has proven useful for single droplets of 2-3mm in diameter [98]. However, applicability of such method for micrometre droplets in a stream encounters the same problem that multi-size droplets require

various excitation frequencies. According to [37], large proportion of droplets attached to the surface and wetted the transducer surface resulting in a hindrance for droplet breakup. The attachment of the droplets to the surface is especially dominant at low droplet velocities and surface temperatures. This has also been investigated for a stream of micro-size droplets [1]. Micro droplets were exposed to a 1.45 MHz ultrasound nebulizer after being released from a droplet generator. Although this method was used for the breaking up of droplets on heated surfaces of 100-300ºC, it was concluded that at ambient temperatures, micro droplets attach to the surface, make it wet and therefore no improvement was observed for droplets disintegration into smaller ones.

3.4.4. Enhanced Heat and Mass Transfer

Improved heat and mass transfer between water droplets and the surrounding air in an acoustic field has been reported in the literature [99-103]. It was concluded that by increasing the relative movement between air/gas particles and droplets, it is possible to increase the evaporation rate [101-103]. Temkin managed to obtain a relationship between the droplet velocity amplitude and the gas particle velocity amplitude as [104]

$$\frac{U_{p0}}{U_0} = \frac{1}{\sqrt{1+(\omega\tau_d)^2}} \tag{3-63}$$

$$\tau_d = \frac{D^2}{18\nu\delta} \tag{3-64}$$

where U_{p0} is the droplet velocity amplitude, U_0 is the gas particle velocity amplitude, ω is the acoustic field frequency and τ_d is the dynamic relaxation time of the droplet as in Equation (3-64). In the latter equation, D is the droplet diameter, ν is the kinematic viscosity of the gas (m^2/s) and δ is the ratio of gas to droplet density. For

enhanced heat and mass transfer, $\frac{U_{p0}}{U_0}$ should tend to zero or a very small value which indicates high velocity of the gas particles with relatively stationary droplets.

Further, according to Kinsler, the gas particle displacement amplitude, ζ, for an acoustic sound wave in a fluid can be obtained as [105]

$$\zeta = \frac{U_0}{\omega} = \frac{P}{\rho c \omega} \tag{3-65}$$

where ρ is the fluid density, c is the speed of the sound wave in the fluid, ω is the acoustic field frequency and P is the acoustic pressure which can be obtained from the acoustic filed SPL from the common equation below where P_{ref} is the reference root mean square pressure amplitude 20×10^{-6}Pa.

$$SPL=20Log\ (P_{rms}/P_{ref}) \tag{3-66}$$

These equations can relate the acoustic field SPL and frequency to the droplet diameter and relative displacement between air/gas and the droplets. Knowing that the ratio of droplet velocity to air velocity is the same as the ratio of droplet displacement to air particle displacement for a harmonic acoustic signal [1], one can obtain the displacement amplitude of various size droplets.

From equations (3-63)-(3-66), it can be concluded that for an acoustic field with higher SPL, the relative movement between air particles and any specific fixed size droplets will be higher. Further, from equation (3-63), it can be concluded that for fixed SPL, larger droplets have higher relative movement compared to smaller droplets. This may affect the heat and mass transfer and improve vaporization of the larger droplets. Another important phenomenon associated with enhanced heat and mass transfer between air particle and droplets in an acoustic field is called acoustic streaming. According to [106], acoustic fields in the range of 150-165 dB at ultrasonic frequencies

should be high enough to form acoustic streaming flows around the droplet which enhances heat and mass transfer by improving the relative movement between droplets and gas particles and enhances evaporation of the droplets. Formation and strength of these streaming flows depends on a dimensionless number called the Stokes number which is defined as [107]

$$St = \sqrt{\frac{\nu}{\omega D^2}} \tag{3-67}$$

where D is the droplet diameter, ν is the kinematic viscosity of the gas (m^2/s) and ω is the acoustic field frequency. Sujith et al investigated the behaviour of droplets in an acoustic field and concluded that the relative displacement between the droplet and gas particles increases as the Stokes number decreases [101]. This means that for a fixed frequency acoustic field, larger droplets tend to be affected more by the acoustic field and the higher relative movement for these droplets results in higher heat and mass transfer. Further, as evident from equation (3-67), the higher the frequency, the lower the Stokes number and the higher the relative movement and heat transfer.

3.5. Closure

Various theories for the interaction between ultrasound and droplets were described. Nearly all the approaches were limited to individual large mm-size droplets. However, for the case of micrometre range stream of droplets, these approaches were not applicable. Enhanced heat and mass transfer may be more appropriate with a single transducer operating at a fixed frequency for a stream of different size droplets. Investigation of this is beyond the scope of this study. However, in the following chapters after identifying the final design for the stepped-thickness transducer, experiments will be performed to scrutinize the effectiveness of using such transducers

as a second stage transducer. This may also shed light to future investigations on the interaction effect and design of transducers to better target these droplets and vaporize them.

Chapter 4: Simulation and Design of Stepped-Thickness Transducers

4.1. Introduction

This chapter presents the development of the stepped-thickness transducers. The aim is to develop a transducer which delivers relatively strong acoustic field for a low power input. To this aim, it is required to obtain the frequencies and the corresponding mode shapes of vibration for a uniform-thickness specimen. Accordingly, the number and location of the axial steps will be identified which helps to develop the stepped-thickness transducers. In addition to axial steps, the other type of steps (circumferential steps) is also introduced to excite the cylindrical shell at mode shapes with various circumferential wave numbers. It is intended to investigate its effect on localization of the vibration with higher amplitudes and also on the acoustic field. In order to do this, ANSYS software is utilized. The reason for choosing this software to perform simulations is that it is a widely used and globally accepted package with accuracy and reliability that has been validated. Although the reliability of ANSYS has been assured in the literature, the obtained results for the uniform-thickness specimen are compared with the experimental ones. Once the reasonable accuracy was ascertained, simulations were continued to develop the stepped-thickness transducers.

The vibration characteristics of the cylindrical shells in this work can be obtained by using the methods explained in chapter 3. However, this process gets very complicated in particular if we deal with 3D analysis. The ANSYS package was used to overcome this complication.

4.2. Details and Specifications of the Simulations

Numerical simulations in this research are performed using powerful software ANSYS R15 Version 15.0.7. Various modules are employed such as modal and harmonic analyses for determining the vibration and acoustic characteristics of various transducers. Moreover, in order to be able to model the piezoelectric material and get the acoustic field inside the transducer, two extensions called 'ExtAcoustics' version 150.45 and 'PiezoAndMEMS' version 150.11 are installed and utilized. The explanations regarding these simulations are summarized below.

4.2.1. Modal & Harmonic Analyses

In order to get the mode shapes and resonance frequencies of the piezoelectric tubes, modal analysis is performed. Further, to get the response of the transducer over a range of frequencies and get the total deformation of the transducer as well as the intensity of the acoustic field generated by the ultrasonic vibration of the transducers, harmonic analysis is performed. These modules include several stages to define the problem completely before running the simulations as

- Engineering Data
- Geometry
- Model
- Setup
- Solution
- Results

Engineering Data: The material properties can be defined in this section. It has engineering data sources where various materials and their properties are listed there

and they can be chosen. Moreover, it is possible to import or create new materials together with their properties. Since the piezoelectric material PZT-5 is not listed, we added it to this section.

Geometry: In this section, one can draw the geometry. It is also possible to import the geometry.

Model: The properties of the model under investigation will be defined here. The coordinate systems can be defined and correlated with various sections of the structure. The materials defined and selected in the 'Engineering Data' section can be attributed to each structure here. It is also possible to do the meshing here. Depending on the geometry of the piezoelectric tube, various mesh types and sizes are chosen, sometimes the default and sometimes the user defined, to have a reasonable meshing considering the obtained results and runtime. For the suitable size of the mesh, mesh quality is considered. As known and according to ANSYS manuals, mesh skewness below 0.95 is acceptable, less than 0.80 is good, less than 0.50 is very good and below 0.25 is considered to be excellent meshing [108]. Therefore, meshing is done in such a way to satisfy the above criteria. This can assure the reliability of the output results. It is worth noting that increasing the number of meshes results in no significant change in the meshing quality, while it affects the computational time noticeably. Therefore, computational time and memory are compromised with the meshing quality.

Setup: This section in modal analysis allows for the boundary conditions to be defined as well as the analysis settings including the number of modes to be evaluated. In this study, the piezoelectric material which is added in 'Engineering Data' and the extension 'PiezoAndMEMS' allows for the piezo body to be selected here. The boundary condition is considered as 'Simply Support-Simply Support' resembling the boundary condition in the experimental setup.

For the harmonic analysis, in addition to the similarities with modal analysis (boundary conditions & material properties), this section allows for the frequency range to be considered. Further, 'ExtAcoustics'extension allows for the acoustic body to be selected which is defined as a uniform box surrounding the piezoelectric tube as in Fig.4-1. This box is where the acoustic field is to be evaluated and the emphasis and importance is inside of the tube. Since the acoustic field inside the transducer is of interest, this box is defined as small as possible to reduce the number of elements and meshes and accordingly reduce the computation time and memory. The acoustic box is defined to be air and therefore, the acoustic properties of air are attributed to the box in this section. The acoustic boundaries can also be defined here which are the boundaries of the box. Moreover, voltages can be applied to the inner and outer surfaces of the piezoelectric tube as the actuation for the vibration. For the experiments, since the employed amplifier gain is 20, 1.8V is selected as the input voltage to have 36V applied to the transducer. However, it is possible to vary voltage in the simulations as well as experiments to observe the effect of voltage on the intensity of the acoustic field. This will also be performed.

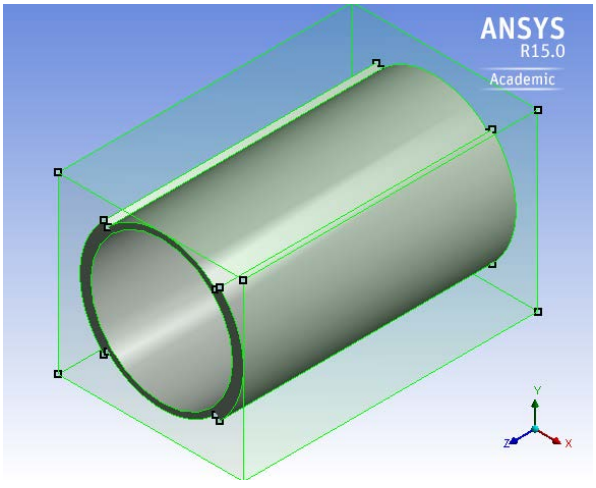

Fig.4-1. The surrounding box as the acoustic body.

Solution: This section allows for the output results to be selected which in this case 'Total Deformation' is chosen to get the mode shapes and frequencies in modal analysis. For harmonic analysis, 'Acoustic Sound Pressure Level (SPL)/Pressure' is also chosen. Further, stress distribution as an extremely important design consideration is taken into account.

Results: The output results defined in the previous section can be visualized here after running the program.

Fig.4.2 depicts the flow chart for the harmonic analysis, the required input and the intended output parameters. Further, Fig.4.3 depicts the flow chart to follow for the whole procedure of the design and development of the transducers in this study.

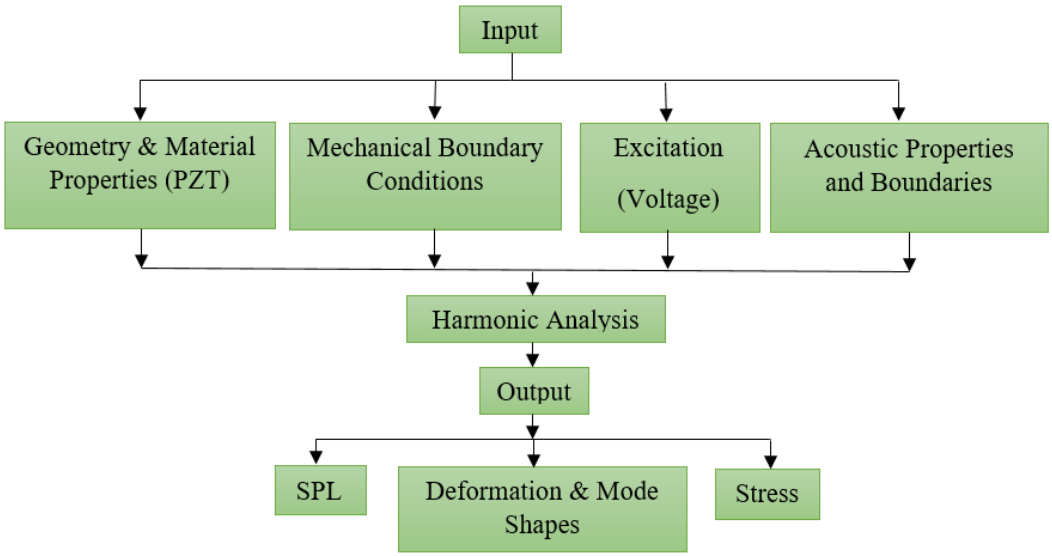

Fig.4-2. Flow chart showing the procedure for Harmonic analysis in ANSYS.

It is worth noting that justification of the suitable dimensions for the uniform-thickness transducer is presented in details in Appendix A. Briefly, a cylindrical shell with outer diameter of 30mm, inner diameter of 26mm, and length of 50mm is chosen. This selection is based on many factors such as availability in the market and affordability,

suitable dimensions for machining and the suitable range of dimensions for the intended application of the transducer.

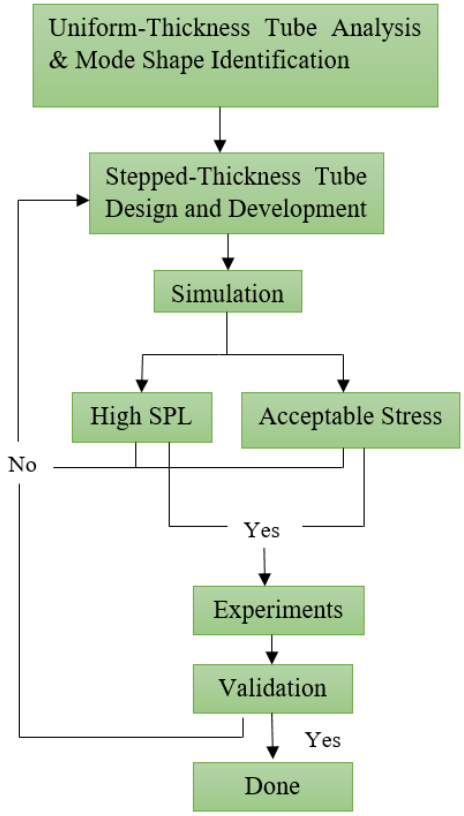

Fig.4-3. Flow chart showing the procedure for the design and development of transducers.

In order to decide on the suitable range of the applied voltage to the transducer, some important factors should be taken into account. The intended application needs a compact device which is portable. Moreover, it may be needed to use the device on batteries where there is no access to the power mains. Therefore, the drive for the device should be designed based on these needs. To drive the transducer, a piezoelectric power amplifier is needed which in this study runs on 18-36V DC power (24V recommended by the manufacturer). Furthermore, a function generator is required to supply the excitation for the electrode layers on the surfaces of the transducer. Currently, a function generator is used for the experimental set-up. However, for the final compact device which is considered as a potential application,

a built-in function generator will be essential. A small function generator module may be needed which requires to be driven by a small battery pack. Although the objective of the current investigation is not to finalize the device for the potential application, the required design considerations and the requirements for it should be carefully taken into account. A typical function generator module runs on approximately 9-12V which can be a 9V battery. Moreover, the output voltage can be 0-3V which provides up to 60V using the piezo driver currently being used in this study with the gain of 20. Therefore, the excitation voltage applied to the electrodes should not exceed 60V. To be on the safe side and avoid running the function generator at its full load (maximum output), 36V is considered. However, the effect of voltage will be investigated and higher and lower voltages are incorporated in the simulations to analyse how it affects the output sound pressure level. In addition, from the literature and performed investigations, acoustic fields of 160 dB were applied to single droplets and it was concluded that the evaporation rate of droplets would be affected and increased [103]. However, lower values of 150 dB did not prove useful. As a consequence, a criterion for the selection of the excitation voltage is that the transducer should be capable of generating acoustic waves with minimum sound pressure level of 160 dB as long as the it does not exceed the depolarization voltage for the piezoelectric material.

4.2.2. Mesh Quality Validation for Simulations

The simulations are performed for specimens with various numbers of axial, circumferential, internal and external steps. To assure the reliability of simulations, suitable meshing should be conducted. All different ranges of mesh skewness and their interpretations were explained in the previous section. An example of the mesh quality (skewness) is depicted in Fig.4-4 for the uniform-thickness specimen (Average: 0.25,

Maximum: 0.926). Further, to assure the precision and accuracy of the simulations performed in this study, Table 4-1 summarizes the skewness values for all the other transducers investigated. Table 4-1 reveals that for all the simulations, meshing is done satisfactorily.

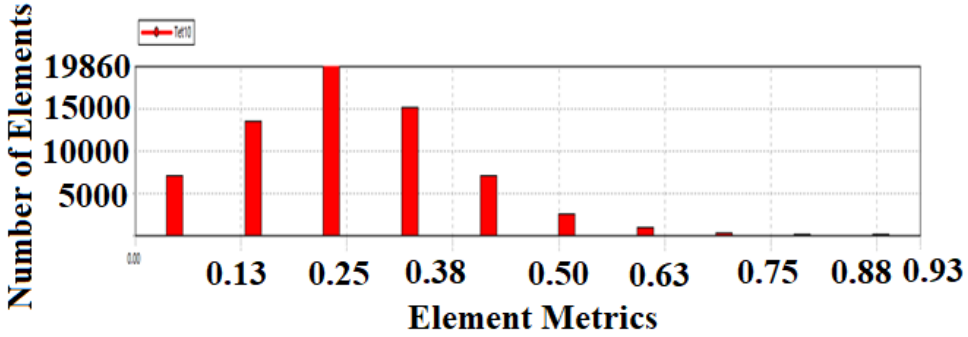

Fig.4-4. Mesh skewness for the uniform-thickness specimen.

Table 4-1. Average and maximum mesh skewness for all the specimens.

	Specimens with the following type and number of steps: (Circum: Axial; Ext: External; Int: Internal)														
Skewness	2 Circum		3 Circum		4 Circum		5 Circum		6 Circum		1 Axial		2 Axial		2 Axial
	Ext	Int	Ext	Int	Ext	Int	Ext	Int	Ext	Int	Ext	Int	Ext	Int	Int-Ext
Average	**0.31**	**0.31**	**0.3**	**0.29**	**0.3**	**0.29**	**0.29**	**0.32**	**0.29**	**0.31**	**0.27**	**0.26**	**0.28**	**0.26**	**0.31**
Max	**0.72**	**0.75**	**0.68**	**0.76**	**0.72**	**0.66**	**0.75**	**0.87**	**0.71**	**0.73**	**0.8**	**0.8**	**0.83**	**0.78**	**0.85**

4.3. Primary Simulation Results for the Uniform-thickness Specimen

Primarily, modal analysis is performed on the uniform-thickness specimen to identify a suitable mode shape similar to that reported in the literature depicted in Fig.4-5. The vibration mode as in this figure is an initial idea for the potential mode shape which has the strongest acoustic field. Moreover, the lower the frequency, the better since higher frequencies tend to overheat the transducer [109] and may lead to fatigue failure [41]. Therefore, it is intended to get the potential mode shape in the low ultrasound range. However, the analysis in this study is not restricted to the potential mode shape and it is just an indication of a suitable mode shape for high SPL; hence, any mode

shape which gives us high SPL and satisfies a suitable range of stress distribution can be identified and chosen.

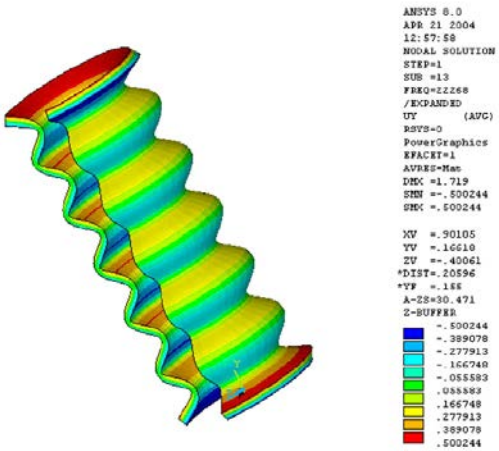

Fig.4-5. The potential mode shape for strong acoustic field obtained from [15] .

The material properties of the piezoelectric (PZT-5L) transducer considered for the study are included in Table 3-4. The reason lying behind choosing this material is that it is a soft piezoelectric material with high coupling factor and piezoelectric charge coefficients which is used where large deflections are required [110, 111]. Hard piezoelectric materials can endure a high level of electrical excitation and due to low dielectric losses, they are suitable for high field applications. Since high field is not the case for this application, high dielectric loss of the soft piezoelectric material which may lead to overheating is not an issue [110]. Instead, high coupling factor and charge constants are suitable resulting in larger amplitude of vibration which is required for stronger acoustic fields with higher SPL [2]. The results show that the potential mode shape occurs around 43.4 KHz and is depicted in Fig.4-6 in ISO and side views. Now that the potential mode shape and the according range of frequency are all identified from the modal analysis, it is required to model the transducer using harmonic analysis to investigate its performance with respect to ultrasound generation. It is worth noting that for the sake of brevity, only the results for the identified stepped-thickness

specimens are presented and the investigations on the other specimens are included in Appendix B. Further, a summary table at the end of the chapter will be presented to compare all the attempted stepped transducers. The identified stepped specimens are considered for machining and subsequent experimental tests.

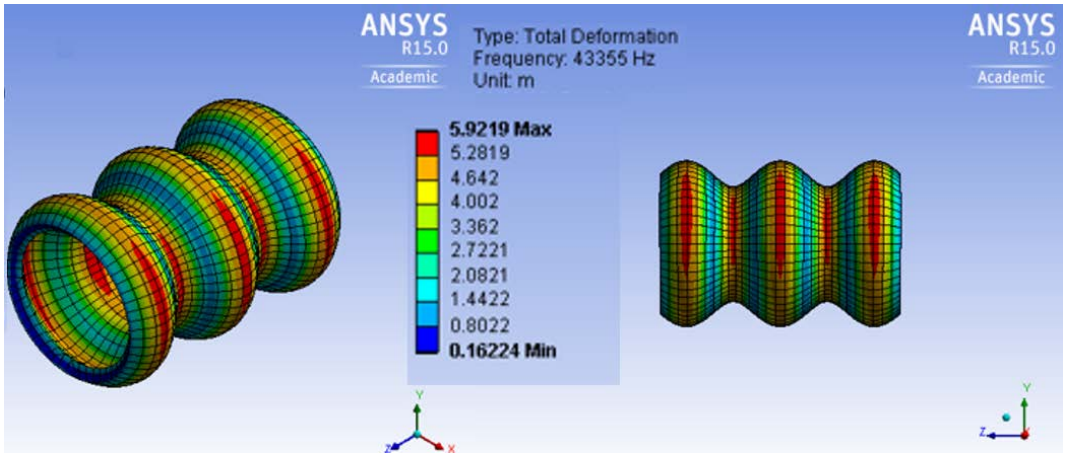

Fig.4-6. Modal analysis results for the potential mode shape of uniform-thickness specimen at 43.4 KHz Left: ISO view, Right: Axial view.

4.4. Simulations for Uniform-Thickness Specimen

The result of the harmonic analysis reveals that the potential mode shape for the uniform-thickness specimen occurs at 43 KHz, Fig.4-7. This is in very good agreement with the result of the modal analysis depicted in the previous section. The results show that the highest level of sound pressure for this specimen occurs at 43 KHz corresponding to the same potential mode shape. The maximum magnitude is around 169.7 dB as seen in Fig.4-8. Further, the value for the centreline of the transducer is in the range of 158-169 dB as in the colour-coded legend of the figure. The average value for the centreline along the length of the transducer is around 164 dB. It is also observed that the acoustic field is quite uniform along each axial line throughout the whole length of the transducer.

The maximum stress is also 3.3 MPa as in Fig.4-9. After obtaining the maximum sound pressure level for the uniform-thickness specimen, two scenarios are to be investigated in an attempt to intensify the resultant sound pressure level. One is to increase the excitation voltage to increase the vibration amplitudes and accordingly intensify the acoustic filed. As mentioned earlier, this simultaneously increases the power consumption. The other one is to localize the vibration within specific regions of the tube through geometrical manipulations to create vibrations with larger amplitudes to achieve higher sound pressure level.

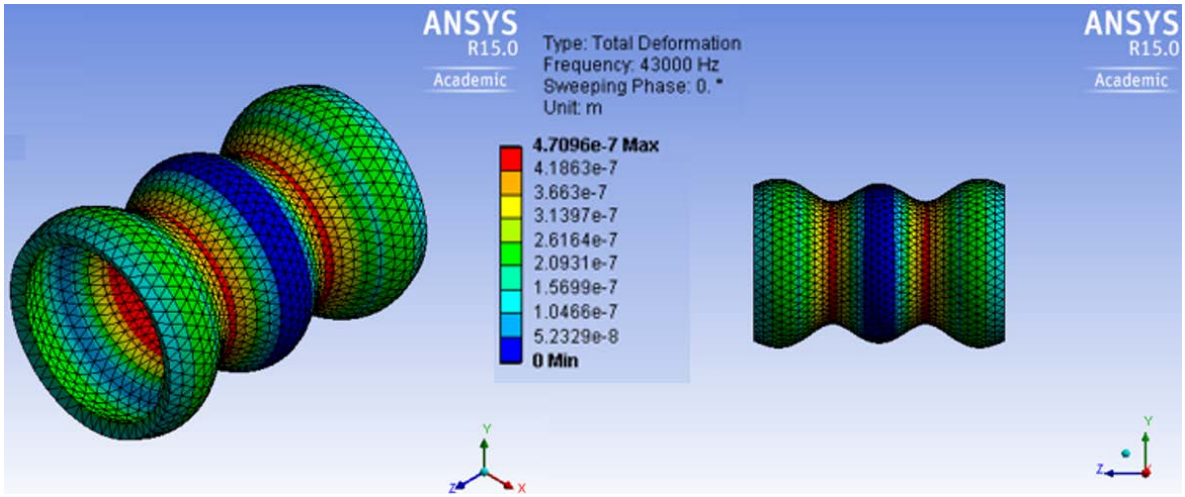

Fig.4-7. Harmonic analysis results for the potential mode shape of uniform-thickness specimen at 43 KHz; Left: ISO view, Right: Axial view.

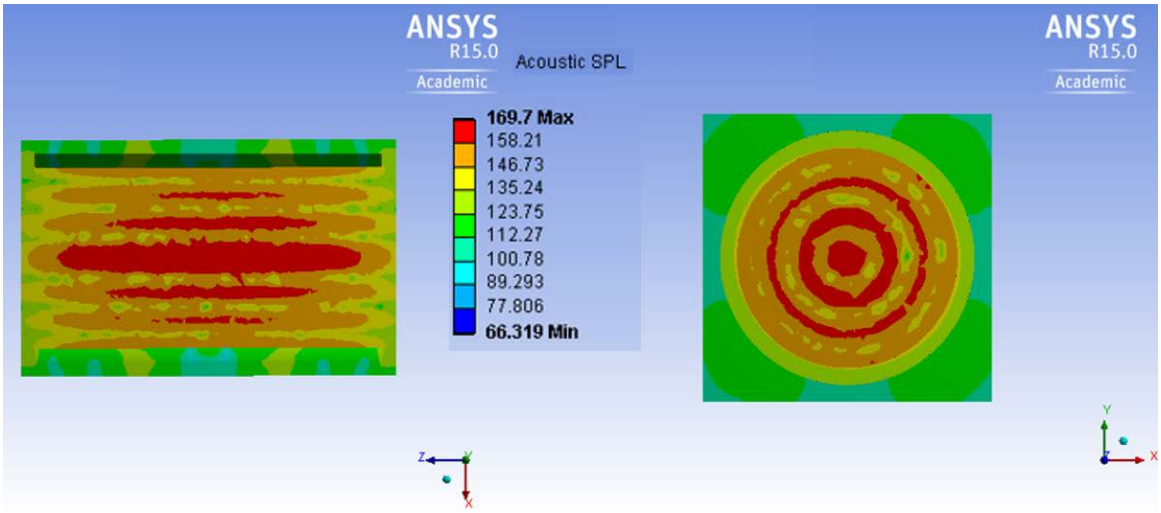

Fig.4-8. Acoustic field in SPL for the uniform-thickness specimen at 43 KHz for 36V; Left: Axial view, Right: Side view.

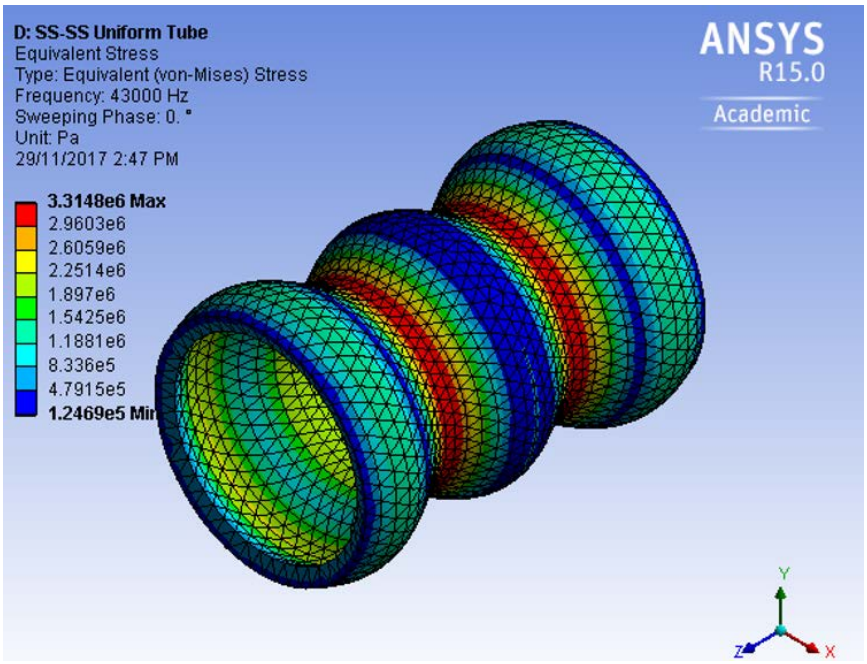

Fig.4-9. Stress distribution for the uniform-thickness specimen at 43 KHz for 36V.

4.4.1. Effect of Excitation Voltage on the Acoustic Field SPL

The same simulation procedure is done on the same uniform-thickness specimen with voltages of 18, 48 and 200V. As explained earlier, in order to be able to run the piezoelectric transducer using the current piezoelectric driver and a compact function generator module which normally has 0-3V output voltage, the output voltage should not exceed 60V as the gain of the piezo driver is 20. However, it is possible to go to higher voltages using a piezo driver with higher gain or a function generator module with higher output voltage range. Nonetheless, in order to study the effect of voltage, the first two voltages were chosen to be lower than 60V and the high voltage of 200V was chosen since the maximum allowed voltage for depolarization of piezoelectric materials is normally a few hundred volts per millimetre thickness (around 300V/mm in our case) [112]. As known, voltage and current supplied to the transducer clarify the power consumption. The piezo driver used in this study has three voltage ranges and a fixed average output current for each of these three voltage ranges [113]. Hence, the power consumption can be judged based on the voltage supplied to the transducer.

Having performed the investigation, exactly the same acoustic filed pattern as in Fig.4-8 is obtained for the other cases. This can be observed in Fig.4-10.

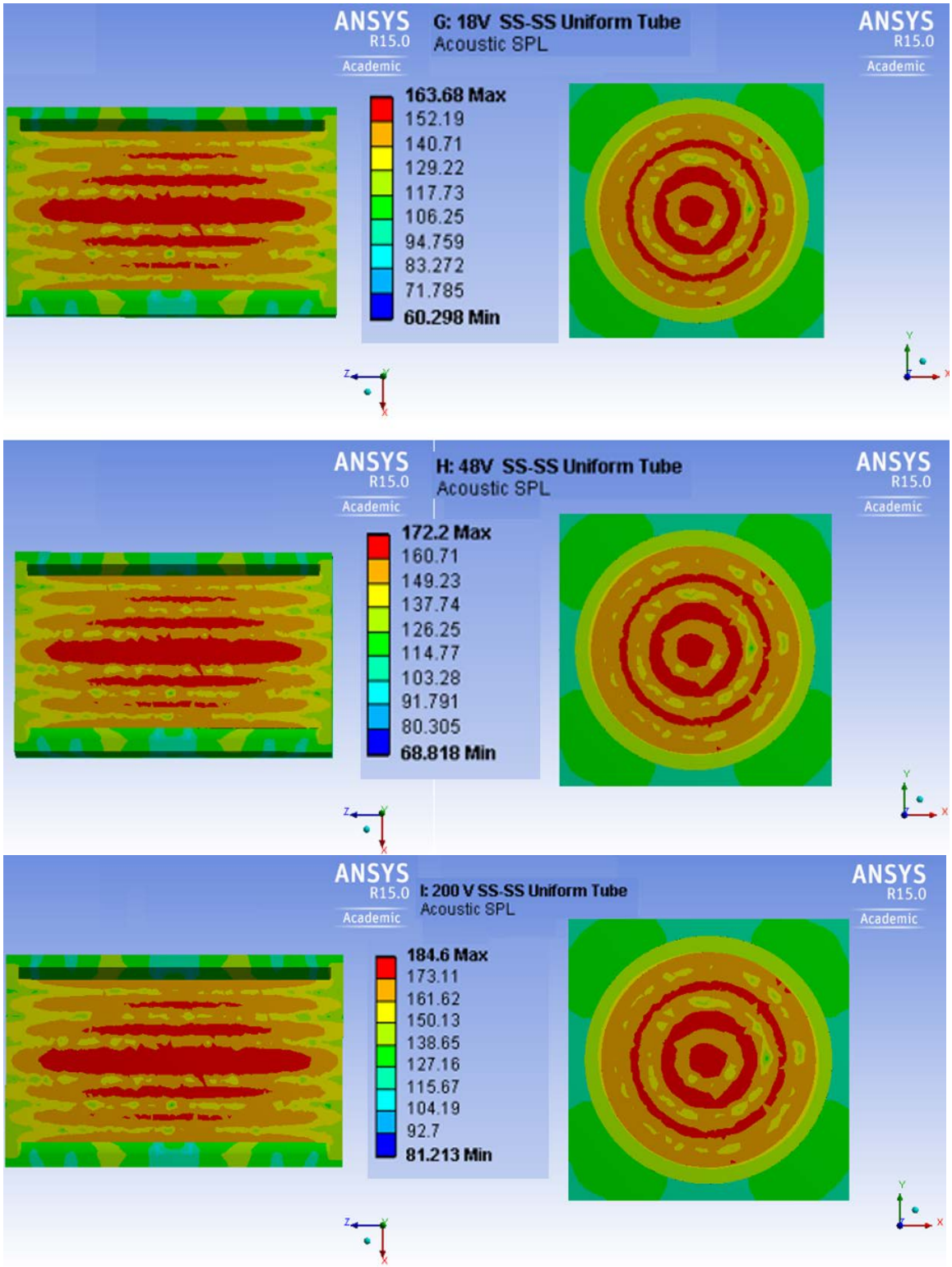

Fig.4-10. Acoustic field in SPL for the uniform-thickness specimen at 43 KHz from axial & side views; Top: 18V; Middle: 48V & Bottom: 200V.

Comparing the acoustic field patterns shows that they are identical. However, colour codes define various ranges for each one. Further, it can be observed that the acoustic field is nearly uniform along the length of the transducer at the centreline. Table 4-2 presents the results. According to the results, the 18V case is not suitable for the intended application considering the threshold value of approximately 160 dB. Using higher voltages instead of 36V increases the output SPL. However, it decreases the efficiency as the increase in the power consumption is more than the increase in the output [87]. It is now important to investigate the effect of geometrical variations on the strength of the acoustic field and then compare the results with the case of the uniform-thickness specimen excited at a higher voltage. Then, it can be logically concluded whether it is worth strengthening the acoustic field by increasing the voltage or not. This will be clarified after the simulations for the stepped-thickness specimens are done in the next sections of this chapter. This will also be obtained experimentally in the next chapter for the sake of validation. The stress distribution for the three tests of 18, 48 and 200V is depicted in Fig.4-11.

Table 4-2. Effect of various input voltages on the sound pressure level.

	Excitation Voltage in V			
	18	**36**	**48**	**200**
Maximum SPL in dB	163.68	169.7	172.2	184.6
Average SPL in dB along centreline	158	164	166	179

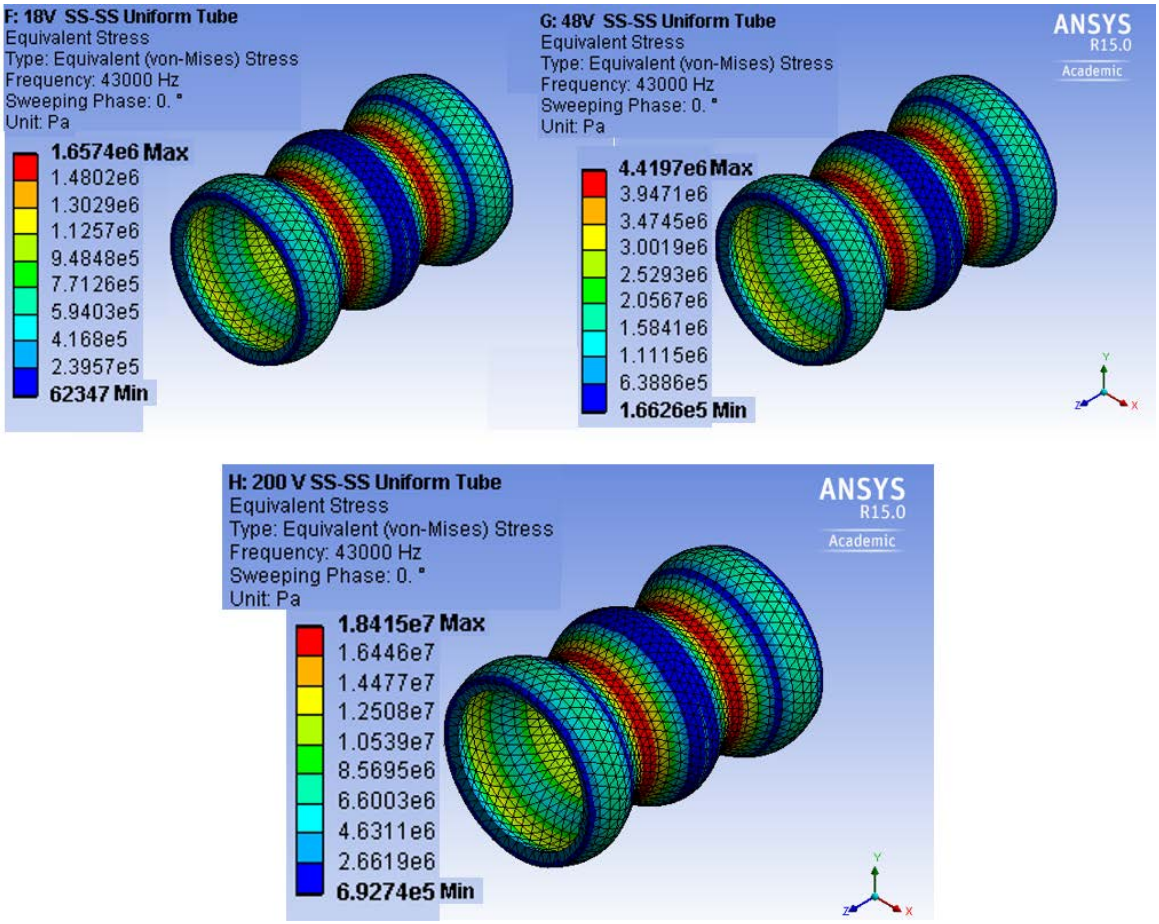

Fig.4-11. Stress distribution for the uniform-thickness specimen at 43 KHz for Top left:18V; Top right: 48V & Bottom: 200V.

4.5. Stepped-Thickness Specimens

According to the potential mode shape from the literature, Fig.4-5, and the results for the uniform-thickness tube, Fig.4-7, it is evident that within this range of frequency, the suitable mode shape has circumferential wave number of zero. This means that the whole circumference is vibrating in-phase at each cross section along the length. However, the tube has regions in counter-phase axially. Therefore, for the current transducer, it seems better to focus on axial steps rather than circumferential ones. However, both types of axial and circumferential steps (using circumferential and axial grooves by machining) are considered for the transducer to assure the most suitable design providing the highest SPL and maximum acoustic amplification. The

hypothesis is to machine the counter-phase area between each two consecutive in-phase regions either axially or circumferentially in order to localize the vibration within those areas; it is intended to achieve a higher vibration amplitude which is required to have stronger acoustic field especially in gas medium [2]. It is anticipated that because of the thinner wall thickness, the same mode shape occurs at a slightly lower frequency compared to the uniform-thickness tube and vibration amplitude increases and gets localized within the thin, machined regions. However, care must be taken regarding stress distribution since large amplitudes of vibration may result in high level of stress concentration and lead to failure. The maximum tensile strength of a soft piezoelectric material is around 47 MPa [114]. Similar values were reported by [115, 116]. Depth of the steps is considered with respect to the machining capabilities as well as stress distribution. Machining the PZT material is cumbersome and requires specific equipment and expertise. Thus, machining dimensions should be consulted with the manufacturing technicians to be practical and feasible. All the steps are 1mm in depth which are obtained by machining either the outer or the inner surface of the uniform-thickness specimen except for the case of internal-external step where half a millimetre is cut from each surface. According to the literature, the more the difference between thicknesses of the thin and thick regions, the more localized the vibration and the more pronounced the mode shape [7]. Hence, since the thickness of the transducer is 2mm, reducing the thickness by half (1mm) for the machined regions seems suitable for localization of the vibration. Further, it is suitable from the machining and manufacturing point of view. Machining to get smaller thicknesses increases the risk of a tear, break or crack in the ceramic type material of the transducer during machining or may result in failure of the transducer while driving due to high stress at thin, machined regions. Machining to get higher thicknesses may not sufficiently localize the vibration. Therefore, 1mm is chosen for the depth of the steps.

According to the obtained results for the uniform-thickness specimen as well as the identified mode shape of vibration in the literature, the following can be considered as a guideline to follow for identification of the suitable mode shape and design for the stepped transducers in this study

1. The first and most important factors are the strongest SPL and minimum stress as well as low ultrasound range of frequency. The last two factors are required to mitigate overheating of the transducer and fatigue failure.
2. Harmonic analysis for the uniform-thickness specimen revealed that within low ultrasound range up to 60 KHz, mode shapes with circumferential wave numbers rather than zero do not occur. However, various axial wave numbers occur.
3. Based on the previous point, there are regions in counter-phase axially but not circumferentially. Accordingly, depending on the axial wave number, transducers with various number of axial steps are investigated satisfying the points raised in point 1.
4. According to points 2 and 3, only axial steps should be considered. However, it is decided to forcibly excite mode shapes with different circumferential wave numbers by localizing the vibration amplitude within the thin, machined regions and investigate the performance considering the points raised in point 1. Although any number of steps can be considered, only two to six circumferential steps are investigated in this study.
5. Design of the axially or circumferentially stepped transducers is done based on points 3 and 4 above and identification of the suitable mode shape for each of them to approve their designs is based on the satisfaction of point 1.

6. Following these guidelines, the analysis is performed to identify the suitable designs. However, it is worth mentioning that this research aims at investigating the feasibility of amplifying the acoustic field for the same input power using geometrical variations such as steps. Thus, the identified designs do not necessarily work for any arbitrary transducer of any dimensions. Nonetheless, the approach followed in this study can be extended to transducers of any dimensions operating at any frequency range and based on the mode shapes, a suitable design can be identified following the same procedure as in this study as outlined.

4.5.1. Transducer with One External/Internal Axial Step

This section includes the investigations on the transducer with one axial step either external or internal and is divided into sections for each of them.

4.5.1.1. Transducer with One External Axial Step

To design this transducer and cut the axial steps on the inner or outer surfaces, the location of these steps should be carefully designed. The simulations for the uniform-thickness specimen clarified the regions of the transducer which should be machined to localize the vibration there. As in Fig.4-12, which shows mode shapes for the uniform-thickness specimen with (3, 0) wave numbers at two close frequencies, one region is in counter-phase with the other regions. It is intended to put the step in this region by machining to localize the vibration within this region and eliminate counter-phase vibration of different regions along the length. More in-phase radiation and better interference of the waves together with larger amplitude of vibration is anticipated to increase the level of SPL. To this aim and taking the location of the

counter-phase region into account, the specimens with one external and internal step are developed and investigated. According to Fig.4-12, the distance between the blue areas which are nodal circles is different. Therefore, two cases are considered based on these two. Once a step of 5.5 mm length is considered corresponding to the case at 33 KHz and once a step of 15 mm length corresponding to the case at 33.5 KHz. A few simulations are performed to accurately define the length of the steps based on the length between these nodal circles in such a way that the mode shapes are symmetric and the waves from each side of the transducer coincide symmetrically within the machined area and the resultant acoustic field shows an increase in the output SPL. Consequently, the better option between these two cases can be identified.

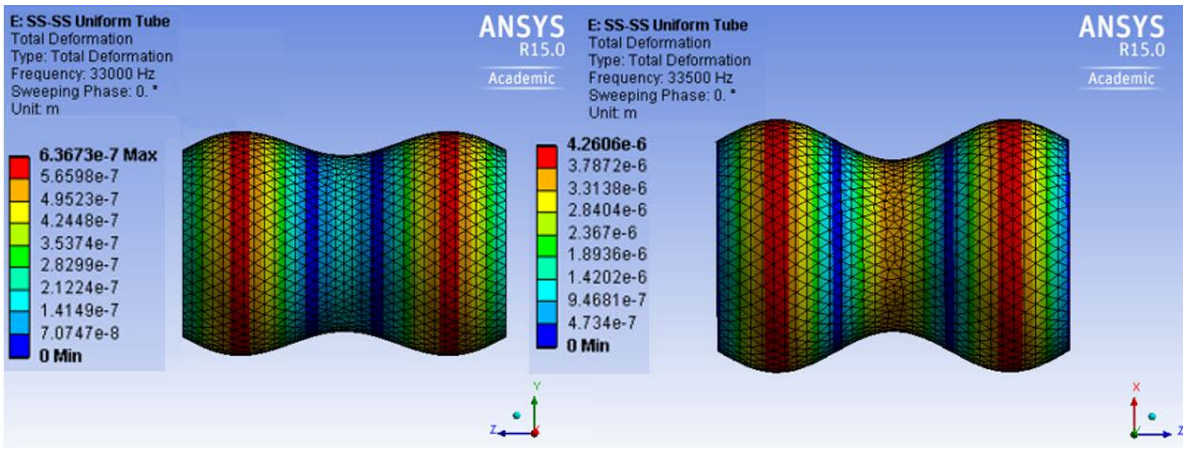

Fig.4-12. Mode shapes with wave numbers (3, 0) for the uniform-thickness specimen, Left: 33 KHz, Right: 33.5 KHz.

The simulations are performed for the specimen with one external axial step of 5.5 and 15 mm as explained above the schematics of which are depicted in Fig.4-13. The maximum value of the acoustic SPL for the specimen with 5.5 mm length step occurs at 36 KHz the mode shape of which is depicted in Fig.4-14. Further, Fig.4-15 illustrates the resultant acoustic field. The maximum level of SPL is 172 dB. As in Fig.4-14, axial

and circumferential wave numbers are (1, 0). This figure clearly reveals that the vibration is localized within the machined region which is red.

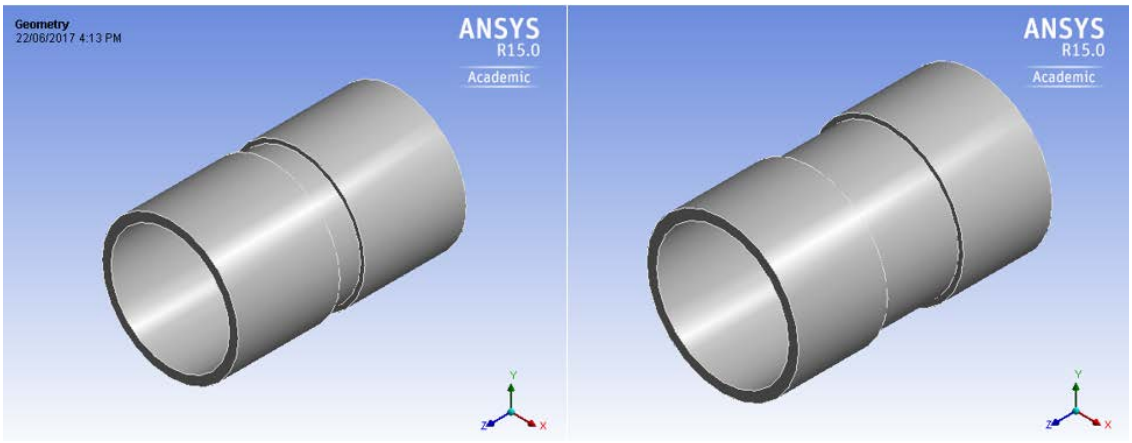

Fig.4-13. Schematic of specimen with one external axial step in ISO view, Left: 5.5 mm length step, Right: 15 mm length step.

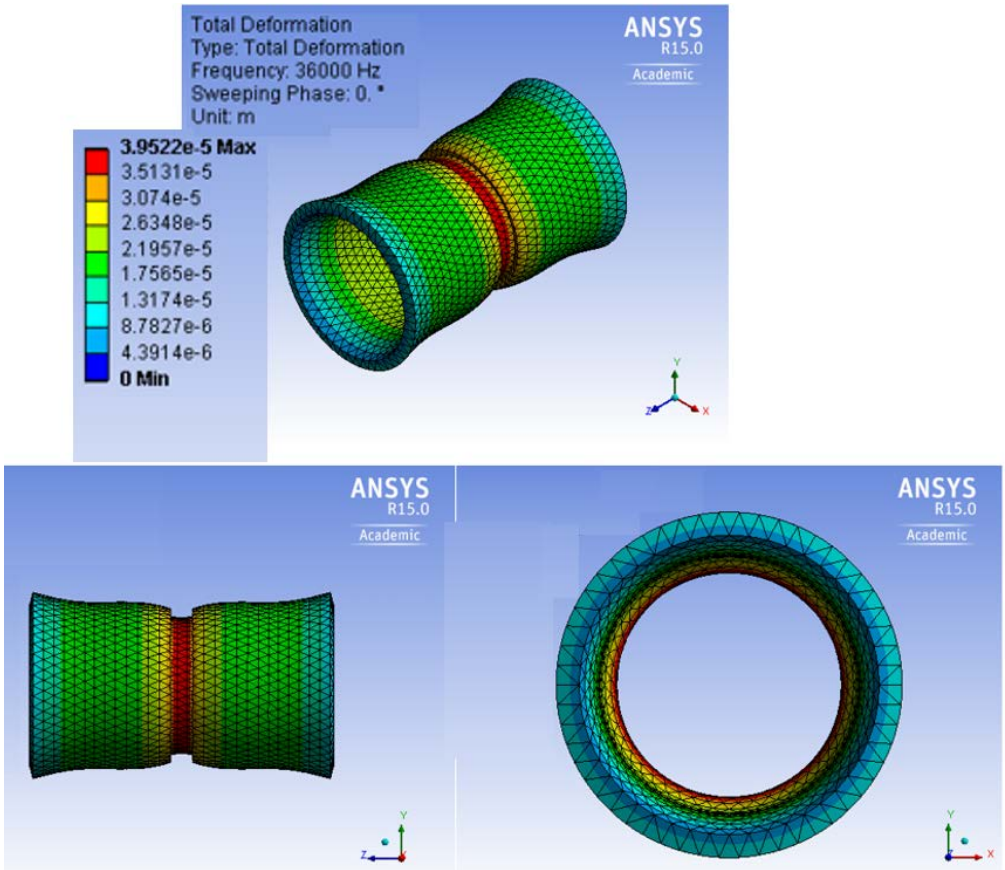

Fig.4-14. Harmonic analysis results for a potential mode shape of the specimen with one external axial step of 5.5 mm length at 36 KHz; Top: ISO view, Bottom left: Axial view, Bottom right: Side view.

Creating this step causes the tube to vibrate uniformly along the length and in-phase with an axial wave number of one and a circumferential wave number of zero. This means that the circumference at any cross section is vibrating uniformly. This results in identical axial views and generates a uniform acoustic field along the length at the centreline, Fig.4-15. The same mode shape for the uniform-thickness specimen occurs at 38 KHz with the maximum SPL of 166 dB as in Fig.4-16. Further, as expected, the reduction in thickness has reduced the frequency for the same mode shape for the stepped specimen. It is also worth noting that the stress distribution for this specimen is in the order of 10^8 Pa, Fig.4-17. This is too high and results in an imminent failure of the transducer.

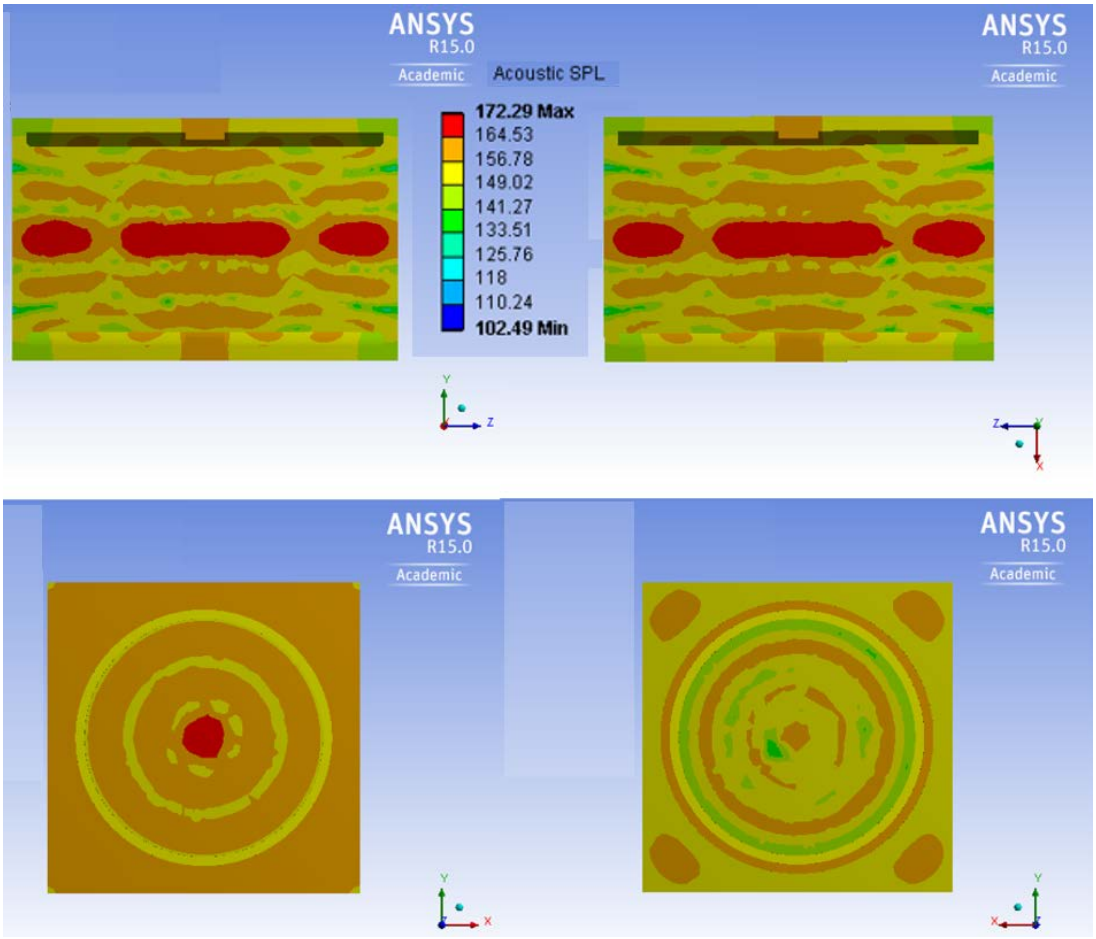

Fig.4-15. Acoustic field in SPL for a potential mode shape of the specimen with one external axial step of 5.5 mm length at 36 KHz; Top left: Axial view on the vertical plane, Top right: Axial view on the horizontal plane, Bottom left: Side view at mid-length, Bottom right: Side view at quarter-length.

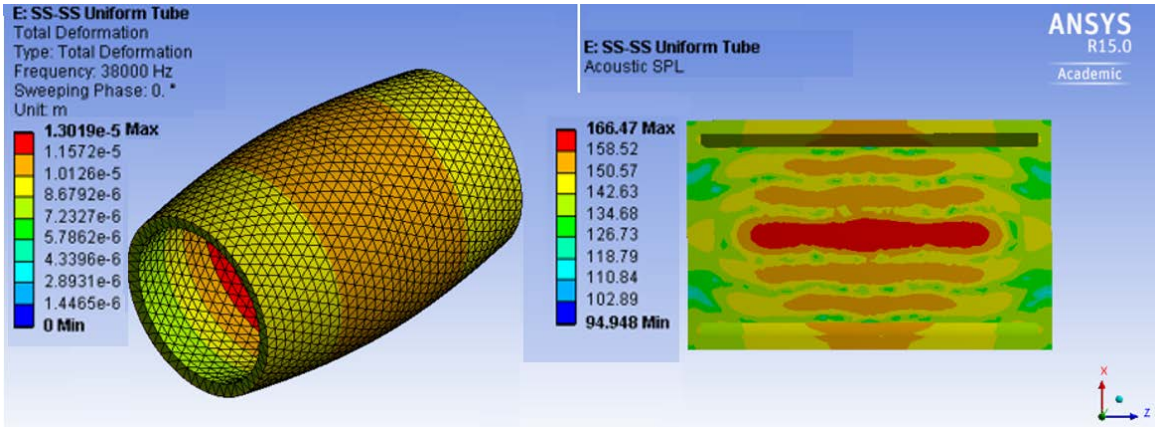

Fig.4-16. Harmonic analysis results and acoustic field in SPL for a potential mode shape of the uniform thickness specimen at 38 KHz; Left: ISO view of mode shape, Right: Axial view of acoustic field.

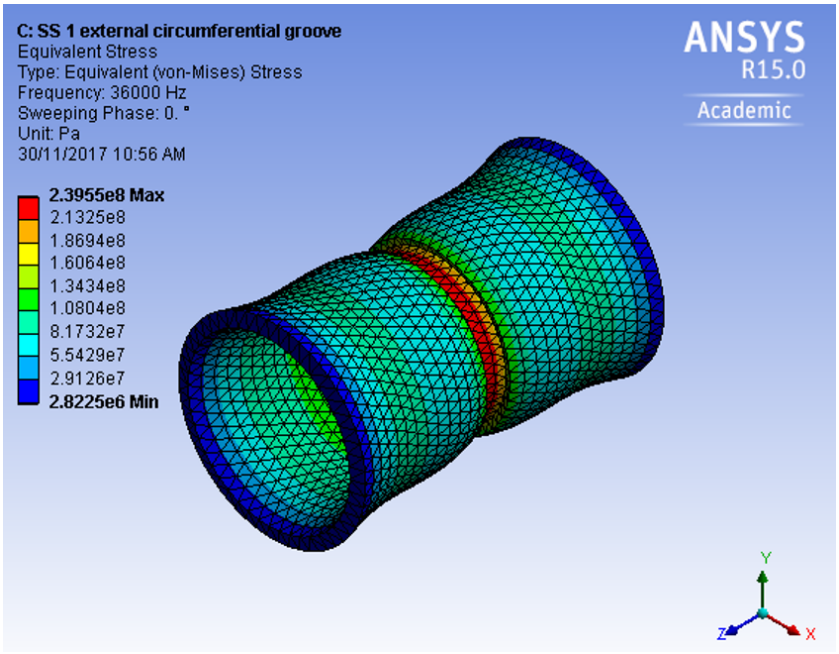

Fig.4-17. Stress distribution for the specimen with one external axial step of 5.5 mm length at 36 KHz.

Similar simulations are performed for the specimen with 15 mm length step. Mesh skewness was not previously reported for this specimen. It is 0.27 on average and the maximum is 0.86. Therefore, the accuracy is satisfied by good quality of meshing. The highest level of the acoustic field in this case occurs at 36 and 39.5 KHz the mode shapes of which are depicted in Fig.4-18. The mode shape at 36 KHz resembles the one for the 5.5 mm length step as in Fig.4-14. However, the vibration is localized

within two regions inside the machined area close to the edges of the steps as the red regions in the axial view. Comparing the resultant acoustic field from left part of Fig.4-19 with Fig.4-15 for the 5.5 mm length step clarifies two points. One is that the level of SPL is lower (165 dB for 15 mm length step vs 172 dB for the 5.5 mm length step). Secondly, the acoustic field at the maximum range does not cover the whole length and quarter-lengths from each end is at a lower level of SPL while this is not the case for 5.5 mm length step. Further, the stress is in the order of 10^7 Pa for this specimen.

For the second mode shape at 39.5 KHz, axial wave number has changed to 5 which is the similar mode shape to Fig.4-7 for the uniform-thickness specimen at 43 KHz. Reduction in thickness has caused the same mode shape to occur at a lower frequency as expected. Comparing the resultant acoustic field in this case with that of the uniform-thickness specimen shows that the maximum level is slightly lower (167 dB vs 169 dB). In addition, many regions inside the transducer are at a lower level of SPL. Further, the uniformity of the acoustic field along the length is lost and there are discontinuities as in Fig.4-19. Therefore, the specimen with a longer step is not superior to the one with a shorter step. Further, the maximum stress is in the order of 10^8 Pa as in Fig.4-20.

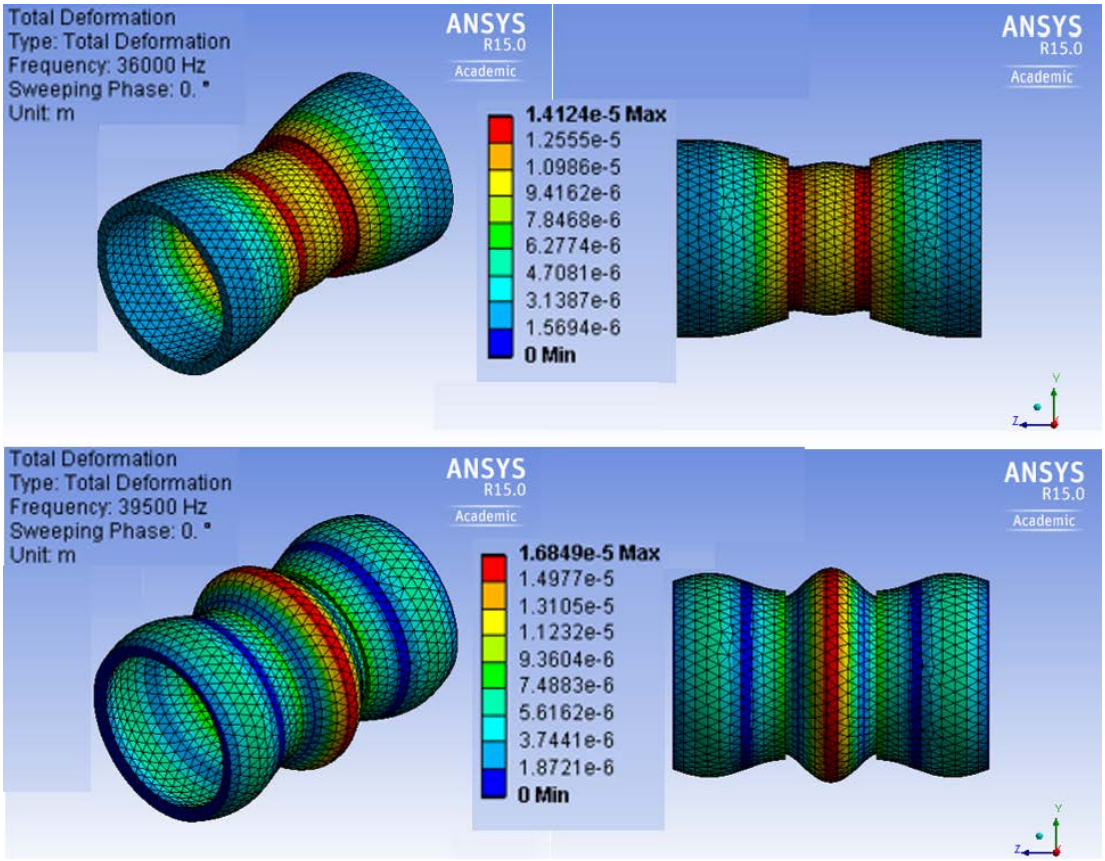

Fig.4-18. Harmonic analysis results for potential mode shapes of the specimen with one external axial step of 15 mm length, Top: ISO and axial views at 36 KHz, Bottom at 39.5 KHz.

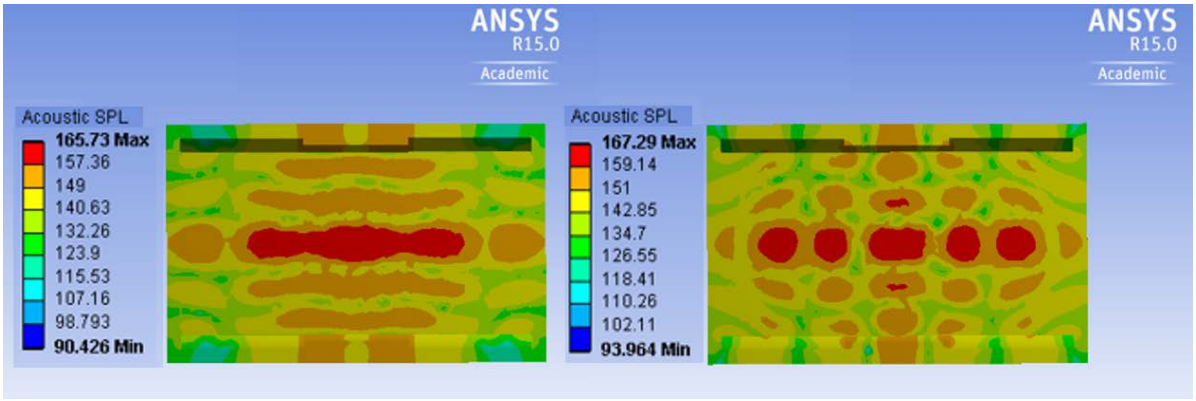

Fig.4-19. Acoustic field in SPL for potential mode shapes of the specimen with one external axial step of 15 mm length; Axial views on the horizontal plane, Left: 36 KHz; Right: 39.5 KHz.

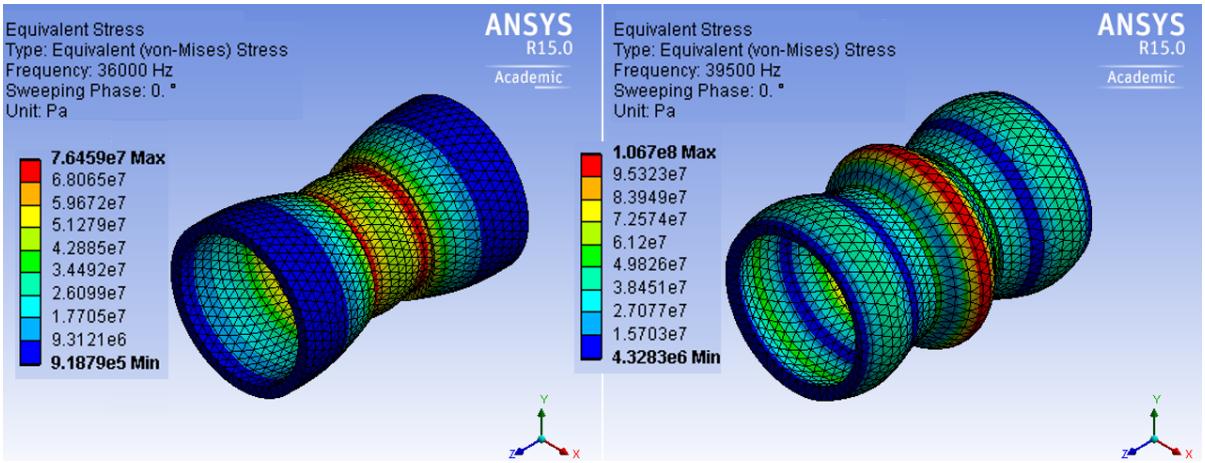

Fig.4-20. Stress distribution for the specimen with one external axial step of 15 mm length at Left: 36 KHz and Right: 39.5 KHz.

4.5.1.2. Transducer with One Internal Axial Step

Development of this transducer is based on the explanations given for the specimen with one external axial step. Thus, two cases are considered again one with 5.5 mm and the other with 15 mm length step. The simulations are performed for the specimen with one internal axial step of 5.5 and 15 mm the schematics of which are depicted in Fig.4-21. An axial cut from the specimen is shown here so that the internal axial step can be seen. The maximum value of the acoustic SPL for the specimen with 5.5 mm length step occurs at 43 KHz the mode shape of which is depicted in Fig.4-22. Further, Fig.4-23 illustrates the resultant acoustic field. The maximum level of SPL is 167 dB. Axial and circumferential wave numbers are (5, 0) similar to the uniform-thickness specimen. The amplitude of vibration is also an order of magnitude larger. However, careful comparison of these two in Figs.4-22 and 4-7 reveals that the maximum amplitude for the uniform-thickness specimen occurs at two regions which are in counter-phase with the other regions, nonetheless, for the stepped specimen here, it is localized within the machined region. This results in a slightly different acoustic field pattern.

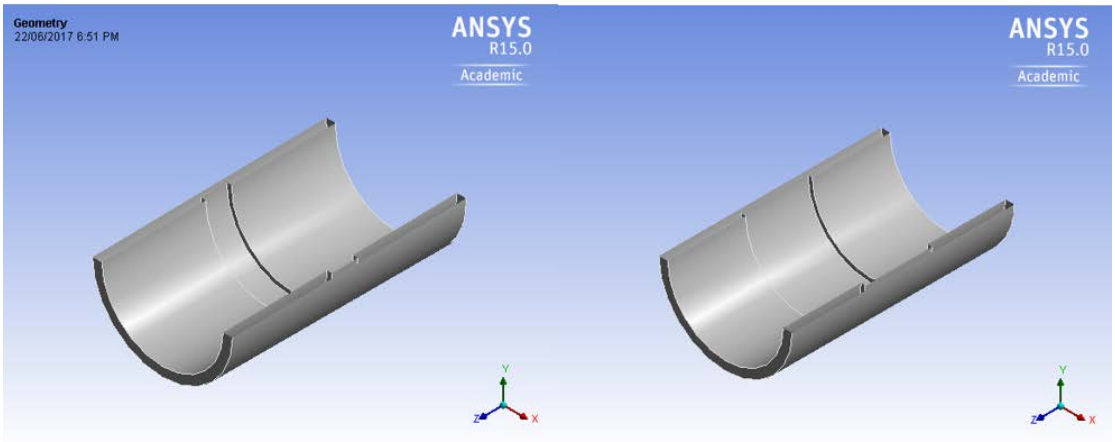

Fig.4-21. Schematic of specimen with one internal axial step in ISO view, Left: 5.5 mm length step, Right: 15 mm length step.

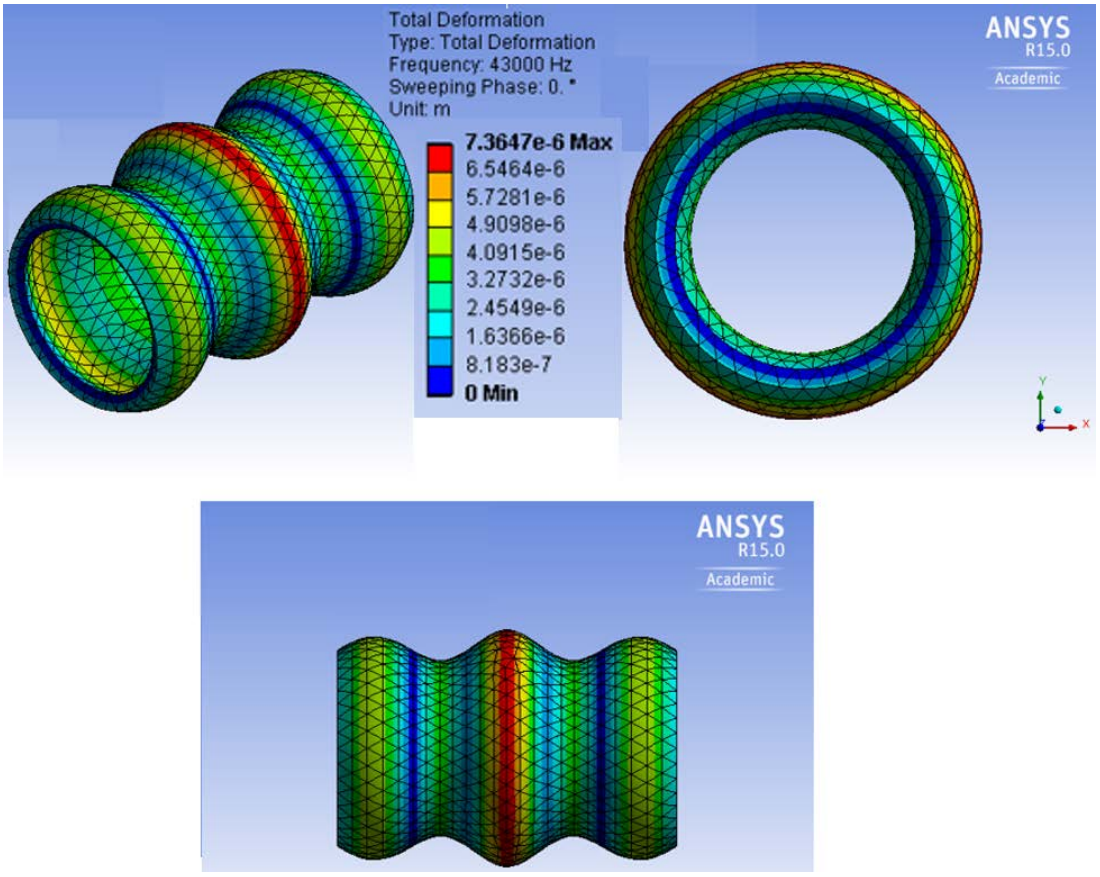

Fig.4-22. Harmonic analysis results for a potential mode shape of the specimen with one internal axial step of 5.5 mm length at 43 KHz; Top left: ISO view, Top right: Side view, Bottom: Axial view.

The axial views of the acoustic field in Fig.4-23 are identical. It is also worth noting that the acoustic field is fairly similar to that of the uniform-thickness specimen and

the maximum level is also very close (167 dB vs 169 dB). The maximum level of stress is around 51 MPa which corresponds to the red region in Fig.4-24. Other regions are at a lower level of stress.

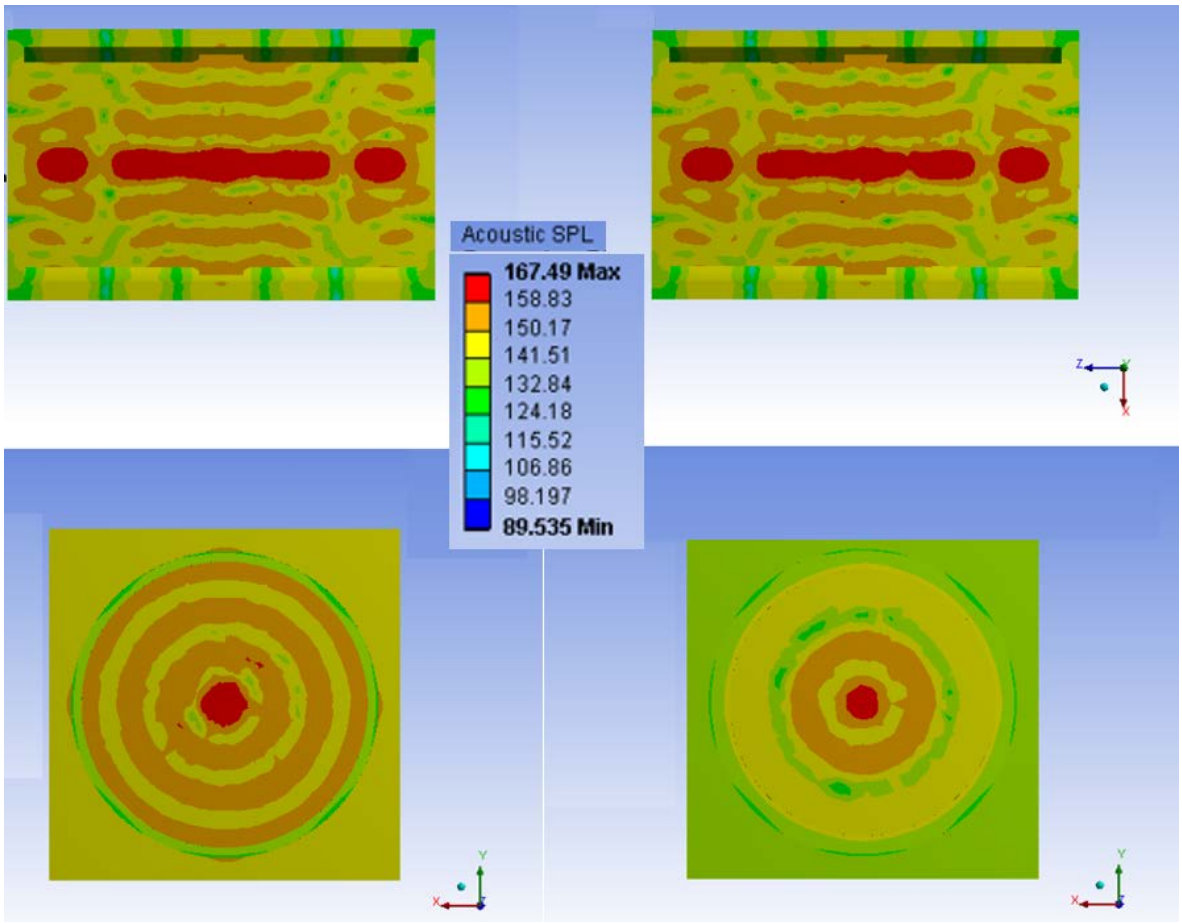

Fig.4-23. Acoustic field in SPL for a potential mode shape of the specimen with one internal axial step of 5.5 mm length at 43 KHz; Top left: Axial view on the vertical plane, Top right: Axial view on the horizontal plane, Bottom left: Side view at mid-length, Bottom right: Side view at quarter-length.

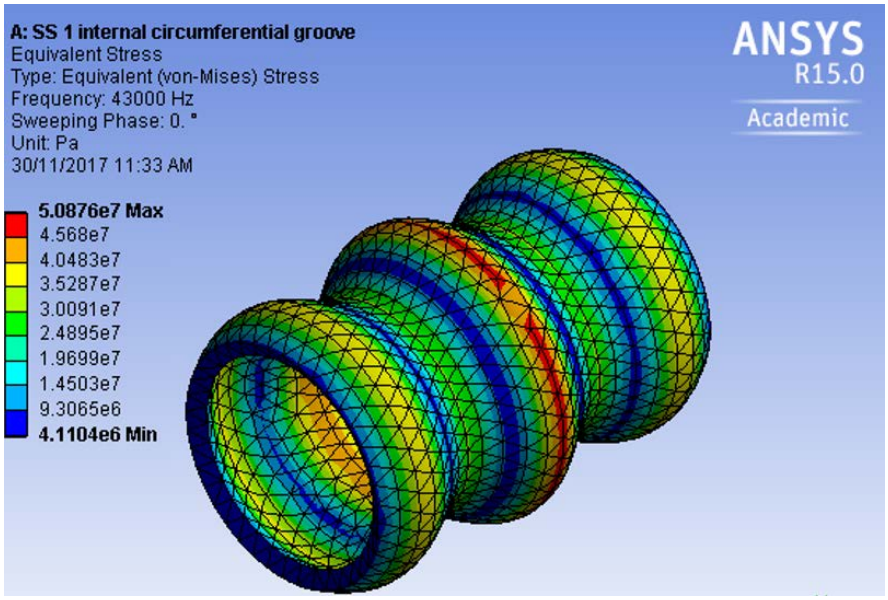

Fig.4-24. Stress distribution for the specimen with one internal axial step of 5.5 mm length at 43 KHz.

Similar simulations are performed for the specimen with 15 mm length step. Mesh skewness was not previously reported for this specimen which is 0.26 on average and the maximum is 0.929. Therefore, the accuracy is satisfied by good quality of meshing. The highest level of the acoustic field in this case occurs at 36 KHz the mode shape of which is depicted in Fig.4-25.

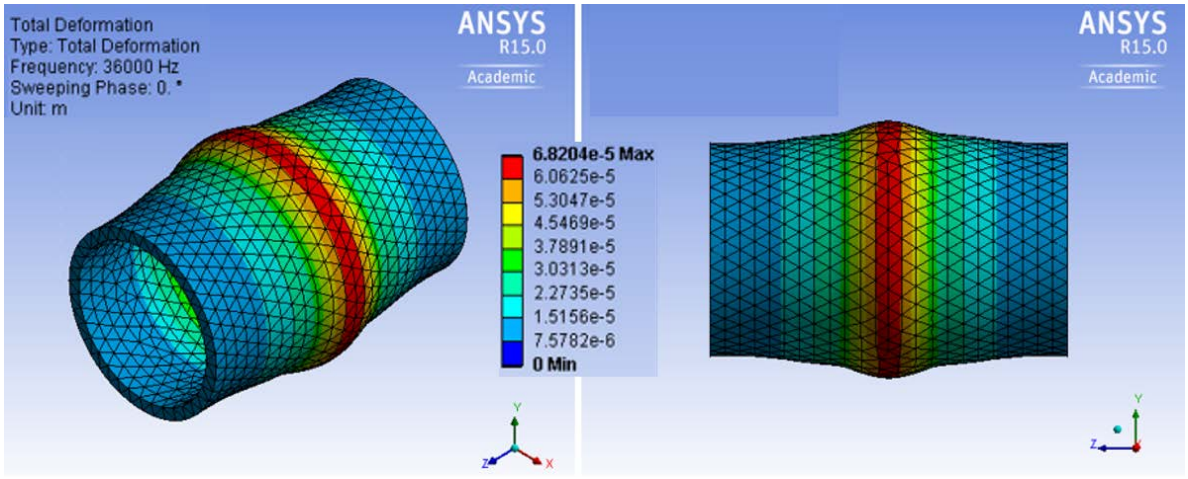

Fig.4-25. Harmonic analysis results for a potential mode shape of the specimen with one internal axial step of 15 mm length at 36 KHz; Left: ISO view, Right: Axial view.

The resultant acoustic field is also depicted in Fig.4-26. The wave numbers are (1, 0) and the vibration is clearly localized within the machined region. However, many parts of the transducer are vibrating at a lower magnitude which is evident from Fig.4-25 and the colour-coded areas. This may result in a nearly focused and restricted acoustic field pattern as in Fig.4-26 where only the area at the centreline and the same length as the machined area is at maximum range of SPL and the rest of the transducer is at lower levels of SPL as evident from axial and side views of Fig.4-26. The maximum stress level is in the order of 10^8 Pa as in Fig.4-27 which is not suitable at all.

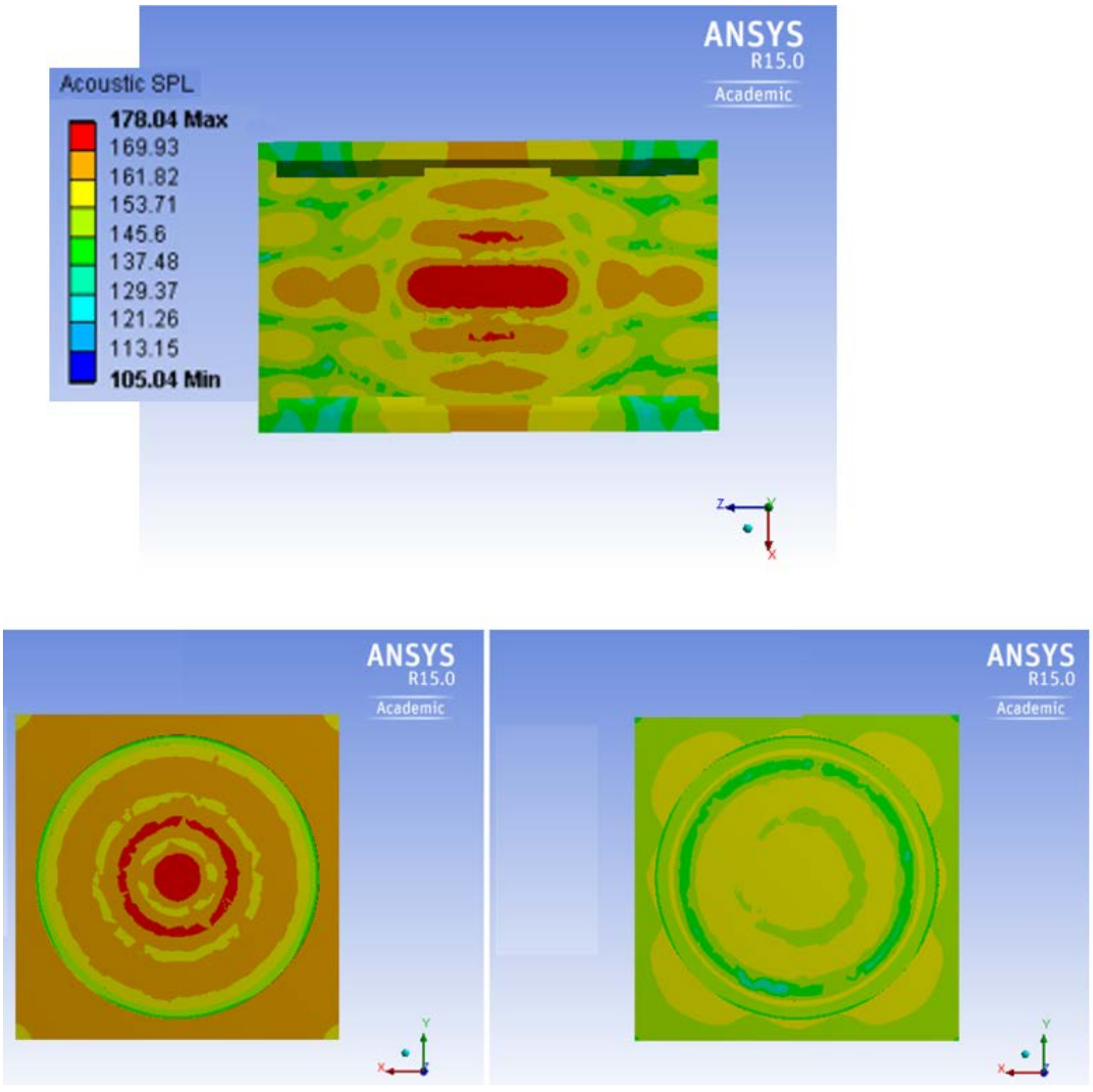

Fig.4-26. Acoustic field in SPL for a potential mode shape of the specimen with one internal axial step of 15 mm length at 36 KHz; Top: Axial view on the vertical plane, Bottom left: Side view at mid-length, Bottom right: Side view at quarter-length.

Comparing the performance of the transducer with the one with 5.5 mm length step reveals that both of them approximately have similar acoustic field ranges for most parts inside the transducer. However, the transducer with 5.5 mm length step has a more uniform and better distributed acoustic field along the length and over all the regions compared to the one with 15 mm length step. To summarise this, for the case of external step, the longer step does not give as high values of SPL and as uniform acoustic field as the shorter one. For the case of internal step, although the SPL is higher than that of the shorter step, it is not uniform and does not cover all the inner parts of the transducer as efficiently as the transducer with the shorter step. Moreover, the stress is in the order of 10^8 Pa compared to 51 MPa for the short steps. Overall, it can be concluded that the one with 5.5mm length step has better performance and is recommended as explained.

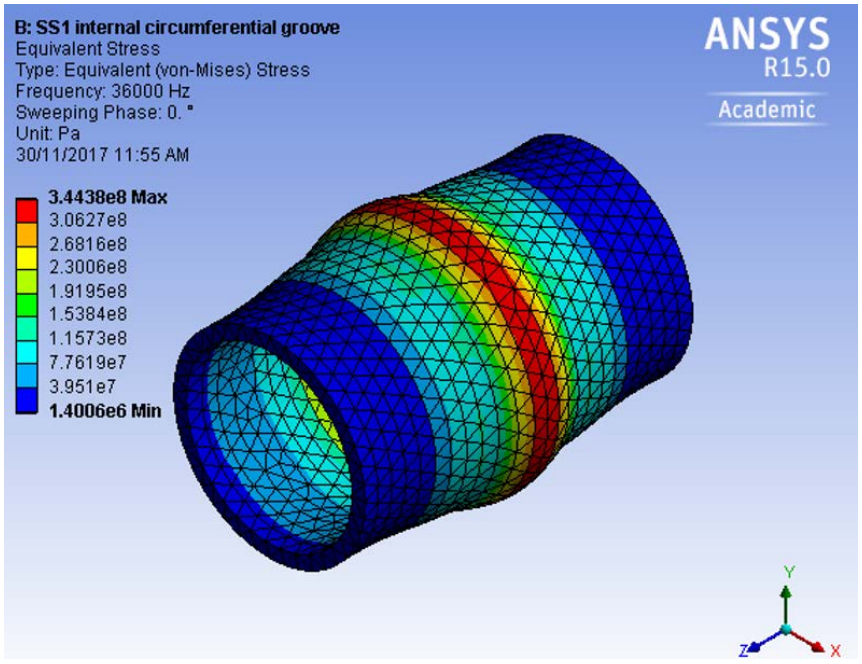

Fig.4-27. Stress distribution for the specimen with one internal axial step of 15 mm length at 36 KHz.

4.5.2. Transducer with Two Internal-External Axial Steps

As discussed earlier for the specimens with one internal and external step, the location of steps for specimens with two steps should be carefully identified. Based on the mode shape for the uniform-thickness specimen in Fig.4-7 with wave numbers of (5, 0), it includes two regions in counter-phase with the other three regions. It is intended to machine the area between each two consecutive in-phase regions in order to localize the vibration within those thin areas and achieve higher vibration amplitudes. Thus, two regions of the tube, which were in counter-phase with the other three regions, were machined by half a millimetre from each of the inner and outer surfaces. Following these explanations, one can come up with two steps each 11.5 mm long and the thick region in between is 7 mm long. The other two regions will be 10 mm long each. The schematic of the developed transducer is depicted in Fig.4-28. The simulations are performed for this specimen and the maximum value of the acoustic SPL occurs at 36 KHz and 42 KHz the mode shapes of which are depicted in Fig.4-29. Further, Figs.4-30 and 4-31 illustrate the resultant acoustic fields. Maximum level of SPL is 173 dB and 170 dB for 36 KHz and 42 KHz, respectively. Axial and circumferential wave numbers are (1, 0) and (5, 0) for 36 KHz and 42 KHz, respectively. The amplitude of vibration for the case of 36 KHz is orders of magnitude larger than that of the uniform-thickness specimen. According to Fig.4-29, nearly all the regions of the transducer are in similar range of vibration amplitude as evident from the colour-coded legend. This results in a quite uniform acoustic field along the length and also symmetric uniform acoustic field at each cross section as in side views of Fig.4-30. However, the stress is in the order of 10^8 as in Fig.4-32 which is not suitable.

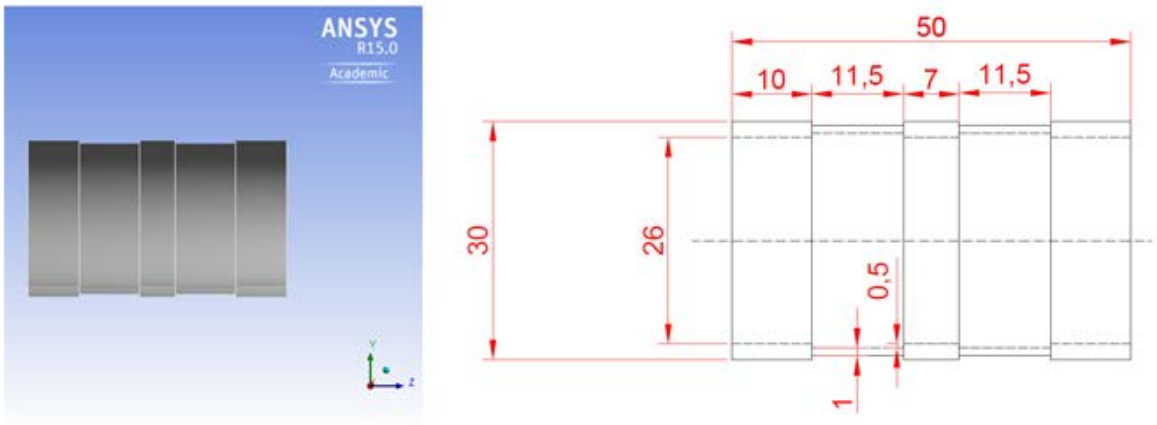

Fig.4-28. Schematic of specimen with two internal-external axial steps.

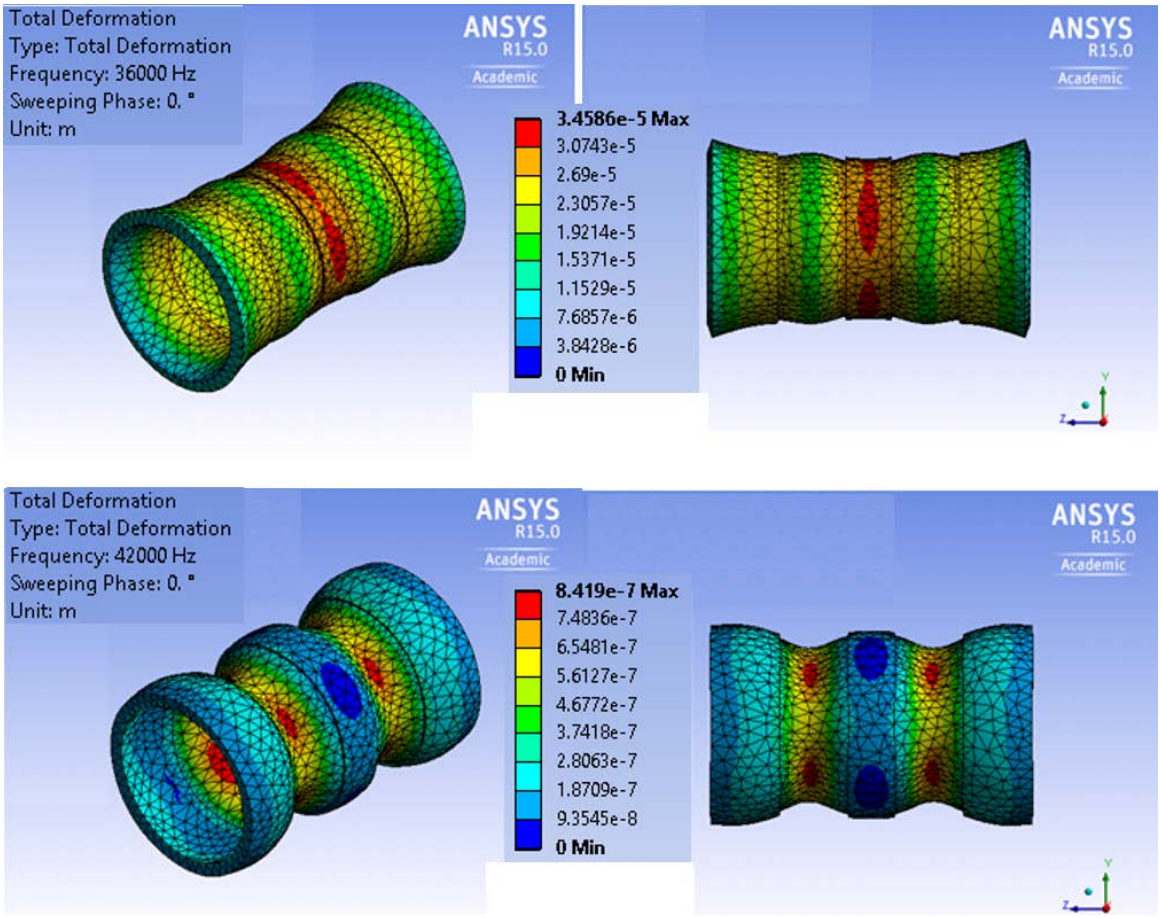

Fig.4-29. Harmonic analysis results for potential mode shapes of the specimen with two internal- external axial steps, Top: ISO and side views at 36 KHz, Bottom at 42 KHz

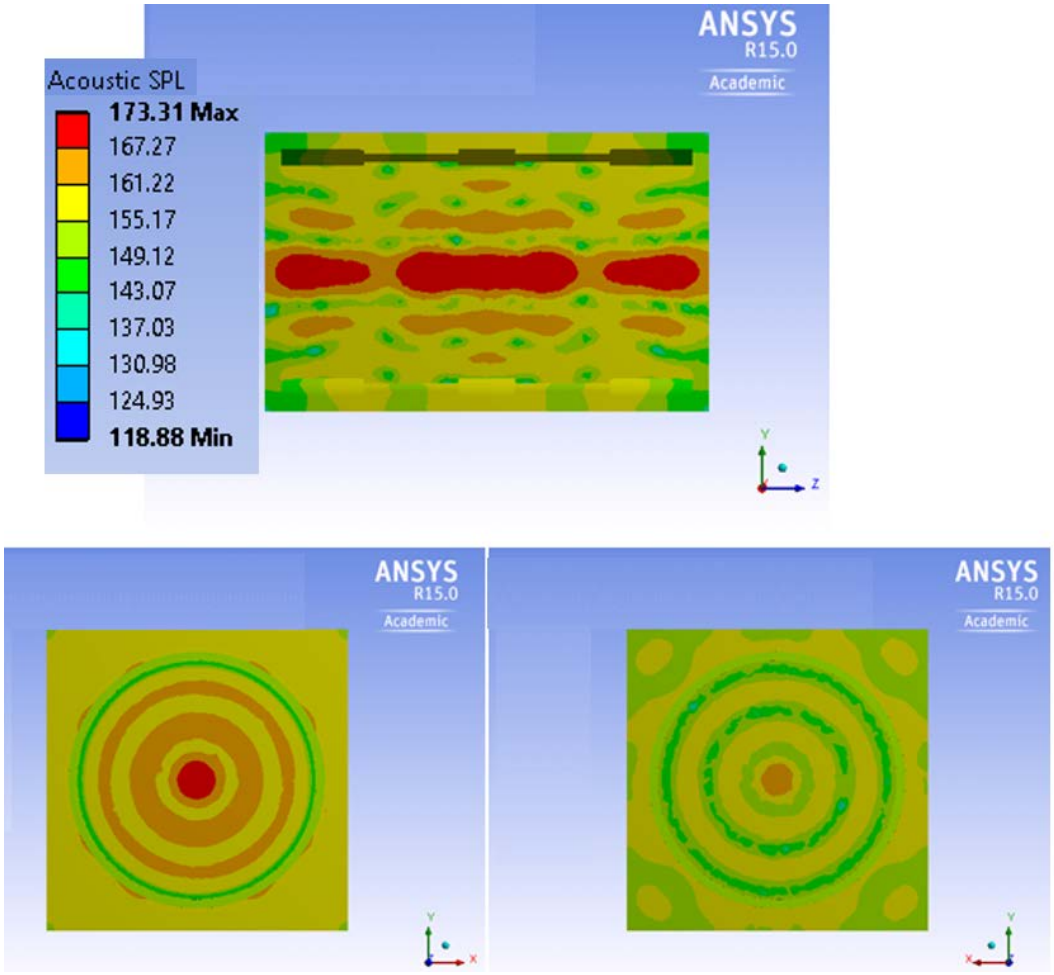

Fig.4-30. Acoustic field in SPL for a potential mode shape of the specimen with two internal-external axial steps at 36 KHz; Top: Axial view on the vertical plane, Bottom left: Side view at mid-length, Bottom right: Side view at quarter-length.

For the case of 42 KHz, the amplitude of vibration is the same order of magnitude as the uniform-thickness specimen. However, the vibration is slightly more localized within the machined regions. The machined regions are vibrating with approximately twice the amplitude as the uniform-thickness specimen. The resultant acoustic field as in Fig.4-31 is quite uniform along the length and the side views also reveal the uniformity along the length and good symmetry. Further, the maximum stress is 5.9 MPa as in Fig.4-32 which is suitable.

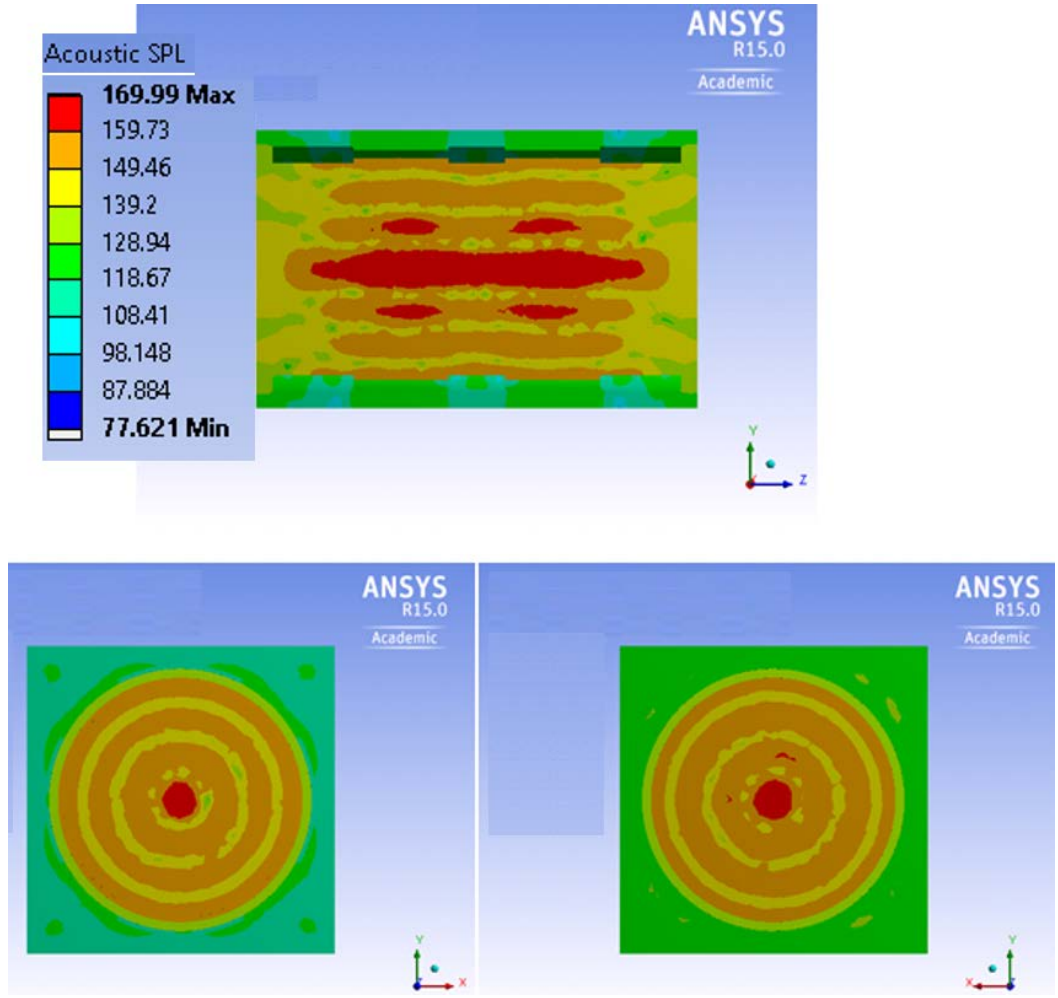

Fig.4-31. Acoustic field in SPL for a potential mode shape of the specimen with two internal-external axial steps at 42 KHz; Top: Axial view on the vertical plane, Bottom left: Side view at mid-length, Bottom right: Side view at quarter-length.

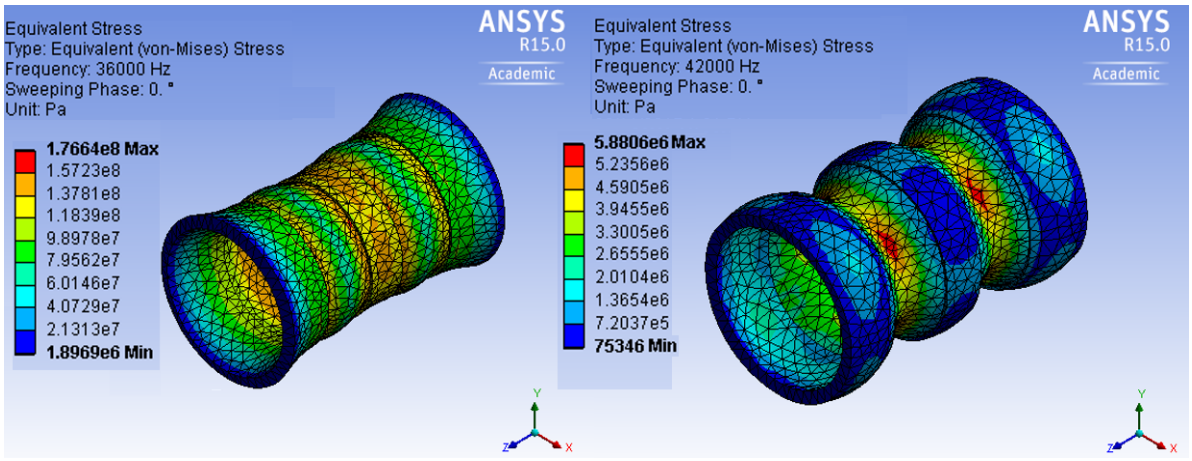

Fig.4-32. Stress distribution for the specimen with two internal-external axial steps at Left: 36 KHz and Right: 42 KHz.

4.5.3. Transducer with Six Internal Circumferential Steps

To excite the transducer at the mode shape with the circumferential wave number of six, the whole circumference is divided into 12 equal sections half of which are thick and the other half are machined as in Fig.4-33. The simulations are performed and the maximum value of the acoustic SPL for this specimen occurs at 31 KHz the mode shape of which is depicted in Fig.4-34. Further, Fig.4-35 illustrates the resultant acoustic field. The maximum level of SPL is 204 dB.

Axial and circumferential wave numbers are (1, 6) as in Fig.4-34. The circumferential wave number is the same as the number of steps; however the vibration is not localized within the machined regions. The thick regions, which are not machined, vibrate at a higher amplitude compared to the machined regions as evident from ISO and side views of the specimen in Fig.4-34. Further, it can be seen from the side view that the peaks in circumference in thick regions are so wide that they cover parts of the machined regions from both sides and therefore, only a very small region inside the machined parts is in counter-phase with the other thick parts. Therefore, many regions including thick and thin parts are vibrating in-phase with an amplitude which is an order of magnitude larger than that of the uniform-thickness specimen. Side views in Fig.4-35 reveal high levels of SPL at various cross sections at mid- and quarter-length of the transducer. Nearly all regions inside the transducer are in orange and red colour coded areas.

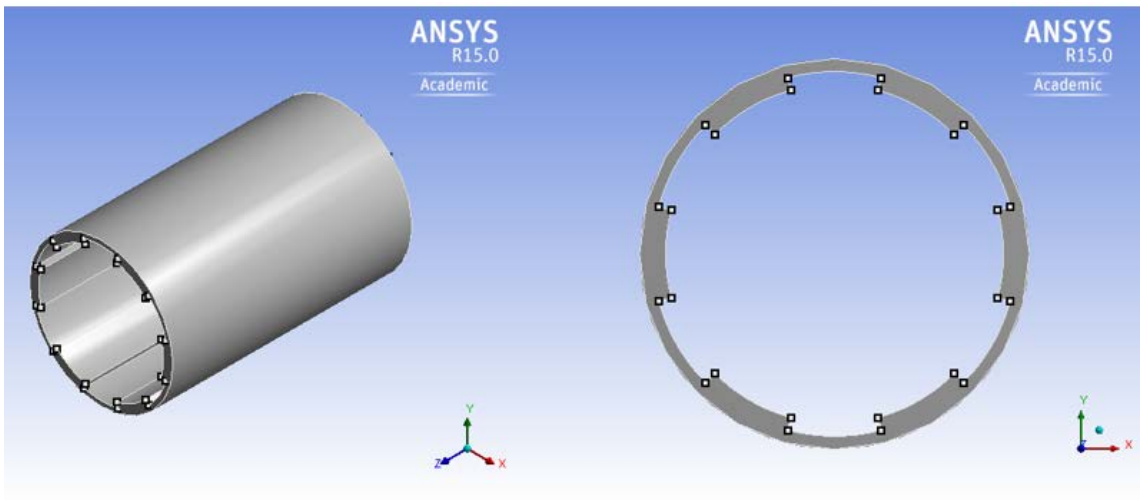

Fig.4-33. Schematic of specimen with six internal circumferential steps; Left: ISO view, Right: Side view.

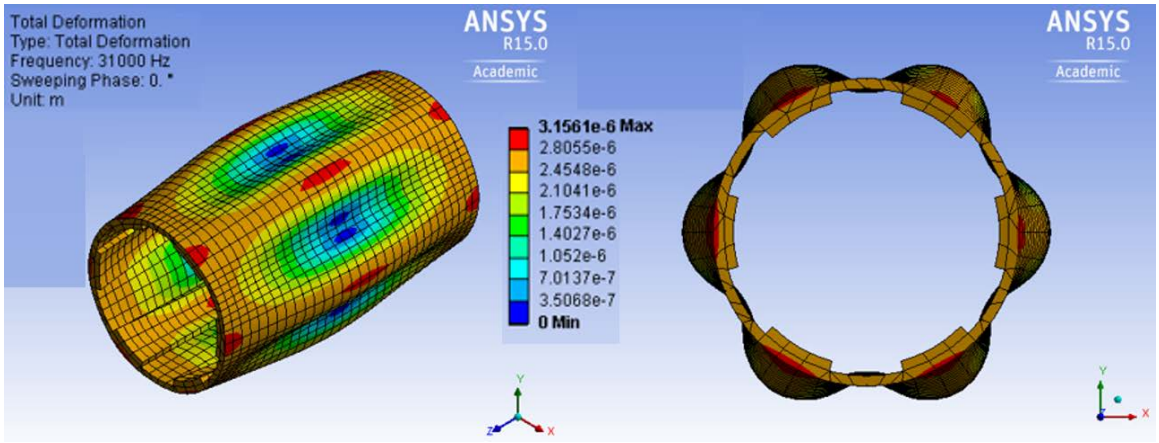

Fig.4-34. Harmonic analysis results for a potential mode shape of the specimen with six internal circumferential steps at 31 KHz; Left: ISO view, Right: Side view.

Due to the asymmetry in the geometry between horizontal and vertical axial views, the resultant acoustic field is also different, however, in both views it maintains a very high level along the length (all in orange and red colour coded areas). The maximum stress is also 28 MPa which is within the safe and suitable range and most regions are at a lower level of stress as in Fig.4-36. Hence, from the viewpoint of stress distribution, the specimen is also performing satisfactorily.

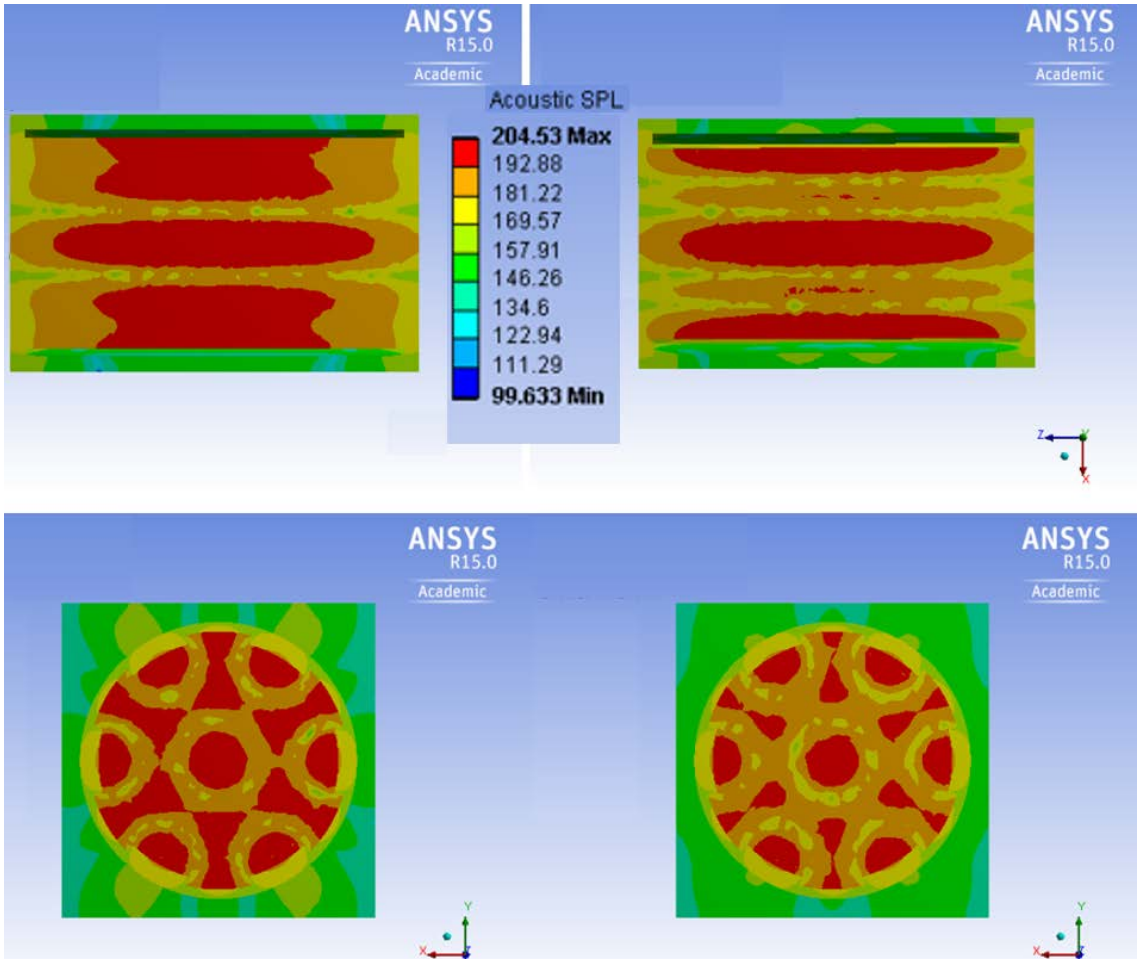

Fig.4-35. Acoustic field in SPL for a potential mode shape of the specimen with six internal circumferential steps at 31 KHz; Top left: Axial view on the vertical plane, Top right: Axial view on the horizontal plane, Bottom left: Side view at mid-length, Bottom right: Side view at quarter-length.

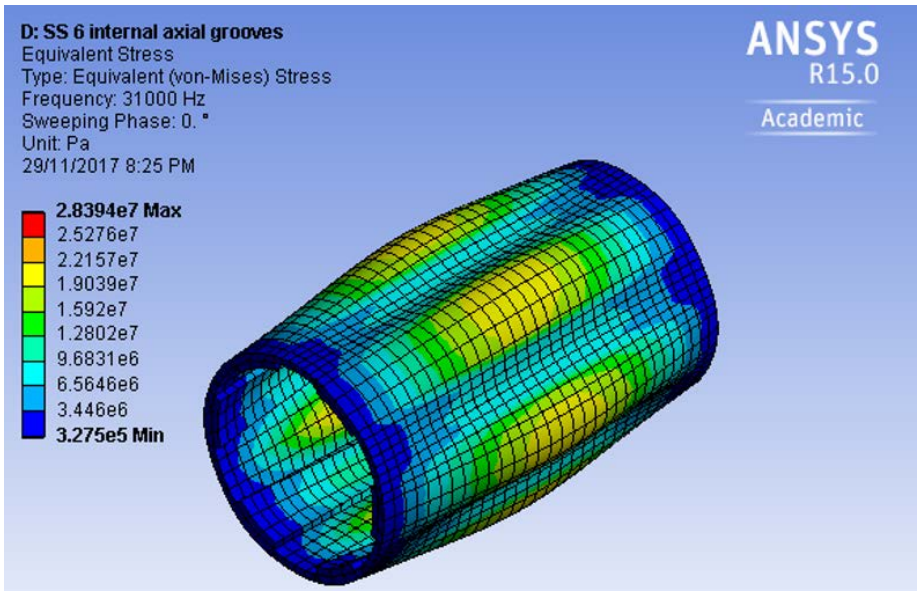

Fig.4-36. Stress distribution for the specimen with six internal circumferential steps at 31 KHz.

4.6. Concluding Remarks

Table 4-3 is a summary of all the investigations performed and all the attempted stepped transducers. Although only the suitable and identified stepped transducers were included in the chapter, this table can be used to compare all of them which helps to identify suitable designs. More detailed explanations for these transducers are included in Appendix B. Some important factors affecting the identification of the most suitable specimens include the maximum level of SPL, uniformity of the acoustic field, symmetry of the acoustic field on horizontal and vertical planes and on any cross section. Further, a very crucial factor is suitable amplitude of vibration and stress distribution. In addition, it is required to consider the process of machining which is generally harder for circumferential steps and more specifically for the internal ones. Considering these points and the results in Table 4-3

1. The specimen with two internal-external steps is preferred and identified as the most suitable one with axial steps.
2. The specimen with six circumferential internal steps is identified as the most suitable one with circumferential steps.
3. In addition to the specimen with two internal-external steps, the transducers with one internal axial step and one external axial step are also chosen to be experimentally tested. It is intended to investigate whether the stress level results from the simulations can be validated or not. For the specimen with one external axial step, the stress level exceeds the limit and it is supposed to fail after some time based on simulations. This will also be clarified using the experimental test on this specimen.

4.7. Closure

Various step configurations were considered. Modes shapes, vibration amplitudes, acoustic radiation and stress concentration were investigated. The results indicates that using thickness variations can effectively localize the vibration amplitude. Further, high level of sound pressure was obtained along the centreline for some of the stepped tubes. However, the localized higher amplitude vibration resulted in very high stress levels in some cases. This may lead to failure of the transducer. Therefore, some configurations were eliminated despite generating high SPLs.

Several factors contributed to the high level of sound pressure along the centreline for some specimens. First, employing a circular cylindrical geometry for the transducer improves the directivity and focus of the emitted sound waves along the centreline. Further, a suitable mode shape of vibration with the circumferential wave number of zero causes the shell circumference to vibrate uniformly and in-phase at any cross section along the length. Although the circumferential wave number was not zero for the specimen with six internal circumferential steps, the shell circumference vibrated quite uniformly and in-phase with minimal counter-phase vibration from various regions around the circumference. This reduces the counteracting effect of those sections emitting waves in counter-phase. Hence, a better constructive interference of the waves at the centreline is achieved leading to a higher sound pressure level.

Further, increasing the voltage increases the SPL and power consumption. However, such increase in SPL is achievable using some of the stepped specimens at the same input voltage and consequently the same power. Therefore, geometrical variations seem a better alternative than increasing voltage.

Table 4-3. Summary of the results and performance of the transducers investigated.

Specimens with the following type and number of steps: (Circum: Circumferential;Ext: External; Int: Internal; UT: Uniform Thickness)								
		Frequency (KHz)	Mode No (m, n)	Max. SPL (dB)	Mode Shape	View of the Acoustic Field	Pros & Cons of the Acoustic Field	Stress
UT		43	(5, 0)	169.7	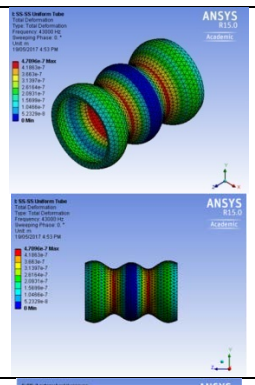	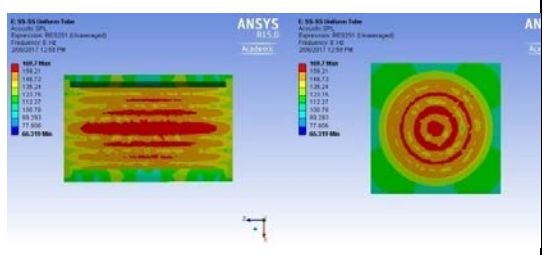	Uniform	3.3MPa Suitable
2 Circum	Ext	34.5	(5, 2)	166.05	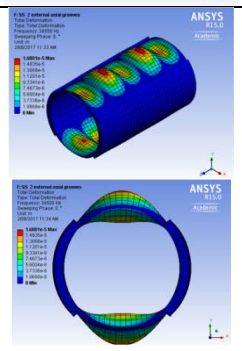	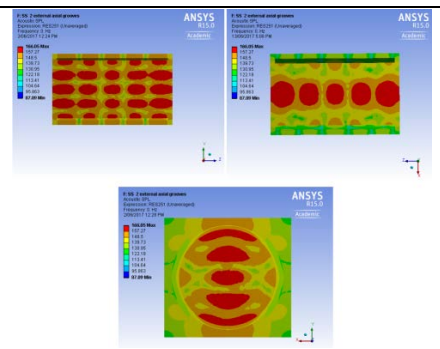	Not as high SPL as UT, No contribution from thick portions, Low SPL in many regions	10^8Pa High & Unsuitable
	Int	35	(1, 6)	175.18	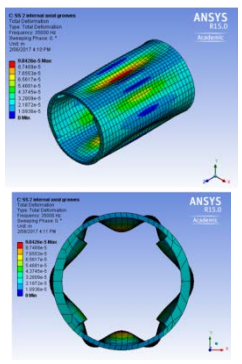	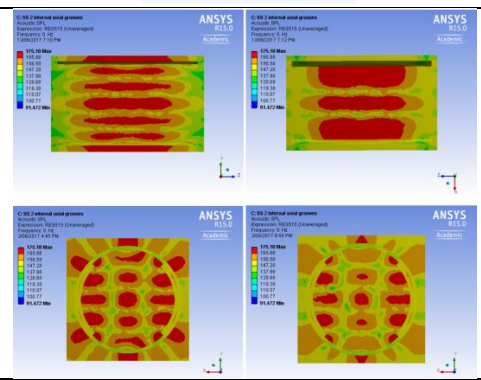	Uniform along mid-length, No coverage for quarter-length on each side, Low SPL in many regions as in side views	10^8Pa High & Unsuitable
		39	(1, 6)	185.7	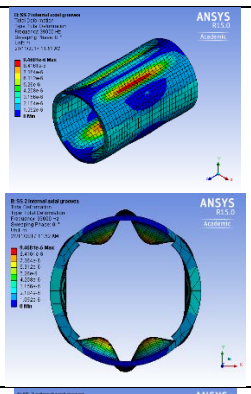	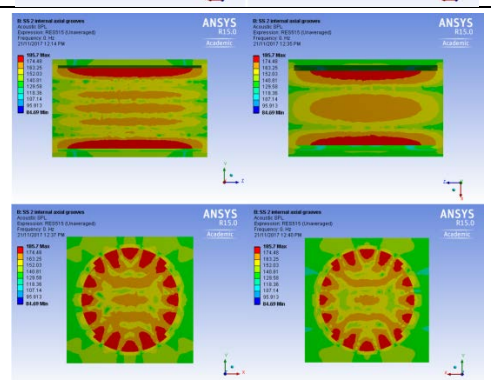	High max SPL, Low focus, Low SPL in many regions	82MPa High & Unsuitable
3 Circum	Ext	31	(3, 0)	168.69	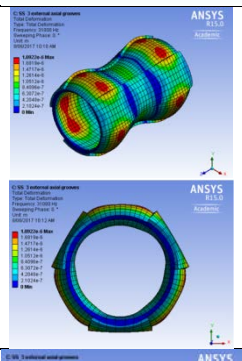	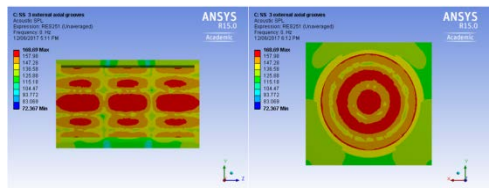	Good symmetry, Uniformity, Not higher SPL than UT	12MPa Suitable
		39	(1, 6)	179.1	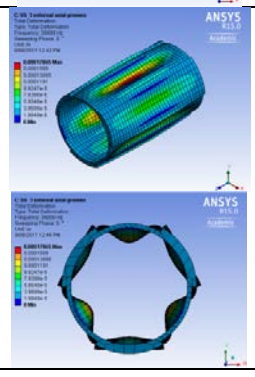	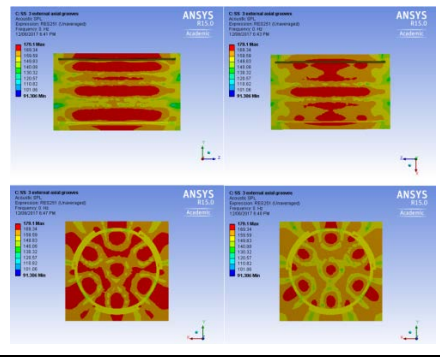	High maximum SPL, Not symmetric in both axial views, Low SPL in many regions as in side views	10^9Pa High & Unsuitable

		Frequency (KHz)	Mode No (m, n)	Max. SPL (dB)	Mode Shape	View of the Acoustic Field	Pros & Cons of the Acoustic Field	Stress
3 Circum	Int	32	(3, 3)	174.2	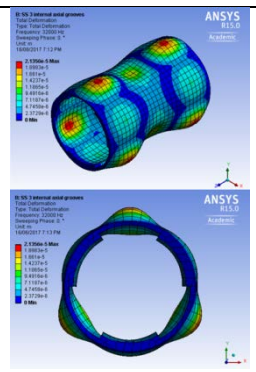	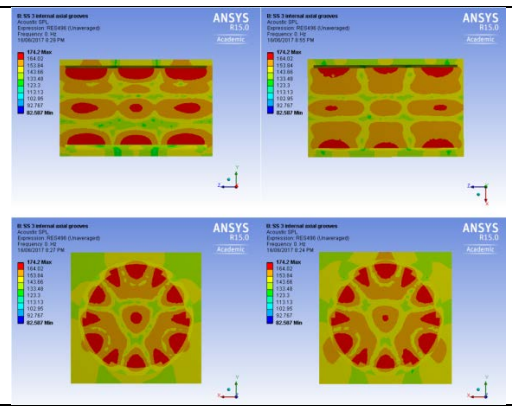	Not symmetric in both axial views, Low SPL in many regions, No good focus	123MPa High & Unsuitable
		39.5	(1, 6)	202.17	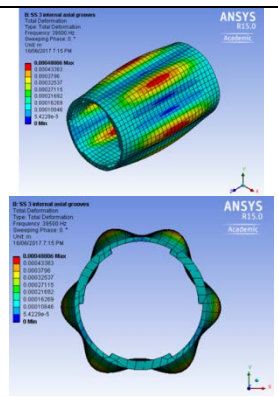	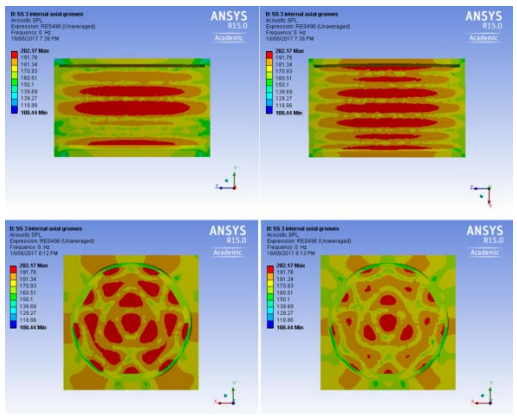	High maximum SPL, Not symmetric in both axial views, High SPL everywhere	10^9Pa High & Unsuitable
4 Circum	Ext	36	(1, 0)	194.78	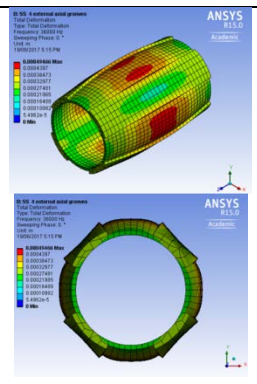	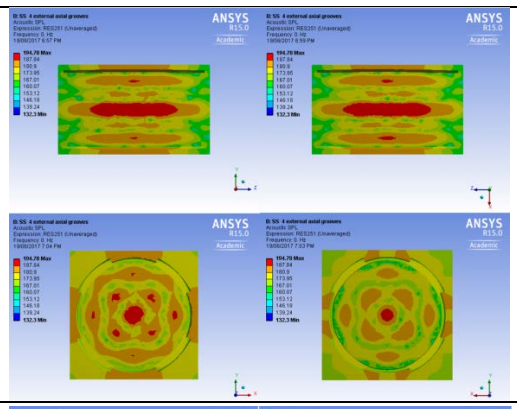	High maximum SPL, Low SPL in many regions	10^9Pa High & Unsuitable
		47.5	(7, 4)	169.69	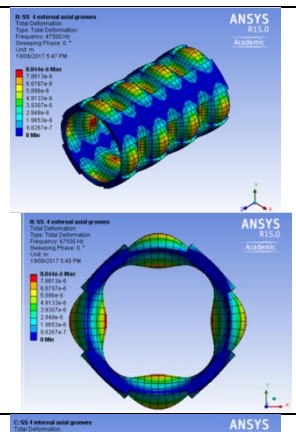	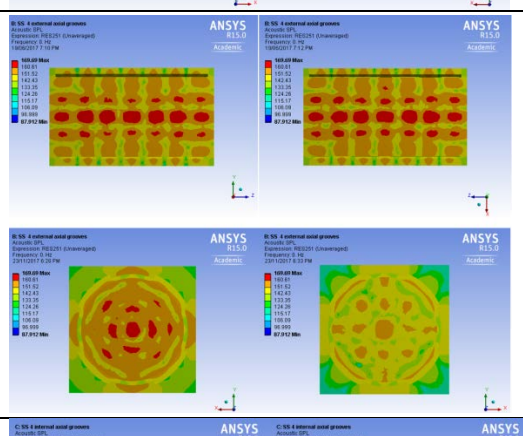	Not higher SPL than UT, Low SPL in many regions	92MPa High & Unsuitable
	Int	37.5	(1, 4)	205.54	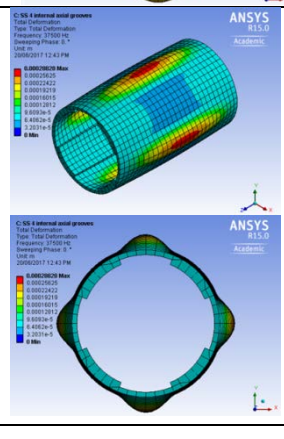	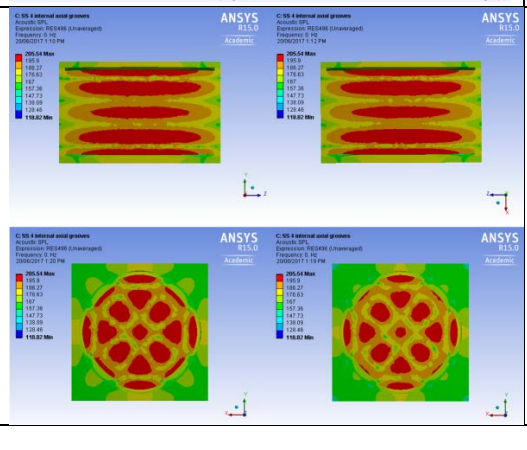	High maximum SPL, Good uniformity, High SPL everywhere	10^9Pa High & Unsuitable

		Frequency (KHz)	Mode No (m, n)	Max. SPL (dB)	Mode Shape	View of the Acoustic Field	Pros & Cons of the Acoustic Field	Stress
5 Circum	Ext	30.5	(3, 0)	171.38	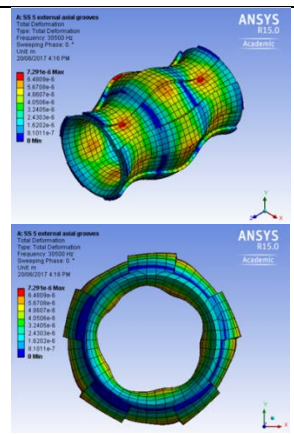	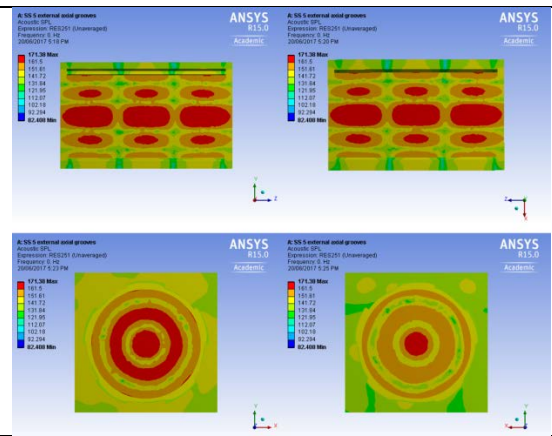	Good symmetry, Good uniformity, Not very high SPL	48MPa Fairly Suitable
	Int	28.5	(1, 5)	173.73	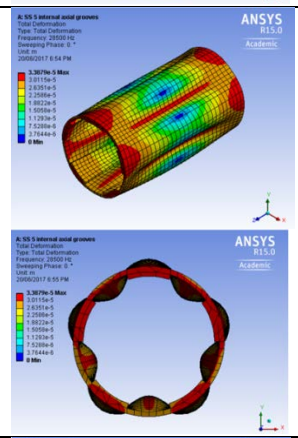	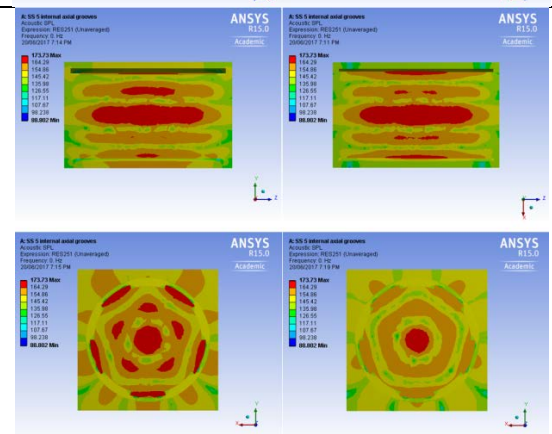	Good symmetry, Good uniformity, Not very high SPL	10^8Pa High & Unsuitable
		41.5	(1, 5)	188.06	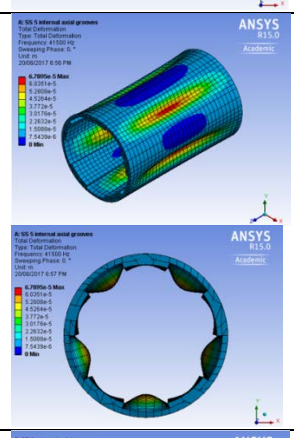	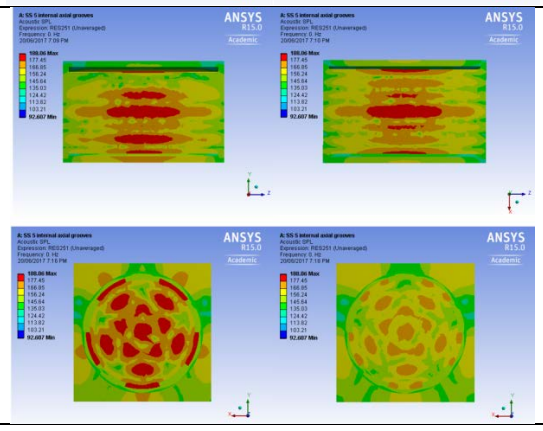	High maximum SPL, Low SPL in many regions, No good coverage along the length	10^8Pa High & Unsuitable
6 Circum	Ext	43	(3, 6)	177.13	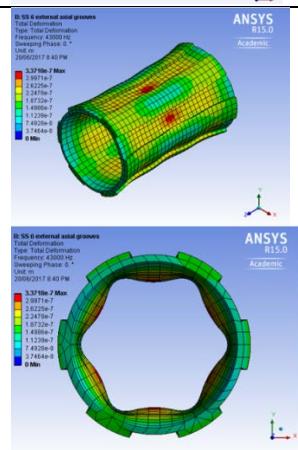	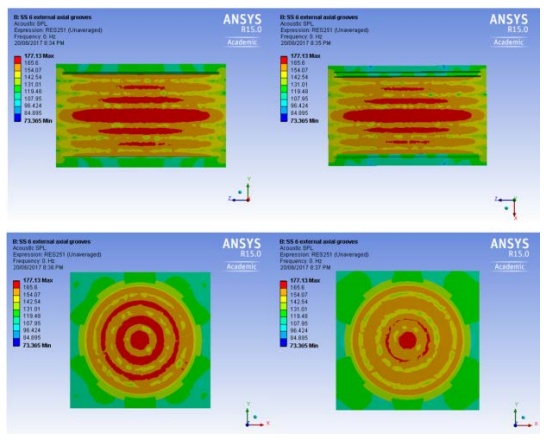	Good uniformity, Good symmetry, Not very high SPL	3MPa Suitable
	Int	31	(1, 6)	204.53	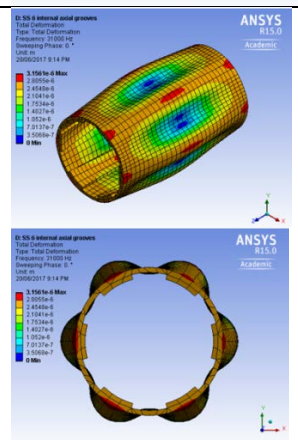	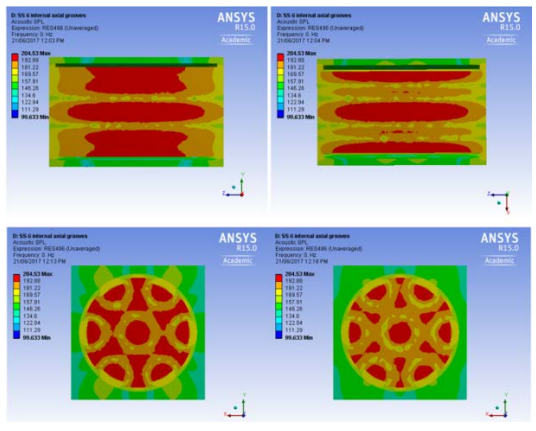	High max SPL, High SPL everywhere, good uniformity, Good coverage along the length	28MPa Suitable

		Frequency (KHz)	Mode No (m, n)	Max. SPL (dB)	Mode Shape	View of the Acoustic Field	Pros & Cons of the Acoustic Field	Stress
1 Axial	Ext	36	(1, 0)	172.29	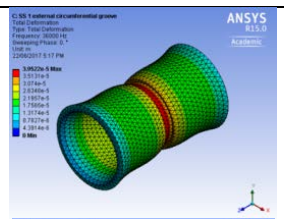	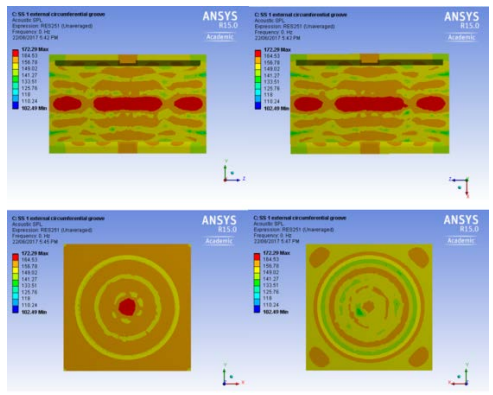	Good symmetry, Good uniformity along the length, Not very high SPL	10^8Pa High & Unsuitable
	Int	43	(5, 0)	167.49	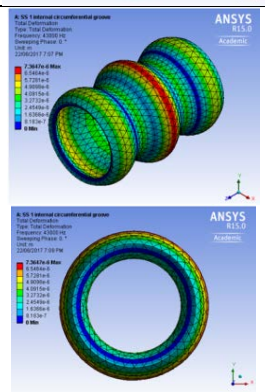	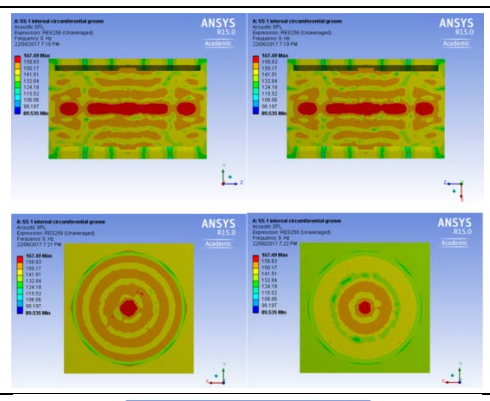	Good symmetry, Good uniformity along the length, Not higher SPL than UT	51MPa Fairly Suitable
2 Axial	Ext	33	(3, 0)	179.31	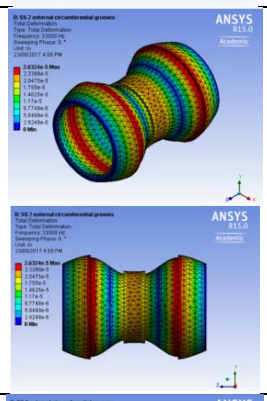	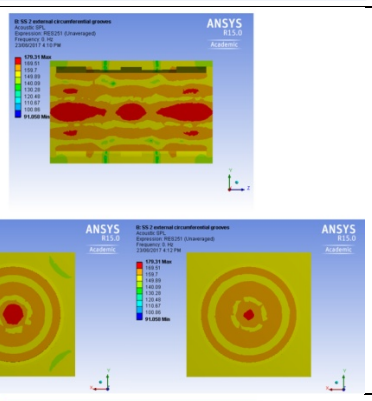	Good uniformity, Good coverage along the length, Not very high SPL	10^8Pa High & Unsuitable
		36	(1, 0)	179.13	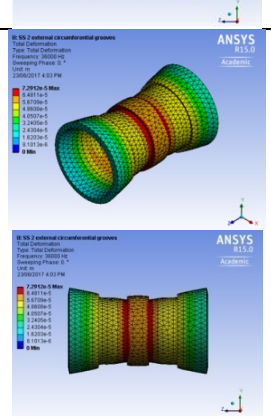	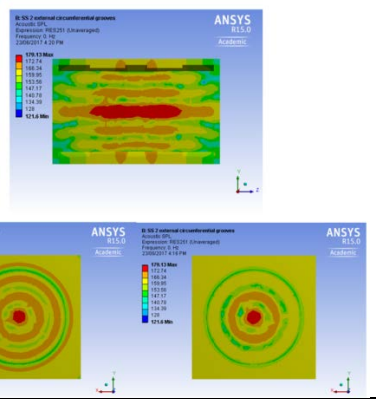	Not very high SPL, No good coverage along the length	10^8Pa High & Unsuitable
	Int	40.5	(5, 0)	172.85	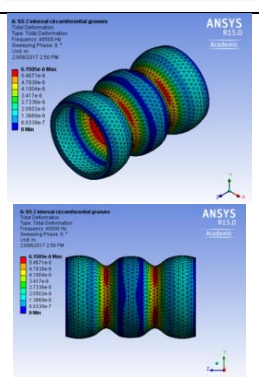	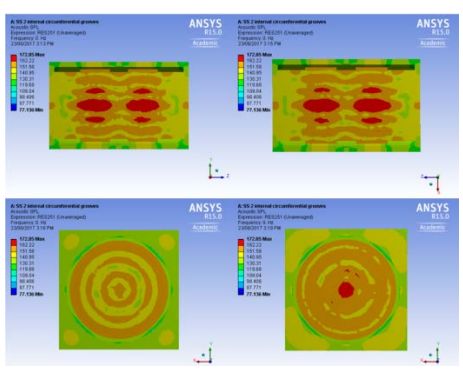	Not very high SPL, No good coverage along the length, Good symmetry	42MPa Fairly Suitable

		Frequency (KHz)	Mode No (m, n)	Max. SPL (dB)	Mode Shape	View of the Acoustic Field	Pros & Cons of the Acoustic Field	Stress
2 Axial	Int-Ext	36	(1, 0)	173.31	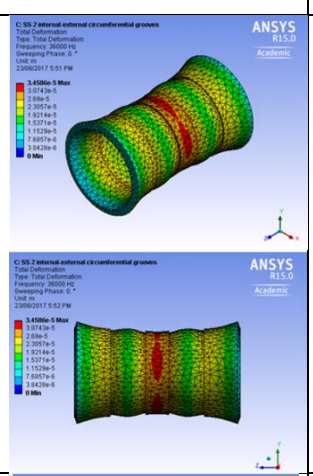	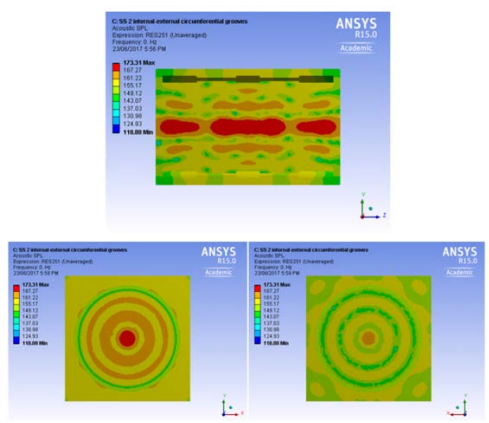	Good symmetry, Good coverage along the length, Good uniformity, Not very high SPL	10^8Pa High & Unsuitable
		42	(5, 0)	169.99	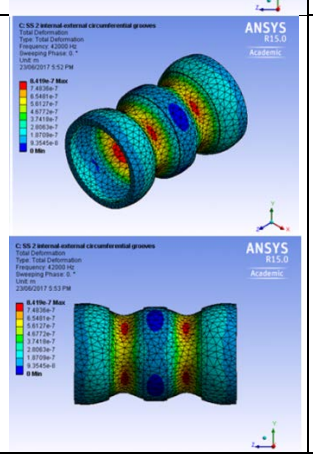	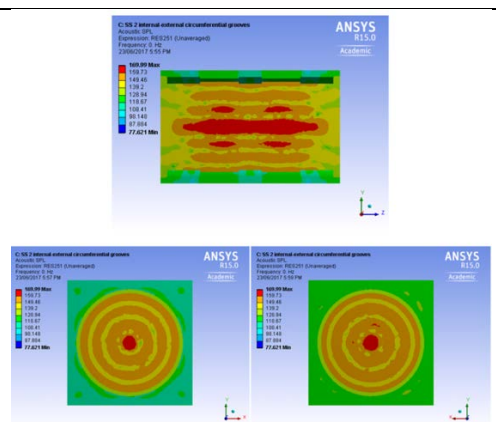	Good symmetry, Good coverage along the length, Good uniformity, Not higher SPL than UT	5.9MPa Suitable

Chapter 5: Experimental Investigations

5.1. Introduction

This chapter covers the experimental investigations conducted in this study. The specimens identified and developed in the previous chapter were machined to the specified dimensions and the tests were performed on them. Performing these experiments is an essential part of this study to validate the simulation results and investigate the performance of the designed and developed transducers. These experiments include one for getting the vibration mode shape and the other for getting the acoustic SPL. Details of the experiments and the required equipment are all explained in the following sections. The experiments are performed several times to assure the repeatability and reliability of the obtained results. It is also worth noting that the frequency corresponding to the highest sound pressure level and the magnitude of the SPL differ slightly from test to test; however, this is not noticeable and does not affect the repeatability of the experiments. Comparison between simulation and experimental results and discussion will be presented in the next chapter.

5.2. Sample Preparation

Having identified the suitable design configurations for the stepped transducers, they are required to be built for the experimental investigations. To do so, machining should be performed as per the design of the developed transducers in the previous chapter. Explanations on the development of these designs were elaborated on in the previous chapter and accordingly, the drawings are prepared to proceed with machining. Fig.5-1 illustrates these drawings used for machining. These were sent to Callaghan Innovation centre in Wellington which had the required equipment for machining

these piezoelectric materials which is a cumbersome task. Fig.5-2 illustrates all the machined specimens ready to be tested experimentally. It is worth noting that since machining removed the electrode layer from the surface of the transducers, they were recoated using a very thin layer of silver epoxy.

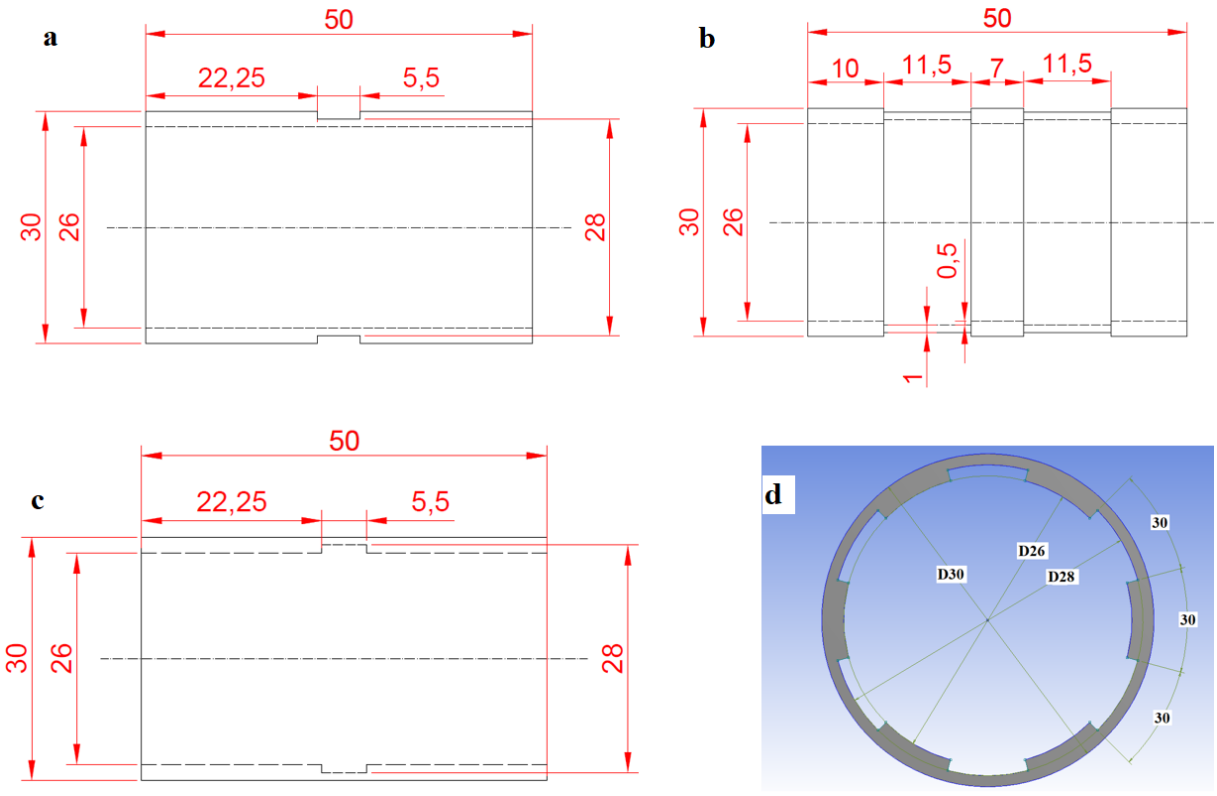

Fig.5-1. Drawings of the specimens for machining: a: specimen with one external axial step; b: Specimen with two internal-external axial steps; c: specimen with one internal axial step; d: specimen with six internal circumferential steps.

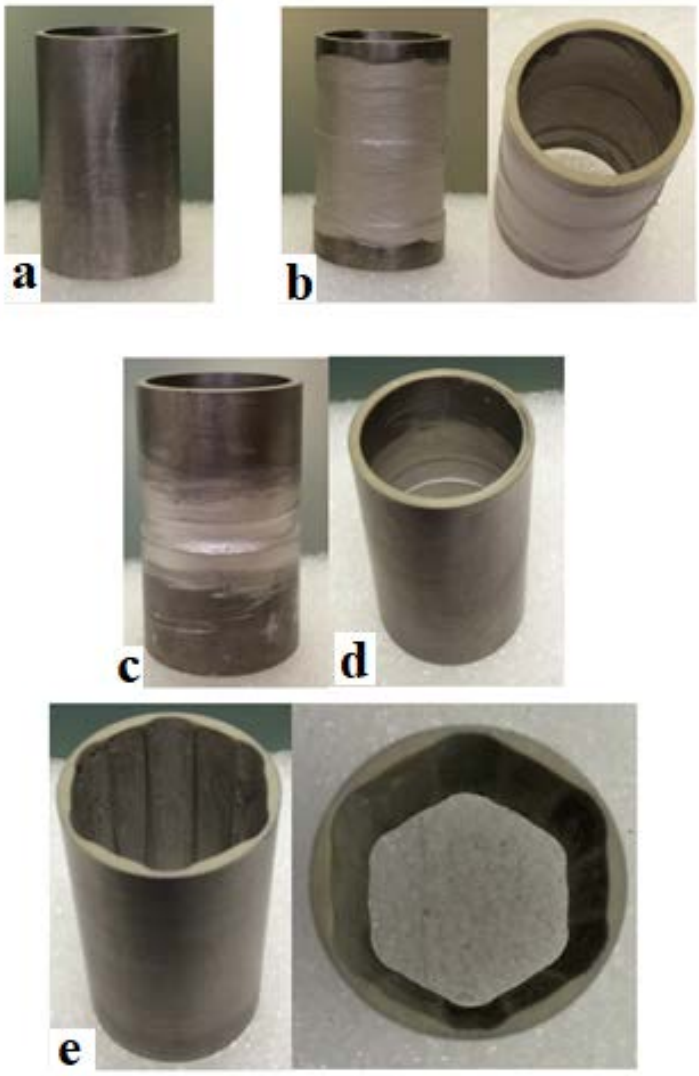

Fig.5-2. Picture of the specimens: a: Uniform-thickness specimen; b: Specimen with two internal-external axial steps from two views; c & d: Specimens with one external axial & one internal axial step, respectively; e: Specimen with six internal circumferential steps from two views.

5.3. Experimental Set-up and Equipment

The experimental rig designed is illustrated in Fig.5-3. The transducer with the conductive silver electrodes on its surface can cause an electric shock if touched when the power supply is on. Therefore, the whole transducer and amplifier are assembled in a transparent Perspex box to comply with the safety regulations. A support on each side of the transducer is designed to hold it. This can be best modelled as Simply Support boundary condition in the simulations. Two guide pipes (white pipes) are also

fitted on both sides of the supports to provide a safe path to insert the microphone into the transducer without the risk of touching the transducer or any electric connection. The microphone is also installed on a thin solid strap as in Fig. 5-3 and inserted in the white pipe and slides in along the centreline so that it does not touch the wall of the transducer and ascertains that all the measurements are performed along the centreline. Further, in order not to affect the acoustic field generated inside the transducer, the microphone and the strap are designed in such a way that only the tip of the microphone goes into the transducer and not the whole microphone or any part of the solid strap. In addition, the supports holding the transducer prevent the accidental entrance of the solid strap in the transducer. Fig. 5-4 depicts the whole experimental set-up and the overall schematic layout is illustrated in Fig.5-5.

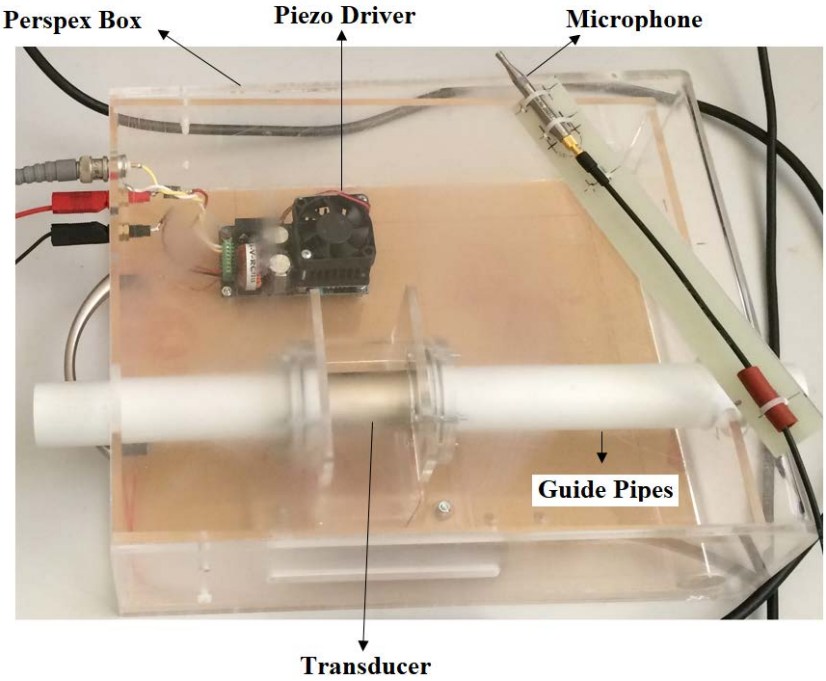

Fig.5-3. Experimental rig.

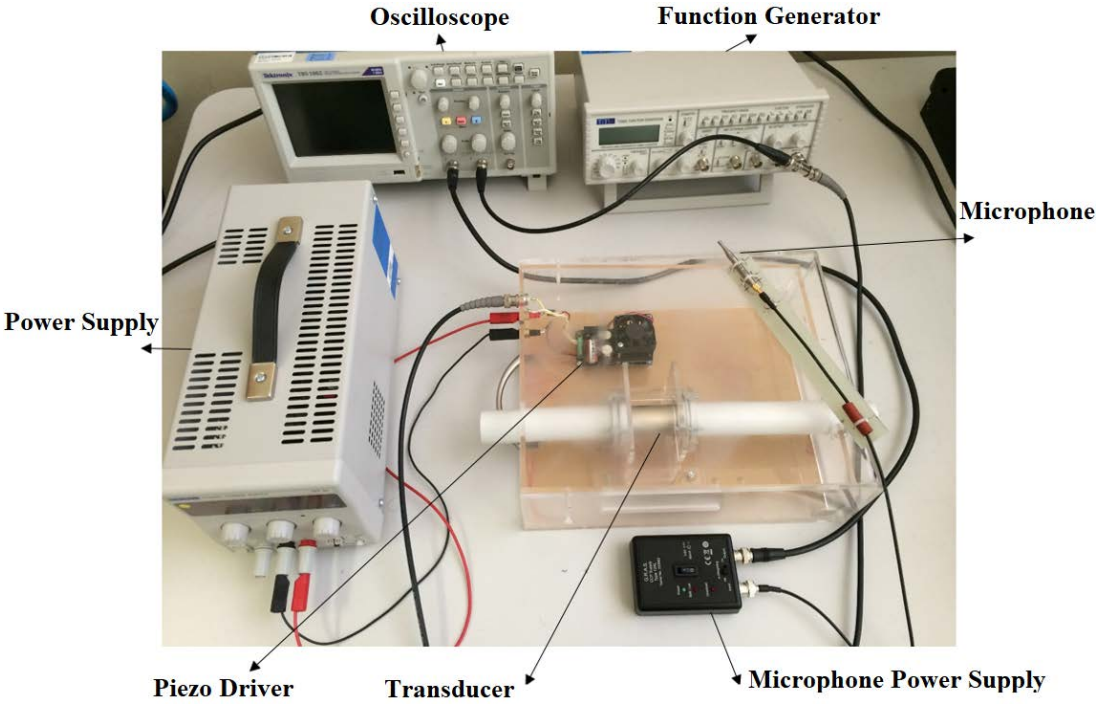

Fig.5-4. Experimental set-up.

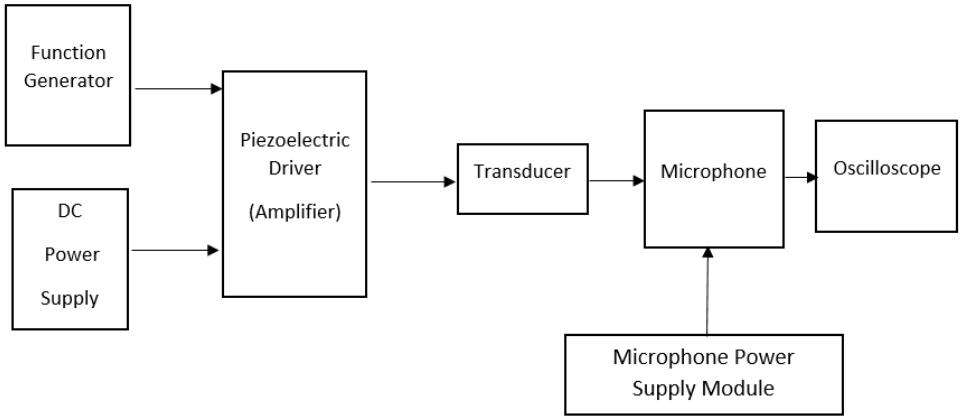

Fig.5-5. Schematic layout of the experimental set-up.

The required equipment to perform the experiments and complement the set-up is a piezo driver which is MX200 200V 1A purchased from Micromechatronics, Inc, PA, USA. It is a complete power supply and high-performance linear voltage amplifier module for driving piezoelectric transducers. The voltage gain of this amplifier is 20 and it works within three ranges of 100V, 150V and 200V depending on the need and

the jumper settings on the PCB board. This piezoelectric power amplifier runs on 18-36V DC power (24V recommended by the manufacturer). The other devices needed are a function generator and a power supply to feed the input excitation signal and voltage, respectively to the piezo driver. The models used are TTi TG550 function generator and TTi EX355R 35V 5A power supply. Further, the required equipment includes G.R.A.S. 46DD 1/8" CCP Pressure Standard Microphone Set as well as 12AL G.R.A.S. CCP Power supply module to measure the output sound pressure level. In addition, an oscilloscope is needed to read the output of the microphone. To this aim, Tektronix TBS1062 oscilloscope is employed.

To obtain the vibration mode shape, Polytec laser scanning vibrometer PSV-400 is used the picture of which is illustrated in Fig.5-6. The device comes with its own computer software and controller set-up as in this figure.

Fig.5-6. Laser scanning vibrometer PSV-400.

5.4. Experimental Protocol

As mentioned earlier, the measurements are for the mode shape of vibration as well as the acoustic measurements. To obtain the mode shape for the intended frequency corresponding to the highest SPL, a laser vibrometer is used with the supporting software package. Using the software, the laser beam for scanning can be controlled and the area to be scanned can be defined. Once the laser beam has suitable focus and is aligned with the scan region defined in the software on the surface of the transducer, the scan is started while the transducer is driven by the piezoelectric driver at the intended frequency. Hence, the surface area defined is scanned and can be observed as a figure as well as a video while scanning is terminated. This provides the mode shape of vibration for the intended frequency.

To perform acoustic measurements, it is intended to obtain the frequency at which the maximum SPL occurs. Further, the uniformity of the acoustic field along centreline at various longitudinal positions along the length of the transducer is investigated. It is desired to obtain the strength of the acoustic field at various locations. Any slight change in the location of the microphone affects the output SPL. Hence, a few locations are considered for each sample to obtain the SPL at those positions in addition to the measurements at the mid-length. For instance, at the beginning of the thin, machined region or at the middle of it or at quarter-length or one-third of the length. Mostly, these are points of interest especially for the thin, machined regions and these are where the maximum deflection is. On the whole, since measuring SPL continuously along the whole length of the transducer is not practical, it is decided to do it at these locations to gain an understanding of the uniformity and strength of the acoustic field along the length.

To do these measurements, the following steps should be followed

1. The piezoelectric driver is driven by the function generator and power supply at the desired frequency and voltage.
2. The microphone is inserted in the transducer along the pipe and centreline of the transducer at mid-length.
3. The output of the microphone is connected to the oscilloscope.
4. Frequency of the vibration at the function generator is varied so that the output of the microphone can be observed continuously on the oscilloscope screen. This step is done to identify the frequency at which the maximum SPL occurs.
5. Once the frequency corresponding to the maximum SPL is identified, uniformity measurements are performed by changing the position of the microphone along the length and driving the transducer at the same frequency and voltage.
6. Once the frequency corresponding to the maximum SPL is identified, the mode shape of vibration is obtained using the laser vibrometer at the same identified frequency corresponding to the maximum SPL.

Fig. 5-7 is the flow chart showing the experimental steps in the order they are conducted in this study. It is worth noting that the output of the microphone is connected through a BNC cable to the oscilloscope. The output of the microphone is voltage which can be easily converted to the sound pressure level in dB by means of the calibration chart provided by G.R.A.S. company in Denmark. The chart and data for the calibration are depicted in Fig.5-8 as provided by the company. The data from the chart is transferred to Microsoft Excel and a formula is fitted to the graph as (R^2=1):

Sound pressure level (dB)=8.6859ln (x)+100.02 (5-1)

where ‘x’ is the output of the microphone read from the oscilloscope screen in mV.

Further, the output sound pressure level in dB obtained from Equation (5-1) can be used in the following formula to evaluate the root mean square of the output sound pressure, p_{rms}, in Pascal (Pa).

Sound pressure level (dB)=20 log p_{rms}+94 (5-2)

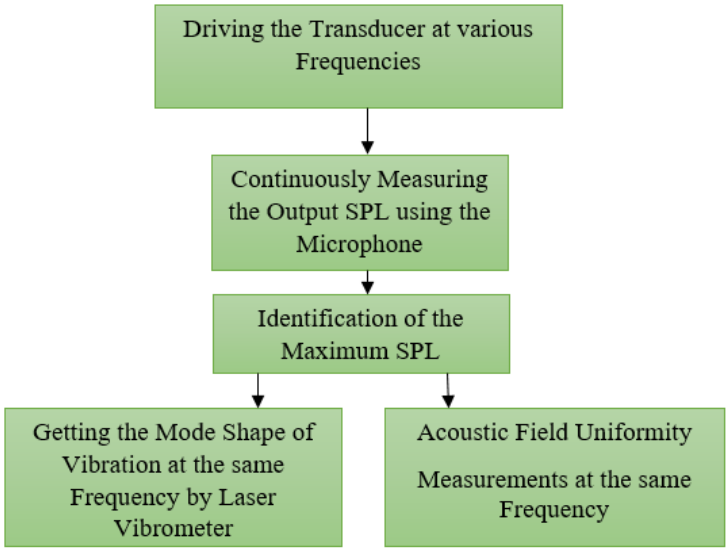

Fig.5-7. Flow chart showing the experimental steps.

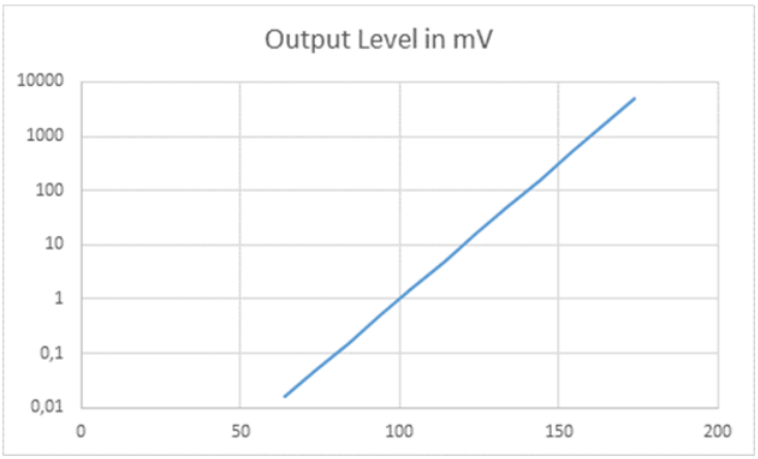

SPL (dB)	Output Level (mV)
64	0,0158
74	0,05
84	0,158
94	0,5
104	1,58
114	5
124	15,8
134	50
144	158
154	500
164	1580
174	5000

Fig.5-8. The calibration chart of G.R.A.S. microphone provided by the company.

5.5. Experimental Results

This section includes the experiments performed in this research and contains acoustic measurements and effect of excitation voltage on the acoustic field. Further, mode shape of vibration is obtained by scanning the surface using laser vibrometer.

5.5.1. Acoustic Measurements

Measurements are performed for all the transducers as per the descriptions given in section 5.4. The results are presented in Tables 5-1 and 5-2. In order to check the uniformity of the resultant acoustic field, the measurements using the microphone are performed along the centreline at a different position rather than the mid-length as evident from the tables. Comparing these results reveals that the acoustic field is quite uniform along the length for the uniform-thickness transducer, though getting slightly weaker moving toward the ends of the tube, and the whole length along the centreline is at a high sound pressure level. All the measurements are performed at the same frequency of 43.22 KHz.

Similarly, for the transducer with one internal axial step, the acoustic field gets weaker moving toward the ends of the tube. All the measurements are performed at the same frequency of 41.70 KHz.

For the transducer with one external axial step, the acoustic field is stronger at approximately 1/3 of the length and is quite similar and uniform at other regions. All the measurements are performed at the same frequency of 37 KHz.

For the specimen with six internal circumferential steps, the acoustic field is very uniform along the length with the maximum around the mid-length. All the measurements are performed at the same frequency of 31.23 KHz.

Table 5-1. Acoustic measurement results at various positions along the length of the transducers.

	Microphone Position			
	Mid-Length Output SPL (dB)	**2-3mm off the Mid-Length**	**1/3 of the Length**	**Quarter-Length**
	Microphone Output Voltage (mV) SPL (dB)			
Uniform-Thickness	1240 161.89	960 159.67	980 159.84	700 156.92
One Internal Axial Step	840 158.51	580 155.29	200 146.04	240 147.62
One External Axial Step	260 148.32	240 147.62	560 154.98	260 148.32
Six Internal Circumferential Steps	2420 167.70	2340 167.40	1780 165.03	1760 164.93

For the specimen with two internal-external axial steps, the measurements using the microphone are performed at various distances off the mid-length all at the same frequency of 42.67 KHz. Once the measurement is done very close to the mid-length at approximately 2-3 mm away (which is approximately the start of the machined region) and once at the middle of the machined region (7-8 mm off the mid-length, approximately 1/3 of the length). The next time, it is done quite close to the end of the machined region. Table 5-2 includes the results revealing that the acoustic field, although at a very high level everywhere along the length, is weaker at the centre and higher off the mid-length specifically along the machined region and at the middle of

it. The reason lying behind this may be attributed to the mode shape of vibration. However, more details and discussions on this issue will be elaborately explained in the following chapter.

Table 5-2. Acoustic measurement results at various positions along the length of the specimen with two internal-external axial steps.

	Microphone Position			
	Mid-Length	**2-3mm off the Mid-Length**	**7-8 mm off the Mid-Length (middle of the machined region)**	**12-13mm off the Mid-Length (close to the end of the machined region)**
Microphone Output Voltage (mV)	1100	2300	2180	1400
Output SPL (dB)	160.85	167.25	166.79	162.94

5.5.2. Effect of Excitation Voltage on the Acoustic Field SPL for the Uniform-Thickness Transducer

In order to investigate the effect of excitation voltage on the sound pressure level, experiments are performed using various excitation voltages and the measurements are made accordingly. A few different voltages are applied including 18 V, 24 V, 36 V, 48 V and 80 V. Selection of these voltages is similar to that explained in the previous chapter. They are all below 60V assuming that a function generator module with a typical output of 3V is used together with the piezo driver with a gain of 20. These values are also chosen since these are normally common ratings for voltage input of many devices or appliances. The piezo driver used in this study has a

maximum of 100 V output using one of the voltage jumpers. Therefore, to be on the safe side not to damage the piezo driver, 80 V is chosen as a maximum threshold to investigate the effect of high voltage. Although any other voltage can be considered as long as it does not damage the piezo driver, it is believed that performing the experiments at these voltages will provide sufficient understanding of the voltage effect on the performance. All these measurements are performed at 42.36 KHz. The results are summarized in Table 5-3. It is evident that the increase in the excitation voltage increases the output voltage of the microphone and accordingly the sound pressure level in dB. The increase is not linear meaning that doubling the input voltage does not double the output voltage of the microphone. Since all the measurements are done at the same voltage range jumper and based on the piezo-driver catalogue, it has a fixed average output current for each of these three voltage ranges (250 mA for 100V jumper) [113], the power delivered to the transducers can be estimated using current and voltage as in Table 5-3.

Table 5-3. Effect of various input voltages on the sound pressure level.

	Excitation Voltage in V				
	18	**24**	**36**	**48**	**80**
Microphone Output Voltage in mV	620	740	980	1220	1560
SPL in dB	155.87	157.40	159.84	161.75	163.88
Average Power (W)	2.25	3	4.5	6	10

The important question as raised in the previous chapter is that whether increasing the input excitation voltage is a suitable method to increase the output or not. According to the simulations performed in the previous chapter, geometrical variations by means of introducing some steps can result in an amplification in the sound pressure level

with the same input power. Therefore, it is not actually worth increasing the voltage which implies increasing the power consumption of the transducer. To find a reliable answer to this question, it is required to experimentally validate the simulation results by achieving higher SPL using stepped-thickness specimens. This will be clarified at the end of this chapter.

5.5.3. Mode Shape of Vibration

The mode shape of vibration is obtained using the laser scanning vibrometer as discussed earlier. It is essential to get the mode shape so that it can be used for the sake of validation for the simulations and to make sure that the transducer is being driven at the intended mode shape based on the simulations. Fig.5-9 illustrates the mode shape of vibration at 43 KHz obtained experimentally for the uniform-thickness transducer. As evident in this figure, there are two peaks on the scanned surface of the transducer which are circled and labelled. More detailed discussion and comparison will be presented in the next chapter between this figure and the one from simulation as well as those of some other specimens. Thus, the validity of the simulations can be verified.

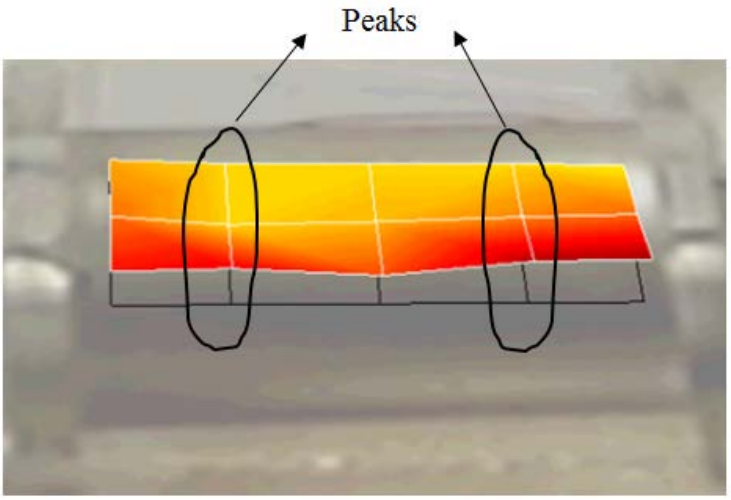

Fig.5-9. Mode shape of vibration for the uniform-thickness specimen at 43 KHz.

Fig.5-10 illustrates the mode shape of vibration for the transducer with one internal axial step at 41.5 KHz. As evident in this figure, there are two peaks on the scanned surface of the transducer which are circled and labelled. These two peaks are slightly more pronounced and more conspicuous than those of the uniform-thickness specimen as in Fig.5-8. Therefore, two peaks are observed as well as three troughs giving the axial wave number of five.

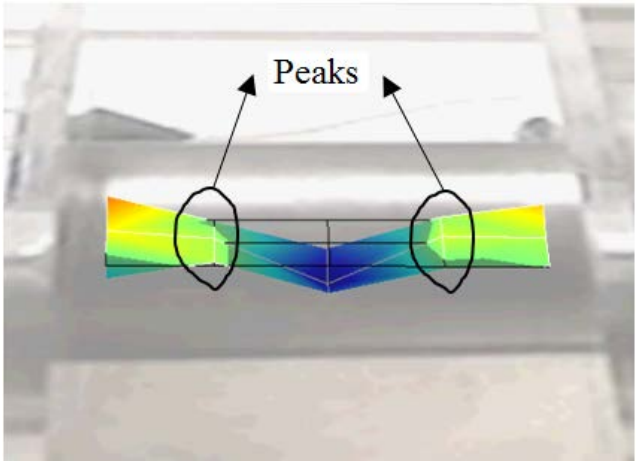

Fig.5-10. Mode shape of vibration for the specimen with one internal axial step at 41.5 KHz.

The mode shape of vibration for the transducer with one external axial step at 36.5 KHz is depicted in Fig.5-11. As evident in this figure, the amplitude of vibration is quite uniform along the length and only a small peak can be observed within the thin, machined region which is not that conspicuous. Therefore, the whole surface of the transducer vibrates uniformly as seen in this figure. Hence, axial and circumferential wave numbers are one and zero, respectively.

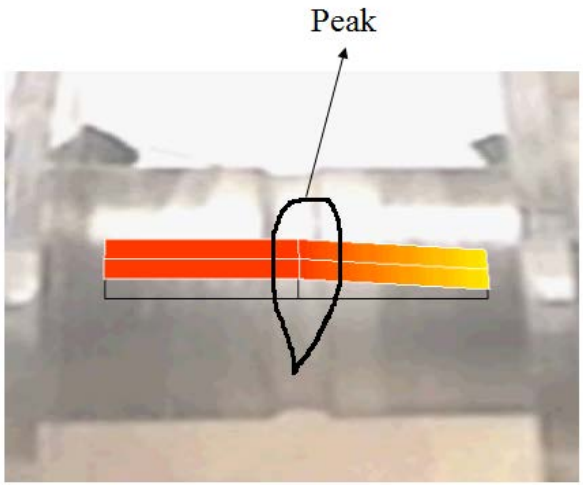

Fig.5-11. Mode shape of vibration for the specimen with one external axial step at 36.5 KHz.

The mode shape of vibration at 43 KHz for the transducer with two internal-external axial steps is illustrated in Fig.5-12. As evident in this figure, there are two peaks on the surface localized within the thin, machined regions which are circled and labelled.

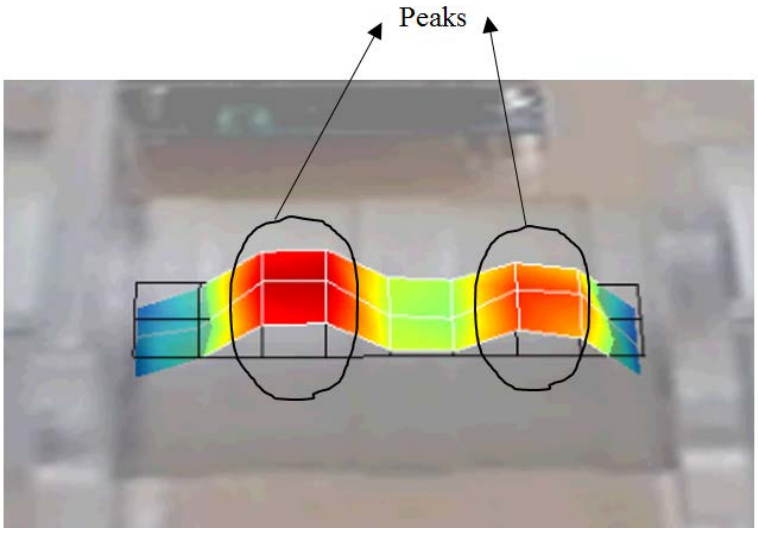

Fig.5-12. Mode shape of vibration for the specimen with two internal-external axial steps at 43 KHz.

The mode shape of vibration at 31 KHz is also depicted for the transducer with six internal circumferential steps as in Fig.5-13 from different views.

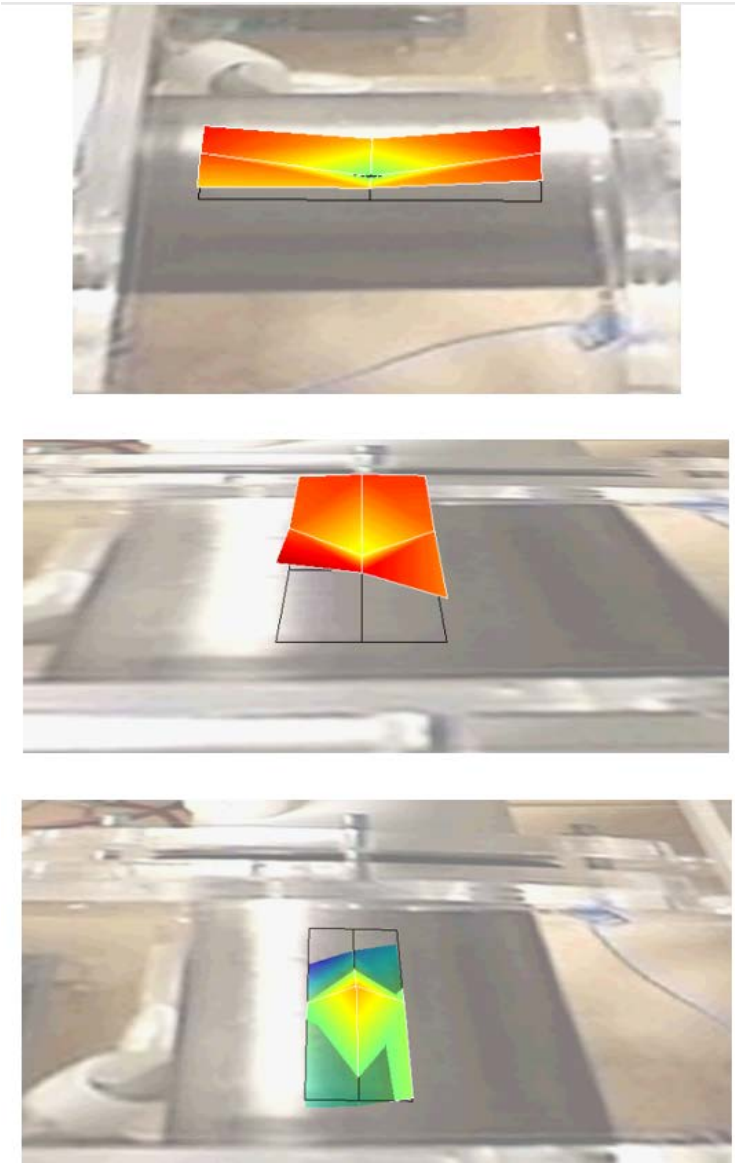

Fig.5-13. Different views of the mode shape of vibration for the specimen with six internal circumferential steps at 31 KHz.

As seen, while the length along the thin, machined region is at a peak, the neighbouring areas are at troughs and vice versa. The middle picture in this figure is for the case

when the thin, machined region is at a trough and the bottom picture corresponds to the case when it is at a peak. As evident in these figures, the axial wave number is one. The area scanned corresponds to approximately one machined area so that the same trend of the obtained mode shape can be attributed to the other regions resulting in six peaks around the circumference giving the circumferential wave number of six.

5.6. Closure

In this chapter, experimental results obtained from the acoustic measurements and laser scanning vibrometry were presented. However, detailed explanations and comparisons are left to the following discussion chapter. Acoustic measurements were performed at various positions along the length of the transducer to check the uniformity of the resultant acoustic field and also to make sure that the highest level of SPL is being measured since in some cases, the maximum does not occur exactly at mid-length. In addition, effect of the excitation voltage on the resultant acoustic field was experimentally obtained. Further, mode shapes of the vibration were obtained at the specific frequencies corresponding to the highest SPL. These mode shapes as well as the obtained level of acoustic field at various positions inside the transducer can be a good source of validation for the simulations performed in the previous chapter. Therefore, in the next chapter, the obtained results on mode shape, acoustic field and voltage effect from simulations will be compared with those from experiments and corresponding discussions will be presented. Table 5-4 is a summary of the obtained results.

It is worth going back to the question raised at the beginning of the chapter regarding introduction of steps or increasing voltage to amplify the acoustic field. The experiments performed in this chapter verified the conclusion based on the

simulations. A higher sound pressure level was achieved using designed geometrical variations for the same input power. The output was approximately two times higher than the uniform-thickness specimen at the same power consumption. Hence, introduction of steps proved to be a better alternative to increasing the excitation voltage and in turn the power consumption. Details and discussions on the conclusion made here will be explained in the next chapter.

Table 5-4. Summary of the results for all the specimens.

Int=Internal; Circum=Circumferential; Ext=External						
Specimen	**Specimen picture**	**Max Mic output Voltage (mV)**	**Max Output SPL (dB)**	**Corresponding Frequency (KHz)**	**Corresponding Mode shape**	**Pros & Cons of the Acoustic Field**
Uniform thickness		1240	161.89	43.22	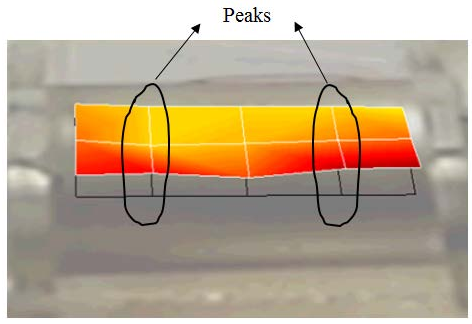	Good Uniformity
1 Int Axial step		840	158.51	41.70	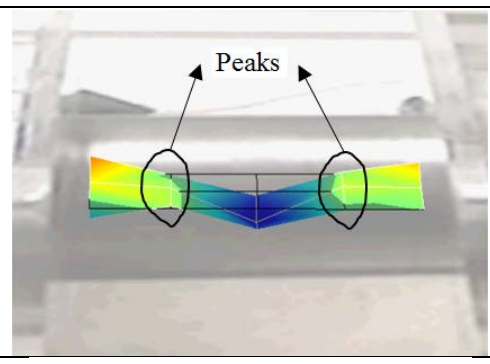	Weak Uniformity
1 Ext Axial step		560	154.98	37	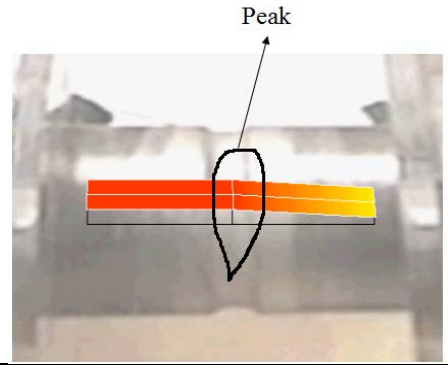	Average Uniformity
2 Int-Ext Axial steps	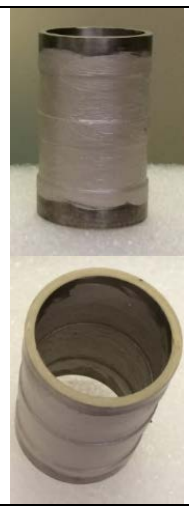	2300	167.25	42.67	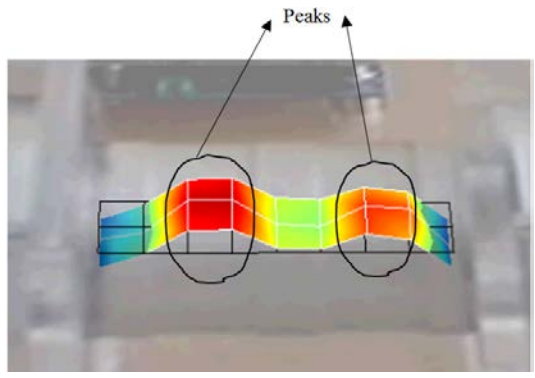	Average Uniformity, but higher SPL than other specimens everywhere along the length
6 Int Circum steps		2420	167.70	31.23	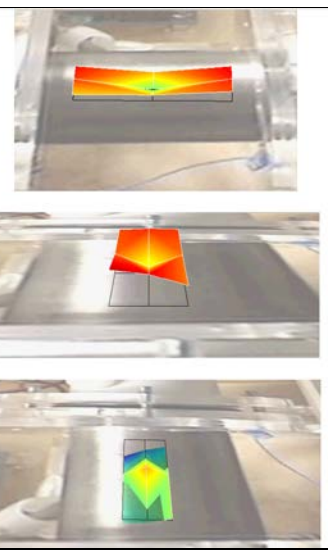	Very Good Uniformity and the highest SPL

Chapter 6: Discussion

6.1. Introduction

In the last two chapters, simulation and experimental results were presented. This chapter presents detailed explanations of the simulation and experimental results. Further, it can serve as a reasonable source of validation for the simulations performed in this study. Discussion is made on the acoustic field and the level of sound pressure, uniformity of the acoustic field, effect of the excitation voltage as well as mode shape of vibration to validate them.

6.2. Acoustic Field and its Uniformity

This section includes the discussions for the acoustic field and its uniformity for various transducers and is divided into sections for each of them.

6.2.1. Uniform-Thickness Transducer

The highest sound pressure level according to the simulations occurred at 43 KHz which was around 169 dB along the centreline at mid-length of the tube. Experimentally, the highest SPL was 162 dB obtained at mid-length and at 43.22 KHz. This reveals that there is reasonable agreement between the simulation and experimental results. While the frequency of the maximum SPL closely follows that of the experiments, the resultant acoustic field has been reasonably predicted by the simulations. Moreover, simulations show that the SPL along the centreline is in the range of 158-169 dB averaging at around 164 dB, while the experimental results revealed an average of around 159 dB along the length. This shows that there is a similar trend obtained from experiments and simulations for the level of sound

pressure from mid-length toward the tube ends along the centreline. In both cases, there are approximately a few dBs reduction in SPL; however, the acoustic field is uniform and high everywhere along the length.

6.2.2. Transducer with One Internal Axial Step

The highest sound pressure level according to the simulations occurred at 43 KHz which was around 167 dB occurring at mid-length along the centreline. The length along the centreline is at a fairly uniform range of SPL averaging at around 159 dB which is higher at the mid-length and gets weaker toward the ends of the tube. Experimentally, the highest SPL was around 159 dB occurring at the mid-length at 41.70 KHz. Measurements performed at various positions along the length proved that the acoustic field gets weaker to around 146 dB moving toward the ends of the tube. This reveals that there is excellent agreement between the simulation and experimental results for the frequency at which the maximum SPL occurs. Moreover, both experiments and simulations show that the acoustic field has a higher SPL at the mid-length which gets weaker moving toward the ends of tube. The average value of SPL along the mid-length from simulations agrees very well with the experimentally obtained maximum SPL of 159 dB.

6.2.3. Transducer with One External Axial Step

The highest sound pressure level according to the simulations occurred at 36 KHz which was around 172 dB occurring at a distance off the mid-length along the centreline. The length along the centreline is at a fairly uniform range of SPL averaging at around 164 dB. Experimentally, the highest SPL was 155 dB obtained 7-8mm off

the mid-length (approximately 1/3 of the length) and at 37 KHz. Measurements performed at various positions along the length proved that the acoustic field is quite uniform along the length except for 1/3 of the length which is higher in SPL. This reveals that there is excellent agreement between the simulation and experimental results for the frequency at which the maximum SPL occurs. Moreover, both experiments and simulations show that the acoustic field has a quite good uniformity along the length at various positions with a few dBs reduction compared to the maximum level. However, the SPL is over predicted by the simulations to a fairly great degree. The integrity of the tube and the electrode layer is influenced by machining and recoating. The silver epoxy layer put on top of the machined region is definitely not as uniform as the original silver electrode layer done by the manufacturer. It may damp the vibration and affect the acoustic radiation. In addition to these manufacturing and machining errors, measurement may be another source of error. The microphone is installed on a solid strap which is inserted into the tube along the centreline. Although measurements are performed several times, they are all done along the centreline. Slight movements of the tip of the microphone to a higher or lower position alter the output voltage of the microphone and correspondingly the output SPL. Since all the measurements for all the specimens are done similarly along the centreline and not at other positions closer to the transducer inner surface, the same was done for this specimen. Another factor may be the performance of the transducer itself which according to the manufacturer has a ±10% tolerance. In addition to these common sources of error for all the specimens, there is another important factor resulting in weaker performance of this specimen. According to the simulations, stress levels exceed the limit for the material of the transducer. The highest stress concentration was within the thin, machined region. Fig.6-1 illustrates the transducer after a few

tests. As expected, cracks were initiated from the thin region and grew toward the tube ends. This definitely affects the performance of the transducer and its vibration and results in lower SPL.

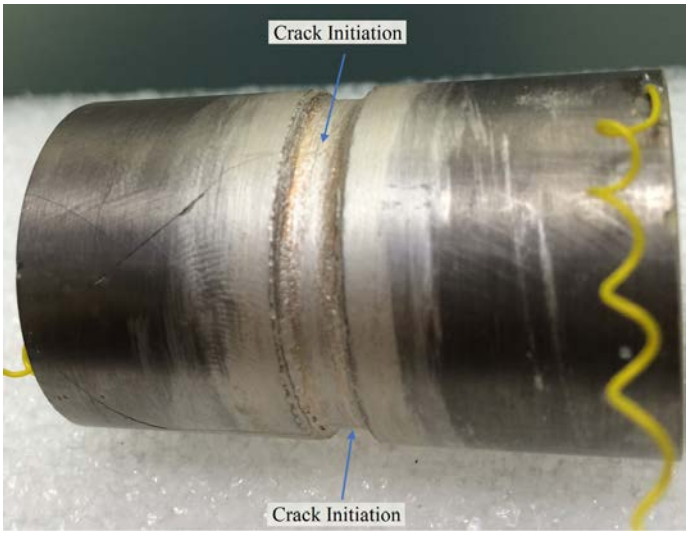

Fig.6-1. Crack initiation and propagation for the specimen with one external axial step.

6.2.4. Transducer with Two Internal-External Axial Steps

The highest sound pressure level according to the simulations occurred at two frequencies, 36 and 42 KHz, corresponding to 173 dB and 170 dB, respectively and along the centreline at a few millimetres off the mid-length and approximately at the middle of the thin region, respectively. Experimentally, the highest SPL was approximately 167.25 dB obtained along the centreline and the thin, machined region at 42.67 KHz (from the beginning until the middle of the machined region). Experiments showed fairly high SPL at around 36-37 KHz, However, not as high as that obtained at 42.67 KHz. This reveals that there is very good agreement between the simulation at 42 KHz and experimental results for both frequency and SPL. Moreover, according to the simulations at 42 KHz, the SPL along the centreline is in the range of 160-170 dB averaging at around 165 dB, while the experimental results

revealed an average of around 164 dB along the length. This reveals that the uniformity of the acoustic field along the length is reasonably predicted by the simulations and there is a very good agreement with the experimental results. In both simulations and experiments, the output SPL decreases a few dBs moving from the machined area toward the mid-length of the specimen or towards the ends of the tube. However, the acoustic field is quite uniform and high everywhere along the length.

6.2.5. Transducer with Six Internal Circumferential Steps

The highest sound pressure level according to the simulations occurred at 31 KHz which was around 204 dB. Experimentally, the highest SPL was around 168 dB obtained at the mid-length and at 31.23 KHz. This reveals that there is excellent agreement between the simulation and experimental results for the frequency at which the maximum SPL occurs. However, the SPL is considerably over predicted by the simulations. Both experiments and simulations revealed that the acoustic field is quite uniform and high along the length of the transducer at the centreline.

Over prediction has occurred for all the specimens that have been experimentally tested. However, for this specimen the over prediction is higher than the other specimens. The reason might be due to several factors. In addition to the common sources of error for all the specimens as stated above in 6.2.3 resulting in a few dBs discrepancy between simulation and experimental results, machining this specimen is believed to have more adverse effects on its performance compared to other specimens. More regions of this specimen are machined and then recoated compared to other specimens. This affects the uniformity and integrity of the transducer structure and influences its performance. Since circumferential steps were required for this

specimen, different cutting tools were employed. However, the best cutter used was not capable of creating completely sharp edges at the step boundaries and it has a very small radius of curvature. All these may contribute to the noticeable lower SPL obtained experimentally compared to the simulations. According to the simulations, the highest SPL belongs to this specimen and experimentally the highest SPL was obtained from this specimen.

6.2.6. Effect of Excitation Voltage on the Acoustic Field for the Uniform-Thickness Transducer

As mentioned in the previous chapters, one alternative to intensify the acoustic field is to increase the excitation voltage. Hence, it was investigated by both simulations and experiments. For the experiments, voltages of 18, 24, 36, 48 and 80 V were tested and for simulations, 18, 36, 48 and 200 V. The results are presented in Table 6-1. As in the table, increasing voltage in both experiments and simulations results in an increase in the acoustic field sound pressure level. Moving from 18 V to 36 V in both cases increases the SPL a few dBs. Increasing the voltage in experiments up to 80 V results in an increase in SPL to around 164 dB. Increasing beyond this point was not performed due to two reasons. First, the piezo amplifier we are using was set to 100 V output voltage and it was decided to keep away from the maximum value for the PCB protection. More importantly, the trend of increase in the SPL was observed to slow down compared to that for the lower voltages. As seen, by increasing voltage beyond 48 V, SPL changes slightly; however, power consumption of the transducer is getting higher and higher. As mentioned in the previous chapter and as will be discussed more in the following sections of this chapter, geometrical modifications proved to be a

suitable alternative to intensify the acoustic field without increasing the power consumption. Simulations were performed at some intervals to obtain the trend of the effect of excitation voltage on SPL. Nonetheless, since there is no restriction, it was decided to perform a simulation at 200 V input to investigate how increasing the voltage to a very high value will increase the SPL. According to the obtained results, increasing the power consumption considerably (through increasing excitation voltage from 48 to 200 V input) increases the SPL by 12 dB. According to the experiments, the increasing trend of SPL slows gradually. Moreover, simulations overestimate which means the increase in practice may be even lower than this value. To conclude, it seems an unsuitable alternative to increase the excitation voltage and simultaneously the power consumption to intensify the acoustic field. However, the effect of the excitation voltage is to increase the SPL but this trend slows down by increasing the voltage.

Table 6-2. Effect of excitation voltage on the sound pressure level.

	Excitation Voltage in V					
	18	**24**	**36**	**48**	**80**	**200**
Average Experimental SPL in dB	155.87	157.40	159.84	161.75	163.88	---
Average Simulation SPL in dB	163.68	---	169.7	172.2	---	184.6

6.3. Mode shape of Vibration

This section includes the discussions for the mode shape of vibration for various transducers and is divided into sections for each of them.

6.3.1. Uniform-Thickness Transducer

The mode shape of vibration was obtained at 43 KHz experimentally and also from simulations. Fig. 6-2 shows these mode shapes. The experimental mode shape consists

of three in-phase areas (one in between and two side areas) and two peaks which are labelled. A similar pattern is observed for the simulation mode shape; however, the simulation result is not in true scale and is in exaggerated scale to better identify the pattern whereas the pattern and peaks in experimental one are not as noticeable as that of the simulation. Checking the amplitude of vibration in the simulations shows that the maximum is less than a micron which is too small and may be the reason why the experimental pattern is not that conspicuous and is not as bold as simulation.

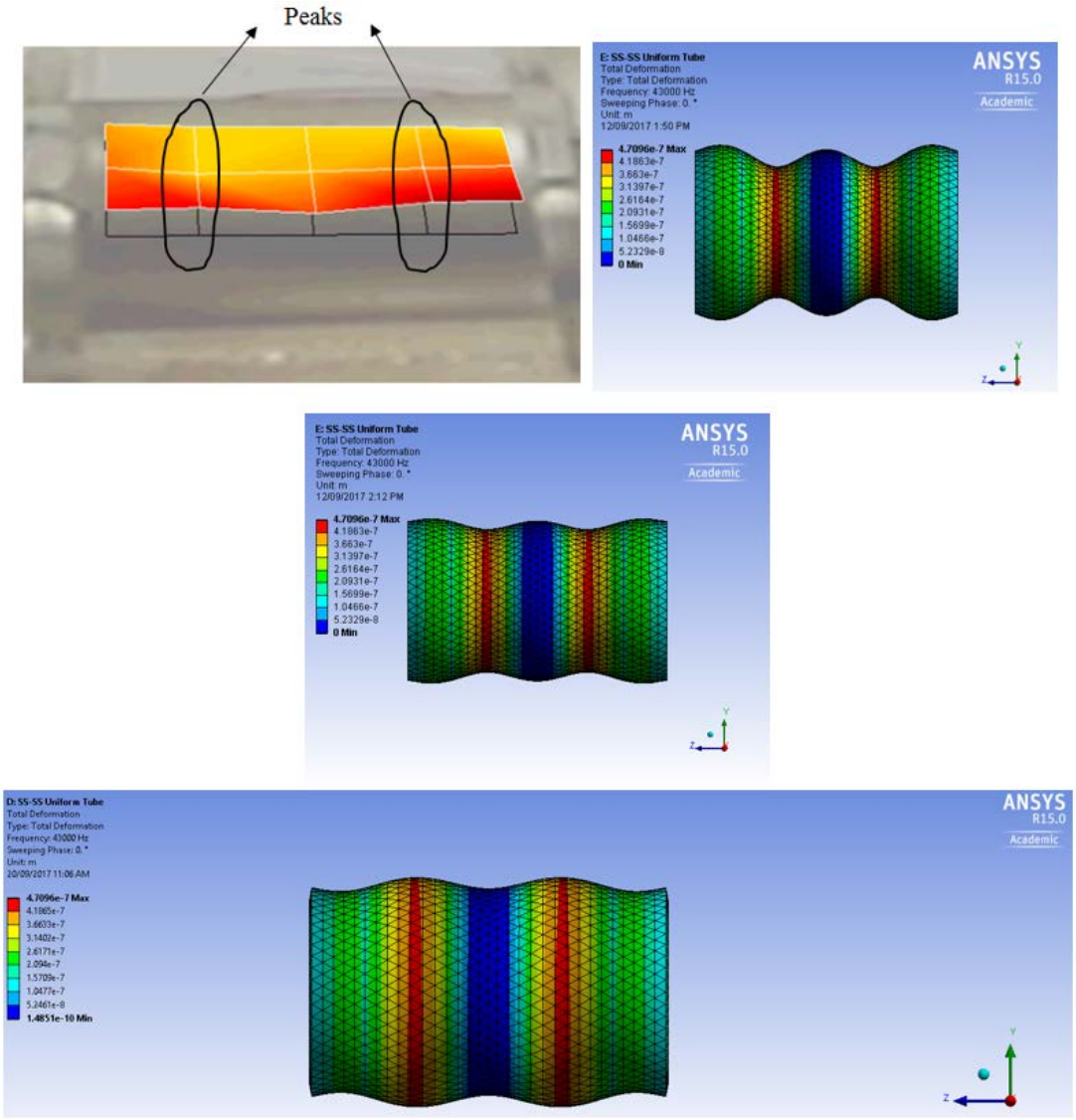

Fig. 6-2. Mode shape of vibration for uniform thickness specimen at 43 KHz; Top left; Experimental, Top right; Simulation in high exaggeration, Middle: Simulation in lower exaggeration; Bottom: Simulation in lower exaggeration when peaks and troughs change positions.

In Fig.6-2 the simulation mode shape is also depicted in the middle with lower exaggeration. Further, the same mode shape in lower exaggeration is depicted at the bottom when peaks and troughs change positions. This resembles the experimental one more than the other pictures with two peaks and three troughs giving the axial wave number of five. Hence, the pattern of the mode shape in simulations follows that of the experiments reasonably.

6.3.2. Transducer with One Internal Axial Step

The mode shape of vibration was obtained experimentally at 41.5 KHz and for simulations at 43 KHz. Fig.6-3 shows these mode shapes. It is worth noting that for the sake of better comparison, the same mode shape from simulation is illustrated at the bottom of this figure when the peaks and troughs change positions. Comparing these mode shapes shows a very good similarity and agreement between the obtained results. Axial wave number is five in both the experimental mode shape and the bottom photo of the simulation with two peaks and three troughs. The circumferential wave number is zero since the tube circumference is vibrating uniformly at any cross section. Therefore, the mode shape can be reasonably predicted by the simulations at the correct frequency.

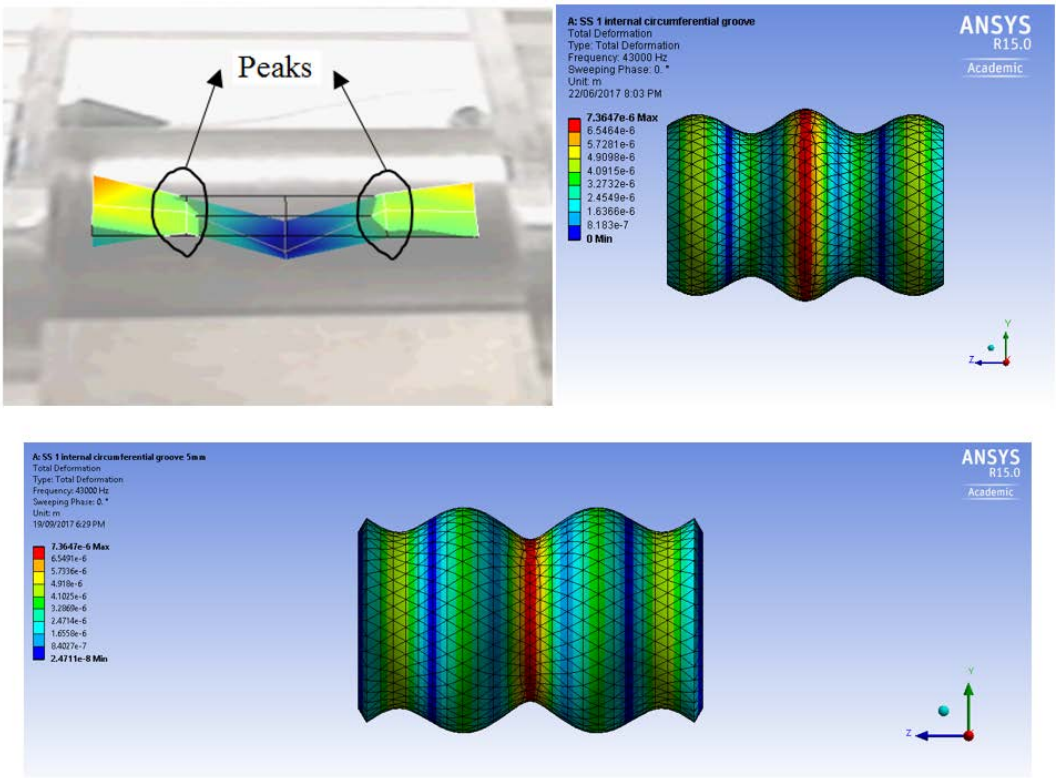

Fig.6-3. Mode shape of vibration for specimen with one internal axial step; Top left: Experimental 41.5 KHz, Top right: Simulation 43 KHz; Bottom: Simulation (The same mode shape when peaks and troughs change positions).

Another issue regarding the mode shape is that this is a similar mode shape with similar wave numbers as the uniform-thickness specimen in Fig.6-2. Based on simulations, the amplitude of vibration is an order of magnitude larger than the uniform-thickness specimen. This may be the reason why the experimentally obtained mode shape is more pronounced in this case with more noticeable peaks and troughs. The experimentally obtained frequency of this mode shape is 41.5 KHz which is slightly lower than 43 KHz for the uniform-thickness specimen. This slight reduction may be attributed to the reduction in thickness over the short length of the machined specimen. However, this slight reduction is not observed in the simulations and in both cases the frequency is 43 KHz. As seen from Figs.6-2 and 6-3, the location of the maximum vibration amplitude for the stepped specimen is shifted to the thin, machined region in

the middle of the specimen with higher amplitude. The acoustic filed SPL for the stepped specimen is a few dBs lower than the uniform-thickness specimen both experimentally (158.51 vs 161.89 dB) and from simulations (167.49 vs 169.7 dB) which shows a very good agreement. This reduction in SPL may be justified by the mode shape and vibration amplitude. The vibration amplitude is larger for the stepped specimen. However, comparing the mode shapes and distribution of the vibration amplitude from the colour-coded regions in Figs. 6-2 and 6-3 reveals that for the stepped specimen, the peaks and troughs are approximately of the same amplitude leading to phase cancellation and only the thin, machined region contributes significantly to acoustic radiation as observed by the acoustic field pattern in Fig.6-4. Nonetheless, for the uniform-thickness specimen, the peaks and troughs are in different ranges of vibration amplitude as can be seen from the colour-coded Fig.6-2. Therefore, a net contribution to acoustic generation is anticipated from these regions as obvious from the pattern in Fig.6-4. Hence, the resultant acoustic field is slightly stronger for the uniform-thickness specimen despite the fact that the stepped specimen has the same mode shape and larger amplitude of vibration.

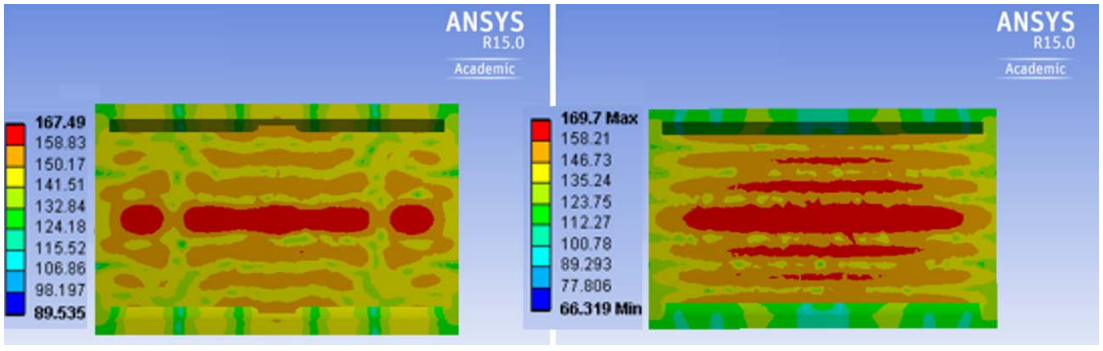

Fig.6-4. Acoustic fields for specimens: Left: With one internal axial step; Right: Uniform-thickness.

6.3.3. Transducer with One External Axial Step

The mode shape of vibration was obtained experimentally at 36.5 KHz and for simulations at 36 KHz. Fig.6-5 shows these mode shapes. It is worth noting that for the sake of better comparison, the same mode shape from simulation is illustrated at the bottom of this figure when the peak and trough change positions. Comparing these results shows that while the axial wave number is one in both cases, the circumferential wave number is zero since the tube circumference is vibrating uniformly. Therefore, the mode shape can be precisely predicted by the simulations at the correct frequency.

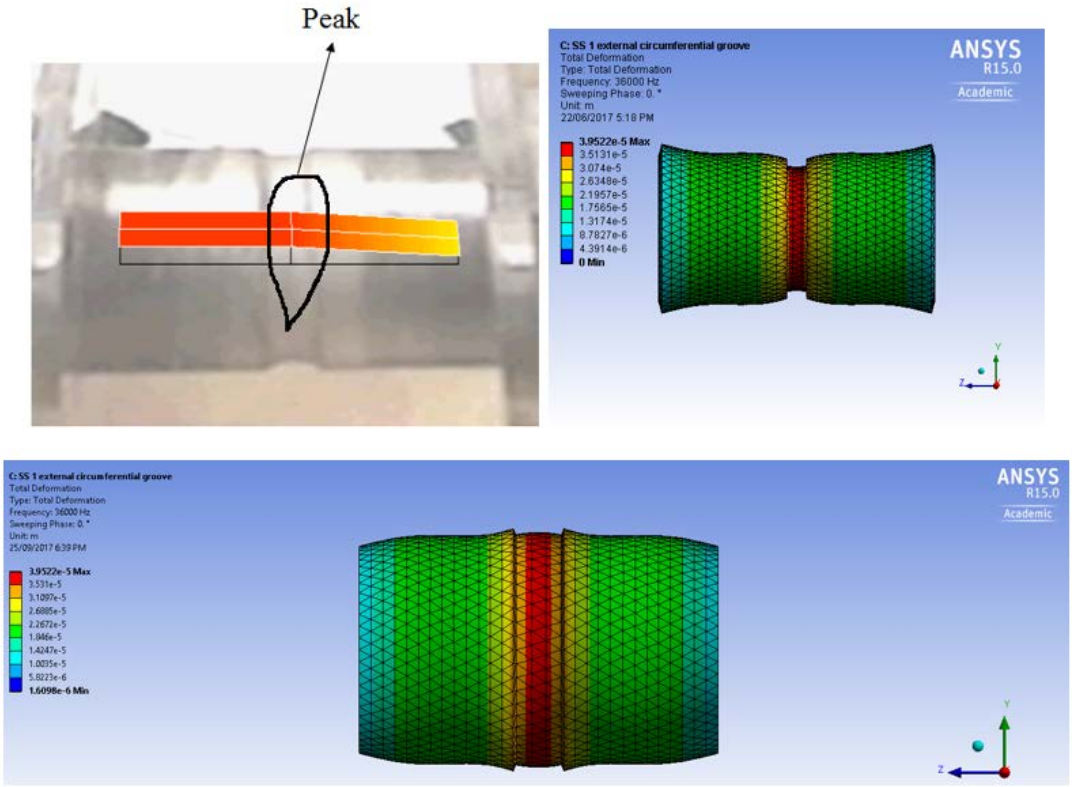

Fig.6-5. Mode shape of vibration for specimen with one external axial step; Top left: Experimental 36.5 KHz, Top right: Simulation 36 KHz; Bottom: Simulation (The same mode shape when peak and trough change positions).

6.3.4. Transducer with Two Internal-External Axial Steps

The mode shape of vibration was obtained experimentally at 43 KHz and for simulations at 42 KHz. Fig.6-6 shows these mode shapes. For the sake of better comparison, the same mode shape from simulation is illustrated at the bottom of this figure when the peaks and troughs change positions. Comparing these mode shapes shows a very good similarity and agreement between the obtained results. The axial wave number is five in both the experimental mode shape and the bottom photo of the simulation with two peaks and three troughs. The circumferential wave number is zero since the tube circumference is vibrating uniformly at any cross section. Therefore, the mode shape can be reasonably predicted by the simulations at the correct frequency. Another issue regarding the mode shape is that this is a similar mode shape with the same wave numbers as the uniform-thickness specimen in Fig. 6-2. According to the simulations, the amplitude of vibration is in the same order of magnitude as the uniform-thickness specimen but is twice larger. The mode shapes obtained experimentally also reveal more conspicuous peaks and troughs compared to the uniform-thickness specimen as evident from Figs.6-2 and 6-6. This shows that the vibration is localized within the thin, machined regions with higher amplitudes. Therefore, the resultant acoustic field should be stronger with higher SPL than that of the uniform-thickness specimen. Based on the experimental results, this has been verified (167.25 dB vs 161.89 dB). However, this increase according to the simulations is not that noticeable from 169.7 for the uniform-thickness specimen compared to 169.99 for the stepped one.

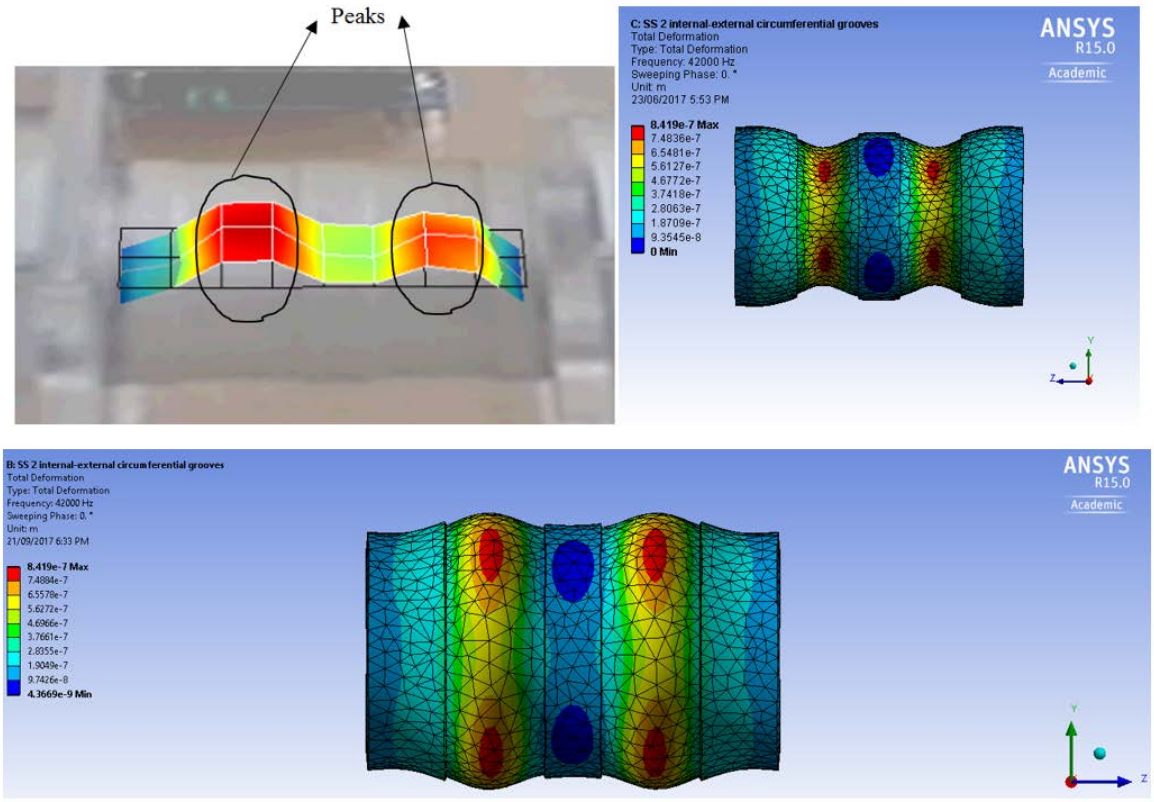

Fig.6-6. Mode shape of vibration for specimen with two internal-external axial steps; Top left: Experimental 43 KHz, Top right: Simulation 42 KHz; Bottom: Simulation (The same mode shape when peaks and troughs change positions).

6.3.5. Transducer with Six Internal Circumferential Steps

The mode shape of vibration was obtained experimentally and also from simulations at 31 KHz. Fig.6-7 shows these mode shapes. Various views of the experimental mode shape are included as well as various views and cut sections from simulations to facilitate comparison. Comparison between these mode shapes reveals that the mode shape is accurately predicted by the simulations.

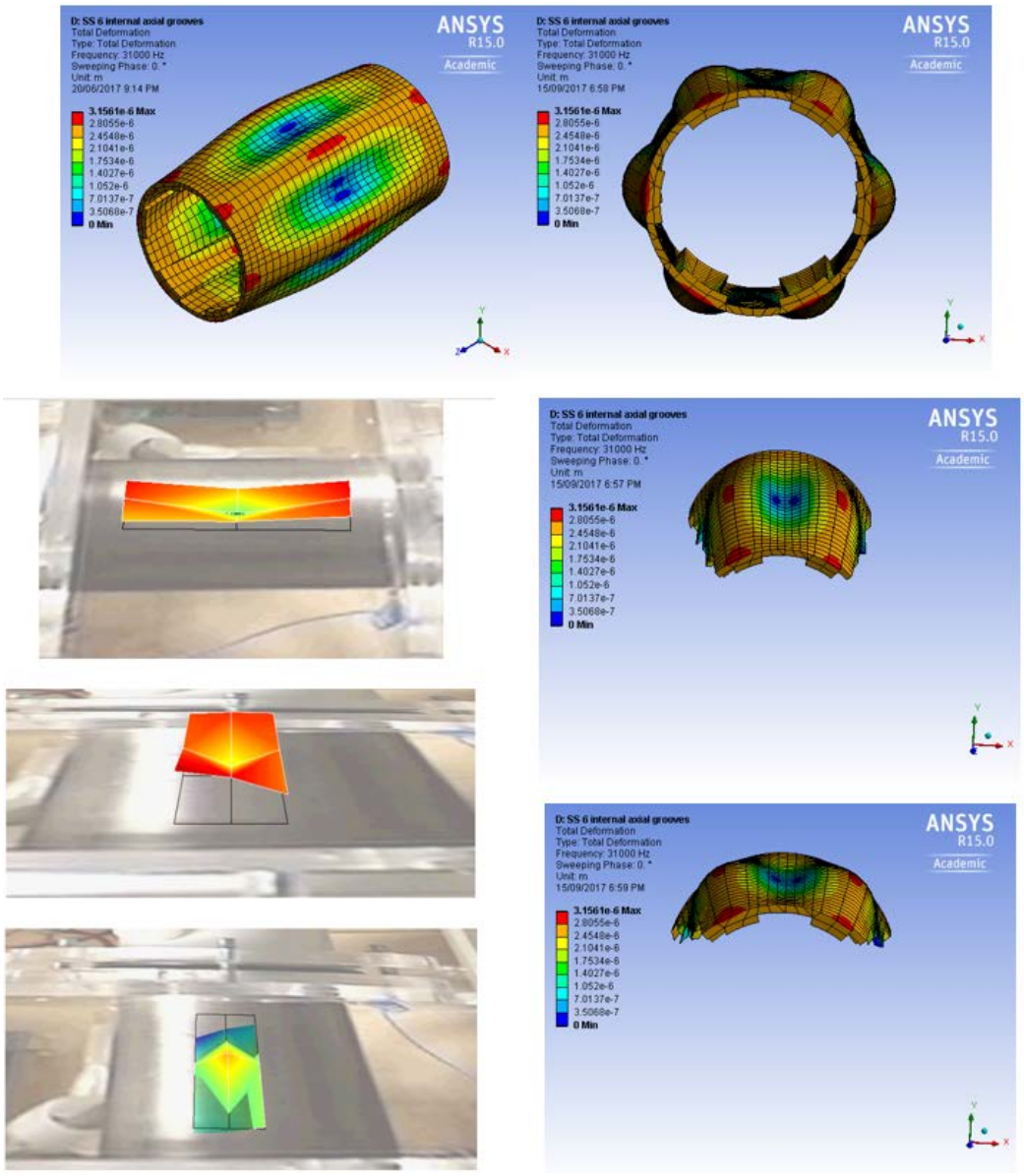

Fig.6-7. Mode shape of vibration for specimen with six internal circumferential steps at 31 KHz; Top: Simulation; Bottom left: Experimental, Bottom right: Cut sections from simulation.

Axial wave number is one as observable from simulations and experiments. The area scanned experimentally corresponds to approximately one machined area so that the same trend of the obtained mode shape can be attributed to the other regions resulting in six peaks around the circumference giving circumferential wave number of six which is also predicted by the simulations.

6.4. Closure

In this chapter, the obtained experimental and simulation results were discussed and compared. For all the cases where experiments were done, simulation results were compared with them for the sake of validation. Table 6-2 summarizes the results from experiments and simulations and facilitates comparison. Based on the results and discussions and as evident in the table, it can be concluded that simulations are in a very good agreement with experiments for the frequency and mode shape of vibration. Further, SPL can be reasonably predicted by the simulations. While for some specimens, the SPL was accurately predicted by the simulations with a few dBs deviation from the experiments, for some specimens SPL was overestimated more noticeably. This discrepancy may be attributed to several factors as elaborately explained. For one of the specimens, the crack initiation and propagation resulted in weak performance of the transducer and considerable deviation from the simulation result. However, this was expected since the stress exceeded the material limit. This test was performed to check the validity of the simulations for stress prediction.

An important conclusion from these results and comparisons is that the same level of SPL for the uniform tube can be easily obtained using some stepped transducers at a lower frequency. This is definitely better from the viewpoint of fatigue and overheating of the transducer. It was shown that it is feasible to amplify the acoustic field at the same input power by introducing steps. It is only required to carefully devise the transducer configuration and identify steps specifications based on the mode shape and frequency of the uniform-thickness specimen within the desired range of frequencies suitable for the intended application. Cylindrical geometry of the transducer considerably affects the focus of the resultant acoustic field. Suitable

localization of vibration with larger amplitudes will also assist. However, stress distribution must also be taken into account for such design process.

Table 6-2. Summary and comparisons between Simulations and Experiments.

Int=Internal; Circum=Circumferential; Ext=External; Exp=Experiment; Sim=Simulation							
Specimen	**Specimen picture**	**Max Output SPL (dB)**		**Corresponding Frequency (KHz)**		**Corresponding Mode shape**	
		Exp	**Sim**	**Exp**	**Sim**	**Exp**	**Sim**
Uniform thickness		161.89	169	43.22	43	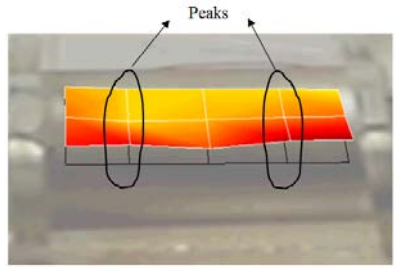	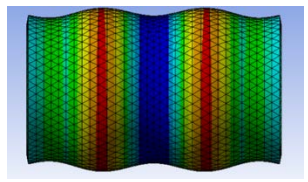
1 Int Axial Step		158.51	167	41.70	43	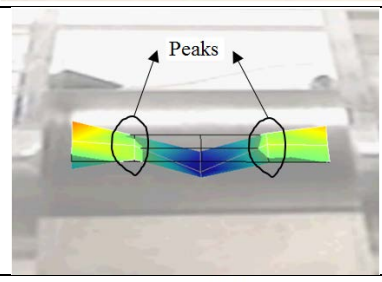	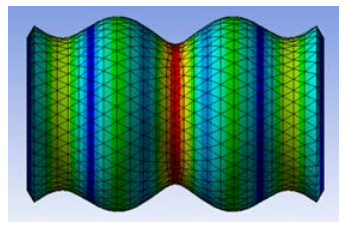
1 Ext Axial Step		154.98	172	37	36	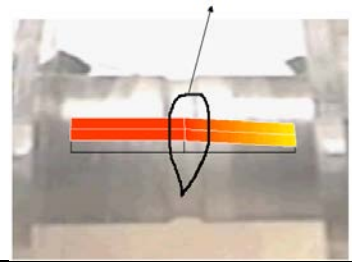	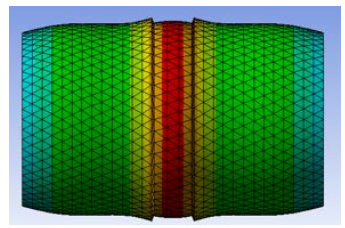
2 Int-Ext Axial Steps	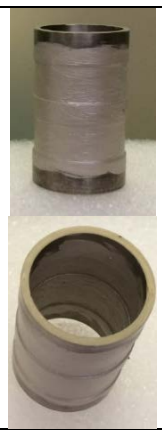	167.25	170	42.67	42	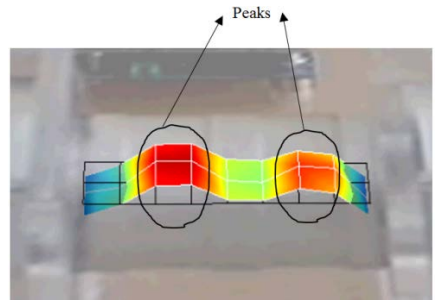	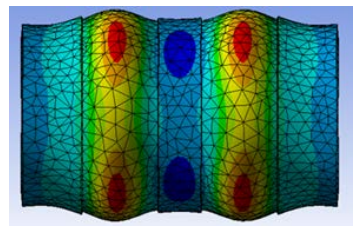
6 Int Circum Steps		167.70	204	31.23	31	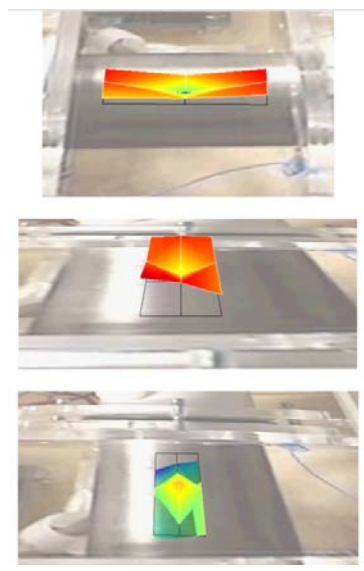	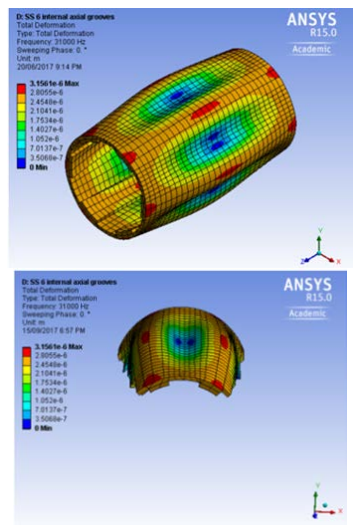

Chapter 7: Droplet Atomization Transducer

7.1. Introduction

This chapter will be devoted to the application of the proposed transducer as the second stage transducer for water particle disintegration in atomization. Since the design considerations for the intended application for atomization were taken into account, it is required to investigate the performance of the transducer and the interaction between the generated acoustic field and the droplets. Hence, in this chapter, the transducer will be experimentally tested to scrutinize its performance and effect on water droplets produced by a nebuliser. The droplets from a nebuliser are directed through a pipe inside the transducer to investigate further breakup of the droplets to smaller ones due to the exposure to the acoustic field. The experimental set-up is modified with some added components to facilitate the experiments for the application. These will be explained in more detail in the following sections of this chapter.

7.2. Preliminary Experiments

To study the effect of the acoustic field from the proposed transducer (with higher SPL at the same input power) on the droplets, the experimental set-up as in Fig. 5-1 was used and the input was connected to the air-droplet mixture. The outlet was measured by a Spraytec RTsizer as in Fig.7-1. It comes with its own software and the laser beams emitted by the lens of the device pass through the air-droplet mixture at the outlet and measure particle size and its distribution.

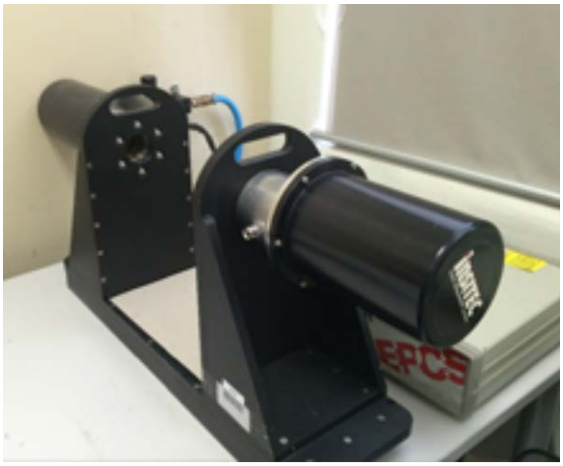

Fig.7-1. Spraytec RTsizer.

In order to get consistent results from the same experiments and eliminate the probable effect of the environment temperature, it was decided to keep the temperature constant. Further, in the first trials which were done immediately after each other, but without any temperature control mechanism, the temperature was approximately constant. However, inconsistent results were obtained. It was concluded that very small changes in the location of the outlet in front of the laser beams affects the reading of the Spraytec software. Hence, some marks were put on the box to perform all the experiments at the same place. Moreover, very slight changes in the height of the outlet pipe (even a few millimetres) was found to affect the reading. Thus, it was decided to compare each set of experiments with the ultrasound on and off separately and perform the acoustic measurement first, take the microphone out, perform the test with ultrasound on. Then, the outlet pipe was not moved at all and only the ultrasound was turned off. Therefore, the effects of the location of the box and its outlet pipe on the reading of the Spraytec were eliminated.

To keep the temperature constant, the experimental set-up was modified by adding two resistance heaters, a fan, a rheostat and temperature sensors at different locations inside the set-up box. A photo of the new modified set-up is depicted in Fig.7-2. As

seen, two resistance heaters are added to heat the box and to monitor the temperature at different locations, three sensors are installed at the inlet, the outlet and one is normally positioned beneath the transducer. To be able to efficiently control the heaters, a rheostat is also installed. A fan is also considered for better circulation of the hot air around the heaters. The location of the fan was found to be at its current position by trial and error to create more uniform temperatures around the transducer inside the box. The piezo driver module was enclosed in a box inside the main box to protect it against high temperatures and some holes were considered for ventilation of the module. During the first experiments, condensation occurred in the pipes and inside the transducer. Hence, temperature was increased to achieve a hotter surface for the pipe and transducer to eliminate or reduce condensation. Condensation extensively affected the performance of the transducer.

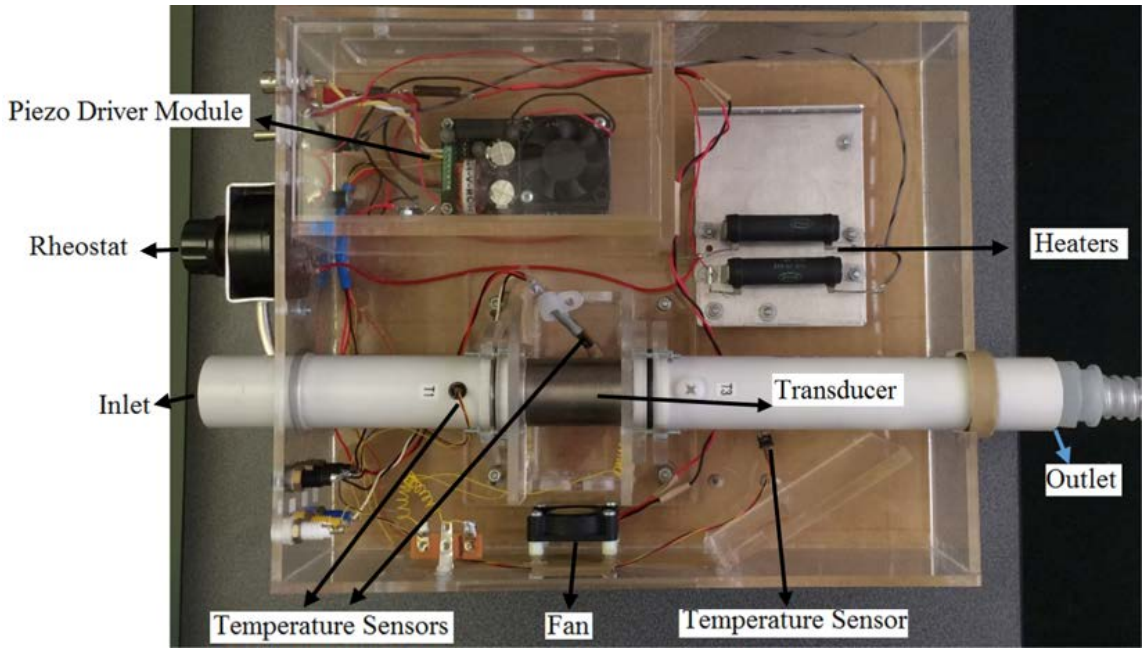

Fig.7-2. New modified set-up.

Further, Fig.7-3 illustrates the overall layout of the experimental set-up and Fig.7-4 is the schematic layout of the set-up. As seen, air flows through a valve to the air flow meter so that the air flow can be controlled. Subsequently, it goes through a heater which is supplied by the analogue power supply. The heated air is then mixed with the droplets from the nebuliser and flows through the transducer set-up where it is exposed to the acoustic field. Finally, the air-droplet mixture flows through the outlet towards the laser beams of the Spraytec where the size measurement is performed. The temperature sensors are reading the temperature at the inlet and beneath the transducer to make sure that temperature is kept constant during different experiments. The sensors are connected to a voltmeter. They are calibrated in such a way that the reading of the voltmeter for 1V corresponds to one degree Celsius.

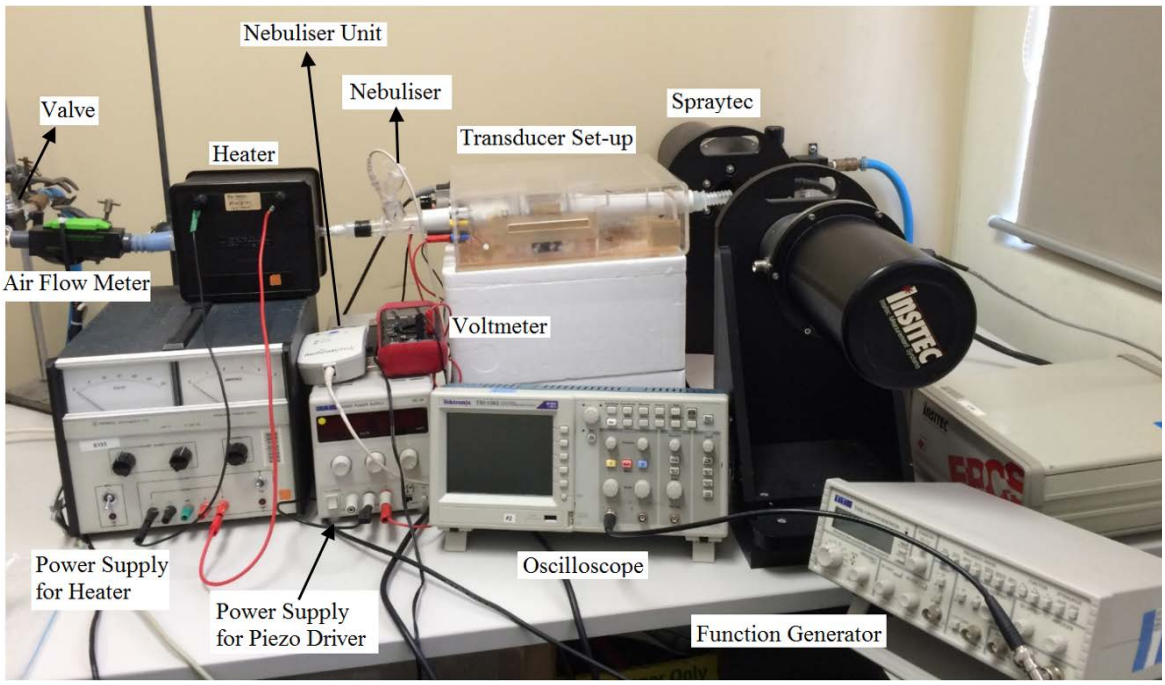

Fig.7-3. Overall layout of the experimental set-up.

Fig.7-5 depicts a typical droplet distribution graph from the Spraytec. However, to facilitate interpreting this graph to obtain the statistics regarding the droplet size and distribution, the Spraytec software is set to give the results in numbers as a chart. To this aim, DV(10), DV(50) and DV(90) are reported which are commonly used to report these statistical results. DV(10) means 10% of droplets are smaller than the value stated. DV(50) and DV(90) are similarly defined.

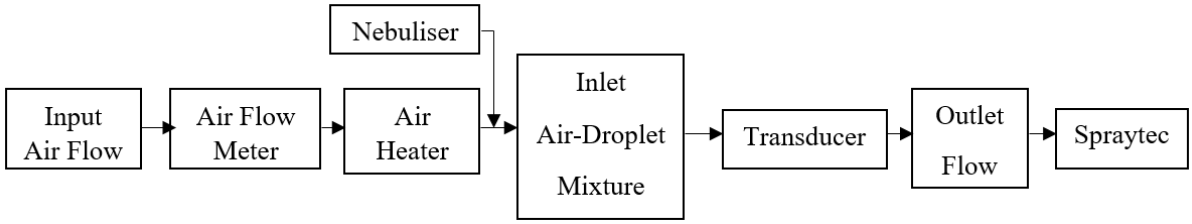

Fig.7-4. Schematic of the experimental set-up.

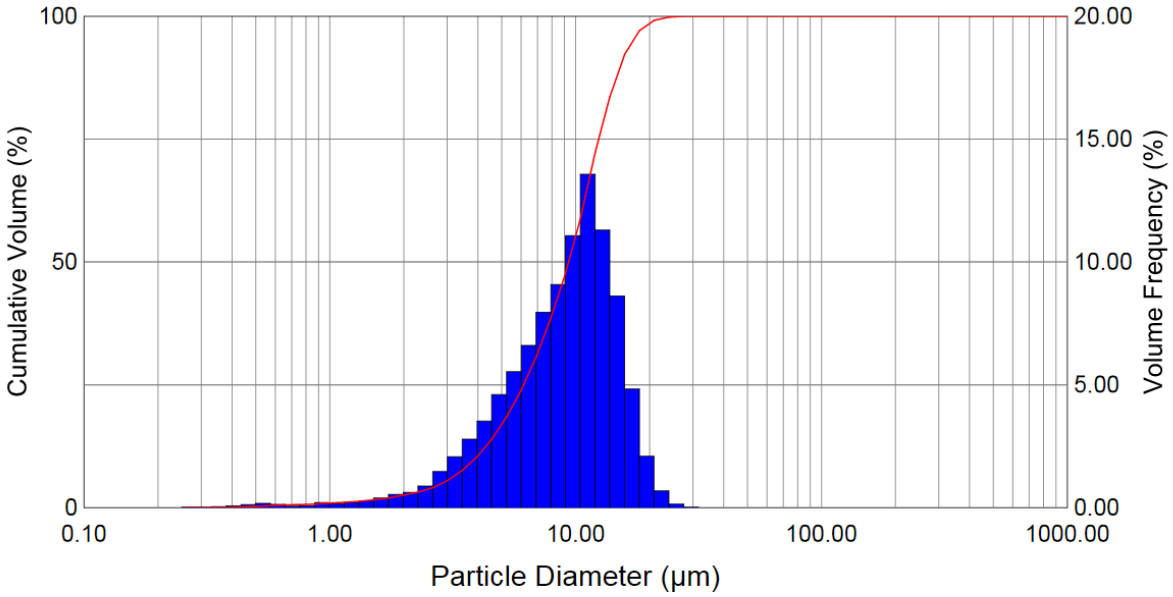

Fig.7-5. Typical droplet distribution from the Spraytec device.

In the first trials with transducers having lower SPL (transducers with one internal or external axial step, uniform-thickness transducer), no noticeable improvement was observed. Sometimes, a slight improvement and sometimes no change and sometimes slight deterioration was observed. During these trials, as already stated, condensation occurred. Hence, the temperature was kept around $30^{o}C\pm1$ for the box as well as the inlet. This was done to avoid condensation on the surfaces of the pipes and transducer. The effect of the temperature could also be investigated on the results. This can be done as a future work. Temperature was increased to eliminate or diminish condensation and also to be able to keep the temperature constant for all the experiments. However, condensation still occurred after running the experiments for quite some time. Hence, experiments were not performed continuously to avoid formation of water on the transducer surface which hinders its performance. Another important factor found out to be influential was the airflow. The airflow was varied from 0.5-3L/min. For the lower limit, the droplets could not suitably reach the laser beams of the Spraytec and did not have the required momentum to pass through the pipes and reach the laser beams. For higher values, nearly all the droplets vaporized and the device did not report any value. Hence, the suitable airflow was found to be 1.5L/min. Higher flow rates resulted in bigger droplets. The reason might be higher coalescence of the droplets at higher flow rates. Thus, all the experiments were performed at the same 1.5L/min. In addition, it was understood that the SPL should exceed a threshold to be influential on the droplet size as reported in the literature [1]. The transducer used by [1] was the same as in [15] with fixed frequency and variable input power, generating maximum of 155 dB at full power. Nonetheless, reviewing their obtained results, there was no improvement in the size of droplets (Appendix 4, A 4.3 [1]). Moreover, acoustic fields of 160 dB were applied to single droplets and it was concluded that the evaporation rate of droplets would be affected and increased

[103]. However, lower values of 150 dB did not prove useful. Hence, the threshold for SPL is estimated to be at least above 160 dB.

7.3. Results

Most of the tests were performed using the uniform-thickness transducer as well as the transducer with two internal-external axial steps. Some of the results are presented in this section. Uniform-thickness transducer was installed in the set-up, flow rate was set to 1.5L/min and temperature was set to 30 ^{o}C±1. First, acoustic measurement was performed to get the highest SPL. As explained in the previous chapters, the transducer performance varied slightly test by test. The frequency at which the maximum SPL occurred as well as the maximum SPL itself changed slightly. Therefore, it was first required to obtain the maximum SPL and immediately after, perform the tests with the droplets. The reason is that the transducer gets off resonance shortly after turning on and this results in weak performance of the transducer. A dynamic resonance control system may be required. However, it was tried to perform the droplet tests as fast as possible after the acoustic measurements to avoid such problem. Further, as stated before, even slight changes in the location of the outlet pipe made changes to the Spraytec reading. Therefore, tests without ultrasound were performed after the tests with ultrasound by only turning off the transducer and no change in the set-up position. This makes Spraytec readings reliable. All the tests were performed for the duration of one minute. As the first trial with the uniform-thickness transducer at 42.64 KHz and 36 V input, the maximum output of the microphone was 1.18 V corresponding to 161.46 dB. Fig.7-6 shows the obtained results for the droplet size from Spraytec for two cases with and without ultrasound. As evident, there is slight improvement in the droplet size. 90% of the droplets are smaller than 7.66 µm with ultrasound and smaller

than 7.81 µm without ultrasound. The improvement is negligible and it can be said that there is no change.

With Ultrasound

****

Process Control Variable Results

Value (Avg)	Max	Min	Variable Title
2.189	3.145	0.709	Dv(10.0) (µm)
4.369	4.680	3.307	Dv(50.0) (µm)
7.656	8.797	6.520	Dv(90.0) (µm)

Without Ultrasound

****

Process Control Variable Results

Value (Avg)	Max	Min	Variable Title
2.245	2.736	0.992	Dv(10.0) (µm)
4.421	4.677	4.022	Dv(50.0) (µm)
7.812	8.693	6.792	Dv(90.0) (µm)

Fig.7-6. Droplet size distribution for the test with uniform-thickness transducer at 42.64 KHz; Top: With ultrasound; Bottom: Without ultrasound.

The next time with the same transducer but at 42.76 KHz and 36 V input, the maximum output of the microphone was 1 V corresponding to 160 dB. Fig.7-7 shows the obtained results. As evident, there is slightly more improvement in the droplet size compared to the previous trial. 90% of the droplets are smaller than 6.70 µm with ultrasound and smaller than 7.17 µm without ultrasound.

With Ultrasound

****

Process Control Variable Results

Value (Avg)	Max	Min	Variable Title
1.969	3.017	0.541	Dv(10.0) (µm)
3.930	4.412	2.463	Dv(50.0) (µm)
6.697	7.623	5.723	Dv(90.0) (µm)

Without Ultrasound

****

Process Control Variable Results

Value (Avg)	Max	Min	Variable Title
2.040	2.854	1.109	Dv(10.0) (µm)
4.101	4.371	3.608	Dv(50.0) (µm)
7.168	8.856	6.557	Dv(90.0) (µm)

Fig.7-7. Droplet size distribution for the test with uniform-thickness transducer at 42.76 KHz; Top: With ultrasound; Bottom: Without ultrasound.

The improvement is around 0.5 µm. However, as mentioned before, in some trials slight improvement was obtained, in some cases no improvement and sometimes, even deterioration. Therefore, a higher level of SPL might be helpful. To this aim, some tests were performed using the transducer with two internal-external axial steps. At 43.06 KHz and 36 V input, the maximum output of the microphone was 2.08 V corresponding to 166.38 dB. Fig.7-8 shows the obtained results. As evident, there is slight improvement in the droplet size. 90% of the droplets are smaller than 7 µm with ultrasound and smaller than 7.55 µm without ultrasound. The improvement is more than the case with the uniform-thickness transducer.

With Ultrasound

****

Process Control Variable Results

Value (Avg)	Max	Min	Variable Title
2.434	3.297	1.964	Dv(10.0) (µm)
4.327	4.852	3.963	Dv(50.0) (µm)
6.997	7.793	6.267	Dv(90.0) (µm)

Without Ultrasound

****

Process Control Variable Results

Value (Avg)	Max	Min	Variable Title
2.385	3.236	1.307	Dv(10.0) (µm)
4.390	4.595	3.945	Dv(50.0) (µm)
7.549	8.800	6.564	Dv(90.0) (µm)

Fig.7-8. Droplet size distribution for the test with the transducer with two internal-external axial steps at 43.06 KHz; Top: With ultrasound; Bottom: Without ultrasound.

In another trial with the same transducer but at 43.18 KHz and 36 V input, the maximum output of the microphone was 2.68 V corresponding to 168.58 dB. Fig.7-9 shows the obtained results. Slightly more improvement in the droplet size is observed compared to the previous trial.

With Ultrasound

****

Process Control Variable Results

Value (Avg)	Max	Min	Variable Title
3.463	4.078	3.202	Dv(10.0) (µm)
4.702	4.894	4.569	Dv(50.0) (µm)
7.732	8.987	6.486	Dv(90.0) (µm)

Without Ultrasound

****

Process Control Variable Results

Value (Avg)	Max	Min	Variable Title
3.314	3.664	2.845	Dv(10.0) (µm)
4.818	5.058	4.585	Dv(50.0) (µm)
8.505	9.521	7.614	Dv(90.0) (µm)

Fig.7-9. Droplet size distribution for the test with the transducer with two internal-external axial steps at 43.18 KHz; Top: With ultrasound; Bottom: Without ultrasound.

Using the same transducer but at 42.85 KHz and 36 V input, the maximum output of the microphone was 1.70 V corresponding to 164.63 dB. Fig.7-10 shows the obtained results. In this case, there is approximately 1 µm improvement in the size of 90% of the droplets.

With Ultrasound

****

Process Control Variable Results

Value (Avg)	Max	Min	Variable Title
4.720	5.450	3.708	Dv(10.0) (µm)
5.496	6.270	4.956	Dv(50.0) (µm)
6.978	9.264	5.945	Dv(90.0) (µm)

Without Ultrasound

****

Process Control Variable Results

Value (Avg)	Max	Min	Variable Title
4.748	6.084	4.452	Dv(10.0) (µm)
5.471	7.004	5.139	Dv(50.0) (µm)
7.958	9.700	5.899	Dv(90.0) (µm)

Fig.7-10. Droplet size distribution for the test with the transducer with two internal-external axial steps at 42.85 KHz; Top: With ultrasound; Bottom: Without ultrasound.

In the last experiment with the same transducer at 42.64 KHz and 36 V input, the maximum output of the microphone was 2.72V corresponding to 168.71 dB. Fig.7-11 shows the obtained results. It is observed that there is even more improvement in the droplet size compared to the previous trial. 90% of the droplets are smaller than 7.83 µm with ultrasound and smaller than 9.20 µm without ultrasound.

With Ultrasound

****

Process Control Variable Results

Value (Avg)	Max	Min	Variable Title
2.761	3.481	1.470	Dv(10.0) (µm)
4.397	4.676	3.884	Dv(50.0) (µm)
7.833	10.030	6.725	Dv(90.0) (µm)

Without Ultrasound

****

Process Control Variable Results

Value (Avg)	Max	Min	Variable Title
3.435	3.737	2.406	Dv(10.0) (µm)
4.662	5.027	4.342	Dv(50.0) (µm)
9.199	10.619	7.635	Dv(90.0) (µm)

Fig.7-11. Droplet size distribution for the test with the transducer with two internal-external axial steps at 42.64 KHz; Top: With ultrasound; Bottom: Without ultrasound.

7.4. Closure

In this chapter, both the uniform-thickness and stepped transducers were used to investigate their performance in one of the intended applications as a second stage transducer for atomization. Experiments were performed at a constant temperature to eliminate the effect of temperature on the results. Further, to avoid getting off resonance since there is no dynamic resonance controller, the experiments were performed as quickly as possible. According to the literature, acoustic fields of 160 dB increased the evaporation rate of droplets while lower values of 150 dB did not make any improvements [103]. Further, no noticeable improvement was observed for the size of droplets in a stream of droplets exposed to an acoustic field of around 155 dB [1]. However, using the transducers, higher SPLs were obtained. Experiments were performed several times and some of them were presented in this chapter. While for the uniform-thickness transducer with approximately 160 dB, the improvement in droplet size is not noticeable, for the stepped transducer with acoustic fields above 160 dB, even more than one micron improvement in the size of 90% of the droplets was obtained. This seems promising and implies that it is possible to use such transducers

to achieve smaller sizes of droplets at only a few Watts of power which may be extremely important for some drug delivery applications. Another conclusion that can be drawn is related to the effect of the acoustic field on specific sized droplets. Checking all the presented results, it can be easily understood that for all the cases, the effect of the acoustic field was more noticeable for DV(90) meaning that larger droplets are more influenced by the acoustic field. Equation (3-63) predicts the same trend. According to this equation, larger droplets result in smaller $\frac{U_{p0}}{U_0}$, which indicates higher relative movement between the droplets and the air particles. This can facilitate the evaporation process of larger size droplets. Further, Equation (3-67) predicts the same trend and better evaporation of larger size droplets due to better heat transfer and higher relative movement caused by smaller Stokes number. To target other size droplets, the same approach can be followed to achieve transducers operating at other frequencies with maximum SPL. This may result in evaporation of smaller size droplets as well. Alternatively, a bundle of such transducers may be employed each operating at a particular frequency targeting specific size droplets.

Chapter 8: Conclusion & Future Works

8.1. Conclusion

In this research, the vibration characteristics of stepped-thickness piezoelectric cylindrical shells for acoustic amplification were investigated. To the best of the author's knowledge, this has not been reported in the open literature. A theoretical approach was employed to obtain the vibration characteristics of these shells. Having validated the approach for the elastic stepped-thickness shells as well as uniform-thickness piezoelectric shells, the matrices were simply modified and updated for a stepped-thickness piezoelectric shell. More importantly, it was intended to scrutinize the feasibility of achieving a stepped-thickness cylindrical piezoelectric transducer with the strongest acoustic field possible for the same input power as a uniform-thickness transducer. Geometrical variations in the form of steps in the thickness were introduced to analyse their effect on the acoustic generation inside the transducer. Extensive simulations were performed to obtain various mode shapes in an attempt to obtain the highest SPL. The hypothesis was to localize vibration with a higher amplitude in the machined regions to get suitable mode shapes producing higher SPL for the same input power. Such localization increases the risk of stress concentration and therefore, stress distribution was also taken into account. This resulted in elimination of some of the transducers with high SPL. However, to verify the stress distribution results obtained from simulations, a transducer with a high stress level was machined and experimentally tested. In addition, the material for the transducer was chosen carefully since it affected the vibration amplitude and correspondingly SPL. By employing a cylindrical shell, the focus of the resultant acoustic field was improved. Further, a suitable mode shape can help achieve a better constructive interference at the centreline of the transducer. All these factors were taken into account to identify a suitable design for the transducer. The proposed design was

validated by experimentally investigating and measuring the strength of the acoustic field through SPL and the vibration mode shape using a Vibrometer. Finally, the performance of the identified transducer in an application as a second stage transducer for atomization was investigated. Detailed results and discussions were elaborately presented in the previous chapters. However, according to the above explanations, the following important results can be summarized

1. Characteristics of the suitable step should be carefully identified with respect to the intended range of frequency and the vibration mode shapes. These two are a function of dimensional requirements for the intended application. This has been successfully performed satisfying research objectives 1 and 2.
2. A transducer with steps in the thickness was identified which produced an approximately twice stronger acoustic field than a uniform-thickness transducer at the same input power. This is a promising result. A circular cylindrical geometry strongly affected the focus of the acoustic waves. Further, introducing steps in the thickness at suitable locations helped amplify the acoustic field satisfying research objective 3.
3. Stress concentration is a crucial consideration for the design of such stepped-thickness transducers as it can result in the failure of the transducer. Simulations can be relied on for stress analysis. This has been successfully considered satisfying research objective 4.
4. The identified transducer in this work was used as a second stage transducer for atomization and successfully reduced the size of 90% of water droplets flowing from a common nebuliser. This is also a promising finding which can be further investigated and extended resulting in numerous applications. Hence, research objective 5 was fulfilled.

5. It was found that an acoustic field of around 160 dB did not affect the droplets considerably whereas SPLs above that had a more conspicuous effect on the droplets size.
6. Larger droplets were more affected by the acoustic field. This may indicate that a number of such transducers may be required to target a wide range of droplet sizes. This may require transducers operating at various frequencies, mode shapes and level of acoustic field (SPL).
7. It was not intended in any way to limit the scope of the work to details and dimensions considered. The feasibility of designing transducers which are more efficient at the same input power was validated. Hence, the approach followed in this work to identify the optimum design can be readily extended and similarly followed to identify the optimum design for an arbitrary transducer of any size and dimensions considering the requirements for the intended application.

8.2. Novelty and Significance

The novelty of this research is that the vibration of stepped-thickness piezoelectric cylindrical shells has never been investigated before, nor have their acoustic radiation characteristics been investigated. Obviously, their application has not been studied either. In this work, acoustic amplification utilizing stepped-thickness piezoelectric cylindrical shells was investigated for the first time and proved to be successful (having nearly two times stronger acoustic field than the identical uniform-thickness transducer) using an optimum design for the stepped transducer at the same input power.

Although the objective of this work was not to deal with the application, the design considerations and requirements for the intended application as a second stage transducer for atomization were taken into account. The transducer succeeded in breaking up water droplets to smaller ones. This has not been reported in the open literature to the best of the author's knowledge.

The significance of the study is underpinned by the wide variety of applications for these transducers in medical/industrial areas such as droplet generation and atomization, ultrasonic humidification, drug delivery and drug preparation for inhalation. As elaborately explained in Chapter 2, there are some disadvantages and downsides to the current devices. Further, for some applications it is required to produce droplets of smaller sizes or even less than a micron. Therefore, investigation and development of ultrasonic transducers as atomizers in order to improve their performance is a matter of great importance. To address the need for such a transducer, this study was performed in an attempt to fill up the gap in the literature.

8.3. Future Works

Since the implementation of steps to circular cylindrical piezoelectric shells proved to be a useful method to amplify the acoustic field at the same input power as a uniform-thickness transducer, future works can be mostly concentrated on various applications such as

- Identifying the optimum design and performance for the stepped-thickness piezoelectric cylindrical shell suitable for any intended application considering its own requirements following the same design procedure as this work.

Further, since the transducer proved useful to break water droplets into smaller ones, the following can be considered as extensions to fully investigate and finalize the transducer for this specific application

- The effects of input air stream temperature and environment temperature can be considered on the droplets evaporation and breakup process. This was considered as a fixed value in our preliminary experiments just to eliminate the effect of temperature, diminish condensation and concentrate on the effect of ultrasound.
- A controller mechanism can be built in to the set-up to keep the transducer at resonance and avoid getting off resonance since it strongly affects the performance of the transducer.
- Transducers operating at various frequencies can be investigated to target droplets of various sizes since larger droplets were affected more in this study.
- Different configurations can be considered for the second stage atomizer such as a bundle of transducers either in parallel or series each consisting of a transducer similar to the optimum-performance transducer as in this study.
- Design of transducers with longer lengths can be identified using the approach proposed in this work to investigate the effect of ultrasound exposure time for the droplets.
- Effect of various air flows on the droplets breakup can be studied.
- The input droplets to the second stage transducer can be generated by a different nebuliser at a different size. Hence, it can be investigated whether the effect of the ultrasound on the input droplets of other sizes will be the same as in this study or not.
- A theoretical study can be performed to investigate and predict the size of micro droplets flowing in a stream (not a single droplet of millimetre range

diameter as nearly all the studies in the open literature) under the effect of ultrasound.

Appendix A

A.1. Preliminary Studies on Suitable Dimensions and Acoustic Intensification Approaches

At the beginning of the project, only an estimate of the required dimensions was available according to the intended application. Since a small size and portability is a matter of great importance for the potential applications of the transducer under study in this research, a compact size for the piezoelectric transducer is to be considered. Another important issue is the price of the transducer since utilization of such a transducer in potential applications is strongly affected by its affordability. The availability of the identified tube dimensions in the market must also be taken into account since customization affects the affordability noticeably.

In addition, the tube should be thick enough so that machining it to obtain circumferential or axial steps is possible and the tube wall thickness should allow for the required machining. This imposes another restriction on the thickness of the tube and therefore, it cannot be very thin. To satisfy this need, a tube which is thick seems suitable and the machined regions will become thin and the vibration will be localized within the thinner regions as intended. Last but not least is the material of the tube which is a ceramic-type material and is consequently hard to machine and specific equipment is needed. This implies that the tube should be large enough so that the machining tools can be inserted inside the tube to cut the required steps. A potential application for the considered transducer is as a second stage transducer for continuous positive airway pressure (CPAP) machines instead of heated humidifiers or for humidification or even drug delivery devices. For such applications, it is preferable to have an in-line transducer which can fit in a breathing tube of about 2cm diameter such as those used in CPAP devices [86]. Therefore, the length should be short enough

to fit in a portable small device and should not be too short to allow for sufficient exposure of the droplets to the ultrasound. Hence, some simulations are performed on various dimensions of the transducer within the specific size range suitable for potential applications. As explained, there are many important design considerations and geometrical restrictions. However, we tried to take into account all the above-mentioned requirements as much as possible. Subsequently, the investigations can be performed on the identified size to analyse the effects of steps on the performance of the transducer. According to the explanations given and restrictions imposed by all the mentioned factors, the following can be summarized:

- ✓ Extremely short tubes cannot be considered since the clamp fixtures considered for the experimental set-up grip approximately 5mm from each side of the tube and the remaining length will be too short. More importantly, the length should be long enough for sufficient exposure of the droplets to the ultrasound.
- ✓ Extremely long tubes cannot be considered since it is required to be possibly in-line with the delivery tube and should also fit in a portable small device.
- ✓ Tubes with very small inner diameters cannot be considered due to the machining process for cutting the steps on the inner surface.
- ✓ Tubes with very large outer diameters cannot be considered since it should be compact, approximately similar size of the connecting tubes and hoses and also not bulky.
- ✓ Very thin tubes should not be considered since the wall thickness should be reasonably thick to machine considering that the piezoelectric tube which is a ceramic-type material is hard to machine accurately and needs specific equipment.

With respect to the above-mentioned considerations, some of the dimensions from some of the companies we contacted are briefly explained here and the reasons not to consider each are elaborated on (many companies were contacted and just some of them are reported here). It is worth noting that a few companies could provide us with any dimension as per our design considerations. However, tooling expenses for the desired dimensions and customization would cost us too much and would be unaffordable. Therefore, we opt for uniform specimens and we machine them to the identified design configuration. An important design consideration is to be able to implement the transducer inexpensively for further investigations to suit it to potential applications. Therefore, a piezoelectric tube which is off-the-shelf and currently produced by the manufacturers is desired.

PI Company (Germany): Among the standard available sizes, suitable outer and inner diameters and lengths for our purpose cannot be found. The lengths are too short as well (30mm). The only choice is outer diameter 40, inner one 38 and length 40 which may be suitable. Nevertheless, it is big in diameter and more importantly too expensive; therefore, disregarded.

Micromechatronics, Inc (MMech), (USA): The longest tube is 20mm which is too short and not suitable.

APC International, Ltd. (USA): The longest standard length is 30mm with big outer diameter of 85 or 44mm. This is too short. Reasonable outer and inner diameters of 30 and 26mm are available with a very short length of 20mm and therefore, disregarded.

Nanjing Hanzhou Technologie Co. LTD: The dimensions of outer and inner diameters and length for the products of this company seem more suitable. A good range of diameter suitable for machining as well as the length which is longer than the standard length of the products from other companies. These tubes are affordable as

well. Therefore, it was decided to choose a product from this company. Outer and inner diameters of 40 and 34 with a length of 50 and another tube with outer and inner diameters of 30 and 26 and a length of 50 are the ones which seem suitable. The latter has a more suitable wall thickness and outer and inner diameters and therefore, it is intended to select and order this transducer to the company for our study.

Appendix B

B.1. Development of the Transducers with Two External/Internal Circumferential Steps

This section includes the investigations on the transducer with two circumferential steps either external or internal and is divided into sections for each of them.

B.1.1. Transducer with Two External Circumferential Steps

To excite the transducer at the mode shape with the circumferential wave number of two, the whole circumference is divided into 4 equal sections half of which are thick and the other half are machined as in Fig.B-1.

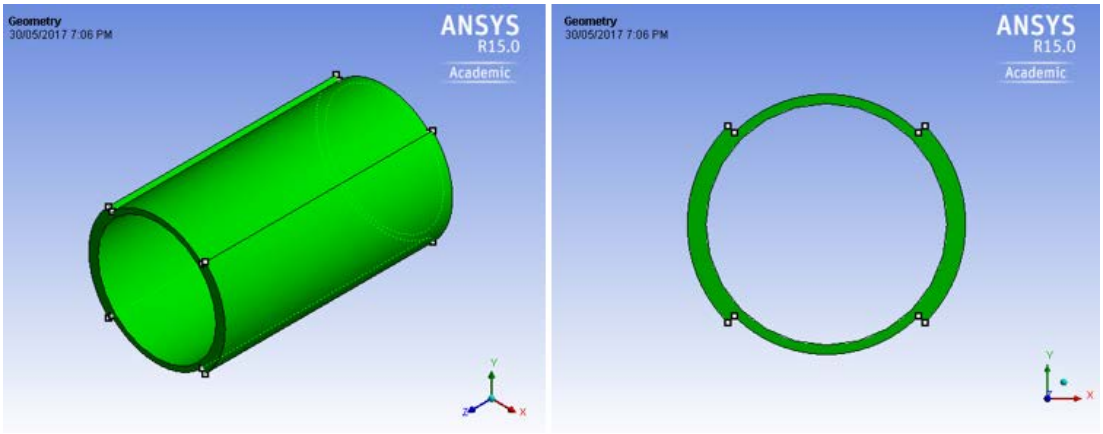

Fig.B-1. Schematic of specimen with two external circumferential steps; Left: ISO view, Right: Side view.

The simulations are performed and the maximum value of the acoustic SPL for this specimen occurs at 34.5 KHz the mode shape of which is depicted in Fig.B-2. Further, Fig.B-3 illustrates the resultant acoustic field at the same frequency from axial and side views. The axial view on the vertical plane reveals that the acoustic field is uniform along the length of the transducer. The side view shows that the constructive interference of the waves radiating from the machined regions intensifies the acoustic

field. On the other hand, the thick regions do not contribute significantly to the resultant acoustic field as can be seen in the side view and the axial view on the horizontal plane. The maximum values of SPL are within the range of 157-166 dB as in the colour-coded legend of the figure and the average is 162 dB. Comparing the mode shape with the one in Fig.4-7 reveals that they both have the same axial wave number (m=5), while the circumferential wave number (n) differs.

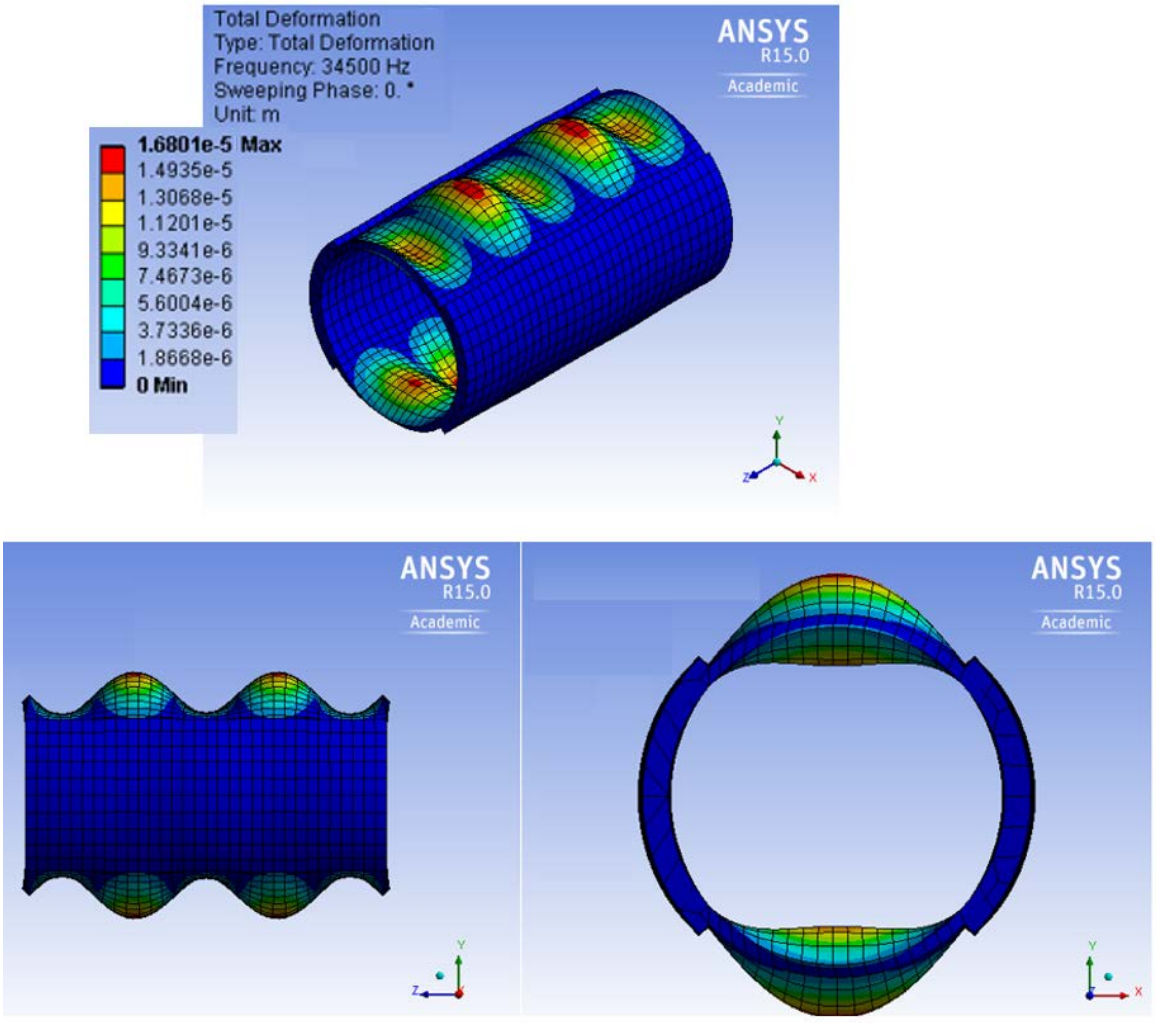

Fig.B-2. Harmonic analysis results for a potential mode shape of the specimen with two external circumferential steps at 34.5 KHz; Top: ISO view, Bottom left: Axial view, Bottom right: Side view.

The whole circumference at each cross section in Fig.4-7 for the uniform-thickness specimen vibrates uniformly, whereas for the stepped specimen, the vibration is localized within the machined regions as in Fig.B-2 and therefore the circumferential wave number is two in this case. Another issue is that the vibration amplitudes in the stepped specimen is orders of magnitude larger than that of the uniform-thickness specimen. However, since many regions are actually not active and not vibrating (or vibrating at a very low amplitude), the maximum amplitude of the resultant acoustic field is slightly lower than the uniform-thickness transducer.

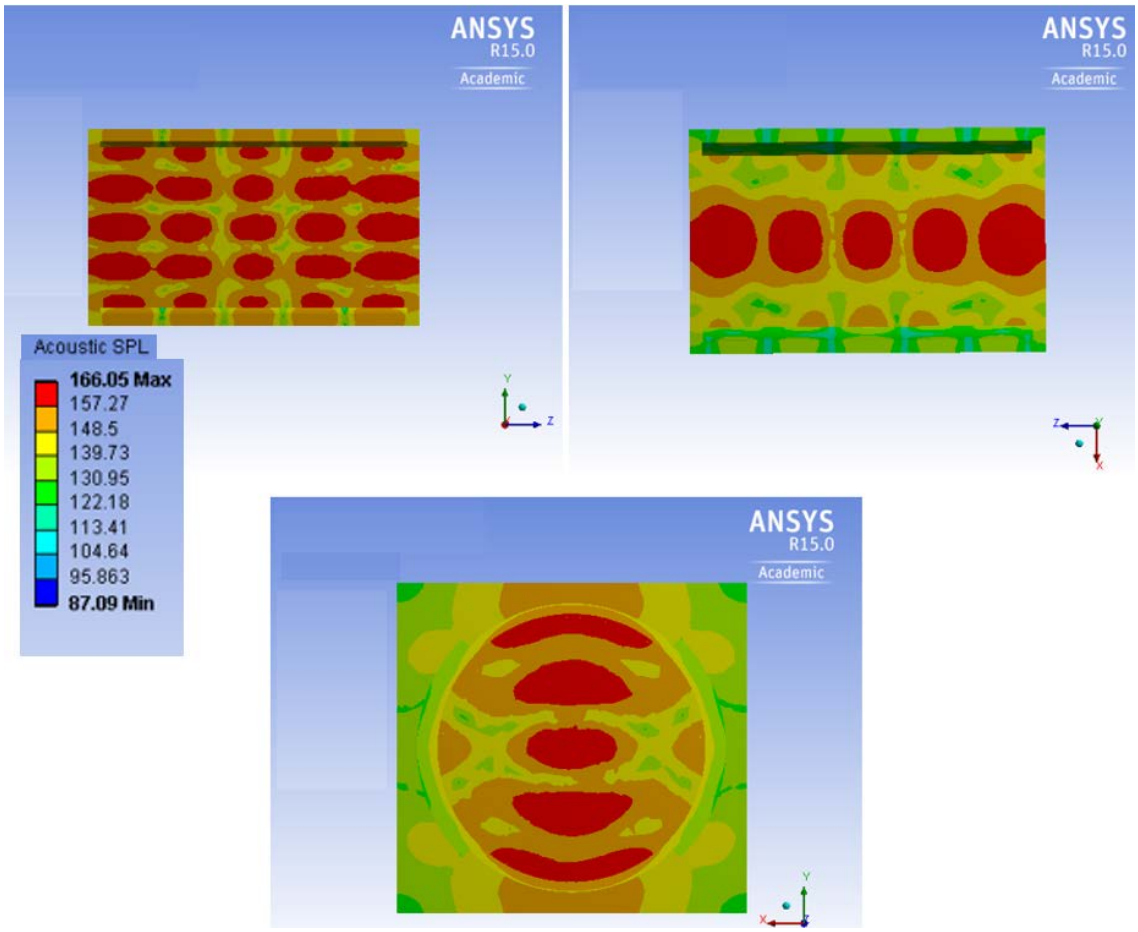

Fig.B-3. Acoustic field in SPL for a potential mode shape of the specimen with two external circumferential steps at 34.5 KHz; Top left: Axial view on the vertical plane, Top right: Axial view on the horizontal plane, Bottom: Side view.

The side view in Fig.B-3 better reveals that the thicker regions are not making conspicuous contribution to acoustic field generation as already mentioned. From the stress point of view, it is in the range of 10^8 order of magnitude as in Fig.B-4. This is beyond the limit for this material and may lead to failure.

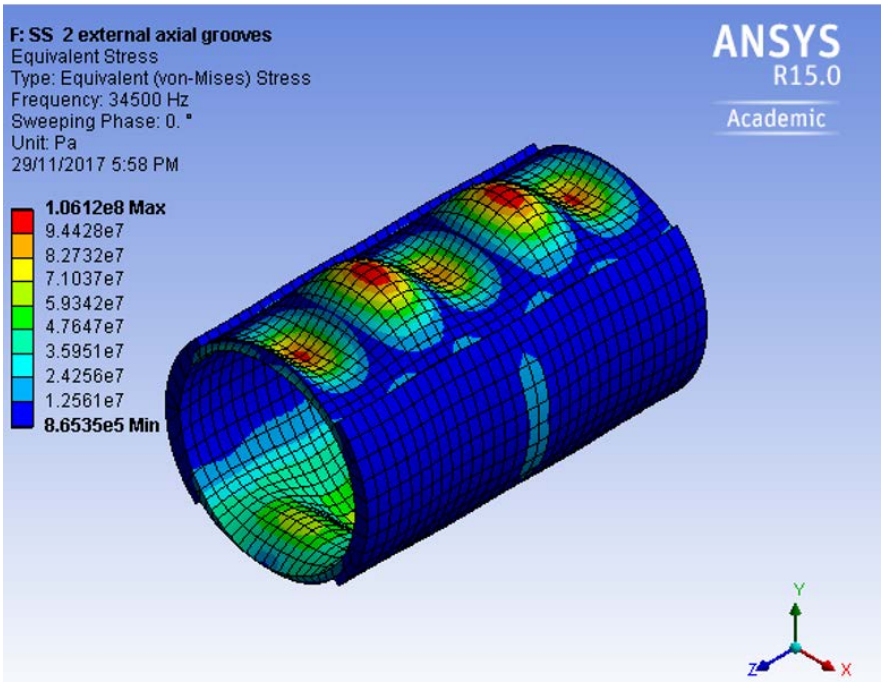

Fig.B-4. Stress distribution for the specimen with two external circumferential steps at 34.5 KHz.

B.1.2. Transducers with Two Internal Circumferential Steps

This specimen is designed in a similar way to the previous one but has internal steps as in Fig.B-5. The maximum value of the acoustic SPL for this specimen occurs at 35 and 39 KHz the mode shapes of which are depicted in Figs.B-6 and B-7. Further, Figs.B-8 and B-9 illustrate the resultant acoustic field for frequencies of 35 and 39 KHz, respectively.

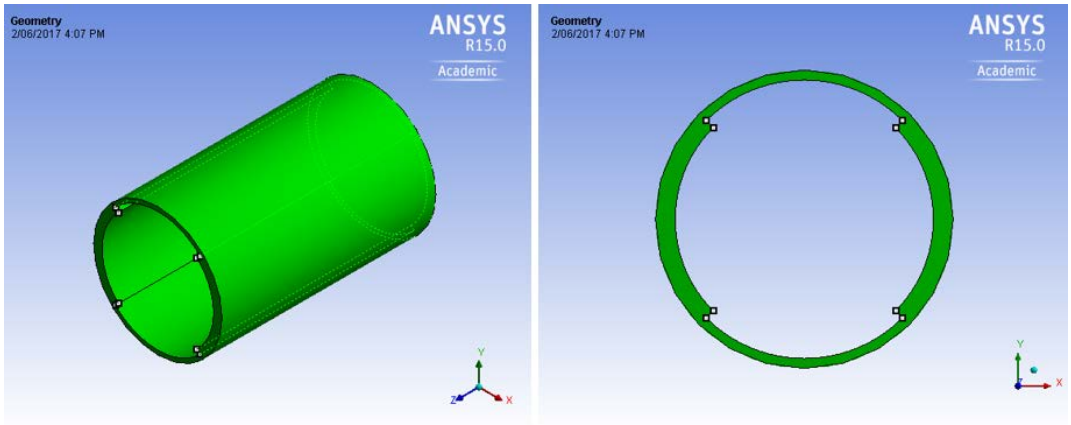

Fig.B-5. Schematic of specimen with two internal circumferential steps; Left: ISO view, Right: Side view.

Axial and circumferential wave numbers for both of the mode shapes are one and six. However, the magnitude of vibration and the pattern of these modes are slightly different as can be observed in Figs.B-6 and B-7. As evident, the magnitude of vibration in both cases is orders of magnitude larger than the uniform tube which again implies the localization of the vibration within the machined regions. In both cases, the larger amplitude of vibration occurs within the machined regions rather than the thicker parts.

Fig.B-8 includes various views of the acoustic field inside the transducer at 35 KHz. The maximum level of SPL is within the range of 166-175 dB with the average of 171 dB. It can be understood that the acoustic field is fairly uniform along the length of the transducer for the mid-plane; however, it is much lower for approximately ¼ of the length of the transducer on each side meaning that around half of the length of the transducer is not at the maximum range (red) according to the colour-coded legend. In addition, two axial views on the horizontal and vertical planes are different. This may be attributed to the fact that although the circumference is divided into equal sections, the vibration pattern differs between thick and thin regions and is localized in the machined regions with two peaks as in Fig.B-6 compared to only one peak in the thick regions.

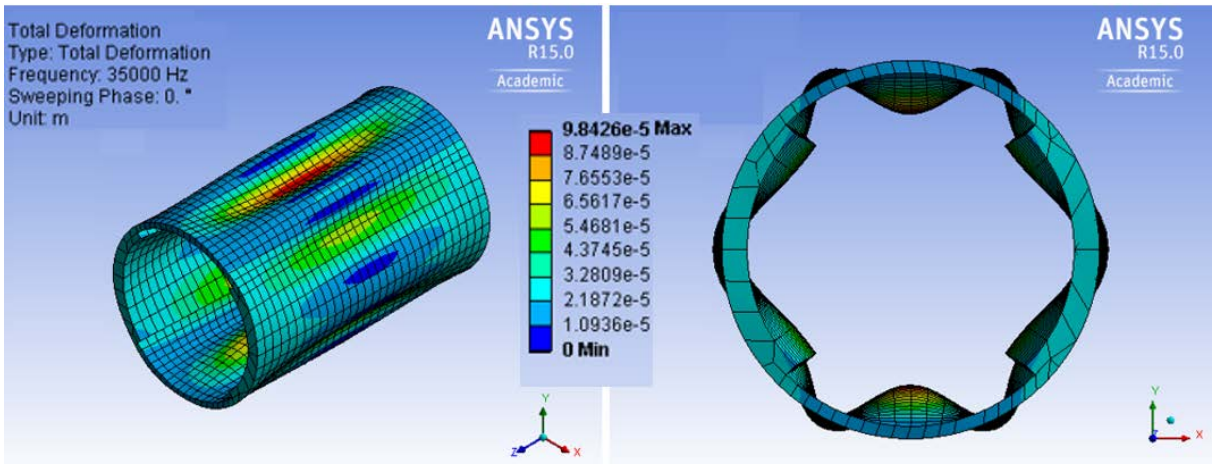

Fig.B-6. Harmonic analysis results for a potential mode shape of the specimen with two internal circumferential steps at 35 KHz; Left: ISO view, Right: Side view.

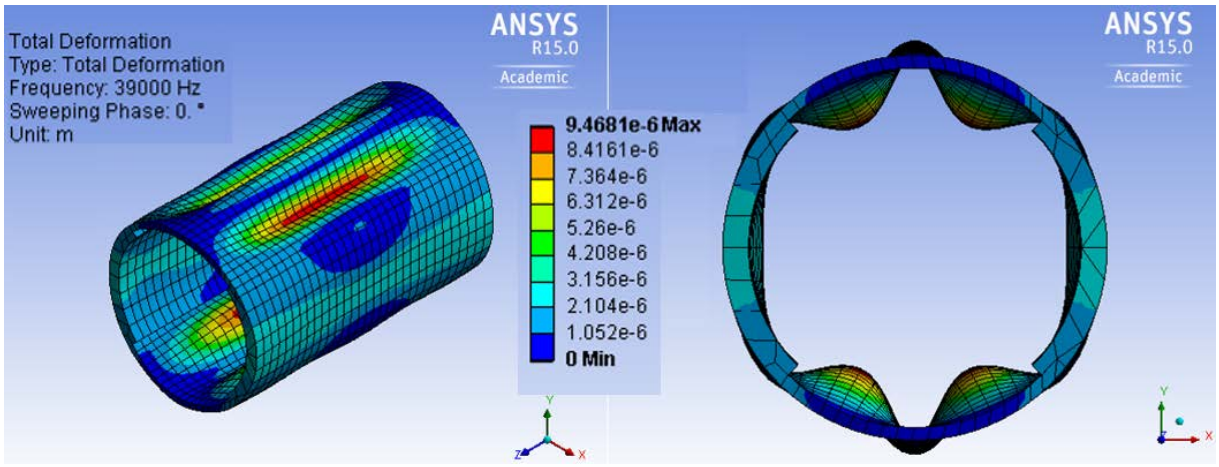

Fig.B-7. Harmonic analysis results for a potential mode shape of the specimen with two internal circumferential steps at 39 KHz; Left: ISO view, Right: Side view.

This can cause the asymmetry between the two axial views on different planes. Side views can also show the reduction in the level of SPL for many regions inside the transducer. These zones are in the range of 147-166 dB averaging at around 156 dB which can be observed by checking the axial and side views. Comparing this with Fig.4-8 corresponding to the uniform tube reveals no conspicuous superiority. While the maximum level of SPL is larger than that of the uniform tube, the acoustic field is not uniform along the length leaving around half of the length of the transducer at a

lower level of SPL. The average level is nearly similar to the uniform-thickness specimen which has uniform acoustic field along the length and for various cross sections as evident in axial and side views of Fig.4-8.

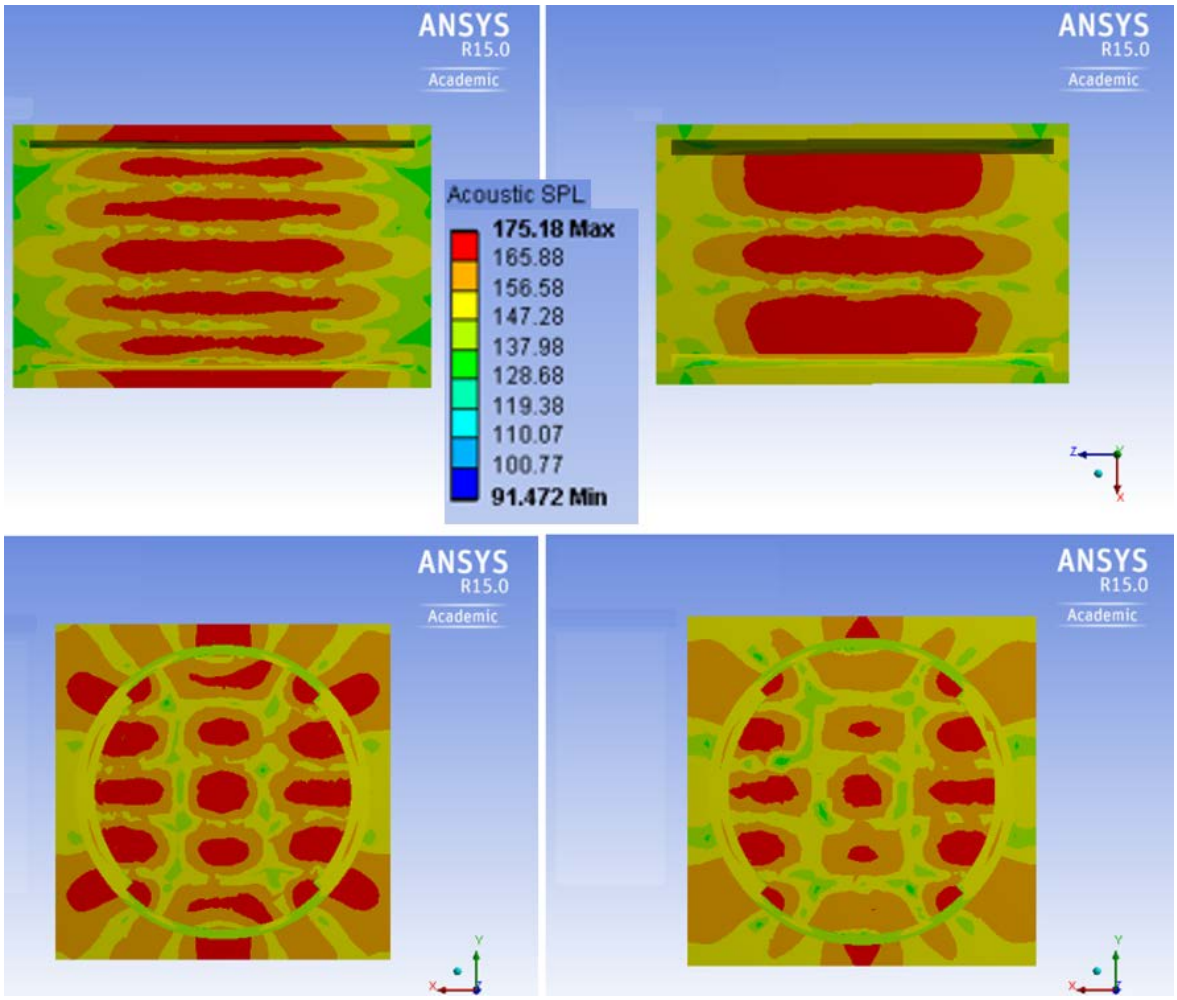

Fig.B-8. Acoustic field in SPL for a potential mode shape of the specimen with two internal circumferential steps at 35 KHz; Top left: Axial view on the vertical plane, Top right: Axial view on horizontal plane, Bottom left: Side view at mid-length, Bottom right: Side view at quarter-length.

It is worth noting that the stress level is in the order of 10^8 which is very high and unsuitable. The red region in the left photo of Fig.B-10 is at the maximum deformation and stress level and may lead to the transducer failure.

Fig.B-9 includes various views of the acoustic field inside the transducer at 39 KHz. The maximum level of SPL is within the range of 174-186 dB with the average of 180

dB. However, it can be seen that the maximum level of SPL occurs near the inner surface of the transducer and most other regions are all in lower levels corresponding to yellow and orange colour codes in the figure. Both the axial and side views clearly show that the centreline is in a lower range of SPL compared to the regions close to the inner surface. Moreover, side views reveal that nearly more than half of the inner parts of the transducer at any cross section (mid- or quarter-length) are in the yellow and orange colour code ranges averaging at around 163 dB. This is not a noticeable improvement compared to the uniform-thickness tube which has the privilege of a uniform acoustic SPL at any cross sectional view along the length of the transducer. While for the uniform-thickness specimen, the maximum stress is in the range of a few MPa (3.3 MPa), it is 82 MPa for this specimen (right photo in Fig.B-10) which is high and may lead to the transducer failure. Further, there is no improvement in acoustic amplification and focus at the centreline compared to the uniform-thickness tube. The maximum SPL is high; however, it is close to the inner surface and not inside the transducer. Therefore, this specimen is not that recommended, especially due to the high stress levels and the risk of failure.

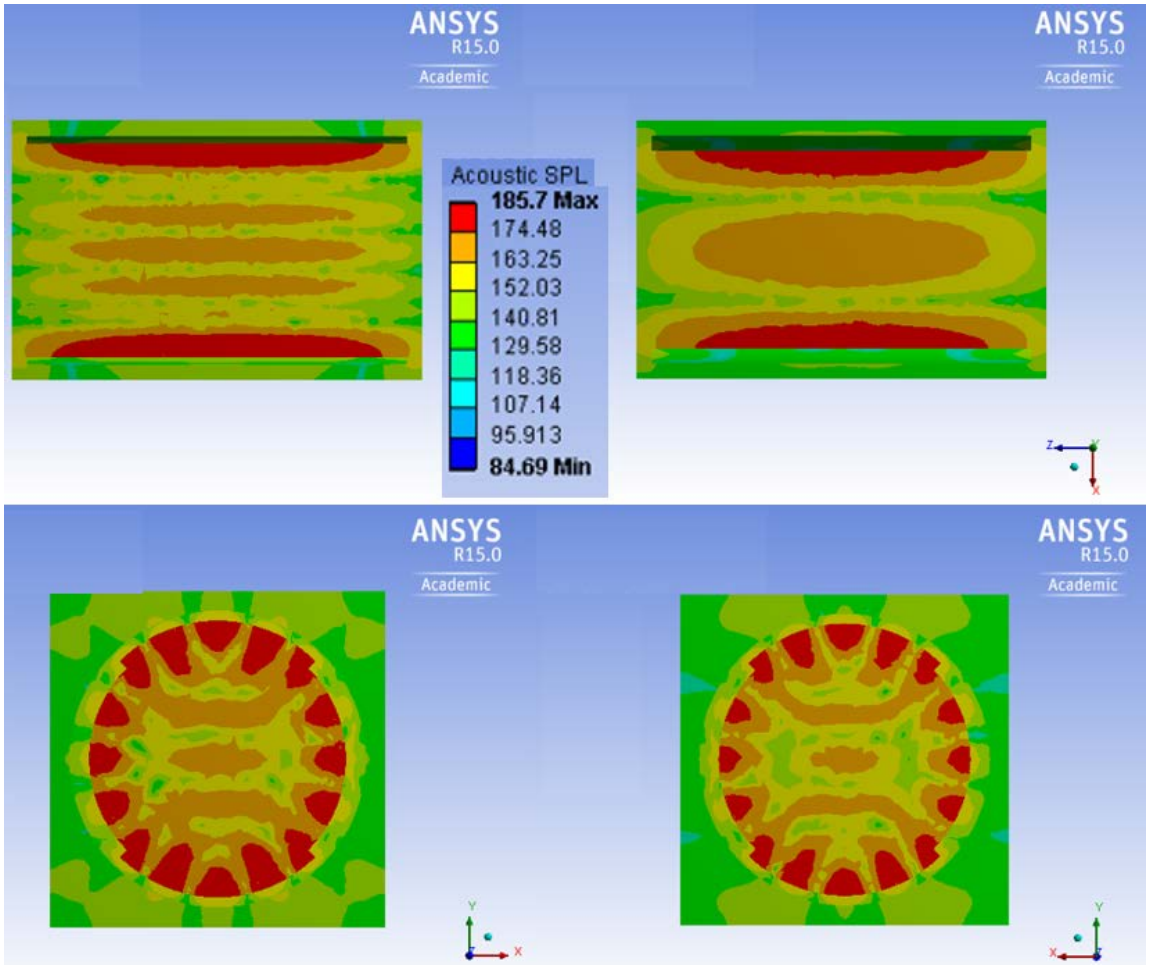

Fig.B-9. Acoustic field in SPL for a potential mode shape of the specimen with two internal circumferential steps at 39 KHz; Top left: Axial view on the vertical plane, Top right: Axial view on horizontal plane, Bottom left: Side view at mid-length, Bottom right: Side view at quarter-length.

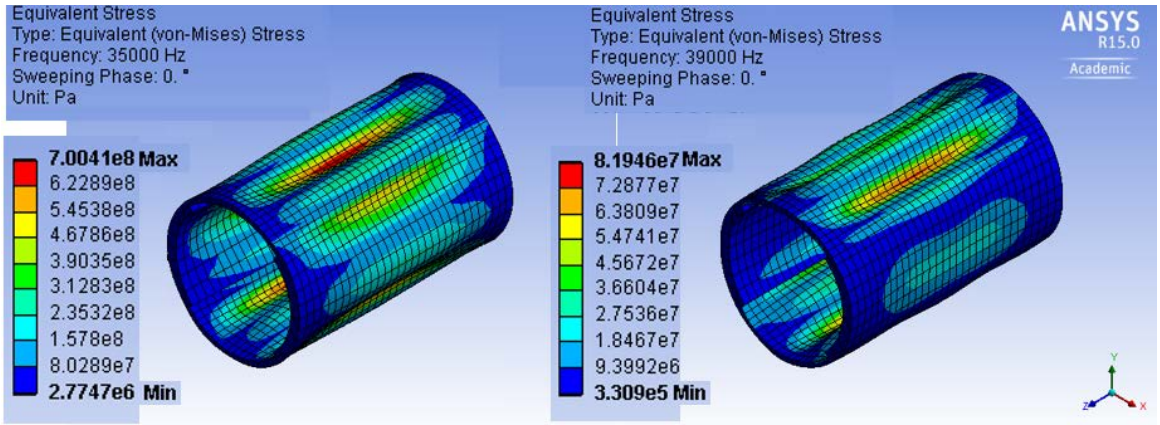

Fig.B-10. Stress distribution for the specimen with two internal circumferential steps at Left: 35 KHz and Right: 39 KHz.

B.2. Development of the Transducers with Three External/Internal Circumferential Steps

This section includes the investigations on the transducer with three circumferential steps either external or internal and is divided into sections for each of them.

B.2.1. Transducers with Three External Circumferential Steps

To excite the transducer at the mode shape with the circumferential wave number of three, the whole circumference is divided into 6 equal sections half of which are thick and the other half are machined as in Fig.B-11. The maximum value of the acoustic SPL for this specimen occurs at 31 and 39 KHz the mode shapes of which are depicted in Figs.B-12 and B-13. Further, Figs.B-14 and B-15 illustrate the resultant acoustic field for frequencies of 31 and 39 KHz the maximum of which is 169 and 179 dB, respectively. Axial and circumferential wave numbers for the mode shape at 31 KHz are (3, 0) and for 39 KHz are (1, 6). It is seen that for the case of 31 KHz, the circumferential wave number is the same as the uniform-thickness tube, while the axial wave number differs. As evident, the vibration is not localized within the machined regions for this frequency and therefore, no improvement is observed for the resultant acoustic field. Comparison of the acoustic fields for this specimen and the uniform-thickness transducer reveals a nearly identical side view due to the same circumferential wave number, while the axial view is slightly different which is caused by various axial wave numbers. It is worth noting that since the two axial views from different planes are the same, only one axial view is depicted. However, since the amplitude of vibration is not that high compared to the uniform-thickness specimen and the vibration is not localized either, the SPL is not superior to that of the uniform-thickness specimen. It is worth noting that the stress distribution is within a suitable range and the maximum is 12 MPa as in Fig.B-16.

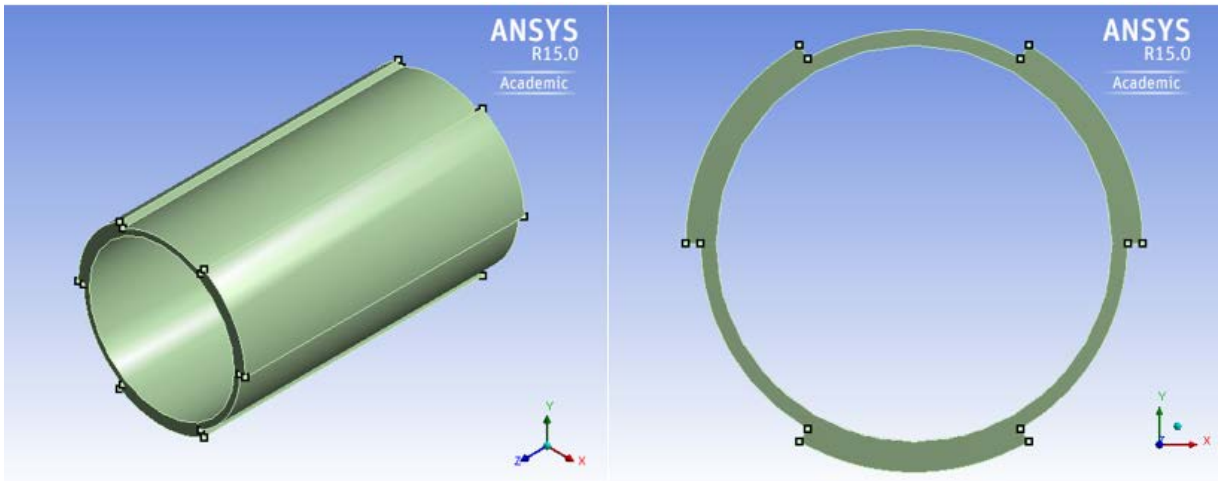

Fig.B-11. Schematic of specimen with three external circumferential steps; Left: ISO view, Right: Side view.

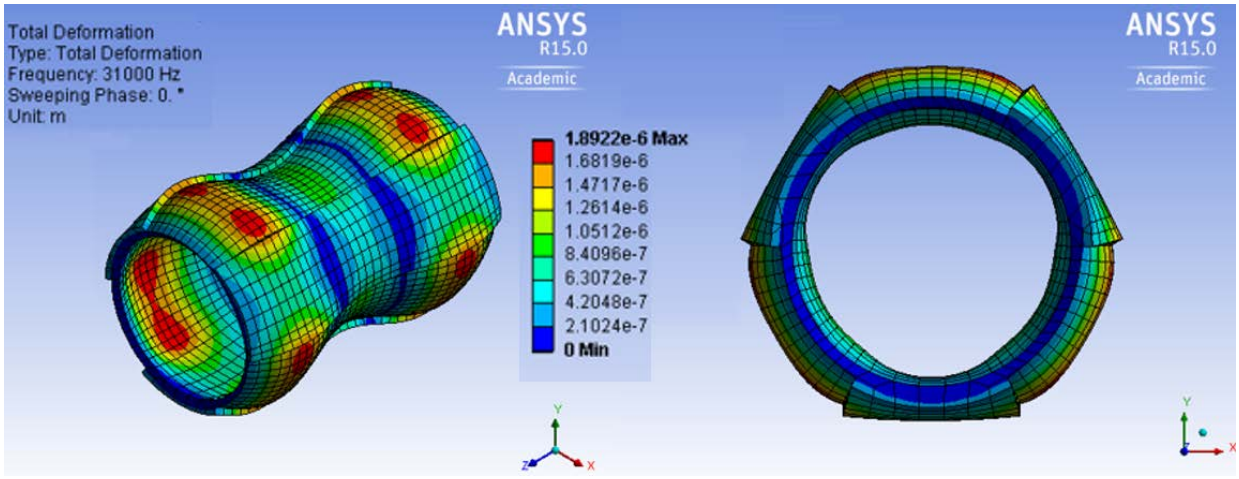

Fig.B-12. Harmonic analysis results for a potential mode shape of the specimen with three external circumferential steps at 31 KHz; Left: ISO view, Right: Side view.

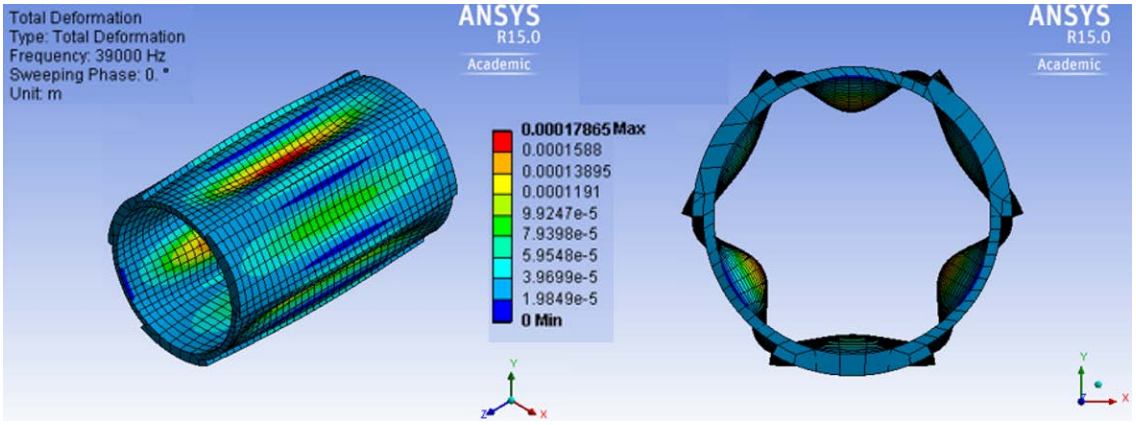

Fig.B-13. Harmonic analysis results for a potential mode shape of the specimen with three external circumferential steps at 39 KHz; Left: ISO view, Right: Side view.

For the case of 39 KHz, the magnitude of vibration is orders of magnitude larger than the uniform tube which again implies the localization of the vibration within the machined regions. Accordingly, the resultant acoustic field has a larger magnitude as in Fig.B-15. In this figure, there are two axial views from horizontal and vertical planes. It is clearly observed that these two axial views differ from each other. The reason may lie behind the fact that the axial views of the transducer itself are different on horizontal and vertical planes. This asymmetry can be a problem of different extent for any transducer with circumferential steps depending on the mode shape of vibration except for the case where the circumferential wave number is zero as in Figs.B-12 and 14.

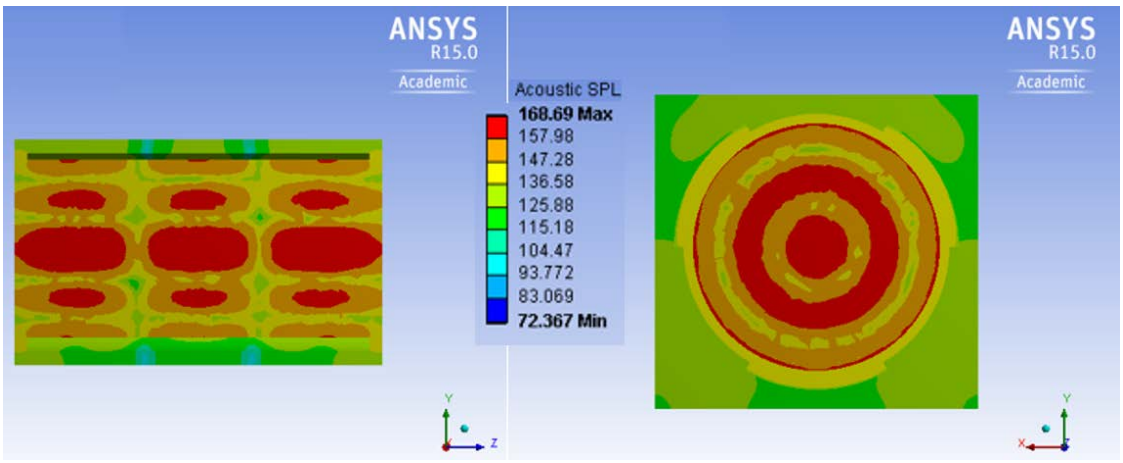

Fig.B-14. Acoustic field in SPL for a potential mode shape of the specimen with three external circumferential steps at 31 KHz; Left: Axial view, Right: Side view.

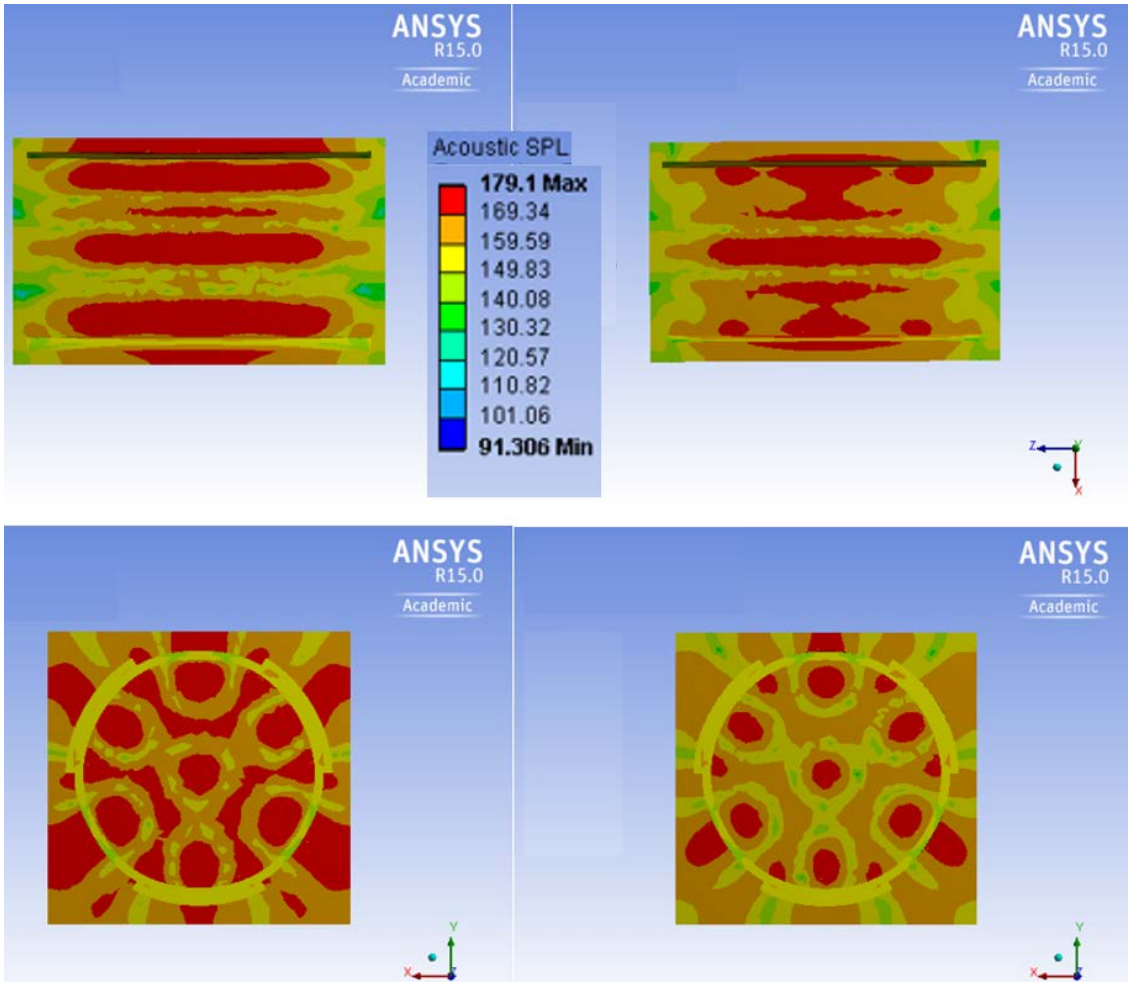

Fig.B-15. Acoustic field in SPL for a potential mode shape of the specimen with three external circumferential steps at 39 KHz; Top left: Axial view on the vertical plane, Top right: Axial view on the horizontal plane, Bottom left: Side view at mid-length, Bottom right: Side view at quarter-length.

Further, the axial views show that for each quarter of the length from each end, the acoustic field is noticeably lower in level compared to the rest of the length of the transducer. This can be also verified from the side views. It means that approximately half of the length is generating acoustic field in the range of yellow and orange colour codes averaging at about 159 dB which is a few dBs higher than the average for the uniform-thickness specimen while the uniformity is lost along the length and for various cross sections along the length. It is worth noting that very high amplitudes of vibration, which is in the order of 10^{-4}, results in extremely high stress levels in the

order of 10^9 at the red regions of Fig.B-16. Hence, this specimen at this frequency is not suitable.

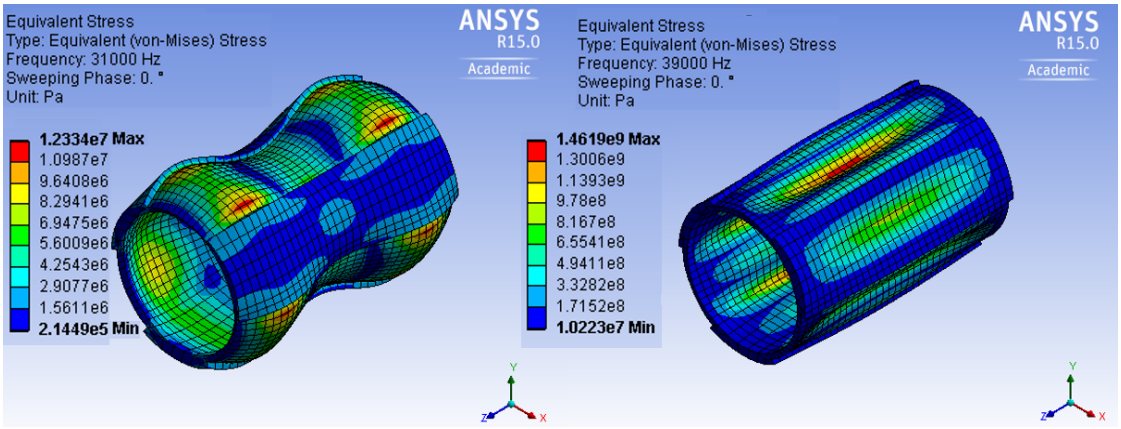

Fig.B-16. Stress distribution for the specimen with three external circumferential steps at Left: 31 KHz and Right: 39 KHz.

B.2.2. Transducer with Three Internal Circumferential Steps

This specimen is designed in a similar way to the previous one but has internal steps as in Fig.B-17. The maximum value of the acoustic SPL for this specimen occurs at 32 and 39.5 KHz the mode shapes of which are depicted in Figs.B-18 and B-19. Further, Figs.B-20 and B-21 illustrate the resultant acoustic field for frequencies of 32 and 39.5 KHz, respectively.

Axial and circumferential wave numbers for the mode shape at 32 KHz are (3, 3) and for 39.5 KHz are (1, 6). It is seen that for the case of 32 KHz, the circumferential wave number is the same as the number of steps and the vibration is localized within the machined regions.

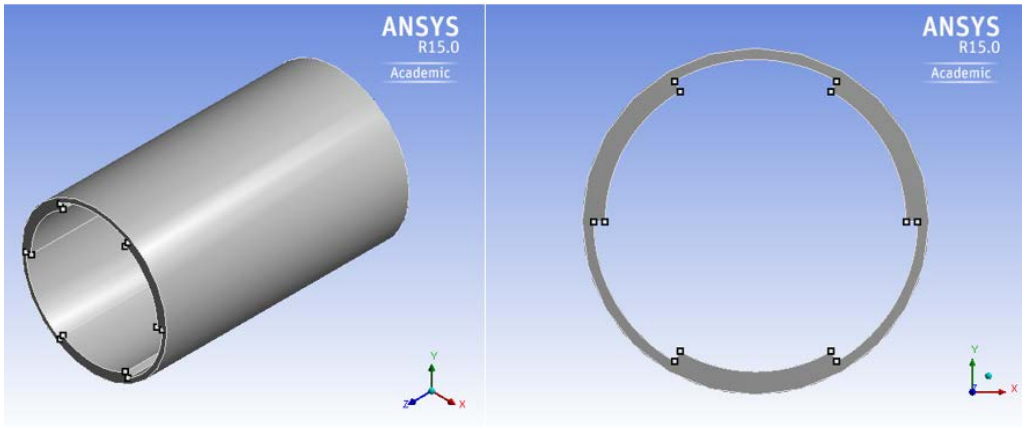

Fig.B-17. Schematic of specimen with three internal circumferential steps; Left: ISO view, Right: Side view.

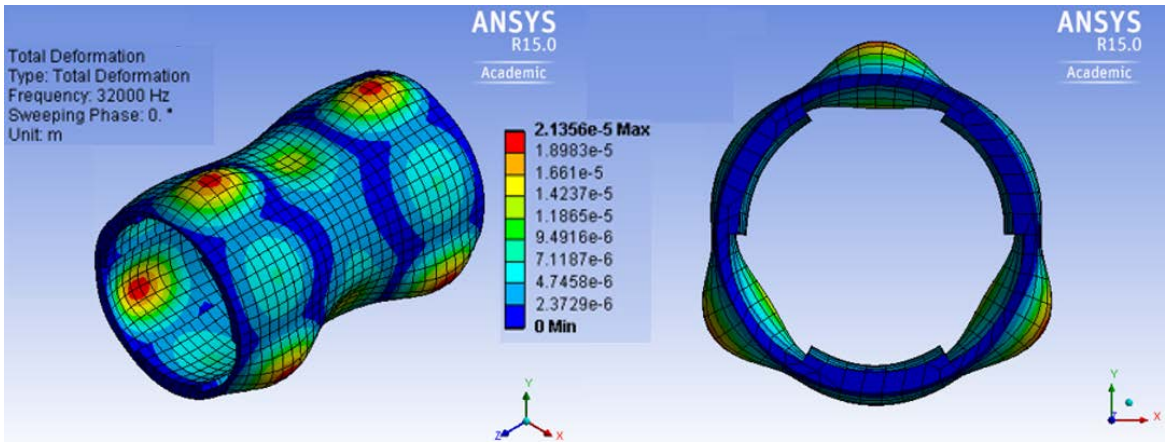

Fig.B-18. Harmonic analysis results for a potential mode shape of the specimen with three internal circumferential steps at 32 KHz; Left: ISO view, Right: Side view.

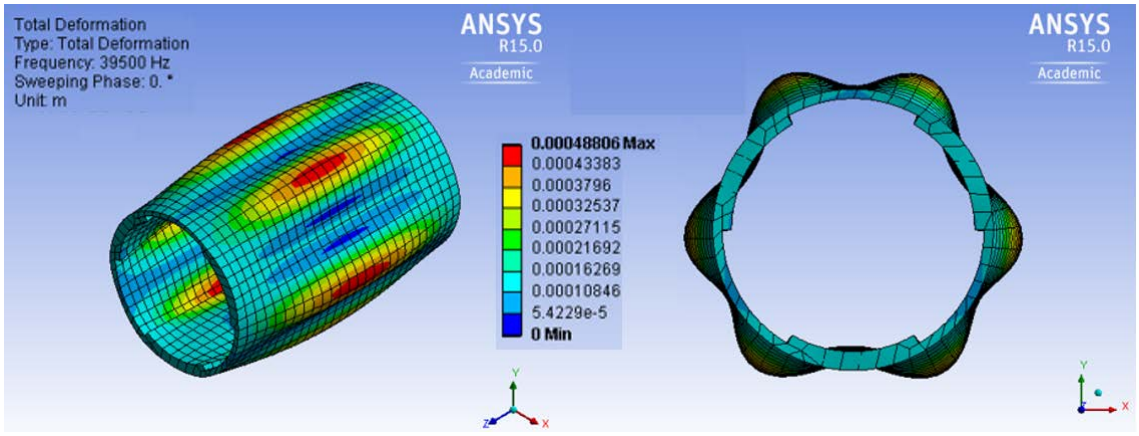

Fig.B-19. Harmonic analysis results for a potential mode shape of the specimen with three internal circumferential steps at 39.5 KHz; Left: ISO view, Right: Side view.

The maximum level of SPL is 174 dB as in Fig.B-20, which occurs around the inner surface of the transducer as well as small regions inside the tube. Since many regions of the transducer are not vibrating or are vibrating at a very low amplitude, the acoustic field in most regions inside the tube is in the range of yellow and orange colour codes averaging at around 153 dB. Hence, there is no specific superiority over the uniform-thickness specimen. Further, regarding the stress level, the red regions in Fig.B-22 are at around 123 MPa which is not suitable and is very high. For the case of 39.5 KHz, the amplitude of vibration is orders of magnitude larger than that of the uniform-thickness tube. Two peaks are observed within each machined region half of each occurring over the thick regions. Since the axial views of the cross section of the transducer on the horizontal and vertical planes are different, it is anticipated to have different axial views of the resultant acoustic field as in Fig.B-21. The maximum level of SPL is 202 dB occurring in many regions fairly uniformly along the length of the tube. Overall, the level of SPL for this frequency and the corresponding mode shape is so high everywhere inside the transducer, though the pattern is to some extent different between the side views at mid- and quarter-length and also between two axial views. However, the stress distribution reveals that the red regions in Fig.B-22 are at a very large level (10^9 Pa) which is not suitable.

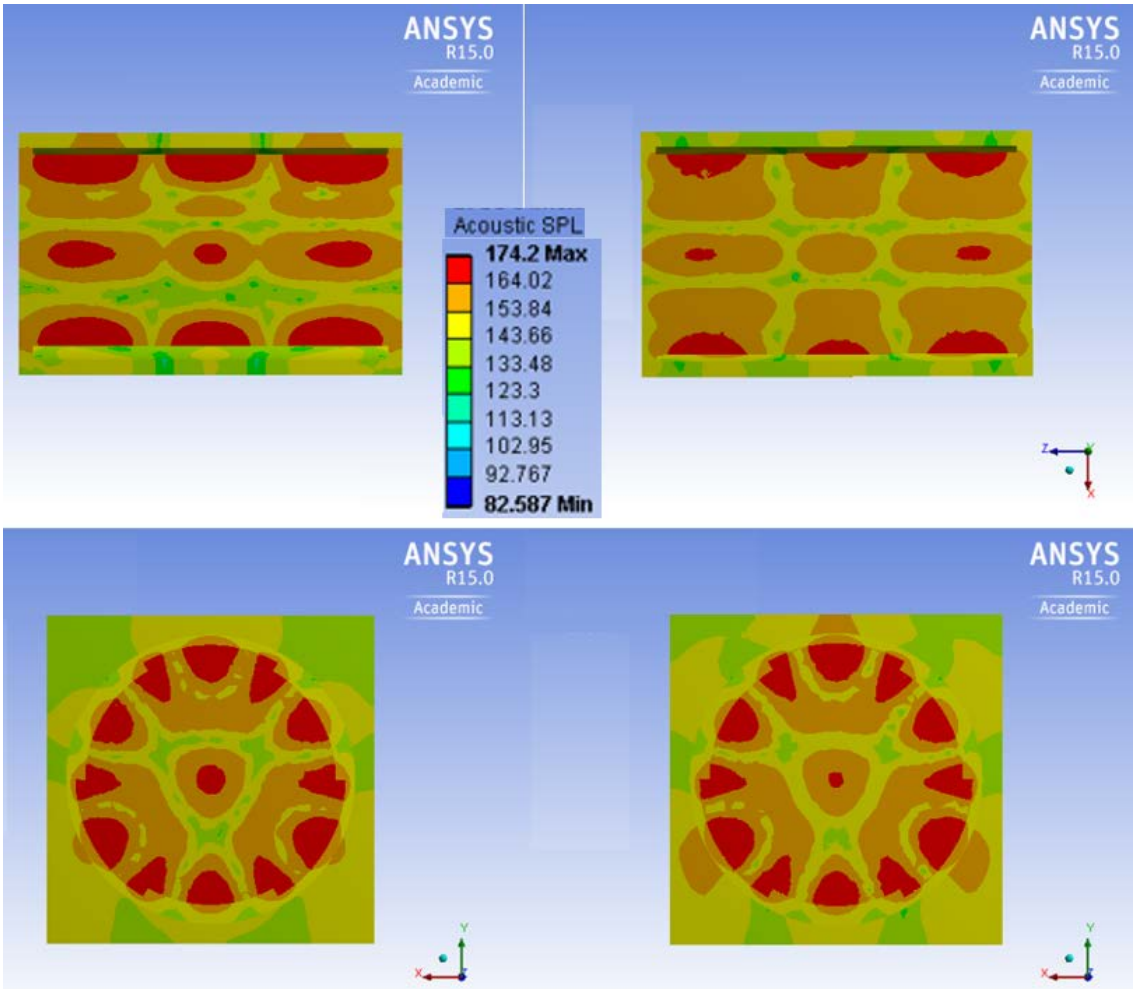

Fig.B-20. Acoustic field in SPL for a potential mode shape of the specimen with three internal circumferential steps at 32 KHz; Top left: Axial view on the vertical plane, Top right: Axial view on the horizontal plane, Bottom left: Side view at mid-length, Bottom right: Side view at quarter-length.

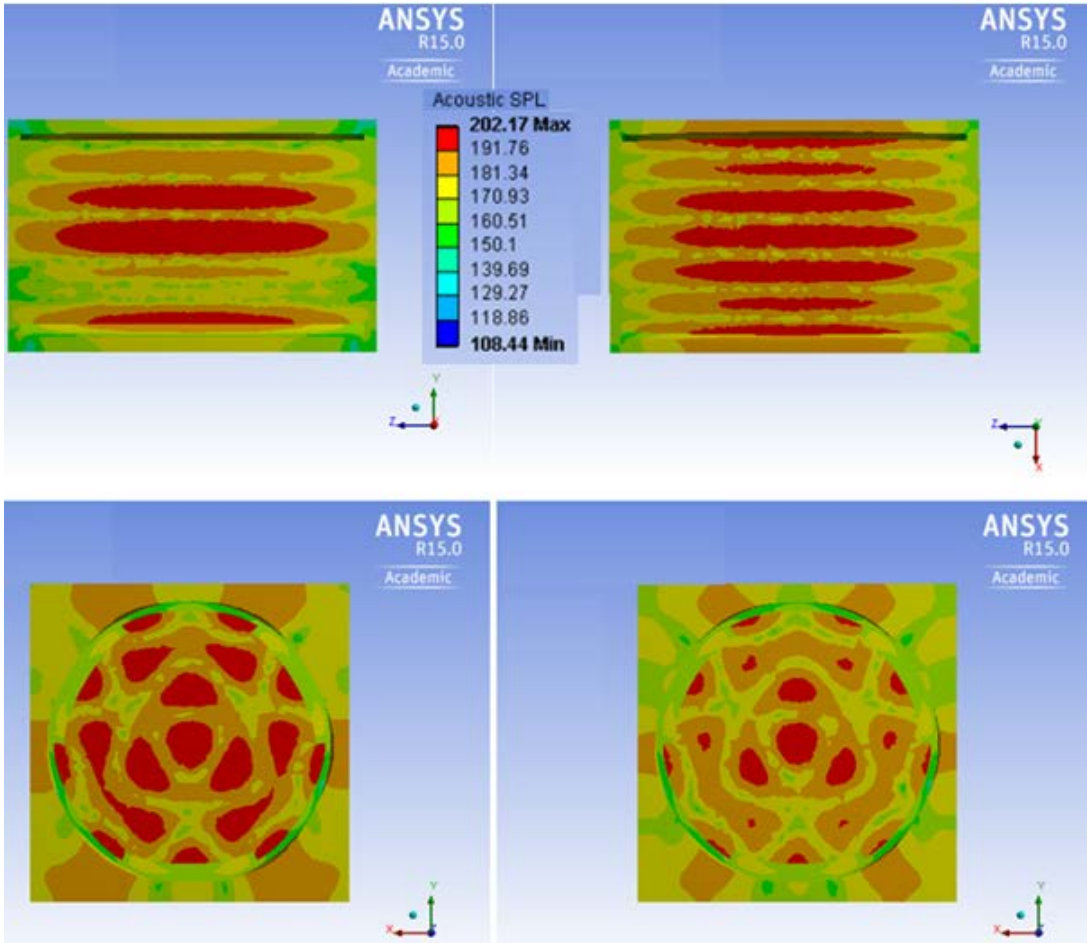

Fig.B-21. Acoustic field in SPL for a potential mode shape of the specimen with three internal circumferential steps at 39.5 KHz; Top left: Axial view on the vertical plane, Top right: Axial view on the horizontal plane, Bottom left: Side view at mid-length, Bottom right: Side view at quarter-length.

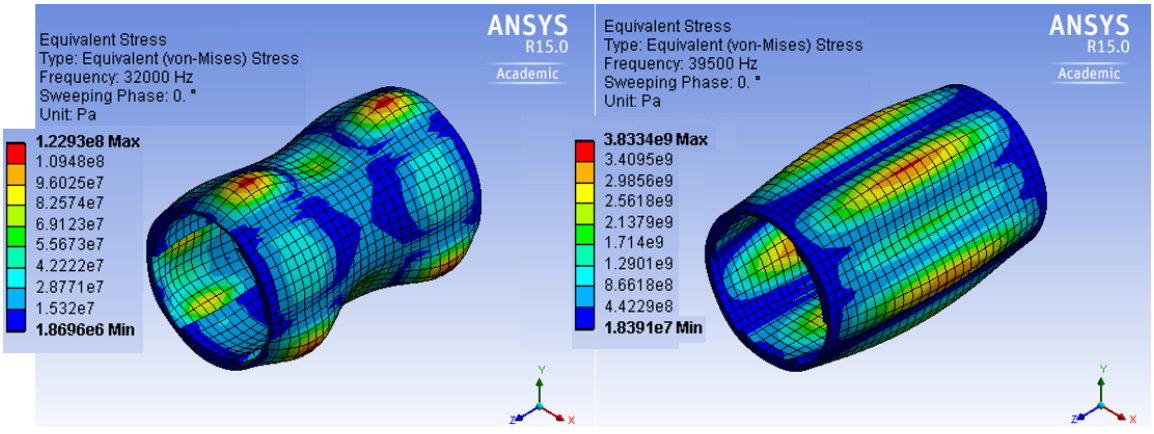

Fig.B-22. Stress distribution for the specimen with three internal circumferential steps at Left: 32 KHz and Right: 39.5 KHz.

B.3. Development of the Transducers with Four External/ Internal Circumferential Steps

This section includes the investigations on the transducer with four circumferential steps either external or internal and is divided into sections for each of them.

B.3.1. Transducer with Four External Circumferential Steps

To excite the transducer at the mode shape with the circumferential wave number of four, the whole circumference is divided into 8 equal sections half of which are thick and the other half are machined as in Fig.B-23. The maximum value of the acoustic SPL for this specimen occurs at 36 and 47.5 KHz the mode shapes of which are depicted in Figs.B-24 and B-25. Further, Figs.B-26 and B-27 illustrate the resultant acoustic field for frequencies of 36 and 47.5 KHz, respectively.

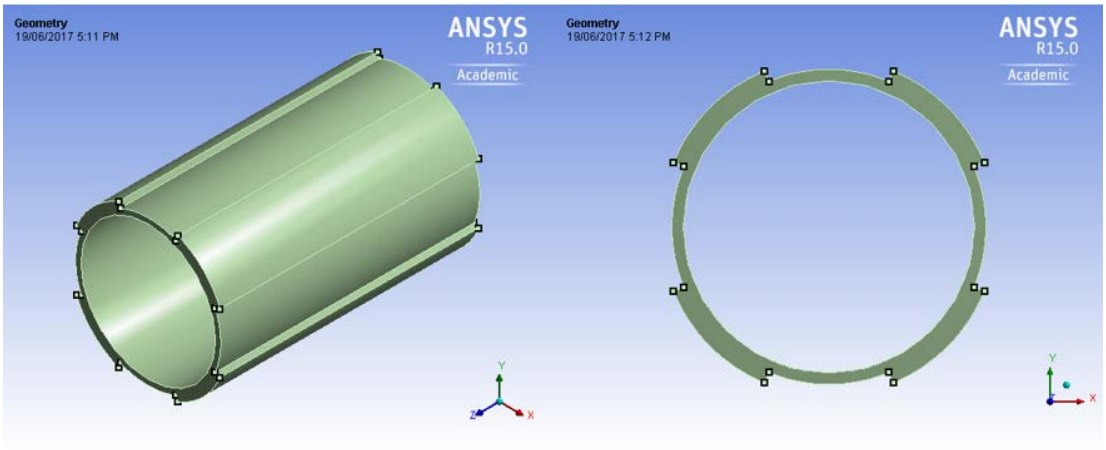

Fig.B-23. Schematic of specimen with four external circumferential steps; Left: ISO view, Right: Side view.

Axial and circumferential wave numbers for the mode shape at 36 KHz are (1, 0) and for 47.5 KHz are (7, 4). The axial wave number for the latter case is the same as the number of steps and the vibration is localized within the machined regions. Due to the symmetry in the geometry, the resultant acoustic field is also the same in both axial

views as in Fig.B-26. The maximum level of SPL is 169 dB which occurs at patches uniformly distributed along the length of the transducer each corresponding to one peak/valley of the mode shape as in Fig.B-25. Many regions inside the transducer are in yellow and orange colour-coded areas averaging at around 151 dB.

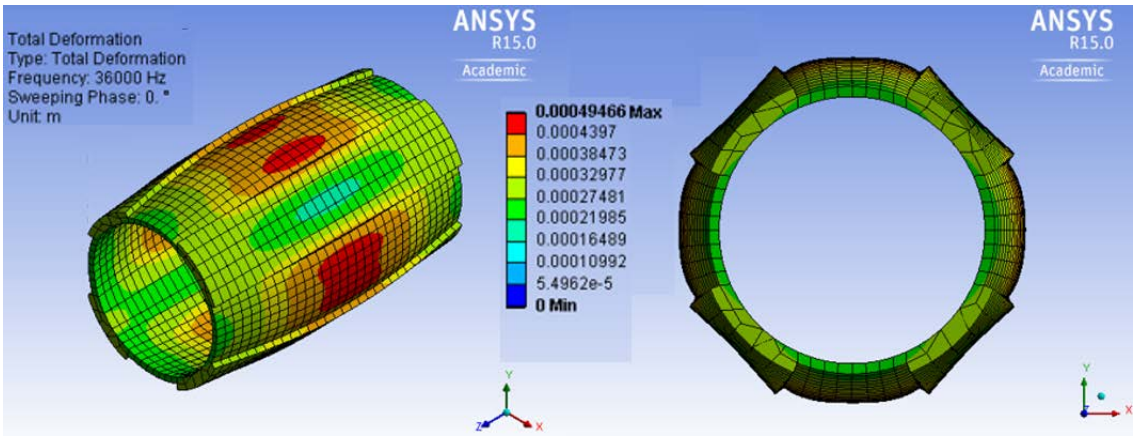

Fig.B-24. Harmonic analysis results for a potential mode shape of the specimen with four external circumferential steps at 36 KHz; Left: ISO view, Right: Side view.

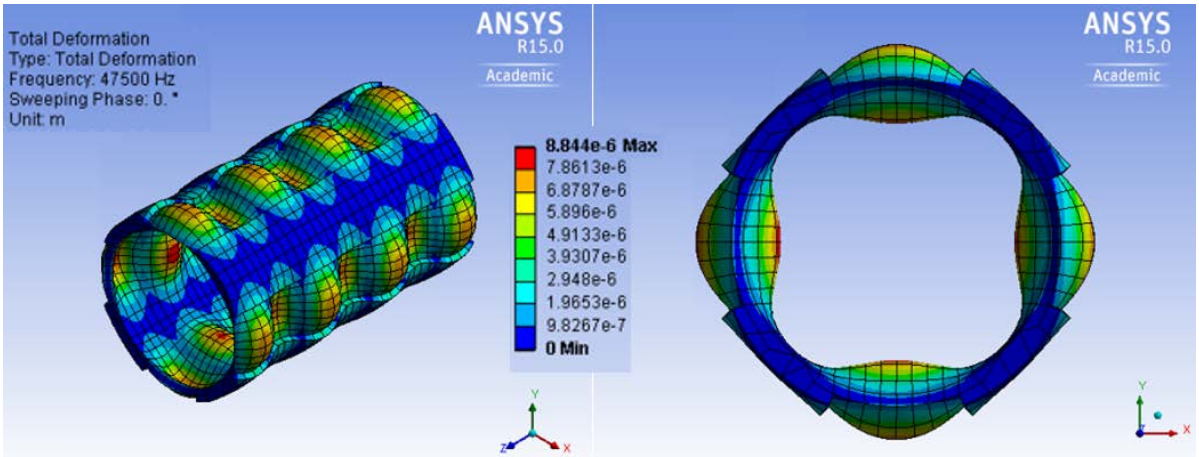

Fig.B-25. Harmonic analysis results for a potential mode shape of the specimen with four external circumferential steps at 47.5 KHz; Left: ISO view, Right: Side view.

The maximum stress is 92 MPa as in Fig.B-28. Consequently, this case is not superior to the uniform-thickness specimen. However, the mode shape corresponding to 36 KHz as in Fig.B-24 has an amplitude of vibration which is orders of magnitude larger than the uniform-thickness specimen. The resultant acoustic field has a much higher

level of SPL at 195 dB which is uniform along the mid-length of the transducer at the centreline. However, it does not cover the quarters from each end of the tube. This can be justified by checking regions of the transducer in various levels of vibration amplitude in Fig.B-24 and the highest levels focusing just around the mid-length. Zero circumferential wave number results in identical axial views as expected.

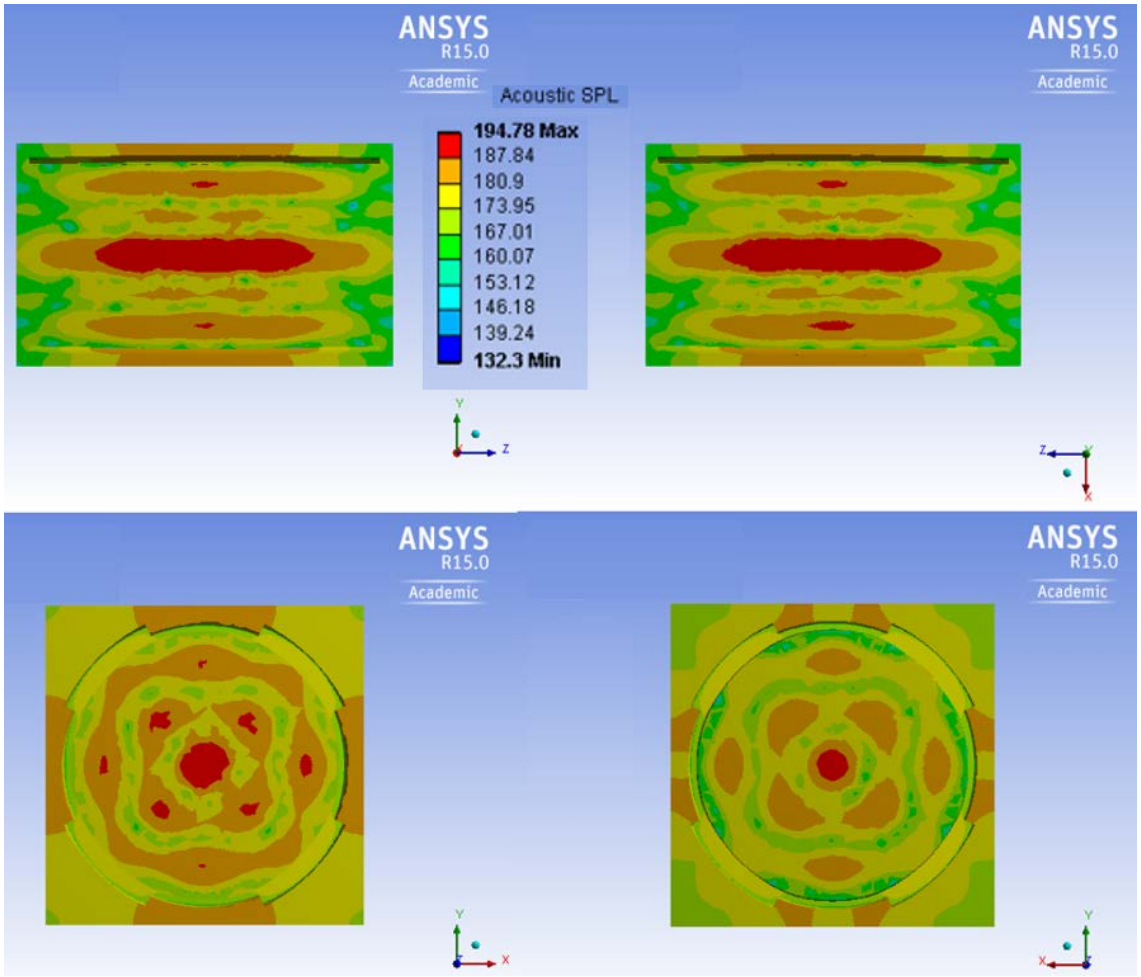

Fig.B-26. Acoustic field in SPL for a potential mode shape of the specimen with four external circumferential steps at 36 KHz; Top left: Axial view on the vertical plane, Top right: Axial view on the horizontal plane, Bottom left: Side view at mid-length, Bottom right: Side view at quarter-length.

Many regions inside the transducer as in axial and side views of Fig.B-26 are in lower levels of SPL corresponding to green, yellow and orange colour codes with the average of around 180 dB. The overall performance in this case is suitable. Although around half of the length (a quarter from each end) is at a lower level of SPL, the magnitude

is still high. However, the stress distribution in most regions is at a very large level (10^9 Pa) which is not suitable as in Fig.B-28.

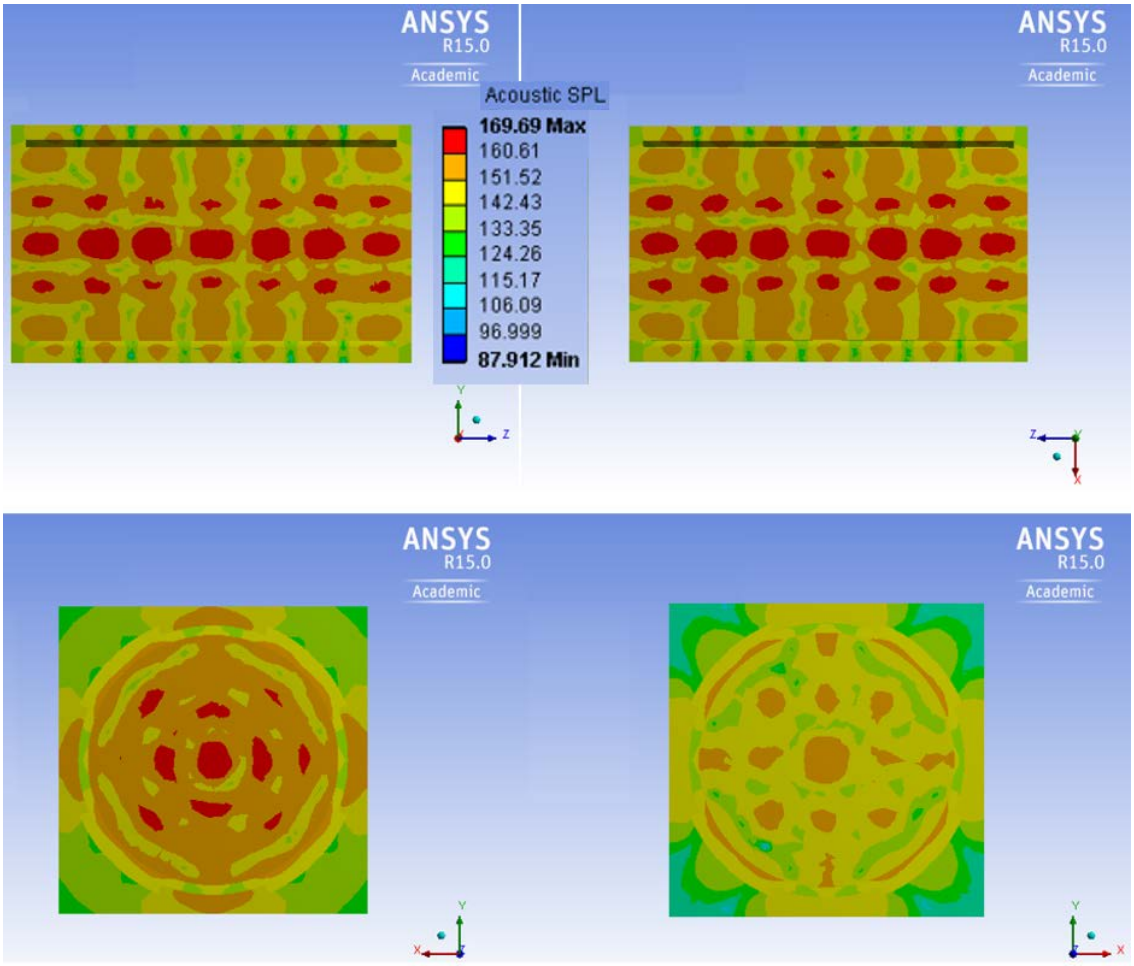

Fig.B-27. Acoustic field in SPL for a potential mode shape of the specimen with four external circumferential steps at 47.5 KHz; Top left: Axial view on the vertical plane, Top right: Axial view on the horizontal plane, Bottom left: Side view at mid-length, Bottom right: Side view at quarter-length.

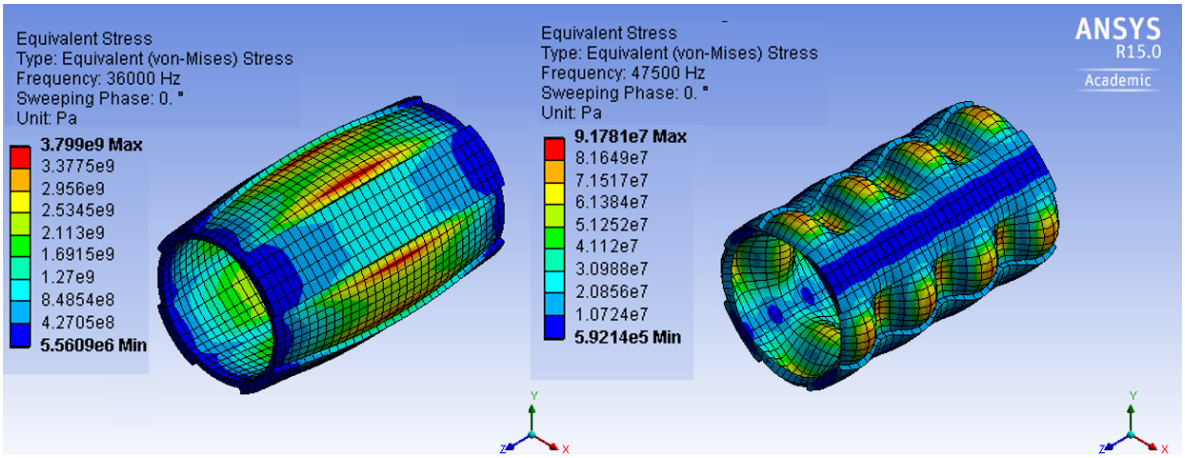

Fig.B-28. Stress distribution for the specimen with four external circumferential steps at Left: 36 KHz and Right: 47.5 KHz.

B.3.2 Transducer with Four Internal Circumferential Steps

This specimen is designed in a similar way to the previous one but has internal steps as in Fig.B-29. The maximum value of the acoustic SPL for this specimen occurs at 37.5 KHz the mode shape of which is depicted in Fig.B-30. Further, Fig.B-31 illustrates the resultant acoustic field.

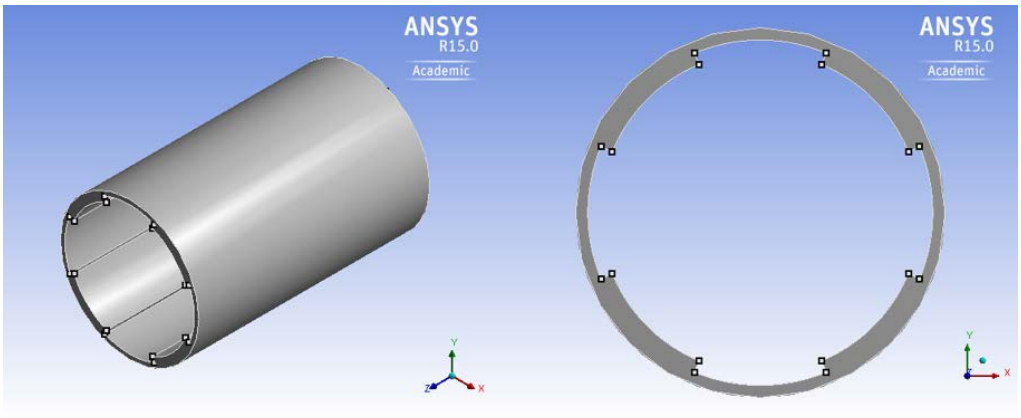

Fig.B-29. Schematic of specimen with four internal circumferential steps; Left: ISO view, Right: Side view.

Axial and circumferential wave numbers are (1, 4) as in Fig.B-30. The axial wave number is the same as the number of steps and the vibration is localized within the machined regions. The amplitude of vibration is orders of magnitude larger than the uniform-thickness case. Due to the symmetry in the geometry, the resultant acoustic field is also the same in both axial views as in Fig.B-31. The maximum level of SPL is 205 dB. The side views at mid- and quarter lengths shown in this figure clearly reveal that the acoustic field is quite uniform along the length as there is a small difference between these two side views at different lengths. However, the stress distribution in the thin, machined regions is at a very large level (10^9 Pa) which is not suitable as in Fig.B-32.

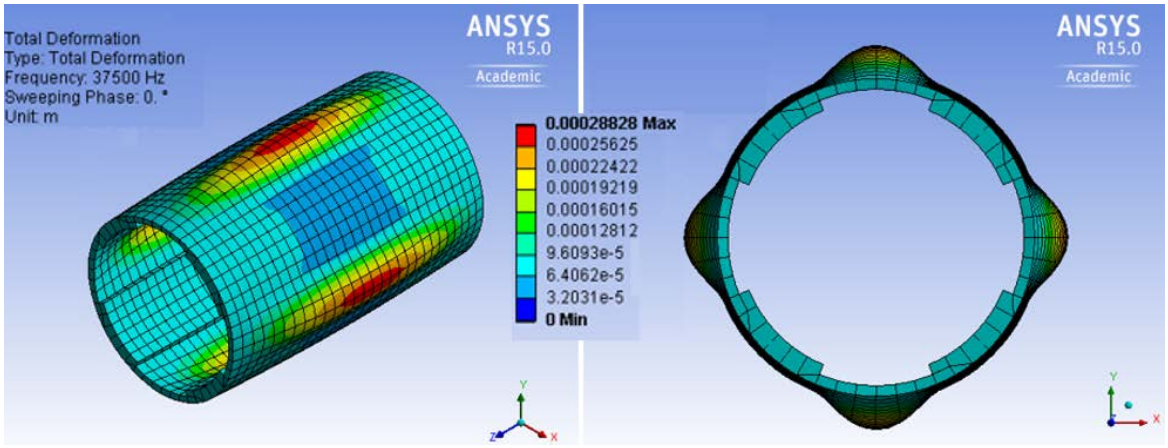

Fig.B-30. Harmonic analysis results for a potential mode shape of the specimen with four internal circumferential steps at 37.5 KHz; Left: ISO view, Right: Side view.

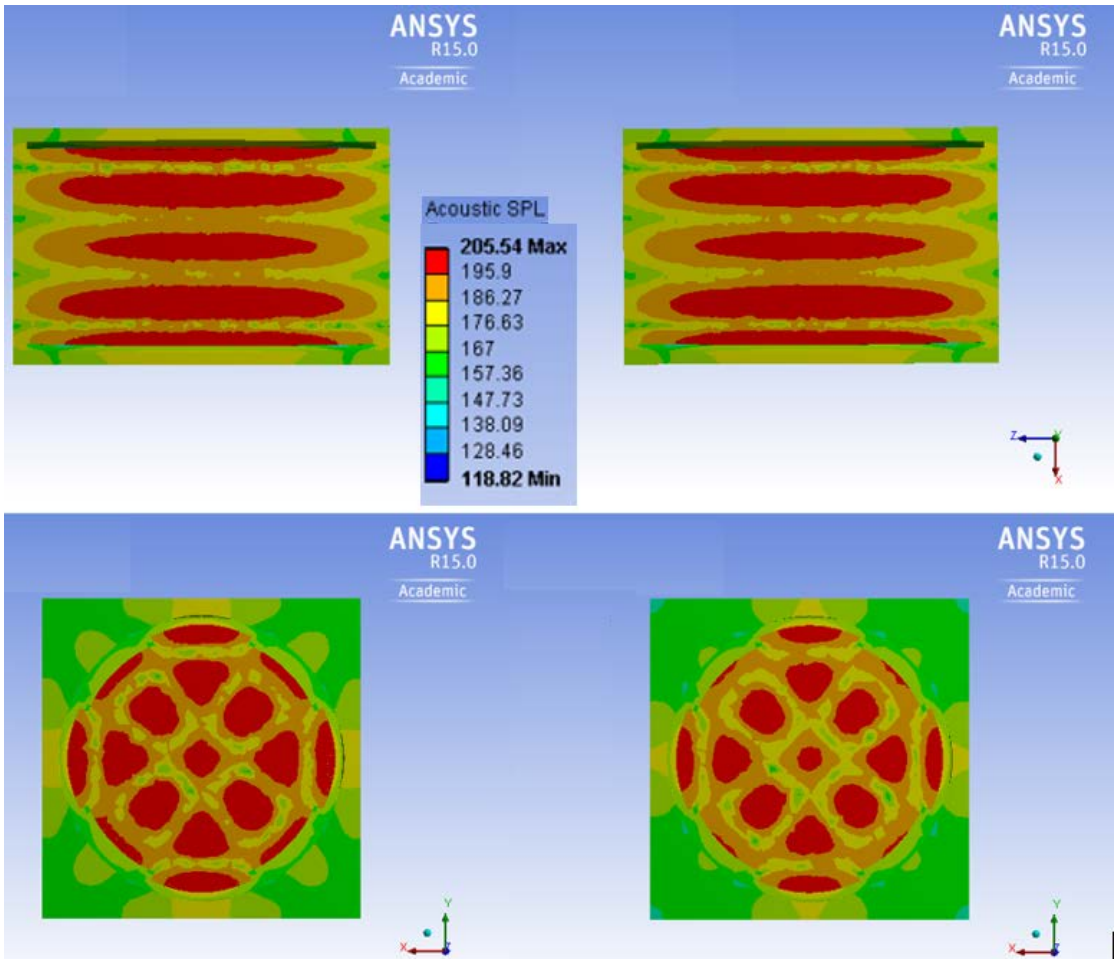

Fig.B-31. Acoustic field in SPL for a potential mode shape of the specimen with four internal circumferential steps at 37.5 KHz; Top left: Axial view on the vertical plane, Top right: Axial view on the horizontal plane, Bottom left: Side view at mid-length, Bottom right: Side view at quarter-length.

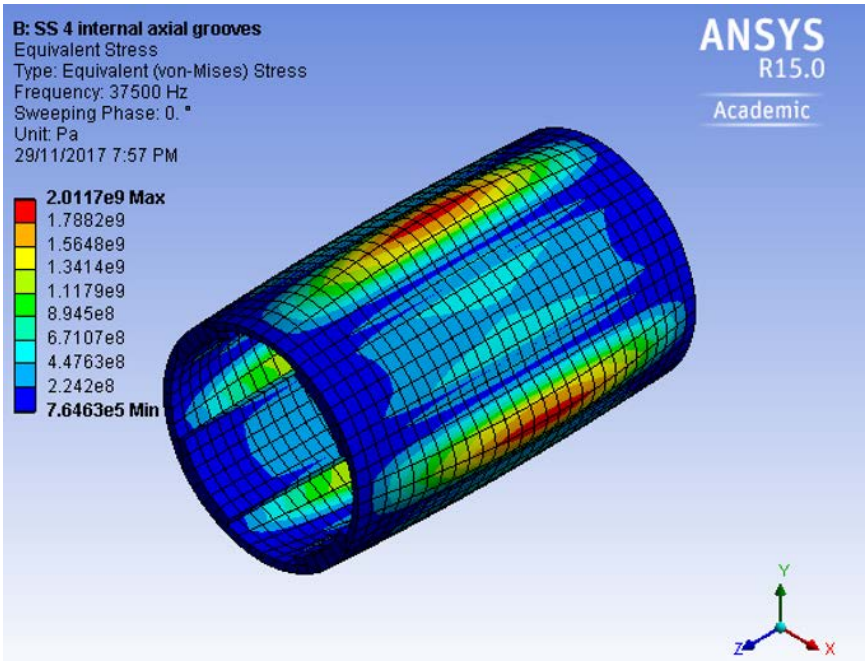

Fig.B-32. Stress distribution for the specimen with four internal circumferential steps at 37.5 KHz.

B.4. Development of the Transducers with Five External/Internal Circumferential Steps

This section includes the investigations on the transducer with five circumferential steps either external or internal and is divided into sections for each of them.

B.4.1. Transducer with Five External Circumferential Steps

To excite the transducer at the mode shape with the circumferential wave number of five, the whole circumference is divided into 10 equal sections half of which are thick and the other half are machined as in Fig.B-33. The maximum value of the acoustic SPL for this specimen occurs at 30.5 the mode shape of which is depicted in Fig.B-34. Further, Fig.B-35 illustrates the resultant acoustic field. Axial and circumferential wave numbers are (3, 0) as in Fig.B-34. Zero circumferential wave number results in identical axial views as mentioned earlier. It is seen that the circumferential wave number is the same as the uniform-thickness tube, while the axial wave number differs.

As evident, the vibration is not localized within the machined regions for this frequency and is uniformly distributed around the circumference.

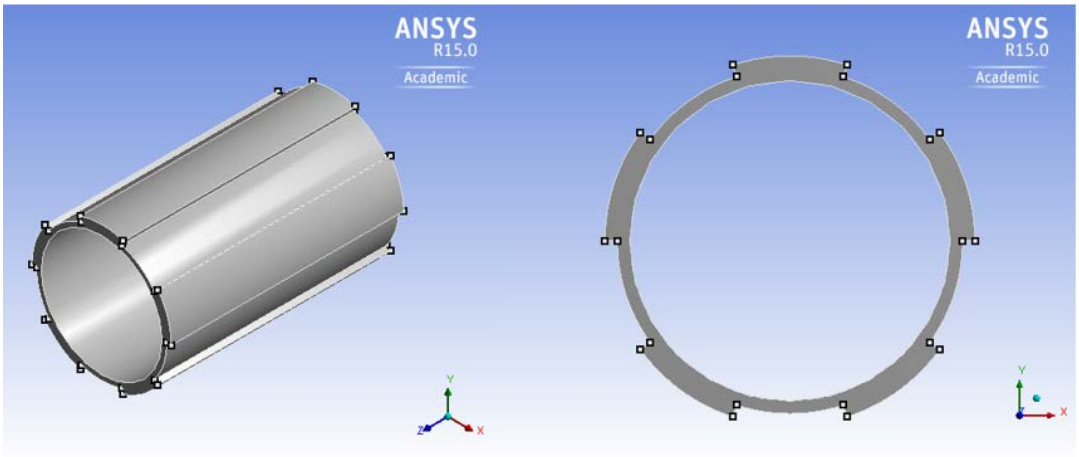

Fig.B-33. Schematic of specimen with five external circumferential steps; Left: ISO view, Right: Side view.

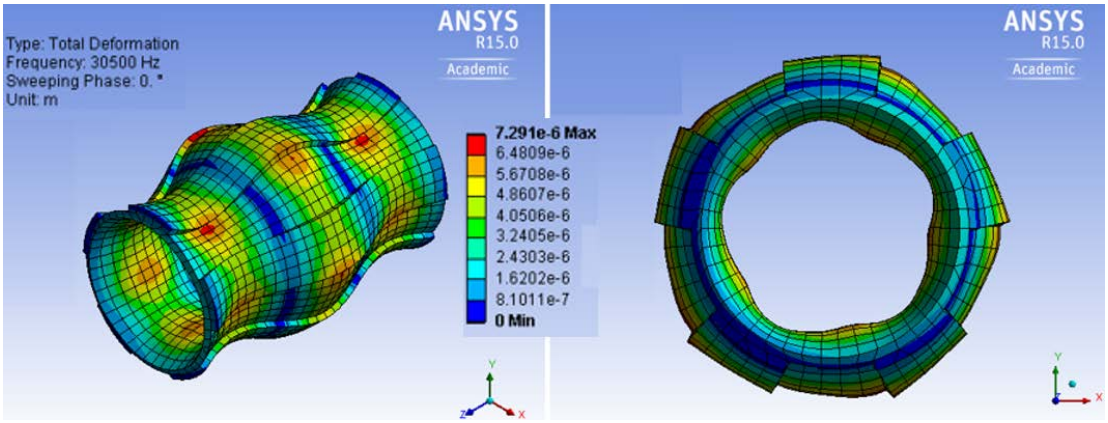

Fig.B-34. Harmonic analysis results for a potential mode shape of the specimen with five external circumferential steps at 30.5 KHz; Left: ISO view, Right: Side view.

Comparison of the acoustic fields for this specimen as in Fig.B-35 and the uniform-thickness transducer reveals a nearly identical side view due to the same circumferential wave number, while the axial view is slightly different which is caused by various axial wave numbers. The maximum level of SPL is 171 dB which is very close to that of the uniform-thickness specimen and the amplitude of vibration is one

order of magnitude larger here. The stress distribution in most regions is at a safe range around 30 MPa and the maximum is 48 MPa as in Fig.B-36.

It is worth noting that at 32 KHz, the wave numbers are (1, 5) and the amplitude of vibration is an order of magnitude larger than that of the uniform-thickness specimen. The vibration is localized within the machined regions, however, since many thick parts of the transducer are not actually vibrating (vibrating at a very low amplitude) and do not take part in acoustic generation, the resultant acoustic field has the maximum level of SPL at 160 dB which is lower than the uniform-thickness specimen.

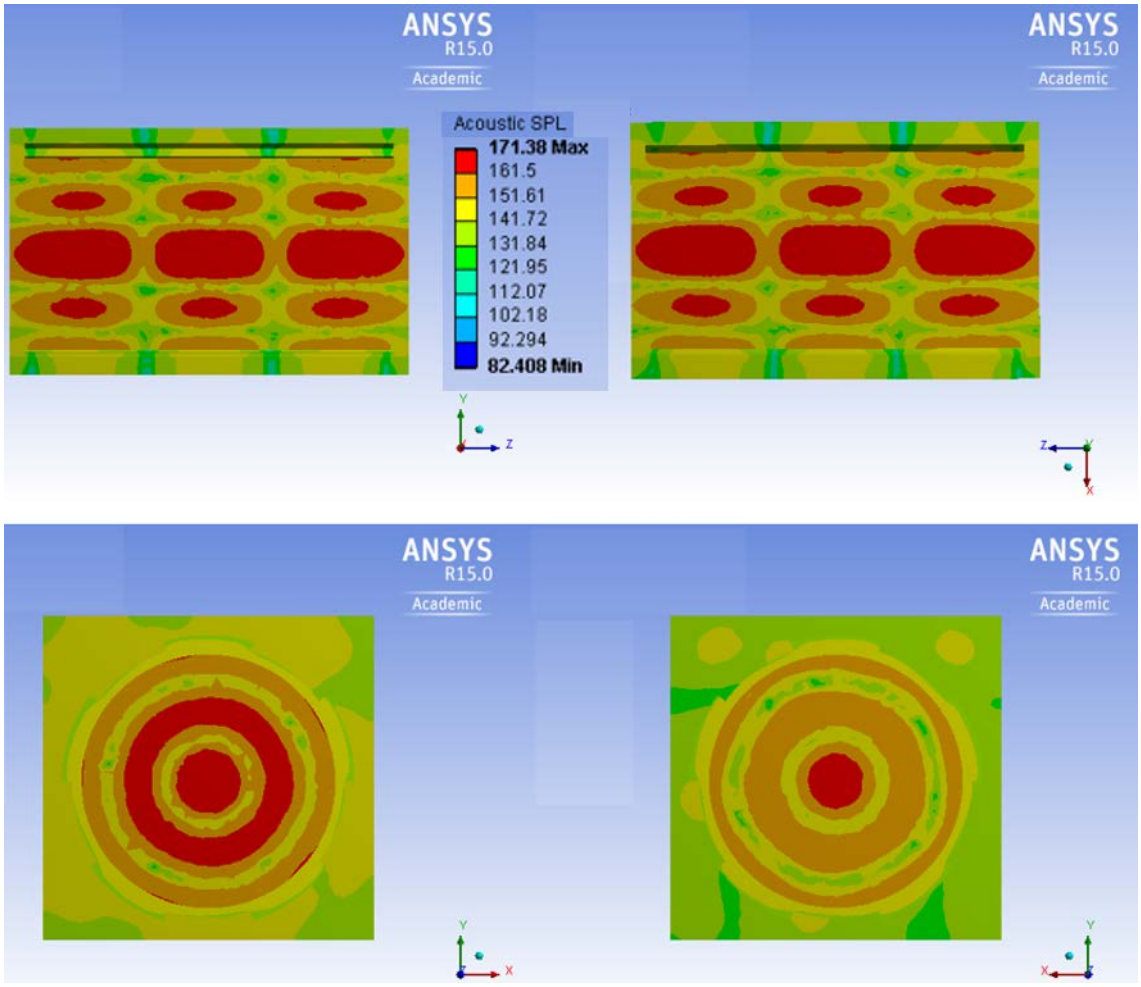

Fig.B-35. Acoustic field in SPL for a potential mode shape of the specimen with five external circumferential steps at 30.5 KHz; Top left: Axial view on the vertical plane, Top right: Axial view on the horizontal plane, Bottom left: Side view at mid-length, Bottom right: Side view at quarter-length.

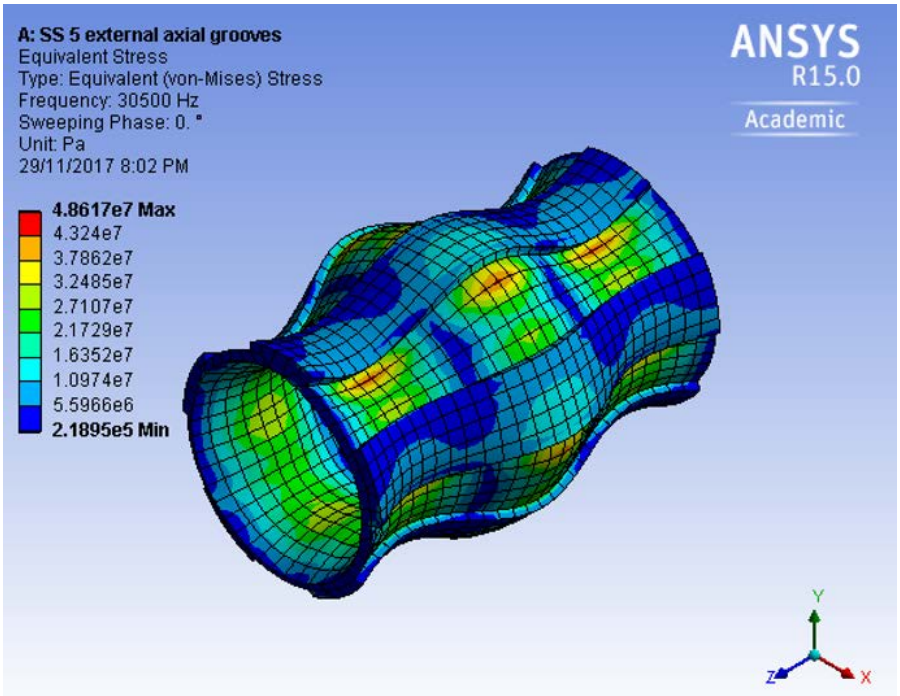

Fig.B-36. Stress distribution for the specimen with five external circumferential steps at 30.5 KHz.

B.4.2. Transducer with Five Internal Circumferential Steps

This specimen is designed in a similar way to the previous one but has internal steps as in Fig.B-37. The maximum value of the acoustic SPL for this specimen occurs at 28.5 and 41.5 KHz the mode shapes of which are depicted in Figs.B-38 and B-39. Further, Figs.B-40 and B-41 illustrate the resultant acoustic field for frequencies of 28.5 and 41.5 KHz, respectively. The maximum levels of SPL are 173 dB and 188 dB, respectively. Axial and circumferential wave numbers for the mode shape at 28.5 and 41.5 KHz are both (1, 5) as in Figs.B-38 and 39. However, there is a difference between them. At 28.5 KHz, the thick regions are vibrating slightly in counter-phase with the machined regions which causes some sort of phase cancellation, while at 41.5 KHz these regions are not vibrating (or vibrating at a very low amplitude) and therefore, the resultant acoustic field has a higher level of SPL as evident by comparing Figs.B-40 and 41. Axial views on horizontal and vertical planes in each case are similar but not exactly identical which is due to the asymmetry in the geometry as

mentioned previously. The amplitude of vibration in both cases is orders of magnitude larger than the uniform-thickness specimen. However, in one case (41.5 KHz), the vibration is localized within the machined regions, whereas in the other case (28.5 KHz), it is approximately uniformly distributed over thin and thick regions in counter-phase causing destructive interference. This causes the SPL to be lower at this frequency compared to the other case.

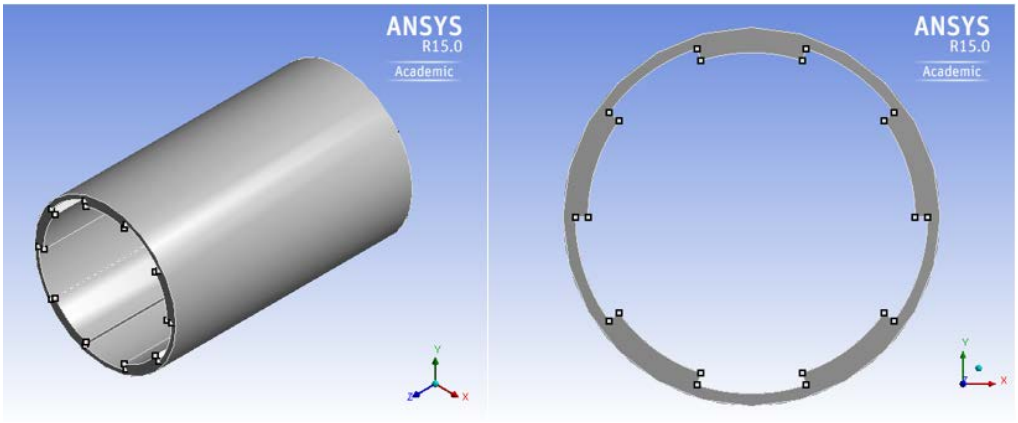

Fig.B-37. Schematic of specimen with five internal circumferential steps; Left: ISO view, Right: Side view.

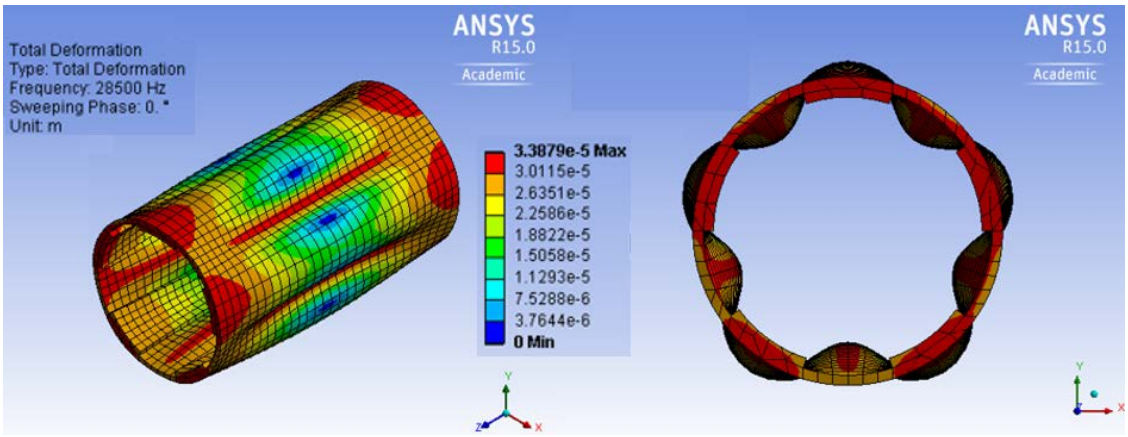

Fig.B-38. Harmonic analysis results for a potential mode shape of the specimen with five internal circumferential steps at 28.5 KHz; Left: ISO view, Right: Side view.

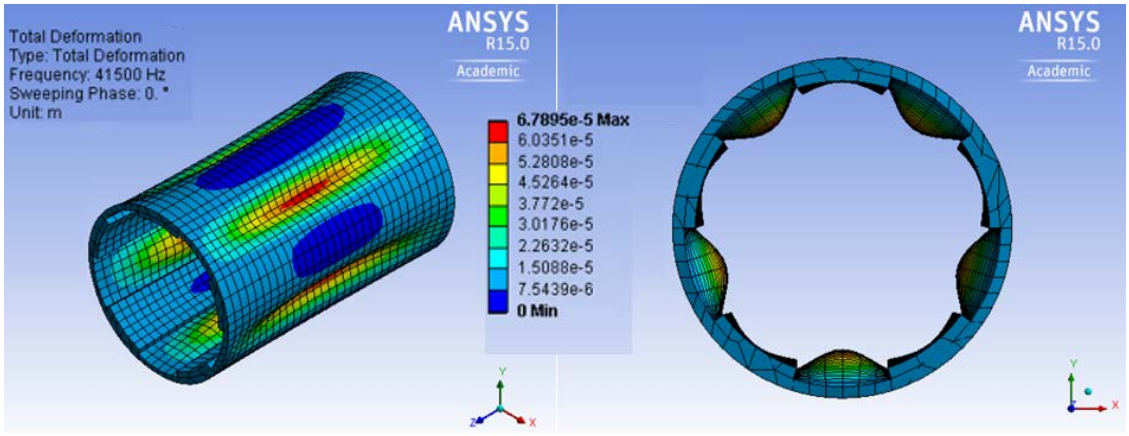

Fig.B-39. Harmonic analysis results for a potential mode shape of the specimen with five internal circumferential steps at 41.5 KHz; Left: ISO view, Right: Side view.

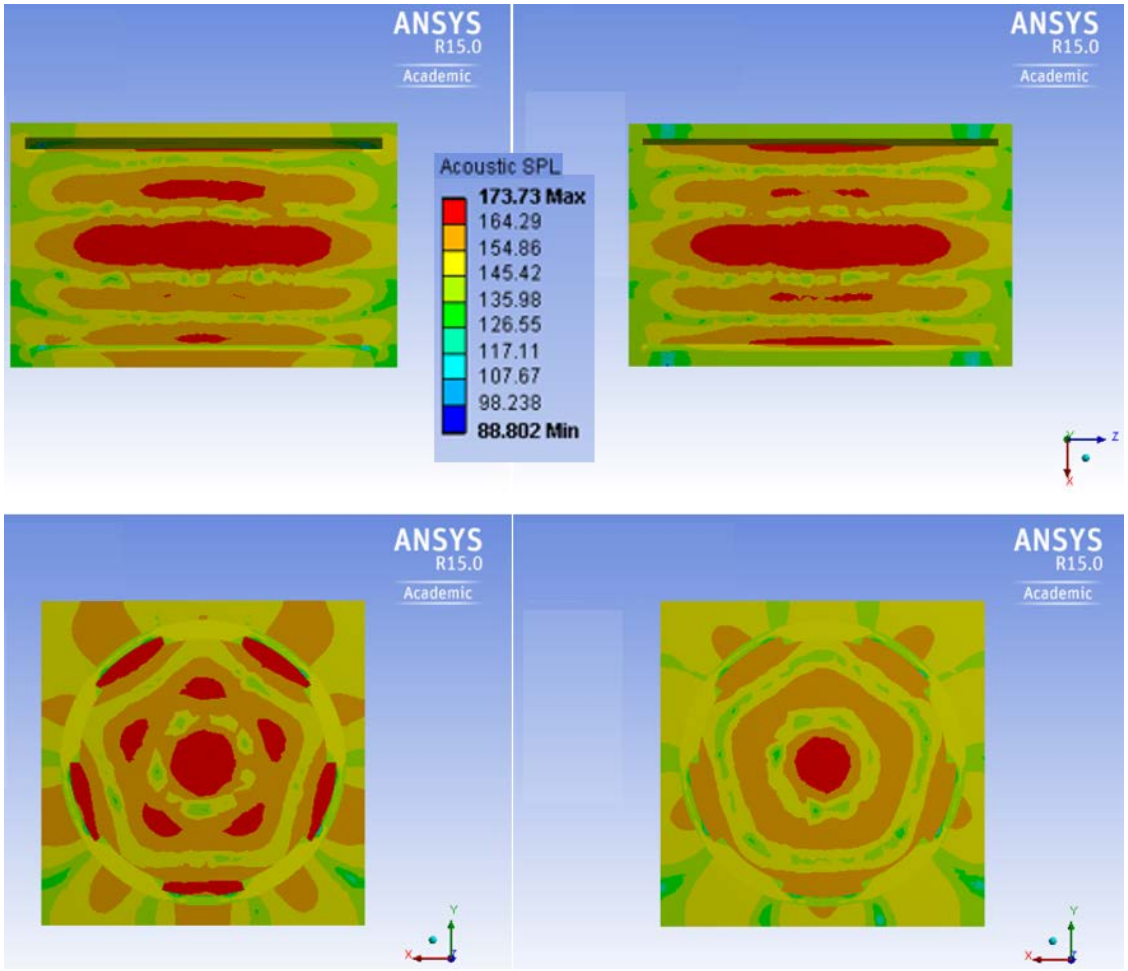

Fig.B-40. Acoustic field in SPL for a potential mode shape of the specimen with five internal circumferential steps at 28.5 KHz; Top left: Axial view on the vertical plane, Top right: Axial view on the horizontal plane, Bottom left: Side view at mid-length, Bottom right: Side view at quarter-length.

Further, side views reveal that there is a noticeable difference in SPL between mid- and quarter- lengths of the specimen for 41.5 KHz. This difference is not that

conspicuous in the case of 28.5 KHz. The acoustic field is more uniform along the length of the transducer at the centreline for 28.5 KHz. This can also be understood by comparing the red regions along the length in Figs.B-38 and 39. Longer length of the specimen is at the maximum range of vibration at 28.5 KHz. The stress distribution for both cases is in the order of 10^8 Pa which is not suitable as in Fig.B-42. For the case of 28.5 KHz, it is in this order in most regions. However, for the case of 41.5 KHz, it is higher in the thin, machined regions. Hence, from the stress point of view, none of these cases are suitable.

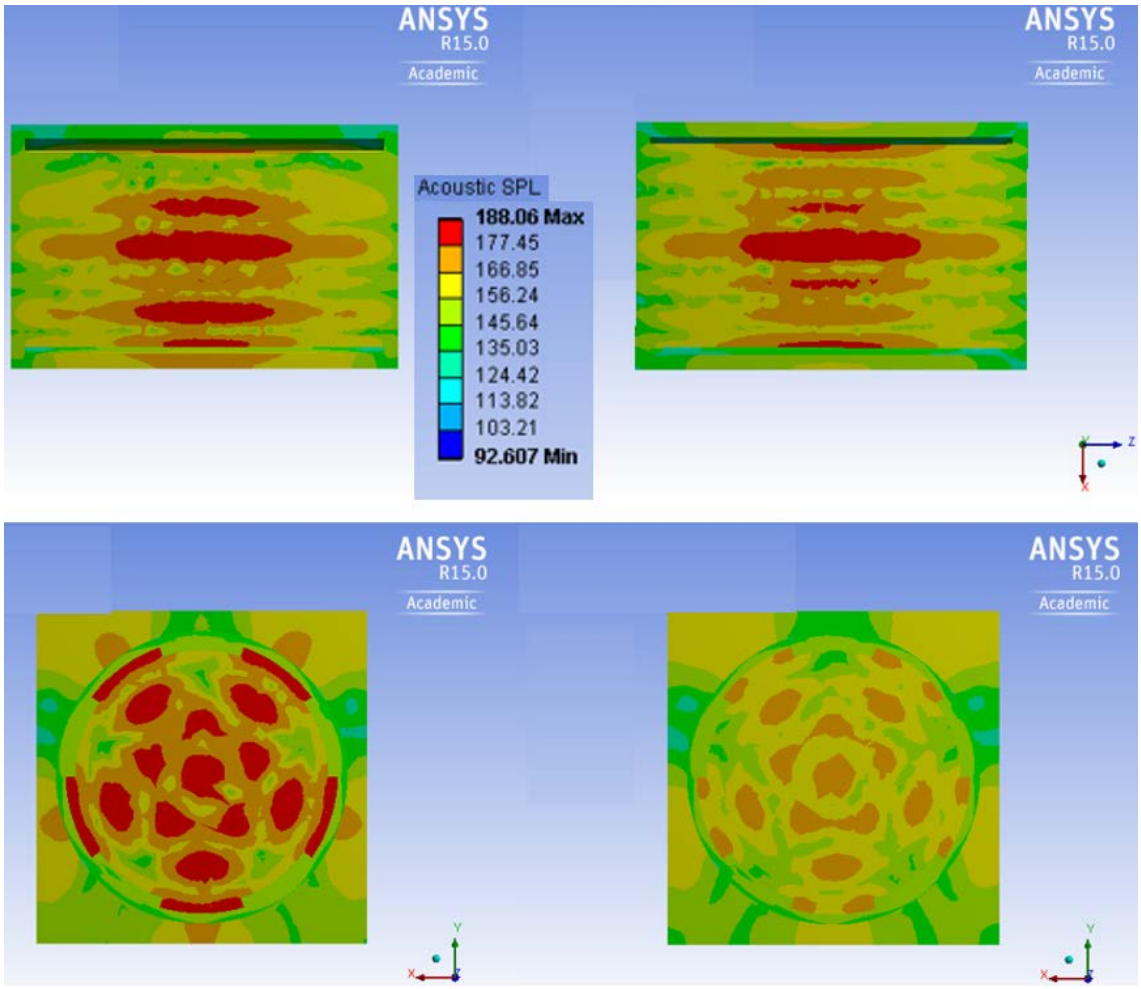

Fig.B-41. Acoustic field in SPL for a potential mode shape of the specimen with five internal circumferential steps at 41.5 KHz; Top left: Axial view on the vertical plane, Top right: Axial view on the horizontal plane, Bottom left: Side view at mid-length, Bottom right: Side view at quarter-length.

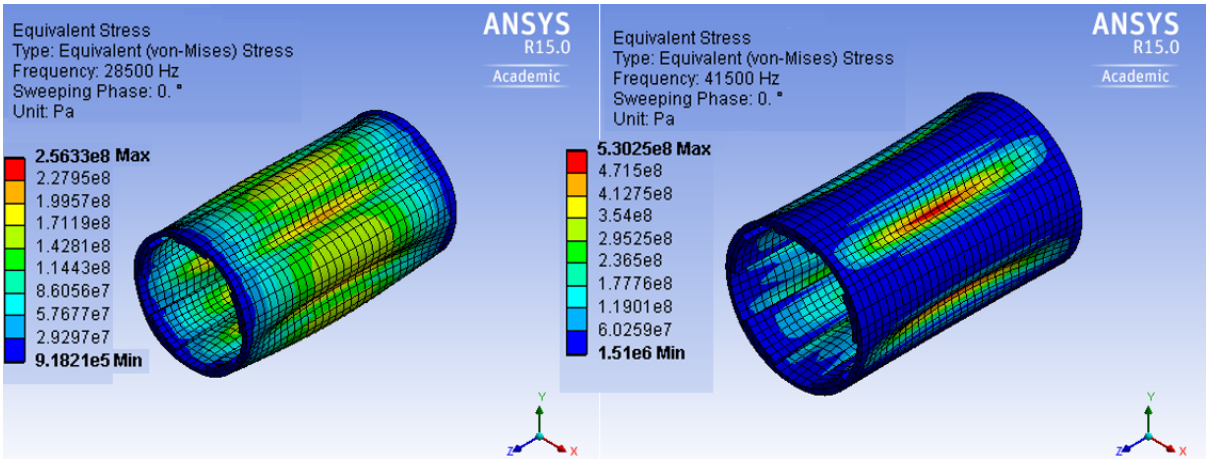

Fig.B-42. Stress distribution for the specimen with five internal circumferential steps at Left: 28.5 KHz and Right: 41.5 KHz.

B.5. Development of the Transducer with Six External Circumferential Steps

To excite the transducer at the mode shape with the circumferential wave number of six, the whole circumference is divided into 12 equal sections half of which are thick and the other half are machined as in Fig.B-43. The maximum value of the acoustic SPL for this specimen occurs at 43 KHz the mode shape of which is depicted in Fig.B-44. Further, Fig.B-45 illustrates the resultant acoustic field. The maximum level of SPL is 177 dB. The circumferential wave number is the same as the number of steps and the vibration is localized within the machined regions. However, the amplitude of vibration is the same order of magnitude as the uniform-thickness case. Nevertheless, the acoustic field has a higher level of SPL which may be due to the localization of vibration within the machined regions. Due to the symmetry in the geometry and the mode shape, the resultant acoustic field is also the same in both axial views as in Fig.B-45.

The maximum level of SPL as the red colour-coded region occurs along the length of the transducer at the centreline. The maximum stress is around 3 MPa which is within a safe and suitable range as in Fig.B-46.

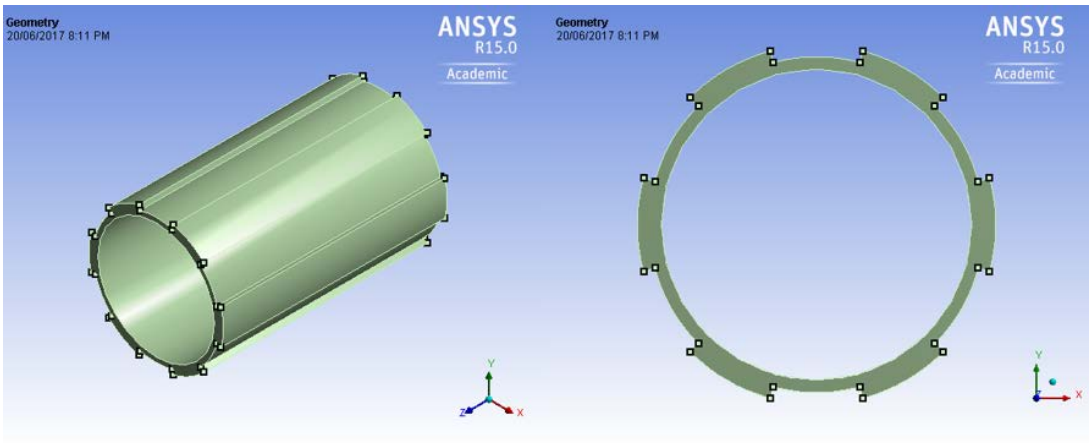

Fig.B-43. Schematic of specimen with six external circumferential steps; Left: ISO view, Right: Side view.

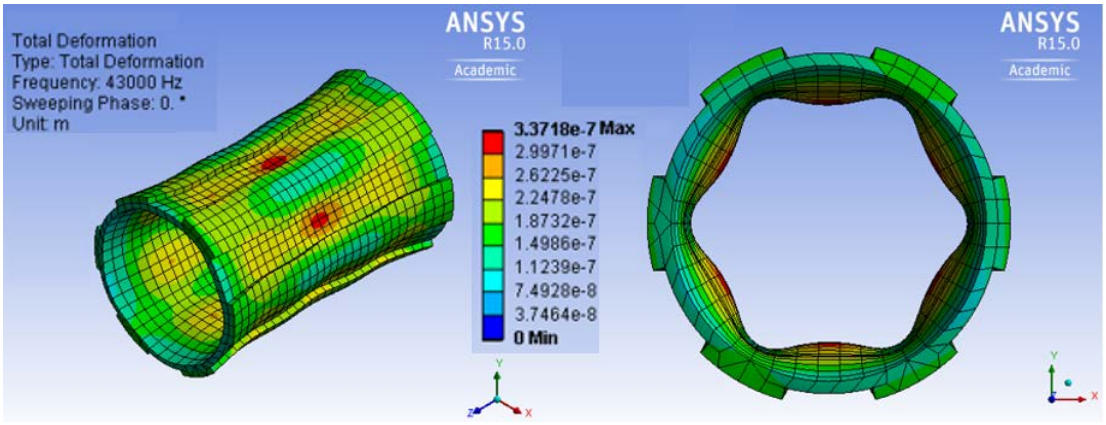

Fig.B-44. Harmonic analysis results for a potential mode shape of the specimen with six external circumferential steps at 43 KHz; Left: ISO view, Right: Side view.

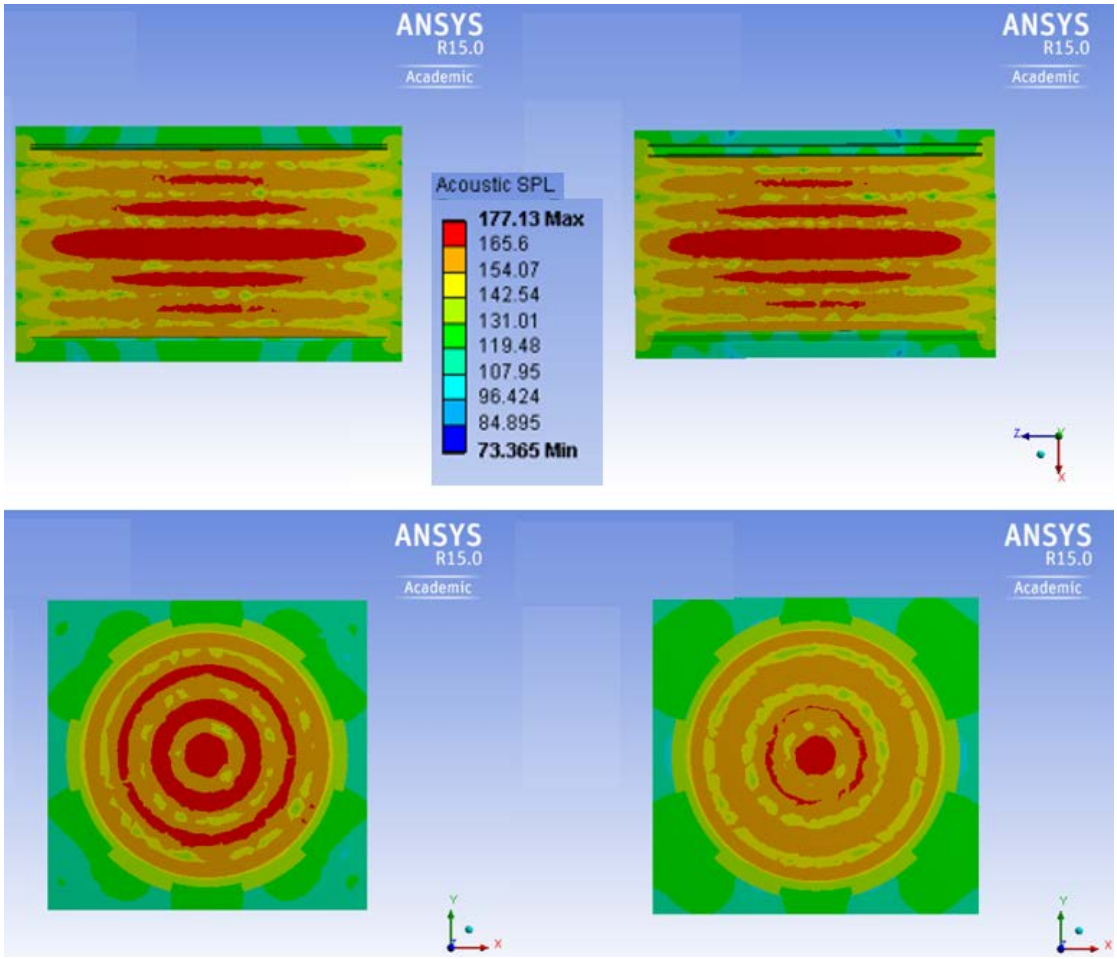

Fig.B-45. Acoustic field in SPL for a potential mode shape of the specimen with six external circumferential steps at 43 KHz; Top left: Axial view on the vertical plane, Top right: Axial view on the horizontal plane, Bottom left: Side view at mid-length, Bottom right: Side view at quarter-length.

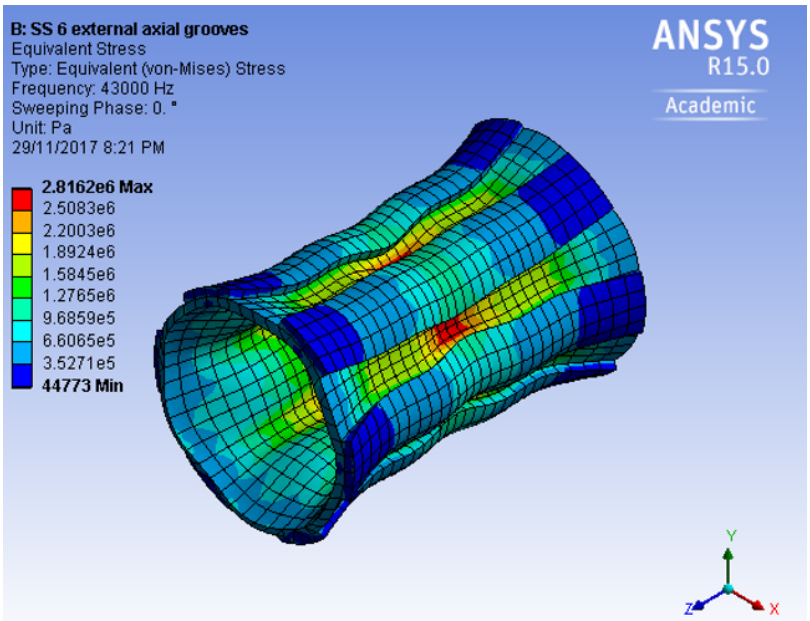

Fig.B-46. Stress distribution for the specimen with six external circumferential steps at 43 KHz.

B.6. Development of the Transducers with Two External/Internal Axial Steps

This section includes the investigations on the transducer with two axial steps either external or internal and is divided into sections for each of them.

B.6.1. Transducer with Two External Axial Steps

As discussed earlier for the specimens with one internal and one external step, the location of steps for specimens with two steps should be carefully identified. Based on the mode shape for the uniform-thickness specimen in Fig. 4-4 with wave numbers of (5, 0), it includes two regions in counter-phase with the other three regions. It is intended to machine the area between each two consecutive in-phase regions in order to localize the vibration within those thin areas and achieve higher vibration amplitudes. Thus, two regions of the tube, which were in counter-phase with the other three regions, were machined by one millimetre from the outer surface. Following these explanations, we came up with two steps each 11.5 mm long and the thick region in between is 7 mm long. The other two regions will be 10 mm long each. The simulations are performed for this specimen which is depicted in Fig.B-47. The maximum value of the acoustic SPL for the specimen occurs at 33 KHz and 36 KHz the mode shapes of which are depicted in Fig.B-48. Further, Figs.B-49 and B-50 illustrate the resultant acoustic fields. The maximum level of SPL for both cases is 179 dB. Axial and circumferential wave numbers are (3, 0) and (1, 0) for 33KHz and 36KHz, respectively.

For the case of 33 KHz, the vibration amplitude is not localized within the machined area. Instead, half of the red region corresponding to the maximum amplitude in Fig.B-48 is on the thin region and the other half on the thick region. The stress is in the order of 10^8 Pa as in Fig.B-51 which is so high and not suitable.

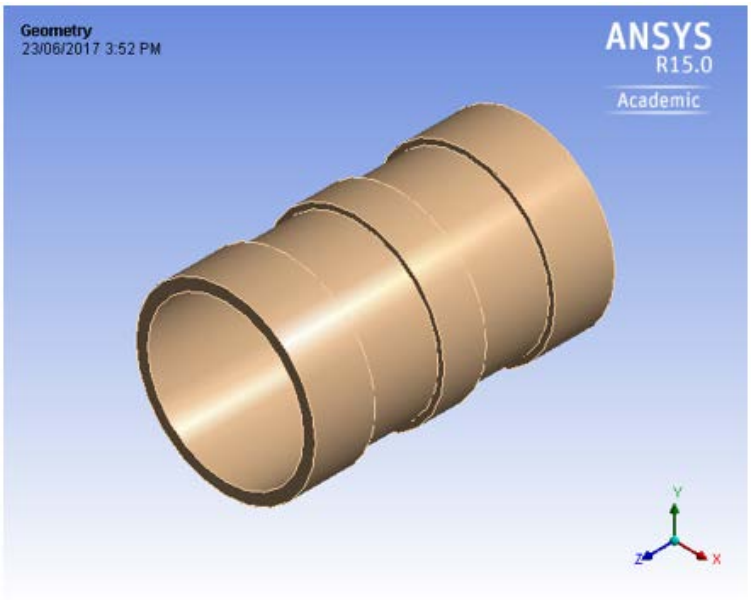

Fig.B-47. Schematic of specimen with two external axial steps in ISO view.

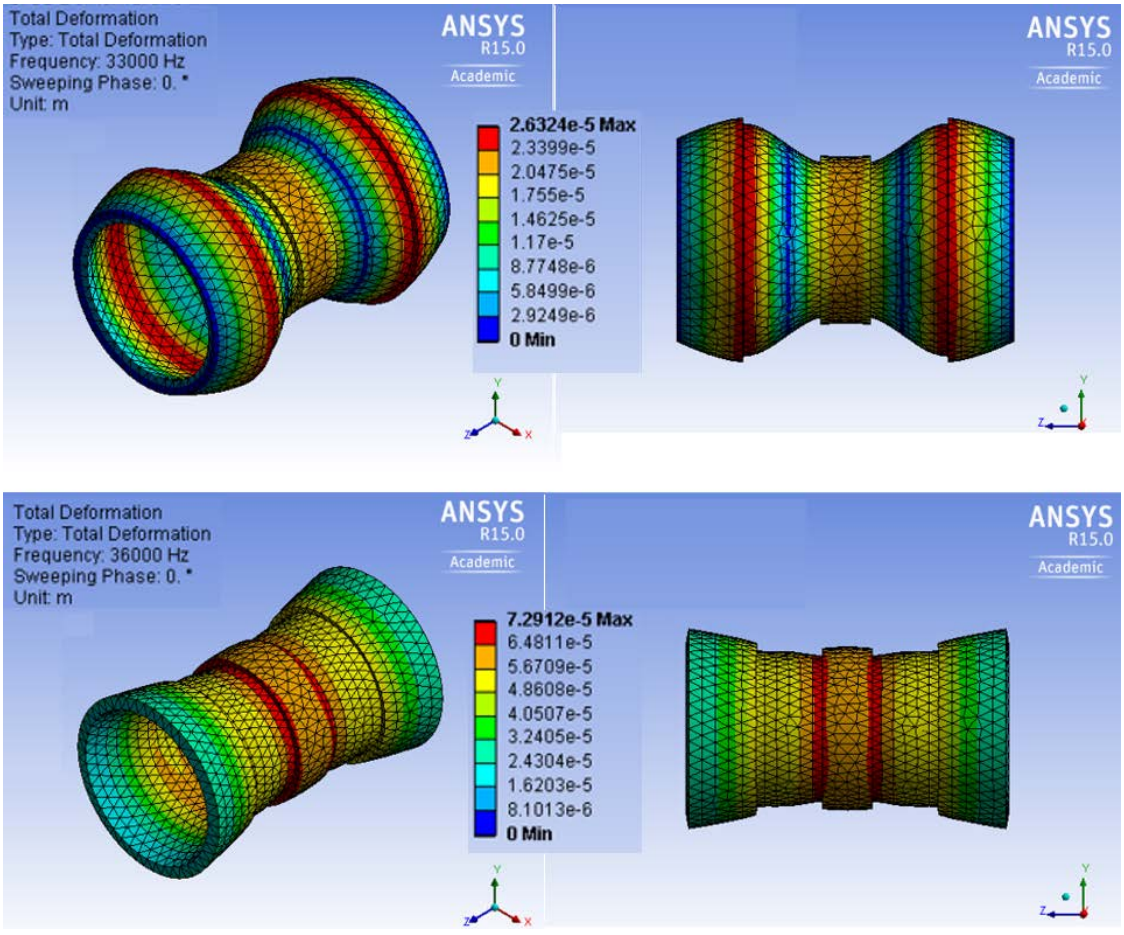

Fig.B-48. Harmonic analysis results for potential mode shapes of the specimen with two external axial steps, Top: ISO and side views at 33 KHz, Bottom: at 36 KHz.

Moreover, although the maximum level is high at 179 dB, axial and side views clearly illustrate that many regions inside the transducer are at lower levels corresponding to yellow and orange colour codes averaging at around 160 dB. Considering all these explanations, this specimen does not seem to be a very suitable alternative compared to some other specimens investigated so far. For the case of 36 KHz, the vibration as in Fig.B-48 is localized close to the edges of the steps and not fully inside the machined region. However, this provides a more uniform acoustic field as in Fig.B-50. Nonetheless, many regions inside the transducer as in the axial and side views of this figure are in the range of green, yellow and orange colour codes averaging at a lower level of SPL.

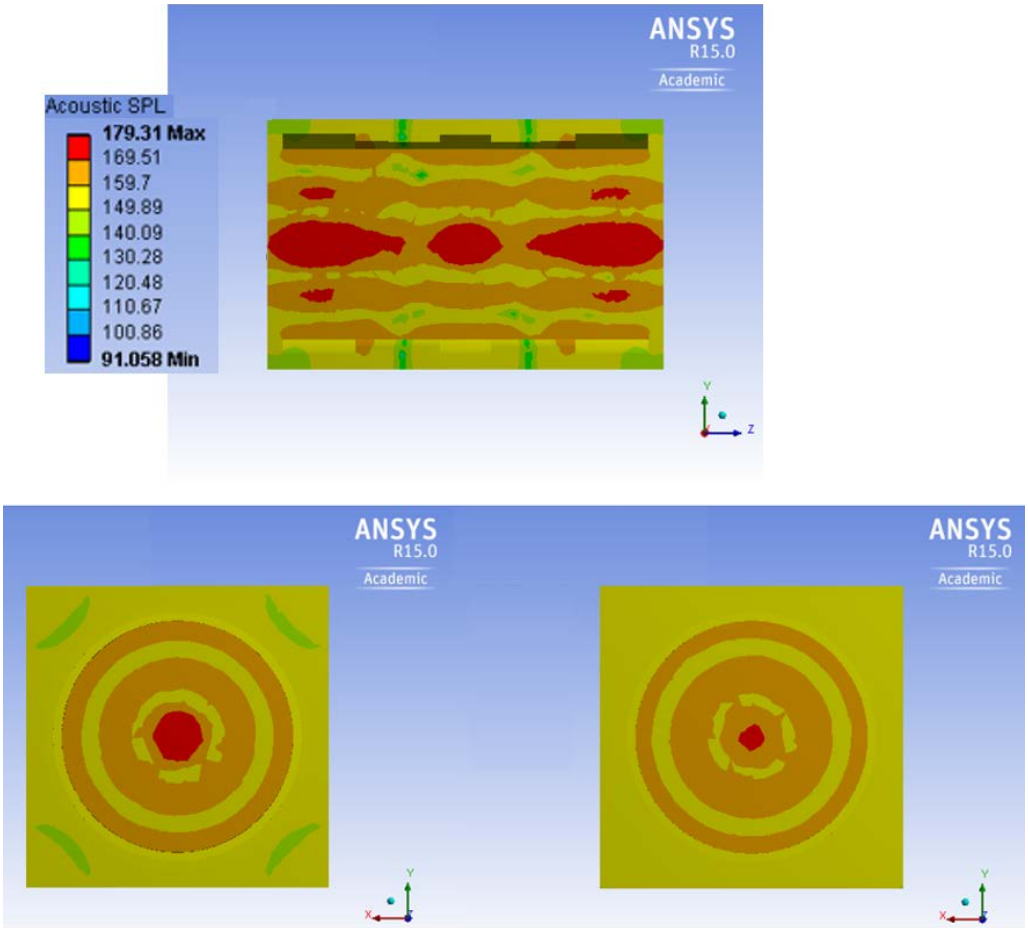

Fig.B-49. Acoustic field in SPL for a potential mode shape of the specimen with two external axial steps at 33 KHz; Top: Axial view on the vertical plane, Bottom left: Side view at mid-length, Bottom right: Side view at quarter-length.

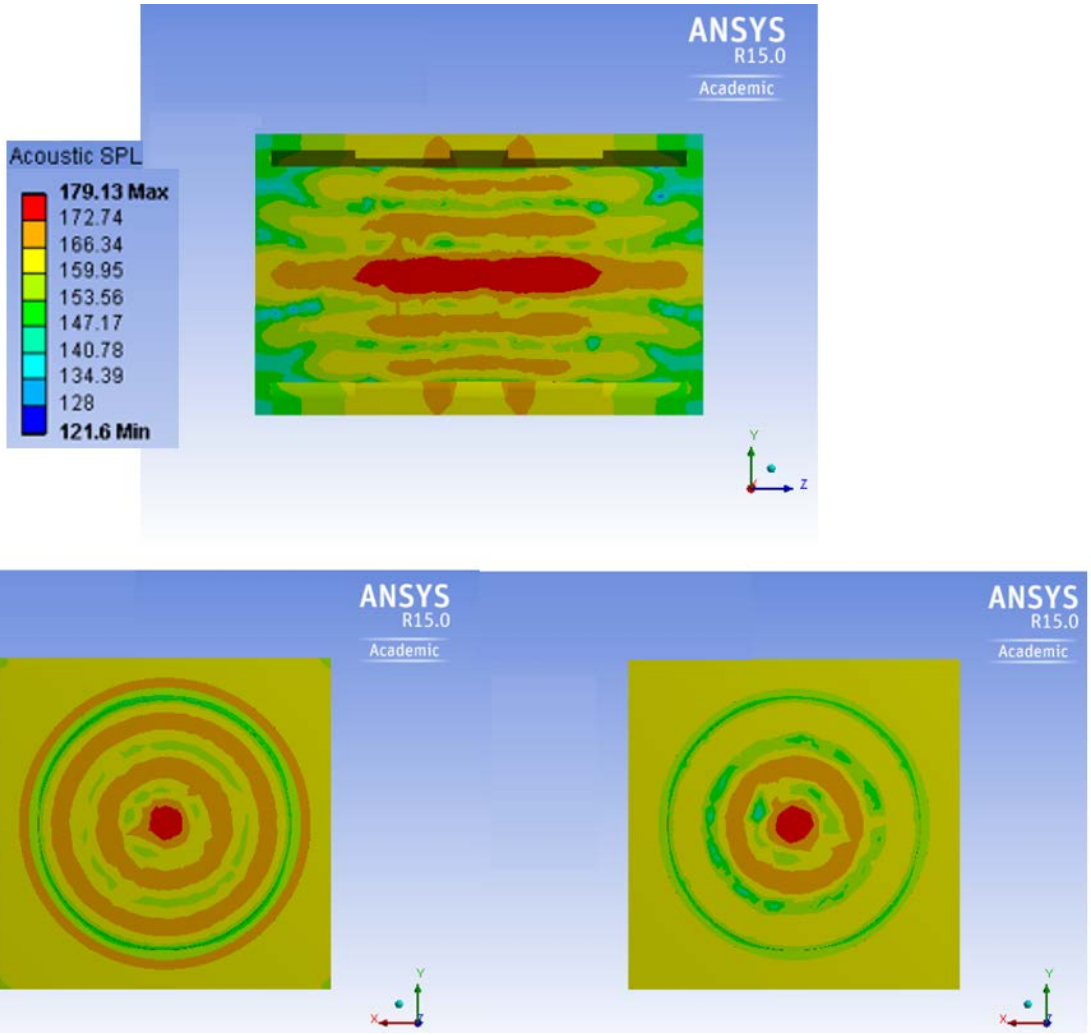

Fig.B-50. Acoustic field in SPL for a potential mode shape of the specimen with two external axial steps at 36 KHz; Top: Axial view on the vertical plane, Bottom left: Side view at mid-length, Bottom right: Side view at quarter-length.

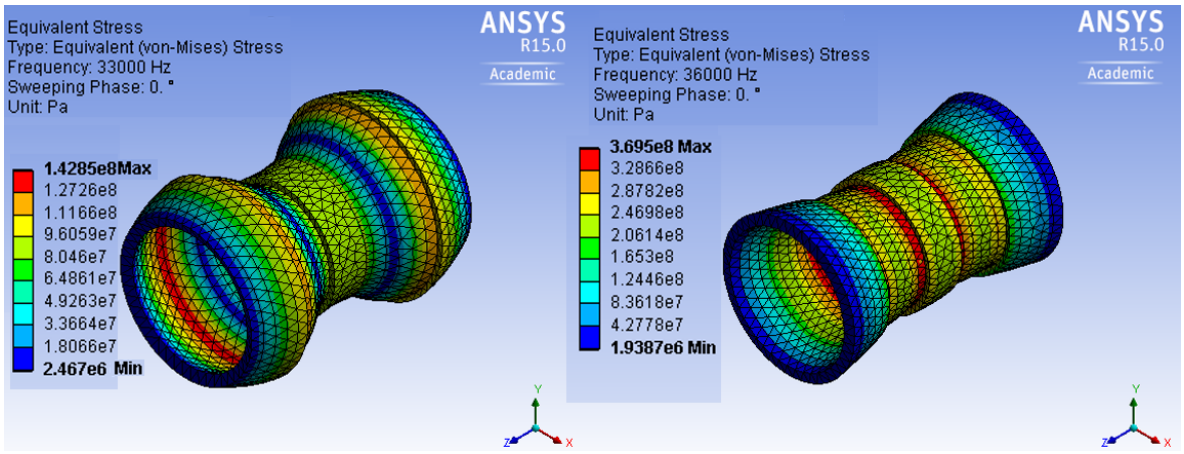

Fig.B-51. Stress distribution for the specimen with two external axial steps at Left: 33 KHz and Right: 36 KHz.

On the whole, this case at 36KHz seems to be a better option compared to the one at 33 KHz. However, the stress is in the order of 10^8 Pa as in Fig.B-51 which is not suitable.

B.6.2. Transducer with Two Internal Axial Steps

This specimen is designed similar to the previous one but has internal steps as in Fig.B-52. The simulations are performed and the maximum value of the acoustic SPL occurs at 40.5 KHz the mode shape of which is depicted in Fig.B-53. Further, Fig.B-54 illustrates the resultant acoustic field. The maximum level of SPL is 173 dB. Axial and circumferential wave numbers are (5, 0). In this case, the vibration is efficiently localized within the machined areas as in Fig.B-53 and all the thick regions are in the blue range of amplitude which corresponds to nearly zero displacement. Analysing Fig.B-54 for the acoustic field clearly reveals the focusing pattern of the acoustic waves from the machined regions. As evident from Fig.B-53, the amplitude of vibration is only one order of magnitude larger than the uniform-thickness specimen and therefore, the acoustic field is slightly stronger. There are some discontinuities in the resultant acoustic field and the range of maximum SPL does not cover many regions inside the transducer. These discontinuities may be due to the fact that the non-machined thick regions are vibrating at a very low amplitude and therefore, do not take part in the acoustic generation noticeably as can be seen from the acoustic pattern in Fig.B-54. Most regions are in yellow and orange bands averaging at a lower level. The maximum stress is around 42 MPa as in Fig.B-55. On the whole, the performance is not superior to the uniform-thickness specimen.

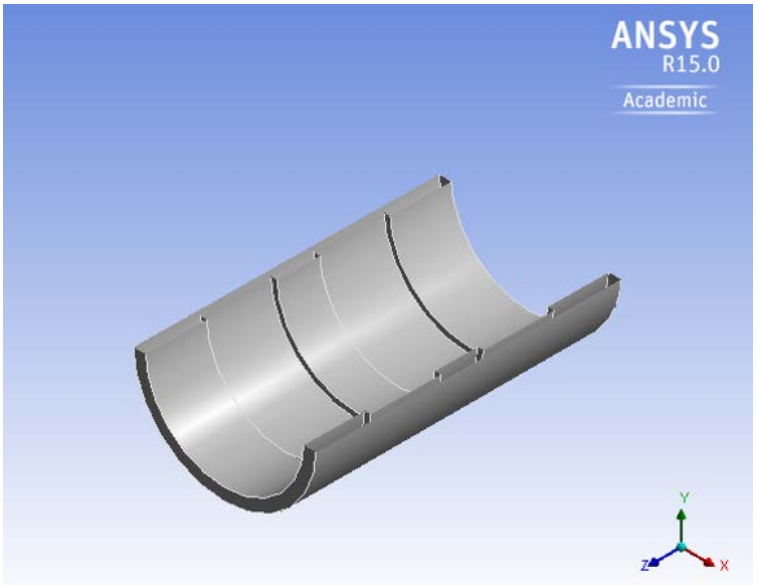

Fig.B-52. Schematic of specimen with two internal axial steps in ISO view.

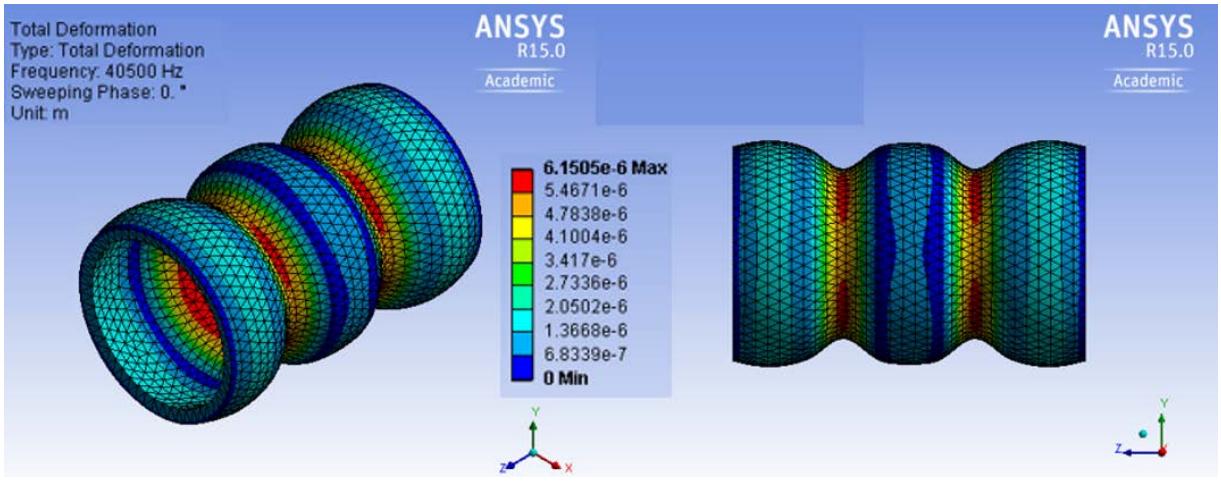

Fig.B-53. Harmonic analysis results for a potential mode shape of the specimen with two internal axial steps at 40.5 KHz; Left: ISO view, Right: Axial view.

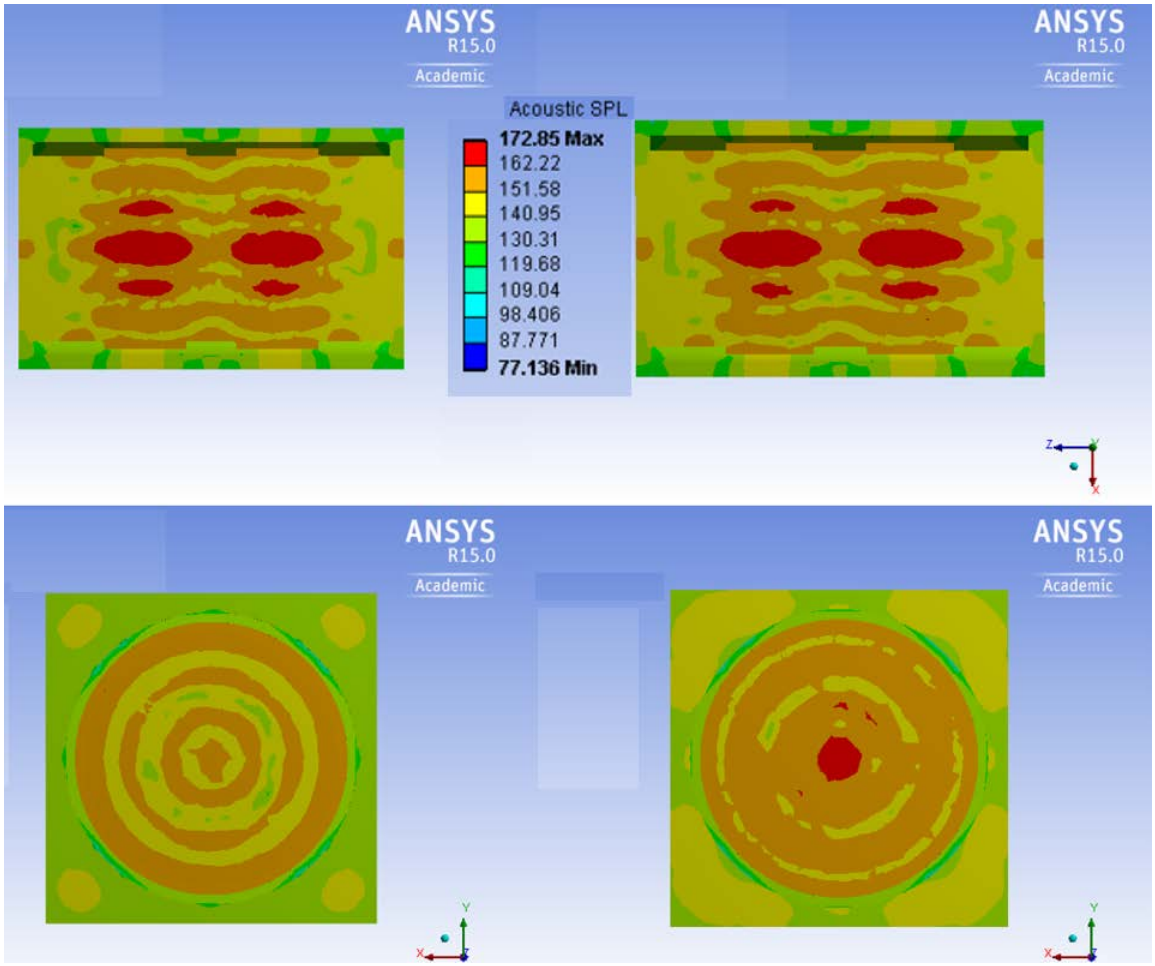

Fig.B-54. Acoustic field in SPL for a potential mode shape of the specimen with two internal axial steps at 40.5 KHz; Top left: Axial view on the vertical plane, Top right: Axial view on the horizontal plane, Bottom left: Side view at mid-length, Bottom right: Side view at quarter-length.

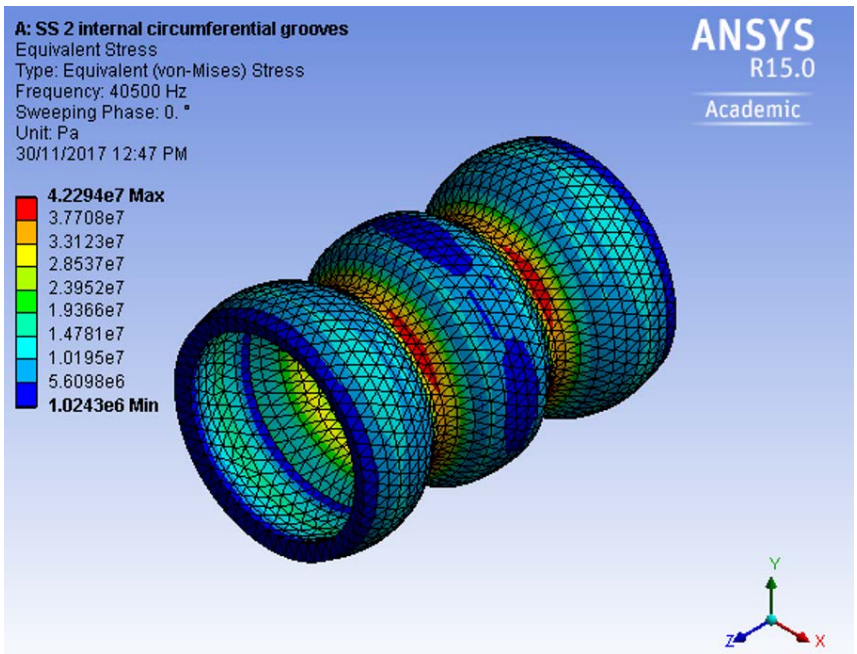

Fig.B-55. Stress distribution for the specimen with two internal axial steps at 40.5 KHz.

Bibliography

[1] M. Protheroe, An Investigation of Droplet Evaporation Characteristics in an Ultrasound Environment. (2014), Auckland University of Technology: Doctor of Philiosophy, Thesis.

[2] J.A. Gallego-Juárez, G. Rodríguez-Corral, and L. Gaete-Garreton, An ultrasonic transducer for high power applications in gases. Ultrasonics, 16(6)(1978). pp. 267-271.

[3] F.M.d. Espinosa and J.A. Gallego-Juárez, A directional single-element underwater acoustic projector. Ultrasonics, 24(2)(1986). pp. 100-104.

[4] M. Toda, Phase-Matched Air Ultrasonic Transducers Using Corrugated PVDF Film with Half Wavelength Depth. IEEE Transactions on Ultrasonics, Ferroelectrics, and Frequency Control, 48(6)(2001). pp. 1568 - 1574

[5] K.R. Sivadas and N. Ganesan, Free Vibration of Circular Cylindrical Shells with Axially Varying Thickness. Journal of Sound and Vibration, 147(1)(1991). pp. 73-85.

[6] L. Zhang and Y. Xiang, Exact solutions for vibration of stepped circular cylindrical shells. Journal of Sound and Vibration, 299(4-5)(2007). pp. 948-964.

[7] A.M. Khalifa, Exact solutions for the vibration of circumferentially stepped orthotropic circular cylindrical shells. Comptes Rendus Mécanique, 339(11)(2011). pp. 708-718.

[8] L. Xu, H. Du, H. Hu, X. Shan, H. Chen, Y. Hu, and X. Chen, Study on the Vibration Characteristics of a Finite-Width Corrugated Cylindrical Shell Piezoelectric Transducer. IEEE Transactions on Ultrasonics, Ferroelectrics, and Frequency Control, 57(6)(2010). pp. 1460-1469.

[9] M. Kurosawa, A. Futami, and T. Higuchi, Characteristics of Liquids Atomization Using Surface Acoustic Wave. Solid State Sensors and Actuators Transducers '97. (1997), IEEE: Chicago, IL

[10] S.C. Tsai, C.H. Cheng, N. Wang, Y.L. Song, C.T. Lee, and C.S. Tsai, Silicon-Based Megahertz Ultrasonic Nozzles for Production of Monodisperse Micrometer-Sized Droplets. IEEE Transactions on Ultrasonics, Ferroelectrics, and Frequency Control, 56(9)(2009). pp. 1968-1979.

[11] J.M. Meacham, A Micromachined Ultrasonic Droplet Generator: Design, Fabrication, Visualization, and Modeling. School of Mechanical Engineering. (2006), Georgia Institute of Technology.

[12] A. Barone and J.A. Gallego-Juarez, Flexural Vibrating Free-Edge Plates with Stepped Thicknesses for Generating High Directional Ultrasonic Radiation. The Journal of the Acoustical Society of America, 51(3)(1972). pp. 953-959.

[13] F. Blum, J. Jarzynski, and L.J. Jacobs, A focused two-dimensional air-coupled ultrasonic array for non-contact generation. NDT & E International, 38(8)(2005). pp. 634-642.

[14] H. Wang and M. Toda, Curved PVDF Airborne Transducer. IEEE Transactions on Ultrasonics, Ferroelectrics, and Frequency Control, 46(6)(1999). pp. 1375 - 1386.

[15] J.V. Garcia-Perez, J.A. Carcel, S.d.l. Fuente-Blanco, and E.R.F.d. Sarabia, Ultrasonic drying of foodstuff in a fluidized bed: Parametric study. Ultrasonics 44(2006). pp. 539-543.

[16] M. Berg, P. Hagedorn, and S. Gutschmidt, On the dynamics of piezoelectric cylindrical shells. Journal of Sound and Vibration, 274(1-2)(2004). pp. 91-109.

[17] S.K. Parashar and A. Kumar, Three-dimensional analytical modeling of vibration behavior of piezoceramic cylindrical shells. Archive of Applied Mechanics, 85(5)(2015). pp. 641-656.

[18] D. Berlincourt, D. Cerran, and H. Jaffe, Piezoelectric and piezomagnetic materials and their function in transducers, in Physical Acoustics. Principles and Methods. (1964), Pt A. Academic Press, New York London. p. 169–270.
[19] K. Hettiarachchi, E. Talu, M.L. Longo, P.A. Dayton, and A.P. Lee, On-chip generation of microbubbles as a practical technology for manufacturing contrast agents for ultrasonic imaging. Lab Chip, 7(4)(2007). pp. 463-8.
[20] J.S. Patton and P.R. Byron, Inhaling medicines: delivering drugs to the body through the lungs. Nature Reviews Drug Discovery, 6(1)(2007). pp. 67-74.
[21] J. Heyder, Deposition of inhaled particles in the human respiratory tract and consequences for regional targeting in respiratory drug delivery. Proceedings of the American Thoracic Society, 1(4)(2004). pp. 315-20.
[22] D.A. Edwards, J. Hanes, G. Caponetti, J. Hrkach, and R. Langer, Large Porous Particles for Pulmonary Drug Delivery. Science. (1997). p. 1868-1871.
[23] R. Langer, Drug delivery. Drugs on target. Science. (2001). p. 58-59.
[24] R. Langer and N.A. Peppas, Advances in Biomaterials, Drug Delivery, and Bionanotechnology. AIChE Journal, 49(2003). pp. 2990-3006.
[25] D.A. LaVan, T. McGuire, and R. Langer, Small-scale systems for in vivo drug delivery. Nature Biotechnolgy, 21(10)(2003). pp. 1184-91.
[26] C.S. Tsai, R.W. Mao, S.K. Lin, N. Wang, and S.C. Tsai, Miniaturized multiple Fourier-horn ultrasonic droplet generators for biomedical applications. Lab Chip, 10(20)(2010). pp. 2733-40.
[27] C.S. Tsai, R.W. Mao, S.K. Lin, Y. Zhu, and S.C. Tsai, Faraday instability-based micro droplet ejection for inhalation drug delivery. Technology (Singap World Sci), 2(1)(2014). pp. 75-81.
[28] J.S. Lass, A. Sant, and M. Knoch, New advances in aerosolised drug delivery: vibrating membrane nebuliser technology. Expert Opinion on Drug Delivery, 3(5)(2006). pp. 693-702.
[29] B.L. Rottier, C.J.P. van Erp, T.S. Sluyter, H.G.M. Heijerman, H.W. Frijlink, and A.H. de Boer, Changes in performance of the Pari eFlow (R) Rapid and Pari LC Plus (TM) during 6 months use by CF patients. Journal of Aerosol Medicine and Pulmonary Drug Delivery, 22(2009). pp. 263-269.
[30] B. Mortimer, G. Saban, A. Samboer, and B. Verveckken, The development of an ultrasonic humidifier for domestic applications Domestic use of Electrical Energy Conference. (1999). p. 138-140.
[31] E.H. Trinh, Compact acoustic levitation device for studies in fluid dynamics and material science in the laboratory and microgravity Review of Scientific Instruments, 56(11)(1985). pp. 2059.
[32] A.V. Anilkumar, C.P. Lee, and T.G. Wang, Stability of an acoustically levitated and flattened drop: An experimental study Physics of Fluids A (Fluid Dynamics), 5(11)(1993). pp. 2763-74.
[33] M. Rein, Phenomena of liquid drop impact on solid and liquid Fluid Dynamics Research, 12(2)(1993). pp. 61-93.
[34] W.T. Shi, R.E. Apfel, and R.G. Holt, Instability of a deformed liquid drop in an acoustic field. Physics of Fluids, 7(11)(1995). pp. 2601-2607.
[35] R. Rioboo, C. Tropea, and M. Marengo, Outcomes From A Drop Impact On Solid Surfaces, Atomization and Sprays, 11(2)(2001). pp. 155-165.
[36] A.L. Yarin, D.A. Weiss, G. Brenn, and D. Rensink, Acoustically levitated drops: drop oscillation and break-up driven by ultrasound modulation. International Journal of Multiphase Flow, 28(2002). pp. 887-910.
[37] A.L. Yarin, Drop impact dynamics: Splashing, Spreading, Receding, Bouncing. Annual Review of Fluid Mechanics, 38(2006). pp. 159-192.

[38] S. Timoshenko, Vibration problems in Engineering (1937): D. VAN NOSTRAND COMPANY, INC.
[39] A.W. Leissa, Vibration of plates. (1969): NASA United States. 362.
[40] J.A. Gallego-Juarez, Axisymmetric Vibrations Of Circular Plates With Stepped Thickness. Journal of Sound and Vibration, 26 (3)(1973). pp. 411-416.
[41] J.A. Gallego-Juárez, G. Rodríguez-Corral, E.R.-F.D. Sarabia, F. Vázquez-Martínez, V.M. Acosta-Aparicio, and C. Campos-Pozuelo, Development Of Industrial Models Of High-Power Stepped-Plate Sonic And Ultrasonic Transducers For Use In Fluids. Ultrasonics Symposium, 2001 IEEE. (2001). p. 571-578.
[42] J.A. Gallego-Juarez, G. Rodriguez-Corral, E.R.-F.d. Sarabia, F. Vazquez-Martinez, C. Campos-Pozuelo, and V.M. Acosta-Aparicio, Recent developments in vibrating-plate macrosonic transducers. Ultrasonics, 40(2002). pp. 889–893.
[43] J.L.S. Emeterio, J.A. Gallego-Juarez, and G. Rodriguez-Corral, High Axisymmetric Modes Of Vibration Of Stepped Circular Plates. Journal of Sound and Vibration, 114(3)(1987). pp. 495-505.
[44] A.M. Al-Jumaily and K. Jameel, Influence of the Poisson Ratio on the Natural Frequencies of Stepped-Thickness Circular Plate. Journal of Sound and Vibration, 234(5)(2000). pp. 881-894.
[45] R.H. Gutierrez, P.A.A. Laura, and R.O. Grossi, Transverse vibrations of plates with stepped thickness over a concentric circular region. Journal of sound and vibration, 69(2)(1980). pp. 285-295.
[46] R.H. Gutierrez and P.A.A. Laura, Transverse Vibrations of Circular Plates with Stepped Thickness. Applied Acoustics, 15(1982). pp. 71-76.
[47] M. Toda and S. Tosima, Theory of Curved, Clamped, Piezoelectric Film, Air-Borne Transducers. IEEE Transactions on Ultrasonics, Ferroelectrics, and Frequency Control, 47(6)(2000). pp. 1421-1431.
[48] M. Toda and J. Dahl, PVDF corrugated transducer for ultrasonic ranging sensor. Sensors and Actuators A: Physical, 134(2)(2007). pp. 427-435.
[49] A.E.H. Love, The small Free Vibrations and Deformation of a Thin Elastic Shell. Philosophical Transactions of the Royal Society of London A, 179(1888). pp. 491-546.
[50] J.D. Watkins and R.R. Clary, Vibrational Characteristics Of Some Thin-Walled Cylindrical And Conical Frustum Shells (1965), Nasa Technical Note; NASA TN D-2729.
[51] A.W. Leissa, Vibration of shells. (1973): NASA, Washington, United States. 438.
[52] W. Soedel, A new frequency formula for closed circular cylindrical shells for a large variety of boundary conditions. Journal of Sound and Vibration, 70(3)(1980). pp. 309-317.
[53] Y.Y. Yu, Free vibrations of thin cylindrical shells having finite lengths with freely supported and clamped edges. Journal of Applied Mechanics 22(1955). pp. 547-552.
[54] C. Wang and J.C.S. Lai, Prediction of natural frequencies of finite length circular cylindrical shells. Applied Acoustics, 59(2000). pp. 385-400.
[55] X.M. Zhang, G.R. Liu, and K.Y. Lam, Vibration Analysis of Thin Cylindrical Shells Using Wave Propagation Approach. Journal of Sound and Vibration, 239(3)(2001). pp. 397-403.
[56] B.r. Li, X.-y. Wang, H.-l. Ge, and Y.-m. Ding, Study on applicability of modal analysis of thin finite length cylindrical shells using wave propagation approach. Journal of Zhejiang University SCIENCE, 6A(10)(2005). pp. 1122-1127.
[57] L. Xuebin, Study on free vibration analysis of circular cylindrical shells using wave propagation. Journal of Sound and Vibration, 311(2008). pp. 667–682.
[58] W. Soedel, Vibrations of shells and plates. (2004): Marcel Dekker, Inc. New York.
[59] N. Ganesan and K.R. Sivadas, Vibration analysis of orthotropic shells with variable thickness. Composite Structures, 35(1990). pp. 239-248.
[60] K.R. Sivadas and N. Ganesan, Vibration analysis of orthotropic cantilever cylindrical shells with axial thickness variation. Composite Structures, 22(1992). pp. 207-215.

[61] Y. Qu, Y. Chen, X. Long, H. Hua, and G. Meng, Free and forced vibration analysis of uniform and stepped circular cylindrical shells using a domain decomposition method. Applied Acoustics, 74(3)(2013). pp. 425-439.
[62] D. Tang, X. Yao, G. Wu, and Y. Peng, Free and forced vibration analysis of multi-stepped circular cylindrical shells with arbitrary boundary conditions by the method of reverberation-ray matrix. Thin-Walled Structures, 116(2017). pp. 154-168.
[63] H.F. TIERSTEN, Linear Piezoelectric Plate Vibrations. (1969), New York: Plenum.
[64] N.T. Adelman, Y. Stavsky, and E. Segal, Axisymmetric Vibrations of Radially Polarized Piezoelectric Ceramic Cylinders. Journal of Sound and Vibration, 38(2)(1975). pp. 245-254.
[65] H.S. TZOU, Piezoelectric Shells Distributed Sensing and Control of Continua. (1993): Kluwer Academic Publishers.
[66] P. Lu, K.H. Lee, W.Z. Lin, F. Shen, and S.P. Lim, An Approximate Frequency Formula for Piezoelectric Circular Cylindrical Shells. Journal of Sound and Vibration, 242(2)(2001). pp. 309-320.
[67] H.J. Ding, R.Q. Xu, and W.Q. Chen, Free vibration of transversely isotropic piezoelectric circular cylindrical panels. International Journal of Mechanical Sciences, 44(2002). pp. 191-206.
[68] J.O. Kim, K.K. Hwang, and H.G. Jeong, Radial vibration characteristics of piezoelectric cylindrical transducers. Journal of Sound and Vibration, 276(3-5)(2004). pp. 1135-1144.
[69] J.O. Kim and J.G. Lee, Dynamic characteristics of piezoelectric cylindrical transducers with radial polarization. Journal of Sound and Vibration, 300(1-2)(2007). pp. 241-249.
[70] A.M. Al-Jumaily and A. Meshkinzar, On the Development of Focused Ultrasound Liquid Atomizers. Advances in Acoustics and Vibration, (Article ID 7861726)(2017). pp. 1-10.
[71] S. Sangwan, R. Condos, and G.C. Smaldone, Lung deposition and respirable mass during wet nebulization. Journal od Aerosol Medicine, 16(4)(2003). pp. 379-386.
[72] O.R. TG, K. LI, H. K, and S. GC, Predicting aerosol deposition during neonatal ventilation: feasibility of bench testing. Respiratory Care, 39(1994). pp. 1162-1168.
[73] S.A. Elrod, B. Hadimioglu, B.T. Khuri-Yakub, E.G. Rawson, and C.F. Quate. Focused Acoustic Beams for Nozzleless Droplet Formation. Ultrasonics Symposium. (Year) of Conference. Chicago, IL: IEEE.
[74] 1.65MHz Nebulizer Boards Catalog. L. APC International, Editor.
[75] Siansonic General atomizing kit Catalog. S.T.C. Ltd, Editor.
[76] Siansonic Mini Nebulizer kit Catalog. S.T.C. Ltd, Editor.
[77] Siansonic High Efficiency Atomizer Transducer Catalog. S.T.C. Ltd, Editor.
[78] A. Lozano, H. Amaveda, F. Barreras, X. Jordà, and M. Lozano, High-Frequency Ultrasonic Atomization With Pulsed Excitation. Journal of Fluids Engineering, 125(6)(2004). pp. 941-645.
[79] M. Kurosawa, T. Watanabe, A. Futami, and T. Higuchi, Surface acoustic wave atomizer. Sensors and Actuators A: Physical, 50(1995). pp. 69-74.
[80] W. Soluch and T. Wrobel Low driving power SAW atomiser. Electronics Letters, 42 (2006). 1432 DOI: 10.1049/el:20062776.
[81] A. Lal and R.M. White. Micromachined Silicon Ultrasonic Atomizer. IEEE ULTRASONICS SYMPOSIUM. (Year) of Conference.: IEEE.
[82] S.C. Tsai, Y.L. Song, T.K. Tseng, Y.F. Chou, B.J. Chen, and C.S. Tsai, High-frequency, silicon-based ultrasonic nozzles using multiple Fourier horns. IEEE Transactions on Ultrasonics, Ferroelectrics and Frequency Control, 51(3)(2004). pp. 277-285.
[83] C.S. Tsai, R.W. Mao, S.K. Lin, E. Chien, and S.C. Tsai, MEMS-based multiple fourier-horn silicon ultrasonic atomizer for inhalation drug delivery IEEE International Ultrasonics symposium. (2011), IEEE. p. 1119-1122.

[84] S. Yuan, Z. Zhou, and G. Wang, Experimental research on piezoelectric array microjet. Sensors and Actuators A: Physical, 108(2003). pp. 182-186.
[85] S. Yuan, Z. Zhou, G. Wang, and C. Liu, MEMS-based piezoelectric array microjet. Microelectronic Engineering, 66(2003). pp. 767-772.
[86] A. Al-Jumaily and P. Reddy, Medical Devices For Respiratory Dysfunction: Principles and Modeling of Continuous Airway Pressure (CPAP). (2012), New York: ASME Press.
[87] T. Li, Y. Chen, and J. Ma, Development of a Miniaturized Piezoelectric Ultrasonic Transducer. IEEE Transactions on Ultrasonics, Ferroelectrics, and Frequency Control, 56(3)(2009). pp. 649-659.
[88] K. Nakamura, Ultrasonic Transducers. (2012): Woodhead Publishing Limited.
[89] Y. Xiang, T. Ma, S. Kitipornchai, C. Lim, and C. Lau, Exact solutions for vibration of cylindrical shells with intermediate ring supports. International Journal of Mechanical Sciences, 44(2002). pp. 1907-1924.
[90] M. Naeem and C. Sharma, Prediction of natural frequencies for thin circular cylindrical shells. Proceedings of the Institution of Mechanical Engineers, Part C: Journal of Mechanical Engineering Science, 214(2000). pp. 1313-1328.
[91] H. Tang and C. Wong, Vibration of a viscous liquid sphere. J Phys. A: Math., Nucl., Gen., 7(9)(1974). pp. 1038-1050.
[92] E. Trinh and T.G. Wang, Large-amplitude free and driven drop-shape oscillations: experimental observations. Journal of Fluid Mechanics, 122(1982). pp. 315-338.
[93] T. Patzek, R. Benner, O. Basaran, and L. Scriven, Nonlinear Oscillations of lnviscid Free Drops. Journal Of Computational Physics, 97(1991). pp. 489-515.
[94] O.A. Basaran, Nonlinear oscillations of viscous liquid drops. Journal of Fluid Mechanics, 241(-1)(2006). pp. 169.
[95] E. Becker, W.J. Hiller, and T.A. Kowalewski, Experimental and theoretical investigation of large-amplitude oscillations of liquid droplets. Journal of Fluid Mechanics, 231(-1)(2006). pp. 189.
[96] T.S. Lundgren and N.N. Mansour, Oscillations of drops in zero gravity with weak viscous effects. Journal of Fluid Mechanics, 194(-1)(2006). pp. 479.
[97] A.L.N. Moreira, A.S. Moita, E. Cossali, M. Marengo, and M. Santini, Secondary atomization of water and isooctane drops impinging on tilted heated surfaces. Experiments in Fluids, 43(2-3)(2007). pp. 297-313.
[98] M. Arai, A. Ishii, and M. Saito, Atomization behaviour and energy analysis for a single droplet impinged on a surface oscillating with ultrasonic frequency. Atomization and Sprays, 17(2007). pp. 601-620.
[99] A. Burdukov and V. Nakoryakov, On mass transfer in an acoustic field. Journal of applied Mechanics and Technical Physics, 6(2)(1966). pp. 51-55.
[100] P. Larsen and J. Jensen, Evaporation Rates of Drops in Forced Convection with Superposed Transverse Sound Field. International Journal of Heat and Mass Transfer, 21(4)(1978). pp. 511-517.
[101] R. Sujith, G. Waldherr, J. Jagoda, and B. Zinn, An Experimental Investigation of the Behavior of Droplets in Axial Acoustic Fields. Journal of Vibration and Acoustics, 119(3)(1997). pp. 285-292.
[102] R. Sujith, G. Waldherr, J. Jagoda, and B. Zinn, A Theoretical Investigation of the Behavior of Droplets in Axial Acoustic Fields. Journal of Vibration and Acoustics, 121(3)(1999). pp. 286-294.
[103] R.I. Sujith, G.A. Waldherr, J.I. Jagoda, and B.T. Zinn, Experimental Investigation of the Evaporation of Droplets in Axial Acoustic Fields. Journal of Propulsion and Power, 16(2)(2000). pp. 278-285.
[104] S. Temkin, Gasdynamic agglomeration of aerosols. I. Acoustic waves. Physics of Fluids, 6(7)(1994). pp. 2294-2303.
[105] L. Kinsler, Fundamentals of acoustics. 4 ed. (2000): New York, Wiley.

[106] N. Kawahara, A.L. Yarin, G. Brenn, O. Kastner, and F. Durst, Effect of acoustic streaming on the mass transfer from a sublimating sphere. Physics of Fluids, 12(4)(2000). pp. 912-923.
[107] A. Hjelmfelt and L. Mockros, Motion of Discrete Particles in a Turbulent Fluid. Applied Scientific Research, 16(1966). pp. 149-161.
[108] ANSYS Meshing Application Introduction, Training Manual. (2009), ANSYS Inc.
[109] A. Lozano, H. Amaveda, F. Barreras, X. Jordà, and M. Lozano, High-Frequency Ultrasonic Atomization With Pulsed Excitation. Journal of Fluids Engineering, 125(6)(2003). pp. 941.
[110] Noliac piezo tutorial: Piezo basics. Noliac. p. 19.
[111] Piezoelectric Ceramic Products: Fundamentals, Characteristics And Applications. PI Ceramic. p. 44.
[112] D. Berlincourt and H.H.A. Krueger, Technical Publication TP-226 Properties of Piezoelectricity Ceramics. Morgan Electro Ceramics. p. 1-12.
[113] MX200 – High Performance Piezo Driver Catalog. Micromechatronics, Inc.
[114] D. Munz, T. Fett, S. Muller, and G. Thun, Deformation and strength behaviour of a soft PZT ceramic. SPIE Conference on Mathematics and Control in Smart Structures. (1998): San Diego, California. p. 84-95.
[115] T. Fett, D. Munz, and G. Thun, Tensile and bending strength of piezoelectric ceramics. Journal Of Materials Science Letters, 18(1999). pp. 1899-1902.
[116] O. Guillon, F. Thiebaud, P. Delobelle, and D. Perreux, Tensile behavior of PZT in short and open-circuit conditions. Materials Letters, 58(6)(2004). pp. 986-990.